Faculty of Science
Department of Imaging and Applied Physics

Assessing the Suitability of Fly Ash Geopolymers for High Temperature Applications

William D. A. Rickard

This thesis is presented for the degree of
Doctor of Philosophy
of
Curtin University

June 2012

Declaration

To the best of my knowledge and belief this thesis contains no material previously published by any other person except where due acknowledgement has been made.

This thesis contains no material which has been accepted for the award of any other degree or diploma in any university.

Signature : …….

Date : …….

Abstract

Geopolymers are an inorganic polymer synthesised from the dissolution and polycondensation of aluminosilicates in alkaline solutions under hydrothermal condition, yielding an amorphous, three-dimensional polymeric framework (Davidovits, 1991). They are a broad class of binding material with applications that range from conventional concrete to high tech, light weight composites for use in aviation. Geopolymers have also shown promise for use in high temperature applications, such as fire proof coatings, structural concrete in fire prone areas and thermal insulation for refractory type applications, due to their intrinsic thermal stability (Barbosa and MacKenzie, 2003a).

This thesis reports on an investigation into the thermal performance of geopolymers synthesised from a range of fly ashes in order to assess their suitability for use in high temperature applications. Five fly ashes from Australian power stations with contrasting chemical properties were used in the study. Geopolymers were synthesised from each of the fly ashes using sodium silicate or sodium aluminate solutions in order to achieve a set range of Si:Al compositional ratios. Thermal analysis was conducted up to 1000 °C using a constant heat rate as well as a heating regime that simulated the conditions during a fire.

The fly ashes were characterised in terms of elemental composition, phase composition, particle size, density and morphology prior to being used to synthesise geopolymers. It was determined that only a portion of each of the fly ashes was available for geopolymerisation and that the reactive Si:Al ratio (amorphous Si:Al ratio) varied greatly between the fly ashes. Collie and Port Augusta fly ashes had relatively low reactive Si:Al ratios (1.15 and 1.84, respectively) whereas Eraring, Tarong and Bayswater fly ashes had high Si:Al ratios (4.98, 8.84 and 7.49, respectively). All of the fly ashes had a predominantly spherical morphology, characteristic of fly ashes, though only the Collie and Port Augusta fly ashes had a significant portion of sub 5 µm particles.

The thermo-physical, mechanical and micro-structural properties of the geopolymers made from each of the fly ashes are presented and the effect of the source fly ash characteristics on the hardened product is discussed. The results varied greatly with fly ash source and the most influential fly ash characteristic was the reactive Si:Al ratio. Fly ashes with a high reactive Si:Al ratio (≥5) were sodium aluminate activated and produced geopolymers with low to moderate as-cured compressive strengths but exhibited excellent dimensional stability during heating and greater compressive strengths after heating. Fly ashes with a low reactive Si:Al ratio (<2) were sodium silicate activated and produced geopolymers with high as-cured compressive strengths but exhibited poor dimensional stability during heating and greatly reduced compressive strengths after heating. All samples exhibited strength improving microstructural changes such as improved inter-particle bonding due to sintering after firing. However, the instability of non geopolymer phases during high temperature exposure led to strength losses in some samples depending on the type and composition of the activating solution.

Geopolymers from three of the fly ashes were assessed for their performance upon exposure to a simulated fire. Solid and low density foamed variants ($\rho \approx 0.9$ g cm^{-3}, $k \approx 0.3$ W $m^{-1}K^{-1}$) of the mixes were used for fire testing. Fire ratings of between 60 and 90 minutes for a sample thickness of 50 mm were achieved. The solid geopolymers exhibited better fire ratings than the low density geopolymers due to their higher water content (as they contained more of the hydrated geopolymer phase). Microstructural analysis of the fire tested samples indicated that the geopolymers were not significantly damaged by dehydration and the fire exposed side exhibited analogous changes to the samples that were gradually heated to 1000 °C.

The results in this thesis indicate that fly ash geopolymers have great potential for utilisation in high temperature applications provided they are synthesised from a source material with suitable physical and compositional characteristics.

Acknowledgements

I would like to acknowledge and thank all the people that have helped me during my PhD as I would not have been able to complete this work without their support.

Firstly I would like to acknowledge the immense contribution of my supervisor, Professor Arie van Riessen. His enduring encouragement, guidance, friendship and support have been critical to the completion of this thesis and my development as a scientist.

I would like to thank all my friends and family and in particular my wife Jessica and my parents, Gillian and David. Their endearing love and support has provided the foundation for which all my achievements have been built on.

Many aspects of the research were beyond my previous experience and as such I benefitted greatly from the technical advice and assistance from many of my colleagues. I would like to thank Jadambaa Temuujin, Ross Williams, Nigel Chen-Tan, Elaine Miller, Rob Hart, Glen Lawson, Ming Lim and Mark Winstanley as well as the other students and staff in the Physics department at Curtin University. Their knowledge and experience with technical equipment in the laboratory has been extremely helpful in my experimental work.

Lastly I would like to acknowledge the facilities and organisations that supported my research. I would like to thank Curtin University and the Centre for Sustainable Resource Processing for providing me with financial support. I would also like to thank the Australian Synchrotron and the staff at the powder diffraction beamline for giving me the opportunity to access their facilities. Finally I would like to acknowledge the facilities, scientific and technical assistance of the Centre for Materials Research and specifically the Curtin University Electron Microscopy Laboratory.

Table of Contents

List of Figures

List of Tables

List of Abbreviations

AS	Australian standard
ASTM	American society for testing and materials
BSE	Backscattered electron
CIF	Crystallographic information file
DSC	Differential scanning calorimetry
DTA	Differential thermal analysis
EDS	Energy dispersive x-ray spectroscopy
FESEM	Field emission scanning electron microscopy
GP	Geopolymer
GPa	Giga Pascals
HTXRD	High temperature x-ray diffraction
ICSD	Inorganic crystal structure database
ISO	International organisation for standardisation
LOI	Loss on ignition
MPa	Mega Pascals
OPC	Ordinary Portland cement
PDF	Powder diffraction file
SE	Secondary electron
SEM	Scanning electron microscopy
SXRD	Synchrotron x-ray diffraction
TEM	Transmission electron microscopy
T_g	Glass transition temperature
TGA	Thermo-gravimetric analysis
Wt.%	Weight per cent
XRD	X-ray diffraction
XRF	X-ray fluorescence spectroscopy

Chapter 1
Introduction

"Happy is he who gets to know the reasons for things."

Virgil (70-19 BCE) Roman poet

1.1 Overview

Geopolymers are a class of material synthesised by the reaction of a solid aluminosilicate with a concentrated aqueous alkali hydroxide solution (Duxson et al., 2007a). They are a broad class of binding material with applications that range from conventional concrete to high tech, light weight composites for use in aviation. Geopolymers have also shown promise for use in high temperature applications, such as fire proof coatings, structural concrete in fire prone areas and thermal insulation for refractory type applications, due to their intrinsic thermal stability (Barbosa and MacKenzie, 2003a).

The designation 'Geopolymer' was first coined in 1979 by Joseph Davidovits, though the technology has been around for much longer. Davidovits (1987) reported that in ancient times synthetic rocks were formed by mixing kaolinite, dolomite or limestone with Na_2CO_3 or K_2CO_3 (obtained from plant ashes or salt lakes) and silica. This mixture produces alkali hydroxides that, when mixed with water, react strongly with the other additives to form a geopolymer-like binding material (van Jaarsveld et al., 1997). Davidovits argues that some of the Egyptian pyramids were made from geopolymers and the fact that they are still standing is a testament to the durability of geopolymers (Davidovits, 1984).

Modern research on alkali activated aluminosilicates began in the late 1930's with research by Feret (1939) and then Purdon (1940). Later, Glukhovsky (1959), Krivenko (1994) and Kovalchuk (2007) provided the foundations of the modern day understanding of alkali activated aluminosilicates (Pacheco-Torgal et al., 2008). An increasing demand for greater performance and lower environmental impact for construction materials has significantly increased the interest in geopolymers over the last 20 years. Nowadays, research on geopolymers involves scientists from all around the world as well as a number of commercial entities who are introducing the technology to the market.

1.1.1 Advantages of Geopolymer materials - Environmental Case

One of the main drivers for the development of geopolymer based materials is due to their environmental credentials. Geopolymer concretes are able to be produced with substantially less CO_2 emissions than an equivalent ordinary Portland cement (OPC) product (Davidovits, 1994a, McLellan et al., 2011). Geopolymers also have the potential to be made using industrial waste materials, such as fly ash, further enhancing their environmental credentials. In a political climate where governments around the world are beginning to tax CO_2 emissions and promote sustainable and environmentally friendly materials, geopolymers are emerging as an essential material of the future.

Concrete is a very important global construction material with consumption second only to water (Sabir et al., 2001). The binding phase which is responsible for the mechanical strength in conventional concrete is OPC. OPC, or commonly abbreviated to 'cement', is produced by the calcination of limestone and silica rich materials according to the following reaction (1.1) (Davidovits, 1991);

$$5CaCO_3 + 2SiO_2 \rightarrow (3CaO, SiO_2)(2CaO, SiO_2) + \mathbf{5CO_2} \quad \textbf{1.1}$$

In this reaction there is a large amount of carbon dioxide (CO_2) produced. For every tonne of cement, there is 0.55 tonne of CO_2 produced that is released into the atmosphere. Furthermore, the high energy requirements of the calcination process requires the combustion of 0.4 tonne of carbon-fuel yielding a total CO_2 emission of 0.95 tonne for every tonne of Portland cement (Davidovits, 1991). However, this value can be as low as 0.5 tonne of CO_2 per tonne of cement by improving process efficiencies and increasing the amount of additives (Worrell et al., 2001). Figure 1-1 shows the regional variation in average CO_2 emissions per tonne of cement produced. The world average at the time of the Worrell et al. (2001) publication was 0.81 tonne CO_2 / tonne cement (equivalent to 0.22 tonne carbon / tonne cement). There will continue to be improvements to production efficiencies but the unavoidable emissions from the calcination of limestone means that OPC production will always be associated with high CO_2 emissions.

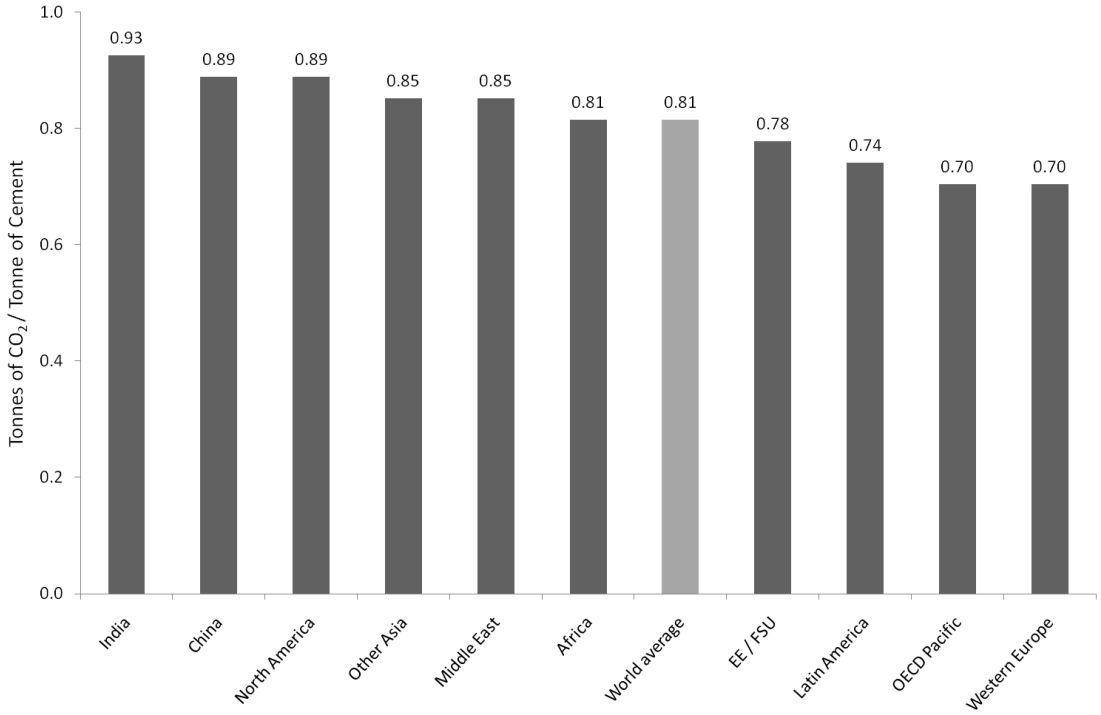

Figure 1-1 Region efficiencies of cement production. Adapted using data from Worrel et al. (2001).

Figure 1-2 shows the rapid rise in total CO_2 emissions globally as well as the contribution from the cement industry. Emissions from cement production (386 million tonnes of carbon in 2008) have more than doubled since the mid 1970s and now represent 4.5 % of global CO_2 emissions (Boden et al., 2010). With the modernisation of China and other emerging countries, the usage of cement is ever increasing and so are the associated CO_2 emissions. The necessity for a low CO_2 cement replacement for ordinary Portland cement is becoming increasingly important.

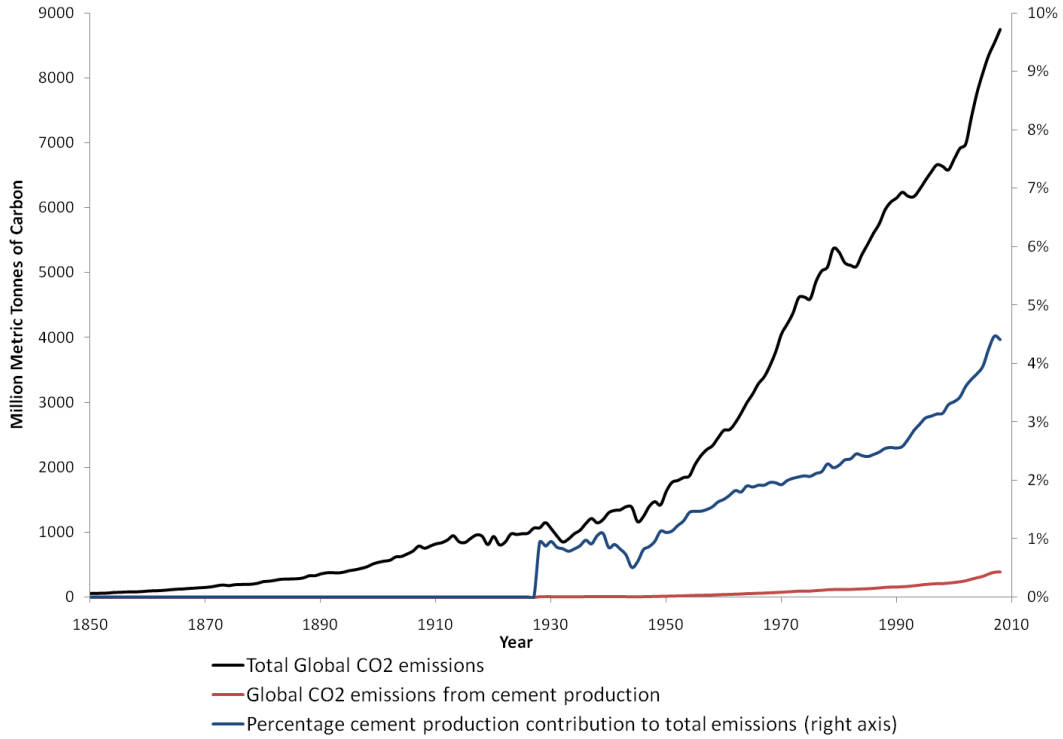

Figure 1-2 Global CO_2 emissions and contribution from the cement industry. Produced using data from Boden et al. (2010).

Geopolymers have attracted much attention as a potential replacement of OPC due to the fact that the production of geopolymer cement creates substantially less CO_2 emissions. There is no CO_2 created in the synthesis of a geopolymer cured at ambient, though some emissions can be attributed to the production of the alkali activator, most notably the alkali silicates. It has been estimated that the total emissions from the production of geopolymer cements are 80 % less than that of ordinary Portland cements (Davidovits, 2000). Other researchers have quoted a lower CO_2 reduction (44-64 %), though either way the reduction is significant (McLellan et al., 2011). The utilisation of geopolymer cement as an alternative to ordinary Portland cement could substantially reduce global CO_2 emissions.

The other potential environmental benefit of the introduction of geopolymer products into the market place is the utilisation of industrial waste products as either the aluminosilicate source or the alkaline activator. Some examples of suitable industrial waste products are fly ash from coal fired power generation, rice husk ash from rice production and sodium aluminate from alumina production. It has been reported that the use of industrial waste products over purer sources, such as metakaolin, further

reduce the CO_2 emissions associated with geopolymers as they generally have a Si:Al ratio closer to target ratios and thus require less alkali silicates in their formulation (Komnitsas, 2011).

By far the most promising and most researched industrial waste product is fly ash. Huge volumes of fly ash are generated around the world (more details in chapter 2). Most of the fly ash is not effectively used, and a large proportion of it is disposed of in landfills. As the need for power increases, the volume of fly ash produced will increase. Geopolymers provide a potential solution as they can utilise this waste product preventing it from going into landfill or tailings dams.

As we become more aware of the effects of CO_2 on the environment, the demand for more environmentally friendly materials will increase. As previously explained, there is a need to substitute low CO_2 cement for ordinary Portland cement and also a need to recycle waste materials, both of which can be facilitated with the use of geopolymers.

1.1.2 Advantages of Geopolymer Materials - Performance Case

Environmental benefits alone will not ensure the acceptance of geopolymer products. Geopolymers, as with any new material, must either match or have improved physical performance characteristics to the materials it replaces. Fortunately, geopolymers have been shown to have superior properties to existing equivalent materials in the areas of mechanical strength (Hardjito and Rangan, 2005), acid resistance (Bakharev, 2005, Temuujin et al., 2011), fire and heat resistance (Kong et al., 2005, Kovalchuk and Krivenko, 2009, Rickard et al., 2011, Temuujin et al., 2012, Temuujin et al., 2010), toxic waste immobilisation (van Jaarsveld et al., 1997, Aly et al., 2008) and industrial adhesives (Bell et al., 2008a). These unique properties allow for a multitude of potential applications for geopolymers which is why the research into geopolymer technology is so diverse.

Some examples in the literature of geopolymers with unique high performance properties include; Kovalchuk et al. (2007) synthesised fly ash based geopolymers

with a compressive strength over 100 MPa only 8 hours after alkali activation; Bell et al. (2009) made caesium based geopolymers that exhibited less than 2 % shrinkage upon heating up to 1200 °C; He et al. (2010) found that for unidirectional carbon fibre geopolymer composites heat treated at 1100 °C, the flexural strength, work of fracture and Young's modulus increased by 76 %, 15 % and 75 %, respectively, relative to their original state; Aly et al. (2008) studied the aqueous leachability of metakaolin based geopolymers and found them to pass the PCT-B leach test (ASTM 1285-02) for low level and intermediate level nuclear waste encapsulation.

It should be mentioned that not all geopolymers exhibit all of these physical properties. Geopolymers can be tailored to suit their intended application which may mean, for example, the mechanical strength being reduced to improve the fire resistance (Temuujin et al., 2009a).

1.2 Research Objectives

This thesis documents the work undertaken to assess the suitability of geopolymers for use in high temperature industrial applications. More specifically, the use of fly ash as an aluminosilicate source material for the synthesis of thermally resistant geopolymers will be investigated. The objective of the research was to characterise the thermal performance of a range of geopolymers synthesised from five different fly ash sources in order to assess their potential for utilisation in high temperature applications.

Fly ash and geopolymer samples synthesised during the study were characterised using a wide range of techniques including mechanical strength testing, thermal expansion, thermal conductivity, density, electron microscopy, x-ray diffraction, x-ray fluorescence and simulated fire exposure. Fundamental research into the chemical and physical processes leading to the observed results was also conducted to develop a better understanding of the behaviour of fly ash geopolymers at elevated temperatures.

1.3 Significance of the Research

Geopolymer products synthesised from fly ash have the potential to provide superior performance compared to existing thermally resistant materials. In addition, there are the associated economic and environmental benefits from their utilisation. As such the development of fly ash geopolymer technology must be encouraged as it can provide significant benefits to the greater community.

The available literature on geopolymers intended for high temperature applications has been primarily focussed on materials made from pure sources such as metakaolin. Duxson et al. (2005, 2007b), Barbosa & MacKenzie (2003a) and Subaer (2005) studied the thermal properties of metakaolin geopolymers. Metakaolin is a relatively pure aluminosilicate source, whereas fly ash contains a significant proportion of non-aluminosilicate phases. This makes fly ash geopolymers inherently more complicated and as such comprehensive research is required before an adequate understanding of their thermal properties can be achieved.

Recent studies have indicated that geopolymers made from fly ash can exhibit equal, if not superior, properties to that of geopolymers made from metakaolin (Kong et al., 2007). The effect of the non-aluminosilicate phases in fly ash geopolymers, most notably iron and crystalline silica, at high temperatures has not been comprehensively characterised. For fly ash geopolymers to be utilised in any high temperature application, an extensive study on the thermal properties of fly ash geopolymers was warranted.

The data and ideas presented in this thesis will be useful to other scientists and commercial companies looking to further develop geopolymer technology, thus aiding in the development and utilisation of environmentally friendly and sustainable materials.

1.4 Research Method

The research involved five major development steps starting with characterisation of the fly ashes and finishing with exposing geopolymers to fire like conditions. At each step a range of techniques were utilised to achieve a sufficient understanding of the material in order to progress to the next step. A schematic describing the research path is presented in Figure 1-3. On the left of the schematic is a reference to the iterative process used for mix optimisation. The bulk of the results presented in this thesis are based on the final iteration samples though this does not imply that the optimisation was exhaustive. Several papers published during the PhD are cited throughout the thesis.

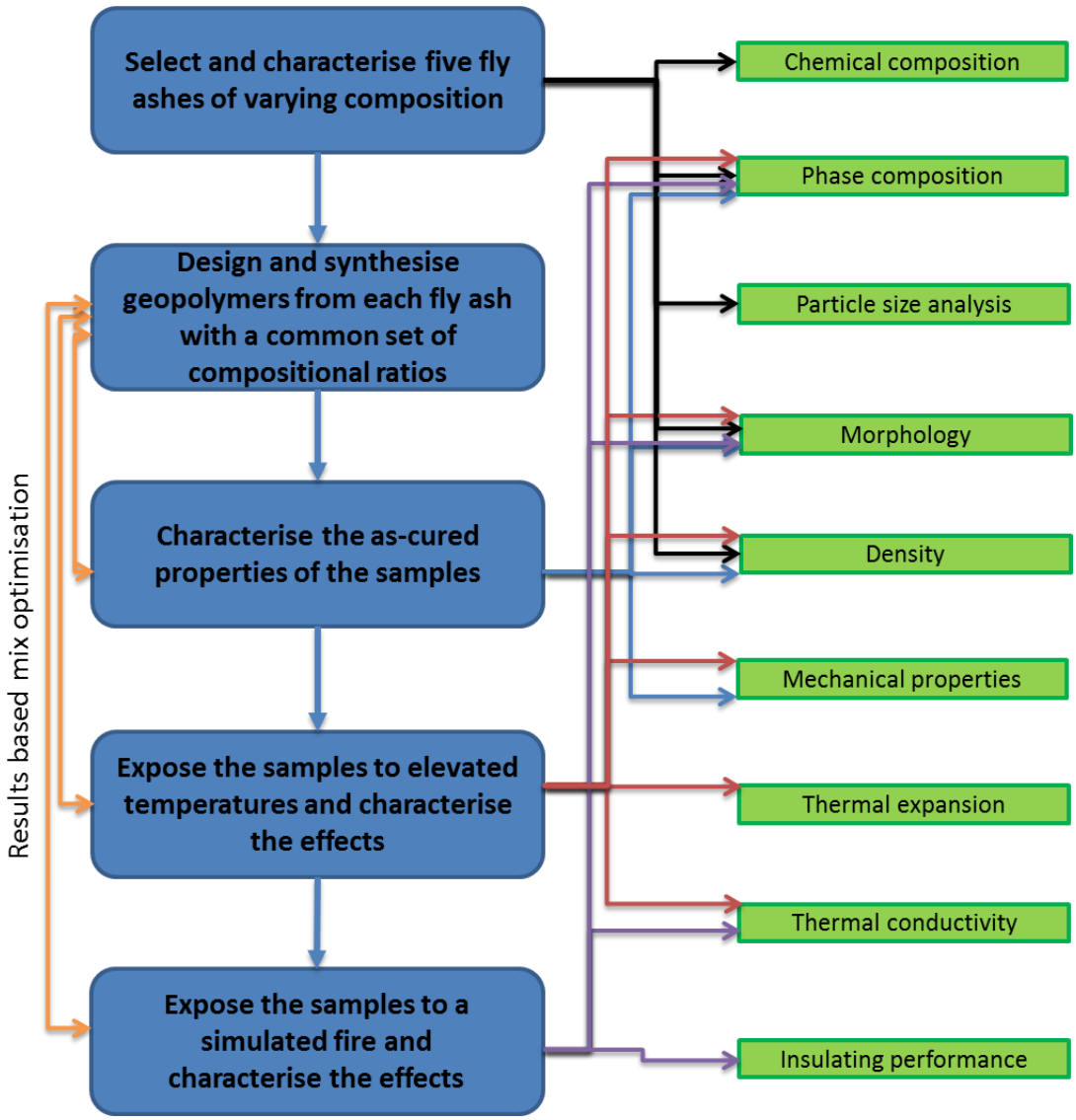

Figure 1-3 Schematic detailing the work flow used during this project.

1.5 Organisation of the Thesis

A conventional thesis format has been used. A thorough literature review of geopolymers in general and more specifically on the thermal properties of geopolymers is covered in chapter 2. Chapter 3 details the experimental methods and equipment used to characterise samples.

Chapter 4 presents and discusses the experimental results on the characterisation of the five fly ashes. Chapter 5 presents and discusses the results from the characterisation of a range of geopolymers before and after high temperature exposure in terms of physical property evolution. Chapter 6 presents the results from the microstructural analysis of the geopolymers before and after high temperature exposure. Chapter 7 presents the results from experiments where solid and foamed geopolymers were exposed to fire like conditions.

Chapter 8 contains the conclusions made in this study and includes suggestions for future research.

CHAPTER 2
LITERATURE REVIEW

"In questions of science the authority of a thousand is not worth the humble reasoning of a single individual."

Galileo Galilei

2.1 Introduction

This chapter explores the available literature associated with geopolymers in general and more specifically on the thermal properties of geopolymers. Also included in this chapter is a review of other fire proofing materials and a concluding section which discusses current and future applications for geopolymers.

2.2 Geopolymer Categorisation and Nomenclature

Geopolymers are generally categorised as a sub-group of a broad group of alkali activated materials, due to their low calcium content (Figure 2-1). However, when calcium containing compounds, such as slag, are used then the more general term alkali activated material is more appropriate.

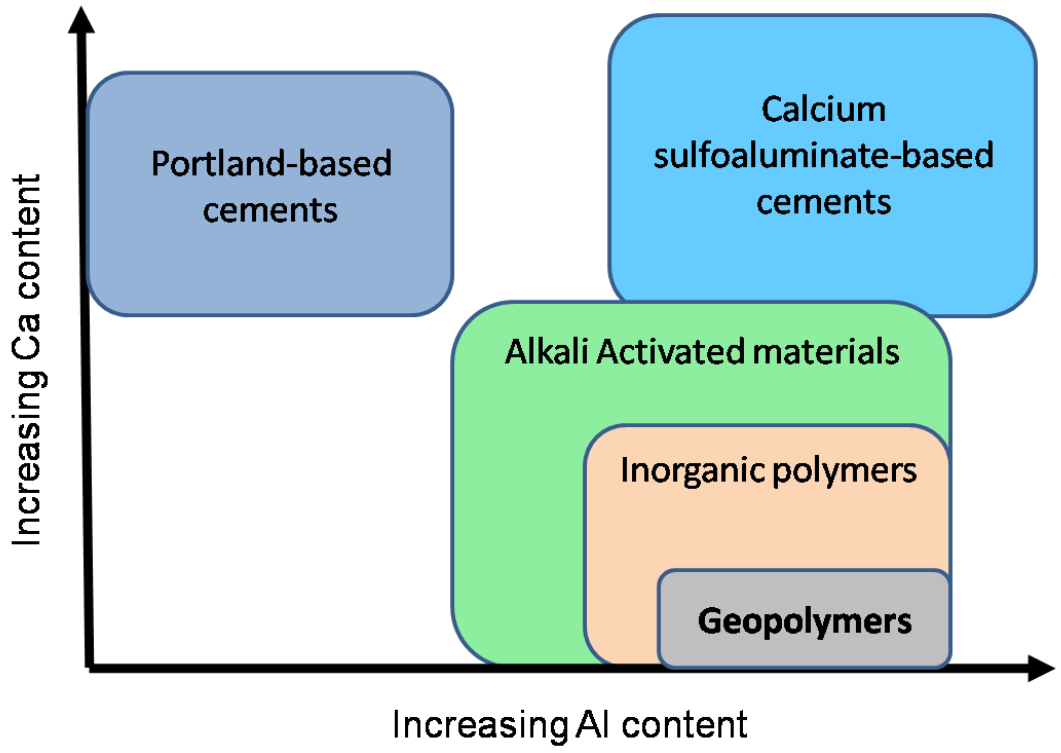

Figure 2-1 A schematic detailing the position of geopolymers in terms of aluminium and calcium content. Adapted from Provis (2012).

The x-ray amorphous reaction products resulting from the reaction of aluminosilicates with alkaline solutions are generally termed ‘Geopolymers’ (Duxson et al., 2007a). However, not all materials that meet the aforementioned characteristics are referred to by this designation in the available literature. This is partially because some research groups began working on the material well before Davidovits coined the term ‘Geopolymer’ in 1979 and continue to use their original designation. Product branding and patenting have also led various groups to vary the nomenclature describing geopolymer type materials.

Other designations for geopolymer type materials found in the literature are ‘low-temperature aluminosilicate glass’ (Rahier et al., 1997), ‘alkali-activated cement’ (Palomo et al., 1999), ‘alkali-activated aluminosilicates’ (Zuda et al., 2006), ‘geocement’ (Krivenko and Kovalchuk, 2007), ‘alkali-bonded ceramic’ (Mallicoat et al., 2008), ‘inorganic polymer concrete’ (Sofi et al., 2007), ‘inorganic polymers’ (Giancaspro et al., 2006), ‘soil silicates’ (Glukhovsky, 1959), ‘hydroceramic’ (Bao et al., 2005) and ‘geopolymeric cements’ (Bell et al., 2008a).

The reaction that forms a geopolymer, as detailed in section 2.4, is generally termed ‘geopolymerisation’. Other papers use a more descriptive nomenclature such as ‘the alkali activation of materials primarily composed of silica and alumina’ (Glukhovsky, 1959).

For the purpose of this thesis, ‘geopolymer’ and ‘geopolymerisation’ will be used to refer the aforementioned class of material and reaction process, respectively.

2.3 Polymer Basics

A polymer is a material whose molecules are made up of a large number of repeating units. Each repeating unit is termed a *monomer* (Challa, 1993). A polymer is formed when the monomers connect to each other via primary bonds to create a long chain.

If the monomer is represented by M, then the resultant polymer can be described by equation 2.1.

$$\text{-M-M-M-M-M-M-} \quad \text{or} \quad [\text{-M-}]_n$$

2.1

Where *n* is the degree of polymerisation of the polymer.

Polymers can be classified as either organic or inorganic. Organic polymers are composed of hydrocarbons and hence most have a string of carbon atoms as the backbone to the polymer. Synthetic organic polymers have been used to develop many useful products such as plastic. Inorganic polymers are composed of a network of atoms that does not have a backbone of carbon atoms. Examples of inorganic polymers are silicates, zeolites, polysilanes and siloxanes. Geopolymers are classed as ‘synthetic inorganic polymers’ due to their repeating aluminosilicate polymer structure. Further details on the structure of geopolymers are provided in the following sections (2.4 & 2.5).

2.4 Geopolymer Reaction Models and Network Structure

Geopolymers have a very similar structure to zeolites and feldspathoids, though geopolymers are largely x-ray amorphous due to their short range ordering. The geopolymerisation reaction that forms a geopolymer is described by equation 2.2 (Davidovits, 1994b, van Jaarsveld et al., 1997). The described reaction is based on a Si:Al ratio of 2.

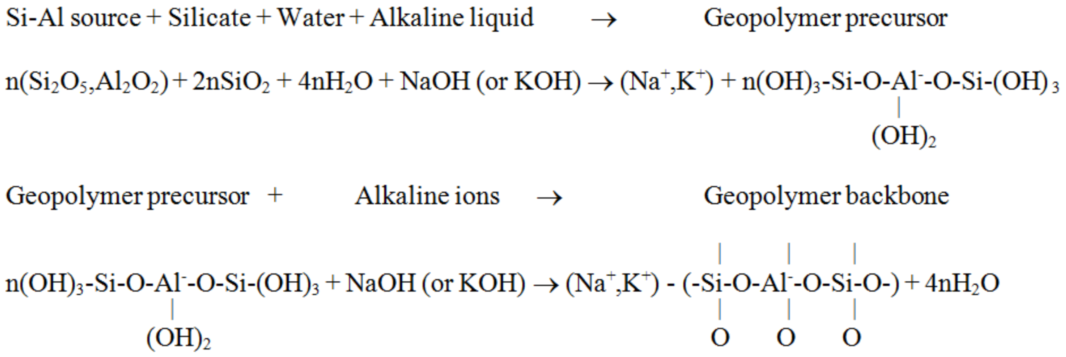

$$\text{Si-Al source} + \text{Silicate} + \text{Water} + \text{Alkaline liquid} \rightarrow \text{Geopolymer precursor}$$

$$n(Si_2O_5,Al_2O_2) + 2nSiO_2 + 4nH_2O + NaOH\ (\text{or } KOH) \rightarrow (Na^+,K^+) + n(OH)_3\text{-Si-O-}\underset{\underset{(OH)_2}{|}}{Al^-}\text{-O-Si-}(OH)_3$$

$$\text{Geopolymer precursor} + \text{Alkaline ions} \rightarrow \text{Geopolymer backbone}$$

$$n(OH)_3\text{-Si-O-}\underset{\underset{(OH)_2}{|}}{Al^-}\text{-O-Si-}(OH)_3 + NaOH\ (\text{or } KOH) \rightarrow (Na^+,K^+)\text{ - }(\text{-}\overset{|}{\underset{\underset{O}{|}}{Si}}\text{-O-}\overset{|}{\underset{\underset{O}{|}}{Al^-}}\text{-O-}\overset{|}{\underset{\underset{O}{|}}{Si}}\text{-O-}) + 4nH_2O$$

2.2

Equation 2.2 describes the reaction to form a sodium or potassium poly(sialate-siloxo) geopolymer. Other geopolymeric networks can be formed depending on the Si:Al ratio. Figure 2-2 details several fundamental poly(sialates) as proposed by Davidovits (1991). Davidovits (1994a) also suggested that as the Si:Al ratio increases, the degree of polymerisation increases and the 3D polymer network expands until the ratio is greater than 3, where a 2D cross-linked network is formed.

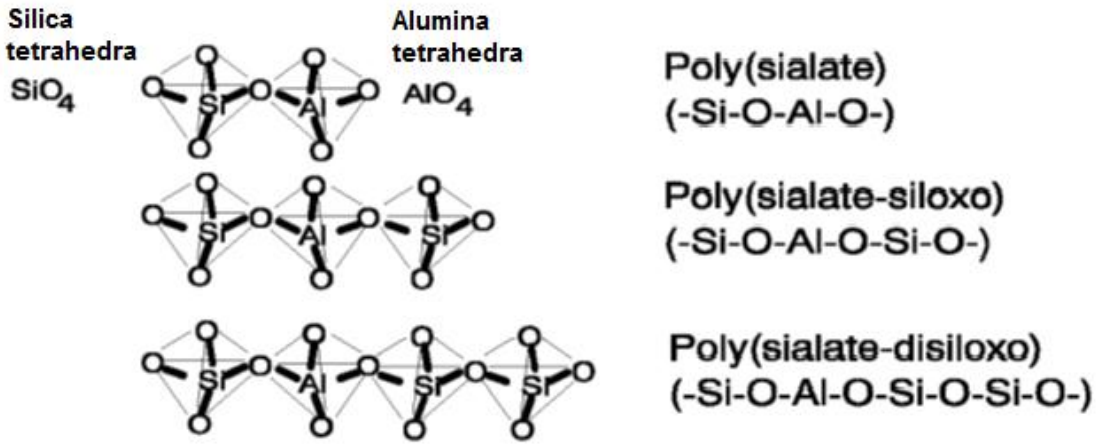

Figure 2-2 Geopolymeric molecular networks. Si:Al ratios of 1:1, 2:1, 3:1. Adapted from (Davidovits, 1991).

The geopolymerisation reaction can be further understood after analysing the reaction model. Figure 2-3 details the geopolymerisation reaction schematic as proposed by van Deventer et al. (2006). This model is generalised for all types of geopolymers though factors such as impurities and morphology in the starting materials may alter the reaction pathway. A specific reaction model of fly ash geopolymers would be somewhat more complicated and has thus far not been published. Fernandez-Jimenez et al. (2005) proposed a model for the dissolution of fly ash which is discussed in section 2.9, though this paper stops short of detailing the full geopolymerisation reaction in fly ash systems.

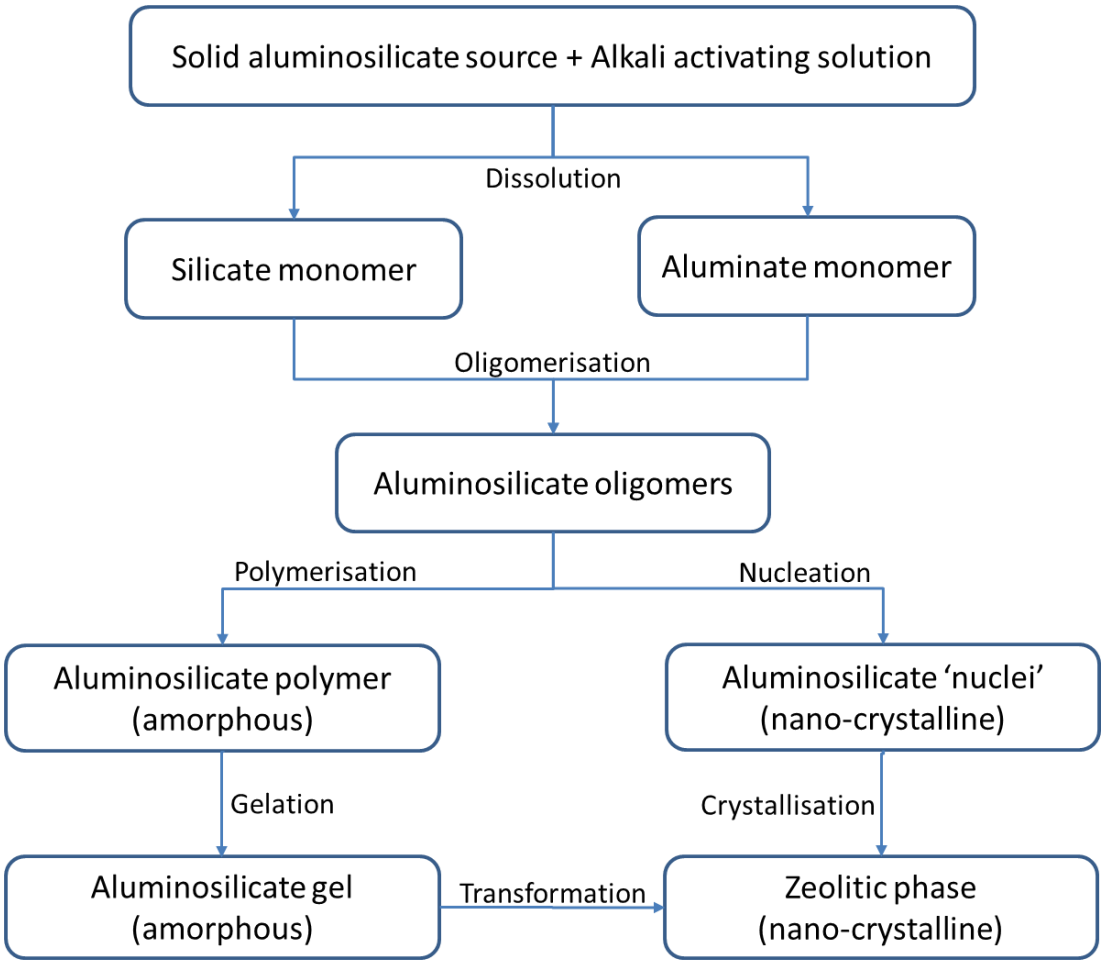

Figure 2-3 Reaction sequence during geopolymerisation. Adapted from van Deventer et al. (2006).

Additional reactions may occur over an extended curing period resulting in small amounts of the aluminosilicate gel transforming to zeolite nano crystals (as described in the reaction sequence above) (Duxson et al., 2006a, van Deventer et al., 2006).

2.5 Binder Ratios

Geopolymers are known to have variable physical properties which are strongly dependant on their relative amounts of silicon, aluminium, alkali and water. The three most significant binder ratios to consider are Si:Al, Na (or K):Al and H_2O:SiO_2. The Si:Al ratio is most critical as it directly determines the molecular network of the geopolymer formed.

Rowles and O'Connor (2003) investigated the effect of the Si:Al and the Na:Al ratios on compressive strength of sodium hydroxide and sodium silicate activated metakaolin geopolymers. They found that both ratios have a significant effect on the compressive strength of the geopolymer (Figure 2-4). The optimum strength they measured was obtained from a geopolymer with ratios Na:Al = 1.29 and Si:Al = 2.50. They noted that the ratios are based on source material measurement and not on the geopolymer gel. The actual Si:Al and Na:Al ratios of the geopolymer gel produced would differ from the calculated as not all of the metakaolin reacted. The unreacted aluminosilicates remain as a secondary phase amongst the amorphous geopolymer gel (Rowles and O'Connor, 2003).

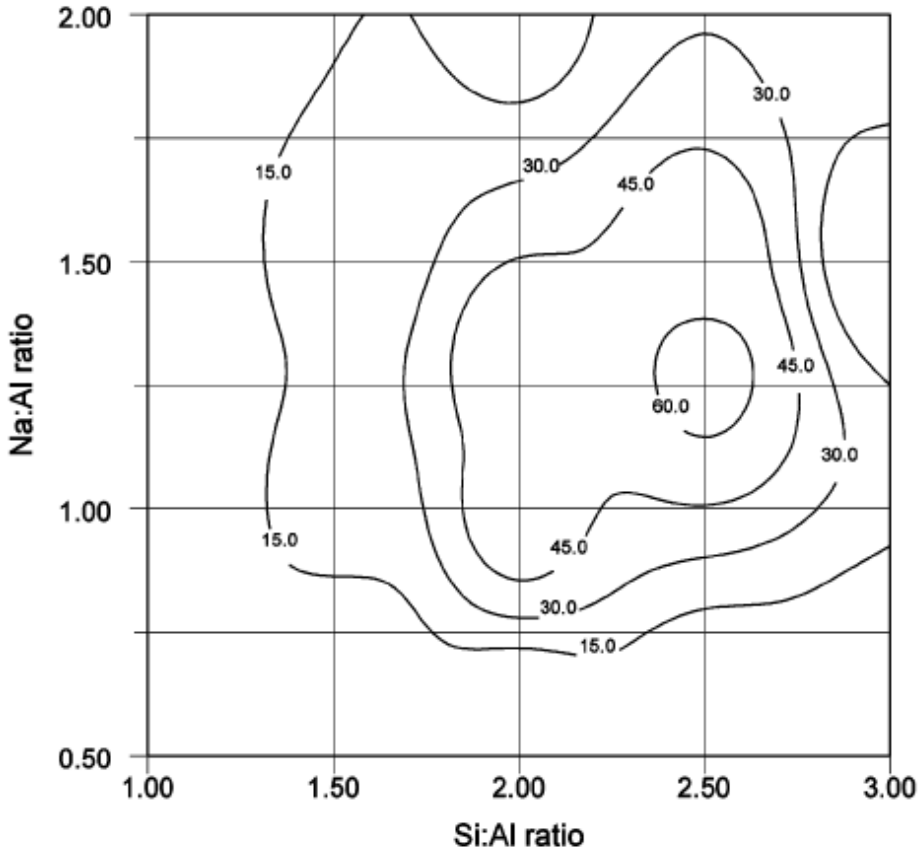

Figure 2-4 The compressive strength (MPa) of metakaolin geopolymers as a function of total Si:Al and Na:Al ratios (Rowles and O'Connor, 2003).

Škvára, Jilek & Kopecky (2005) produced a comparable geopolymer composition ratio map to the Rowles & O'Connor study using fly ash instead of metakaolin as the aluminosilicate source. They investigated how the compressive strength varied as a

function of the wt.% of Na_2O and the SiO_2:Na_2O ratio (Figure 2-5). A maximum compressive strength of 55 MPa was obtained at 7.8 wt.% Na_2O and a SiO_2:Na_2O ratio of 1.27. The rapidly changing compressive strength gradients in the 'y' direction in Figure 2-5 indicate that the wt.% of Na_2O has a significant effect on the compressive strength, more so than the SiO_2:Na_2O ratio.

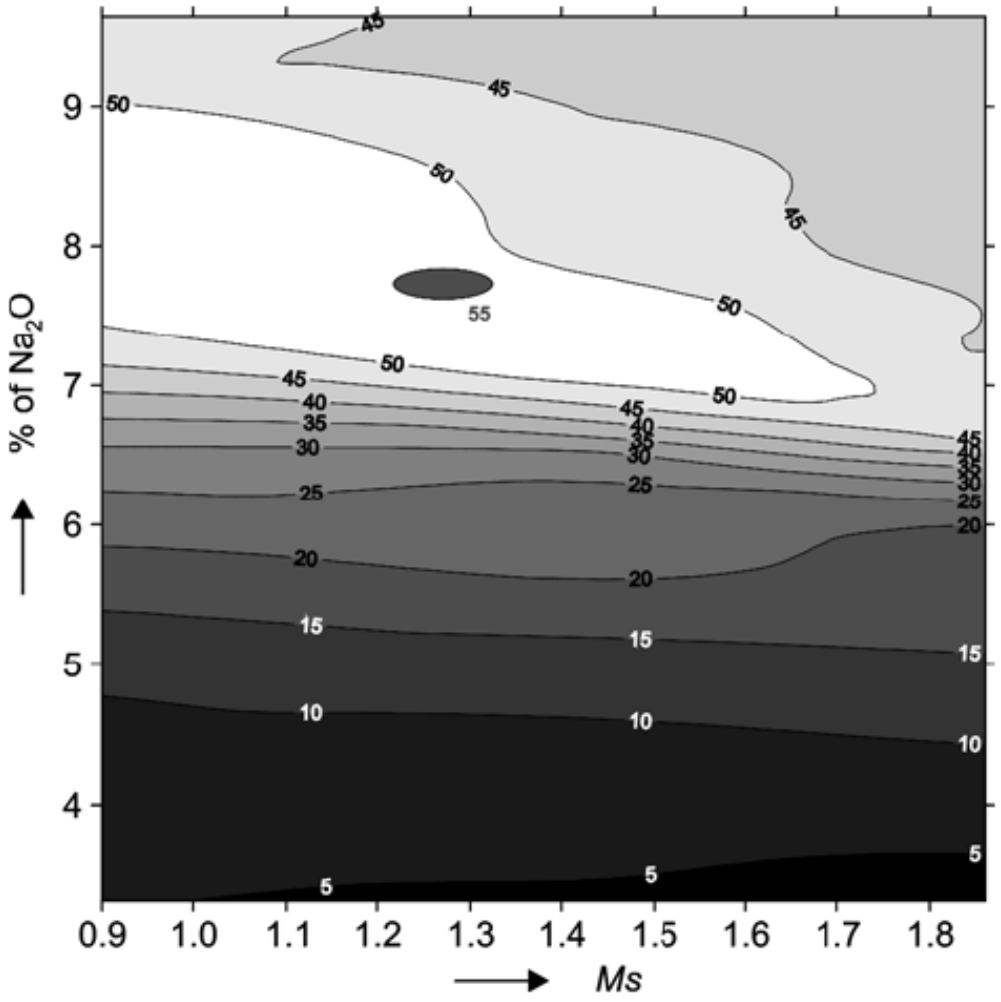

Figure 2-5 Fly ash geopolymer compressive strength (MPa) as a function of Na_2O and SiO_2:Na_2O weight ratio (Ms) (Škvára et al., 2005).

The water to geopolymer solids ratio also has a critical effect on the bulk properties. Rangan (2007) found that the physical properties of fly ash geopolymers decrease as the water to geopolymer solids ratio surpassed 0.16 though the workability of the mixture increased.

A point to note is that throughout this thesis reference is made to the Si:Al ratio of geopolymers as a compositional variable. Unfortunately, it is difficult to ascertain the exact Si:Al of geopolymer binder unless careful analysis is undertaken in a SEM. Papers tend to quote the Si:Al ratio of geopolymer even if they are aware that some of the precursor material has not been dissolved. There is also the likelihood that the Si:Al will vary within the geopolymer gel, for example the Si:Al may be higher in regions adjacent to unreacted silica sources. Thus, there is a global Si:Al ratio (inclusive of unreacted material) and the actual Si:Al ratio of the gel (average Si:Al determined by analysis of the gel phase after geopolymerisation). This has been directly measured by Williams et al. (2011) who observed a difference in Si:Al ratio of the gel due to the incomplete dissolution of the source material in metakaolin geopolymers.

2.6 Aluminosilicate sources for geopolymer synthesis

Geopolymers are a versatile material that can be produced from a wide range of precursor materials. Materials suitable for use in geopolymer synthesis must contain aluminosilicates that are soluble in an alkaline solution of moderate to high pH. It is also desirable to have precursors with a fine particle size to ensure rapid dissolution in the alkaline solution.

The form or structure of aluminosilicates affects the rate of dissolution in an alkaline environment. Crystalline aluminosilicates such as mullite and quartz dissolve much slower than amorphous aluminosilicates. As such, crystalline phases are considered inert during geopolymerisation (Williams and van Riessen, 2010) as they do not dissolve significantly during the liquid phase of the reaction.

Other critical source material properties are morphology (affects workability of slurry during mixing and casting), concentration of calcium (affects setting rate) and the presence of other phases such as organics and crystalline minerals. Table 2.1 lists the commonly used aluminosilicate sources and some details of their typical compositions.

Table 2.1 Common aluminosilicate sources for geopolymer synthesis.

Source	Typical Composition	
	Reactive Aluminosilicates	Secondary Phases
Metakaolin	$SiO_2 + Al_2O_3$ = 80 – 99 % Si:Al = 1	Kaolin, rutile, quartz, muscovite
Fly ash (class C)	$SiO_2 + Al_2O_3$ = 30 – 50 % Si:Al = 1-10	CaO usually ≥ 10 % Iron oxides, quartz, mullite, unburnt coal (< 6%)
Fly ash (class F)	$SiO_2 + Al_2O_3$ = 30 – 70 % Si:Al = 1-10	CaO usually < 10 % Iron oxides, quartz, mullite, unburnt coal (< 6 %)
Volcanic ash	$SiO_2 + Al_2O_3$ = 50 – 90 % Si:Al = 5-15	Iron oxides, quartz, feldspar, trace heavy metals
Rice husk ash	SiO_2 = 85 – 95 % Si:Al >> 10	Quartz, cristobalite, unburnt rice husks
Blast furnace slag	$SiO_2 + Al_2O_3$ = 5 – 20 % Si:Al = 1-10	CaO = 30 – 50 %, periclase, quartz, calico-olivine, mayenite, calcite, mullite

Metakaolin is derived from the calcination of kaolin, a clay that can be found all around the world. The calcination process of kaolin can take up to 24 hours at temperatures between 500 °C and 900 °C, commonly 700 °C. The effect of the calcination is the dehydroxylation and amorphisation of the aluminosilicates. Metakaolin is a very pure source of amorphous aluminosilicates making it highly suitable for geopolymerisation. However, due to the platy morphology of metakaolin, geopolymers made from this source require more water than other aluminosilicate sources (Kong et al., 2007). Metakaolin based geopolymers are regarded as an ideal system for fundamental research as they generally do not contain significant portions of secondary phases. Commercial applications of metakaolin based geopolymers are limited due to the added cost of calcining kaolin.

Fly ash is a residue from coal fired power stations. It is highly variable as its composition and morphology are dependent on the coal type and burning conditions during production. It typically consists of a glassy aluminosilicate phase, crystalline phases and some unburnt carbon. Fly ash is very fine (often > 75 % passing 45μm

sieve) and the bulk of the particles have a spherical morphology. Fly ash based geopolymers have great commercialisation potential due to their economic and physical characteristics. Fly ash can be classified as either class C, F or N (ASTM C618-08a, 2008), though class N is rarely used in geopolymers. Fly ash will be discussed in detail in section 2.9.

Volcanic ash consists of rock, mineral, and volcanic glass fragments smaller than 2 millimetres and is produced by volcanic activity. Volcanic ash is generally coarser than other aluminosilicate sources and is often sieved to extract the finer portion for use in geopolymers. Unlike fly ash, volcanic ash has a blocky or pyramidal particle morphology (Heiken, 1972).

Rice Husk Ash (RHA) is generated by the burning of rice husks. On burning, cellulose and lignin are removed leaving behind a high silica ash (Siddique et al., 2011). RHA usually contains around 85 – 90 % amorphous silica and has a highly porous, convex morphology similar to that of the original rice husk. Rice husk ash is used as a silica additive in geopolymers.

Silica fume and fumed silica (slightly different characteristics) are synthetic silica sources. They are widely available and can be used as a solid silica additive (Prud'homme et al., 2010) or can be dissolved in the activating solution when used with geopolymers (Brew and MacKenzie, 2007).

Ground Granulated Blast Furnace Slag (GGBFS), or simply slag, is a by-product of the steel making industry. It typically contains glassy aluminosilicates and crystalline phases. It has a similar morphology to fly ash though the grinding process does produce a greater portion of non-spherical particles. GGBFS is often used as a reactive calcium source (usually CaO or $Ca[OH]_2$) to initiate room temperature setting of geopolymers. This allows geopolymers to be cured on site in a similar manner to other cementitious materials. Other slags, such ladle slag (produced in electric arc furnaces) are also used in geopolymers (Bignozzi et al., 2010).

Aluminosilicate sources can be beneficiated for use with geopolymers. Grinding or sieving will increase the surface area of the source material, which will increase its

reactivity during geopolymerisation. Temuujin et al. (2009b) demonstrated that the compressive strength of geopolymers can be increased when using a mechanically activated fly ash. Other beneficiations, such as the removal of unreacted carbon and inert crystalline material, can also be used to improve geopolymer properties (Chen-Tan, 2010).

2.7 Activating solutions for geopolymer synthesis

Geopolymers can be produced with a range of activating solutions. The type of alkali, pH of solution and presence of dissolved silicates or aluminates can all be varied. The dissolution kinetics as well as product availability and cost play a significant role in the selection of activating solution. The bulk of the research on geopolymer activating solutions has been conducted on sodium hydroxide, sodium silicate, sodium aluminate, potassium hydroxide and potassium silicate solutions. These solutions are widely available and there is a good understanding of their role in the geopolymerisation process. Geopolymers have also been synthesised from caesium based solutions (Bell et al., 2009) and lithium based solutions (O'Connor and MacKenzie, 2010).

The concentration of the solution greatly affects the geopolymerisation process. Wang et al. (2005) found the flexural strength, compressive strength, and apparent density of metakaolin geopolymers increased significantly as the NaOH concentration of the activating solution increased from 4 to 12 mol/L. This was attributed to the enhanced dissolution of the metakaolin particulates in a more alkaline solution.

2.8 Geopolymers Synthesised from Industrial Wastes

Geopolymers can be produced from industrial waste material instead of pure, virgin materials. Industrial waste products most suitable for the production of geopolymers are ones that contain high levels of reactive (amorphous) aluminosilicates

(Bouzoubaâ et al., 1999). Some examples of industrial waste products suitable for geopolymers are fly ash from coal fired power stations and slag from blast furnaces. Waste industrial caustic solutions such as Bayer liquor (sodium aluminate + organics) from the production of alumina can also be used in the synthesis of geopolymers (Jamieson et al., 2012). Geopolymers created from waste products instead of pure materials are likely to be significantly cheaper to produce. They would also create an avenue for recycling of waste material which would benefit the environment and increase efficiency (Rangan, 2007).

The disadvantage of using industrial waste materials as a substitute for pure materials is that they commonly contain significant concentrations of impurities. Many of these impurities, such as quartz and mullite, are largely inert in geopolymer synthesis, though other impurities, such as organics and activated carbon, are likely to adversely affect the material formed.

2.9 Fly Ash

Coal fired power plants remain a major contributor to the total electricity produced around the world and are the dominant power source in Australia. The process of combusting coal produces waste materials like fly ash and bottom ash. These products were originally treated as waste and disposed of in landfills. Fly ash has been shown to be an effective supplementary cementitious material (SCM) in OPC products (Helmuth, 1987). Fly ash can also be used in geopolymers as a source of aluminosilicates which is distinct from Portland cement where it is used primarily as a fine filler (Bouzoubaâ et al., 1999).

Fly ash based geopolymers have great potential due to their cost, environmental and performance benefits over other geopolymer source materials. The following subsections explore the available literature on fly ash and fly ash based geopolymers.

2.9.1 Fly Ash Formation

Fly ash is formed when coal is passed through an incinerator, where combustibles are consumed at temperatures in excess of 1400 °C. The heat causes the inorganic mineral impurities in the coal to become fluid, volatile or to react with oxygen. During cooling the residual unburnt material may form crystalline solids, spherical amorphous particles or condense as coatings on particles (Kutchko and Kim, 2006). The particles that are suspended in the flue gas are typically transported with the gas to cleaning systems. The material collected in the cleaning systems is called fly ash. The residue which is not suspended in the flue gas coagulates and falls down to form bottom ash (Goodwin, 1993, Malhotra and Mehta, 1996).

2.9.2 Fly Ash Classification

Fly ash is classified by composition into three classes according to ASTM C618-08a Standard Specification for Coal Fly Ash and Raw or Calcined Natural Pozzolan for Use in Concrete (2008). This standard defines three classes of fly ash with set physical and compositional requirements as described in Table 2.2. The maximum calcium oxide content, usually used to differentiate class F and class C fly ashes, is not specified in the standard for all classes, though a sub note states that Class C fly ashes contain a total calcium content, expressed as calcium oxide (CaO), higher than 10 wt.%.

Table 2.2 Chemical and physical requirements for fly ash classification according the ASTM C618-08a.

Requirement	Class		
	N	F	C
$SiO_2 + Al_2O_3 + Fe_2O_3$, minimum wt.%	70	70	50
Sulfur trioxide (SO_3), maximum, wt.%	4.0	5.0	5.0
Moisture content, maximum, wt.%	3.0	3.0	3.0
Loss on ignition, maximum, wt.%	10.0	6.0	6.0
Amount passing 45 µm sieve, minimum wt.%	66	66	66
CaO content, wt.%			> 10

Class F fly ash is produced from the combustion of anthracite or bituminous coal and has a low calcium content (typically 2 - 6 wt.%) (Manz, 1999). Class C fly ash is produced by the combustion of lignite or sub-bituminous coal and has high calcium content (typically > 10 wt.%) (Malhotra and Mehta, 1996). Class N fly ashes require calcination to induce satisfactory properties whereas class F and C have pozzolanic properties.

Class F fly ash typically contains the crystalline minerals hematite (Fe_2O_3), magnetite (Fe_3O_4), mullite ($3Al_2O_3.2SiO_2$), quartz (SiO_2) and sillimanite ($Al_2O_3.SiO_2$). Class C fly ash typically contains alkali sulphates, anhydrite ($CaSO_4$), calcium aluminosulphate ($4CaO.3Al_2O_3.SO_4$), free CaO, periclase (MgO), quartz (SiO_2) and tricalcium aluminate ($3CaO.Al_2O_3$) (Malhotra and Mehta, 1996). Many of the common minerals in class C fly ashes, with the exception of periclase and quartz, undergo a pozzolanic reaction with water.

Fly ashes can be enhanced after classification to form a more desirable product. Particle size can be refined by use of a variety of beneficiation technologies. Other enhancements remove undesirable impurities such as residual coal to boost the wt.% of the aluminosilicates (Chen-Tan, 2010). This research will focus on class F fly ashes due to their low calcium content and availability in Australia.

2.9.3 Fly Ash Characterisation

Fly ash is a powdery material made up of small glass spheres consisting primarily of silicon, aluminium, iron, and calcium oxides (Goodwin, 1993). Fly ash is a highly variable material; the chemical and physical properties of fly ash particles are a function of the mineral matter in the source coal, the combustion conditions, and post-combustion cooling rate (Kutchko and Kim, 2006). However, classified fly ash from a particular power station will maintain some consistency with time if there are no major changes to the burning conditions or coal source.

Size & Morphology

Fly ash is typically a very fine powder. The particle size range of fly ash is normally between 1 and 150 μm (Berry and Malhotra, 1980), though typically at least 75 % of fly ash is formed with a particle size less than 45 μm (Malhotra and Mehta, 2002).

The high temperature and rapid cooling of non-combustible material in the flue gases of coal fired power stations causes it to coalesce into a spherical shape. Expansion of trapped volatile matter can cause the particle to expand to form hollow or porous particles. Figure 2-6 displays a range of the typical morphologies of fly ash particles as imaged with a scanning electron microscope (SEM). The micrographs give an indication of the size distribution of the fly ash spheres and the various impurities present in the material.

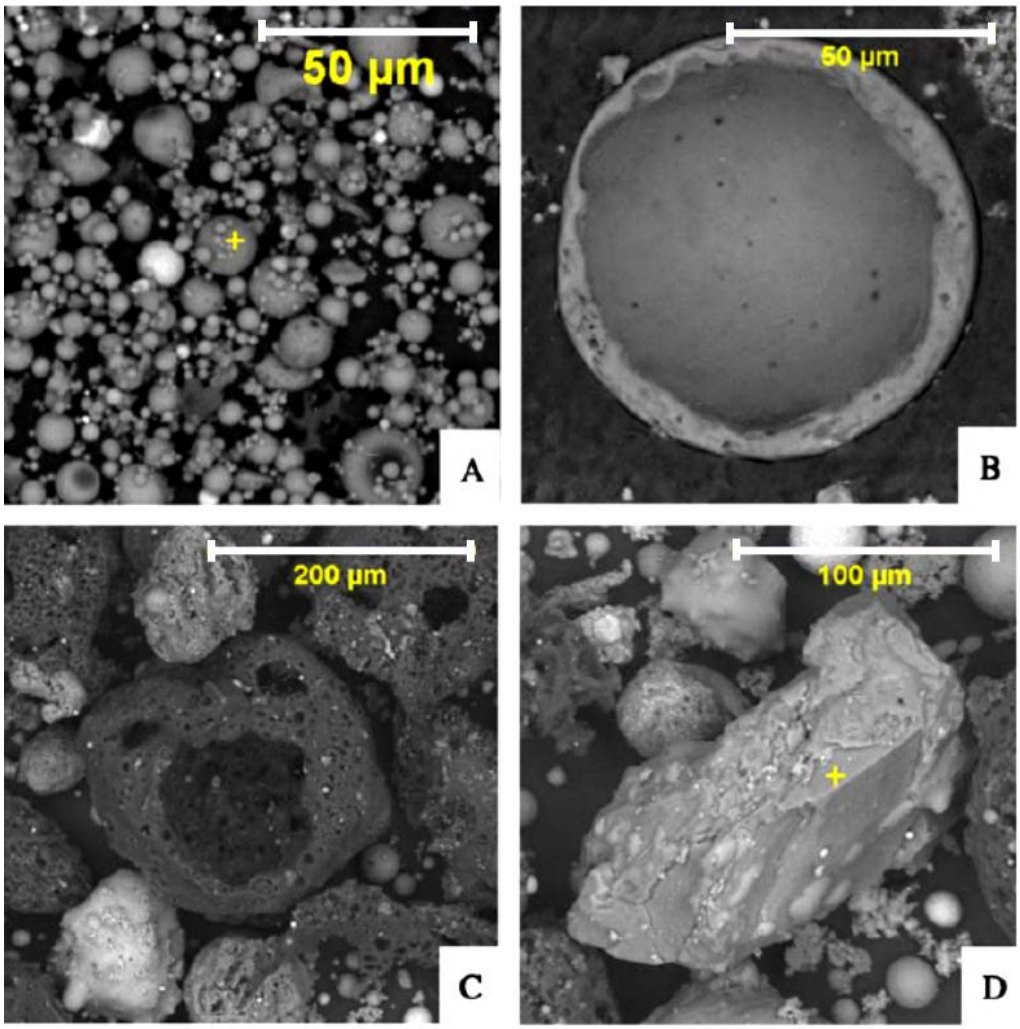

Figure 2-6 SEM micrographs of a class F fly ash. Backscattered electron (BSE) images of (A) typical fly ash spheres; (B) hollow cenosphere cross-section; (C) unburnt carbon particle; (D) mineral aggregate (quartz); (Kutchko and Kim, 2006).

Chemical Composition

The bulk chemical composition of fly ash is usually determined quantitatively by x-ray fluorescence (XRF) or inductively coupled plasma mass spectrometry (ICP-MS). It is difficult to comment generally on the composition of fly ash due to their inherent variability, however classified fly ashes will at least conform to the compositional guidelines described in Table 2.2.

The composition of 6 Australian class F fly ashes as reported by Fly Ash Australia (2011) are listed in Table 2.3. Even in this small selection of fly ashes the wide variability in chemical composition is evident.

Table 2.3 Published chemical composition of 6 Australian class F fly ashes. Data from Fly ash Australia (2011) except for Tarong fly ash where the data is from Zaeni et al. (2010).

Oxide	Collie	Eraring	Tarong	Pt Augusta	Bayswater	Mt Piper
SiO_2	51.8	64.2	66.2	49.4	70.7	69.4
Al_2O_3	26.4	25.5	25.2	29.7	20.7	22.4
Fe_2O_3	13.2	3.9	4.4	3.0	3.9	1.4
CaO	1.6	2.3	0.2	4.9	1.1	0.3
K_2O	0.7	1.2	0.3	1.2	1.1	2.2
TiO_2	1.4	1.0	1.7	2.2	0.9	1.0
MgO	1.2	0.7	0.2	2.7	0.8	0.3
Na_2O	0.3	0.5	0.1	3.2	0.3	0.2
P_2O_5	1.4	0.3	0.1	1.0	0.2	0.1
MnO	0.1	0.1	0.1	0.1	0.1	0.0
LOI (1000 °C)	0.5	1.2	1.1	0.5	1.0	2.0
Sum of aluminosilicates	78.2	89.7	91.4	79.1	91.4	91.8
Sum of alkali's	1.0	1.8	0.4	4.4	1.4	2.4
SiO_2/Al_2O_3	2.0	2.5	2.6	1.7	3.4	3.1
Si:Al (molar)	1.7	2.1	2.2	1.4	2.9	2.6
Fineness (% passing 45 µm sieve)	86 %	89 %	N/A	86 %	97 %	86 %

Important compositional variables in fly ashes are Si:Al, iron oxide content and calcium content. The Si:Al ratio in the fly ash will either set the Si:Al for the resulting geopolymer if using an alkali only activating solution or affect the composition of the activating solution (for example sodium silicate or sodium aluminate) if trying to achieve a particular Si:Al ratio geopolymer. Iron oxides have been shown previously to negatively affect the dissolution of aluminosilicates (Chen-Tan et al., 2009) and thermal performance (Rickard et al., 2010) in geopolymers and their presence in fly ashes is regarded as disadvantageous. Calcium oxides have cementitious properties and influence the setting time of geopolymers. This can be advantageous, though may introduce problems such as reduced workability and flash setting (Davidovits, 1994b).

Bulk chemical composition provides a preliminary indication as to the suitability of each of the fly ashes as precursors for geopolymers, though it is limited by the fact that there is no information about the reactivity of the aluminosilicate component or the structure of the non-aluminosilicate phases. Detailed knowledge about the suitability of a fly ash can be determined by combining the bulk composition information with phase composition information (Williams and van Riessen, 2010).

Phase Composition

Phase composition is commonly determined by x-ray diffraction (XRD). Qualitative phase analysis can be achieved using data from a laboratory diffractometer and phase search/match software. Absolute quantitative phase abundance of fly ashes requires much more expertise and is usually done using an internal standard (to enable the amorphous component to be quantified) in conjunction with full pattern modelling (Rietveld, 1969). Synchrotron radiation XRD provides better resolution and increased sensitivity for phases with significant overlapping reflections with other phases and detection of minor phases, respectively.

The phase composition of fly ashes varies between the power plants they were sourced from, though all indicate that fly ashes are primarily amorphous. Typical crystalline phases found in fly ashes are quartz, mullite and various iron oxides such as hematite (Matsunaga et al., 2002). The amorphous content of fly ash typically constitutes between 40 and 70 wt.%. An example of the phase composition of a class

F fly ash is presented in Table 2.4 as determined by Williams (2006). The author of the same study also determined the amorphous content using a combination of XRD and x-ray fluorescence (XRF) as detailed in Table 2.5.

Table 2.4 XRD results detailing the composition of Collie fly ash (2006 batch) (Williams, 2006).

Component	Composition (wt.%)
Amorphous	61.6 ± 0.7
Quartz	19.9 ± 0.3
Mullite	15.0 ± 0.3
Hematite	1.3 ± 0.1
Maghemite	2.2 ± 0.1

Table 2.5 Composition of the amorphous component of Collie fly ash (2006 batch) (Williams, 2006).

Oxide	Composition (wt.%)
SiO_2	51.6 ± 0.1
Al_2O_3	23.4 ± 0.1
Fe_2O_3	15.2 ± 0.1
CaO	1.75 ± 0.01
Other amorphous	8.05 ± 0.07
LOI	3.0 ± 0.1

In general, crystalline material in fly ash is inert during alkali activation though it can affect the geopolymers properties. Mullite in fly ash is not directly detrimental to a resultant geopolymer though its presence indicates that a portion of the alumina is not available for dissolution as it is locked up in a crystalline phase. Fly ashes with high concentration of mullite are likely to produce poor geopolymers due to the lack of amorphous alumina. The presence of quartz can act as a fine aggregate and as its thermal expansion is different to the geopolymer gel, it can damage the structure during heating (Subaer, 2005). Crystalline iron oxides also have a differential thermal expansion to the geopolymer gel and in addition will change phase at high temperatures, further stressing the structure.

2.9.4 Fly Ash Reaction Models

The reaction model for alkali activation of fly ash differs from that of metakaolin due to the presence of impurities and a vastly different morphology. Currently, because of the complexity of the system, a quantitative reaction sequence has not been published. Fernandez-Jimenez et al. (2005) proposed a model for the dissolution of certain types of fly ash particles in an alkaline environment. They reported that fly ash activation and the dissolution rate strongly depends on the pH of the activator system. Figure 2-7 details the model proposed by Fernandez-Jimenez et al.

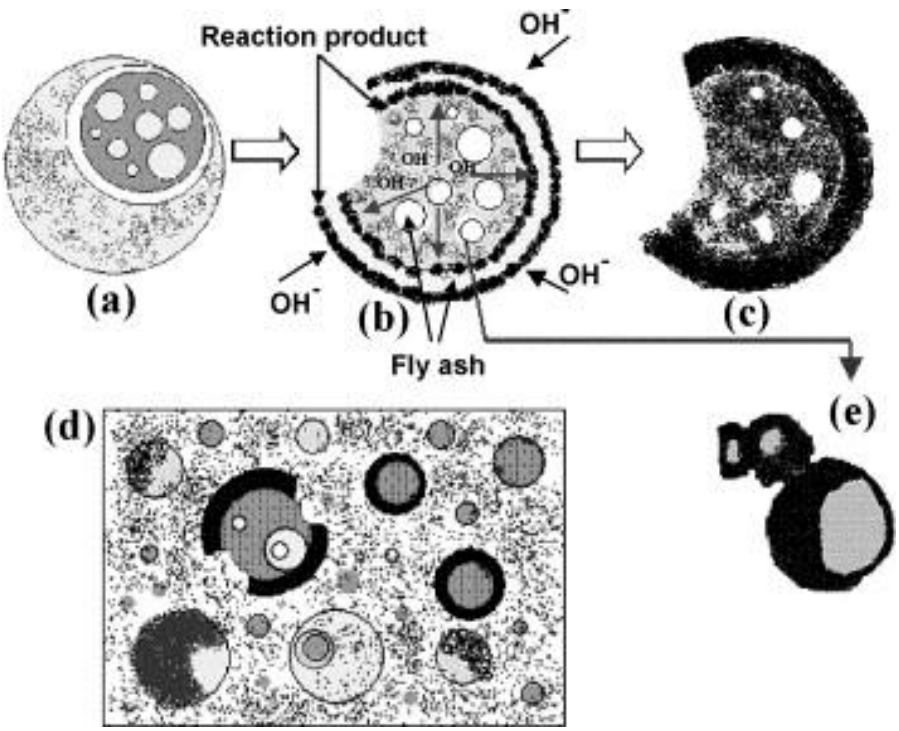

Figure 2-7 A descriptive model of alkali activation of fly ash (Fernandez-Jimenez et al., 2005). Details of each step provided in the text below.

Figure 2-7 (a) shows a fly ash sphere at the onset of the dissolution process where a small area of the shell has been dissolved. The dissolution of a plerosphere (spheres within a sphere) is used in this example. Figure 2-7 (b) details the bi-directional attack of the alkaline liquid on the fly ash sphere. The external dissolution continues while alkaline liquids that have penetrated into the sphere begin to dissolve the sphere from the inside out. Consequently the reaction products (aluminosilicate gel) form on both the inside and the outside of the sphere. The reaction products which form within the larger spheres can block the alkaline liquid from further reacting

with smaller particles within leaving them unreacted after the dissolution process, Figure 2-7 (e). The dissolution process is not uniform throughout the gel and variations occur due to localised changes in pH and fly ash particle size. Figure 2-7 (c) shows an almost completely dissolved fly ash particle. Figure 2-7 (d) shows a typical fly ash geopolymer with a range of completely, partially and undissolved fly ash particles amongst the geopolymer gel (Fernandez-Jimenez et al., 2005).

The aforementioned model is limited as it does not describe the alkali activation of solid fly ash spheres. As yet, a complete fly ash reaction model is yet to be published.

2.9.5 Fly Ash Based Geopolymers

Fly ash is an highly suitable source material for geopolymers because it contains reactive aluminosilicate glass of a fine particle size which is conducive to solid-state chemical reactions (Majko, 2004). This makes fly ash ideal as a substitute for metakaolin in geopolymers with major savings in material cost. It is also widely available around the world due to the ubiquitous nature of coal fired power stations.

Classified fly ash (class C or F) is regarded as the most suitable for geopolymer production. This is because unclassified fly ashes may include a fraction of large particles and contain relatively high concentrations of undesirable materials such as unburnt coal. It is also very important that a fly ash is well characterised prior to use as the amount and Si:Al ratio of the reactive aluminosilicates will greatly affect the properties of the synthesised geopolymer. Formulating the geopolymer mixture based on amorphous composition of the fly ash produces samples with a significantly higher compressive strength than those formulated using the bulk composition (Williams and van Riessen, 2010).

Fly ash based geopolymers have comparable, and in some cases superior properties to metakaolin based geopolymers. Rangan (2007) produced fly ash geopolymer concrete with a compressive strength of over 80 MPa. Škvára, Doležal et al. (2005) produced blended fly ash/slag geopolymer concrete with a compressive strength of 164 MPa. Kong et al. (2007) found that fly ash based geopolymers exhibited

increased strength retention after heating than equivalent metakaolin based geopolymers due to their pore structure being conducive to the evaporation of water without damaging the microstructure.

The use of fly ash based geopolymers can also result in financial and environmental benefits when compared with traditional OPC products. As a waste product fly ash can be cheaply obtained as power stations wish to avoid having to dispose of it in landfill/tailings dams. Recent studies have shown that fly ash geopolymers can be synthesised with a 44–64 % reduction in greenhouse gas emissions and 7 % lower to 39 % higher cost compared with OPC, depending on a range of factors such as source material locations (McLellan et al., 2011).

2.10 Microstructure of Geopolymers

Geopolymers are rarely synthesised as a pure single phase material due to incomplete dissolution or the presence of impurities. A typical geopolymer comprises of at least two different phases. The main phase is a glassy amorphous gel. The other phases, referred to as secondary phases, are comprised of partially dissolved starting materials and crystalline impurities. The presence of secondary phases in geopolymers has the potential to reduce their physical properties, however, certain phases, such as quartz, can act as a fine aggregate which can serve to pin cracks and improve compressive strength (Subaer, 2005).

Recent studies have shown small zeolitic crystals form in poly(silate) geopolymers. These crystals are of the order of a few unit cells which make them difficult to detect using conventional XRD techniques. The amount of zeolitic crystals in a geopolymer has been reported to increase over time as parts of the aluminosilicate gel crystallises (van Deventer et al., 2006).

Electron microscopy has been used effectively as a tool to analyse the microstructure of geopolymers and their precursors. SEM analysis has been used to characterise sample morphology, porosity, defects such as cracks, identify reacted/unreacted

regions and the role of aggregates. Figure 2-8 and Figure 2-9 illustrate typical microstructures of metakaolin and fly ash geopolymers, respectively. The unreacted aluminosilicate source material amongst the amorphous geopolymer gel is common in all geopolymers. Geopolymers that have improved dissolution of the source material have a greater proportion of amorphous gel to unreacted aluminosilicates (Kriven et al., 2003). Other features such as crystallites (zeolitic or otherwise) and aggregates are also commonly observed.

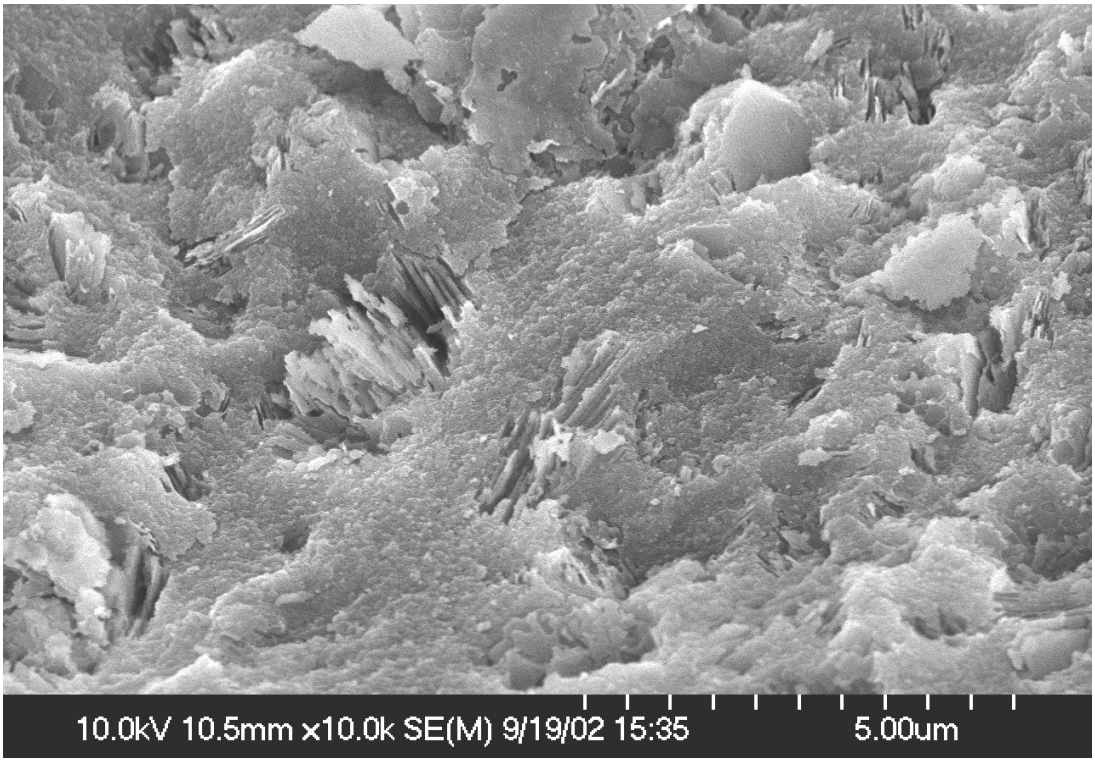

Figure 2-8 SEM image of a metakaolin geopolymer showing reacted (smooth regions) and unreacted regions (platy particles) (Kriven et al., 2003).

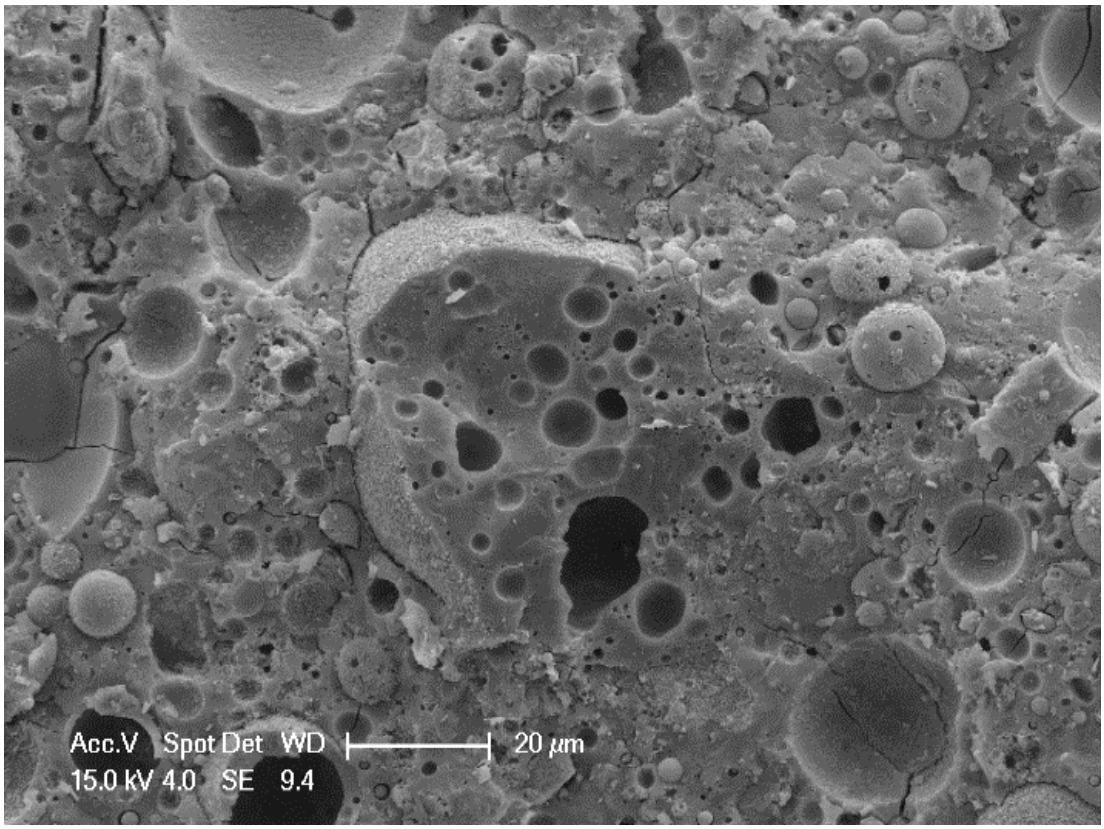

Figure 2-9 SEM micrograph of a fly ash geopolymer. Note the unreacted and partially reacted fly ash particles amongst the geopolymer gel (Rickard, 2007).

Transmission electron microscopy (TEM) has been used to analyse the structure of geopolymers at very high magnifications (Gordon et al., 2005, Maitland et al., 2011). TEM micrographs have been used to demonstrate the lack of long range order in the microstructure of geopolymers, confirming the amorphous nature of their structure (Figure 2-10) (Gordon et al., 2005). Maitland et al. (2011) studied metakaolin geopolymers in a TEM and found them to have a variable pore structure with pore widths ranging from sub-nanometre to several tenths of a millimetre. Selected area electron diffraction (SAED) has also been used to identify the amorphous geopolymer gel from the crystalline secondary phases (Blackford et al., 2007).

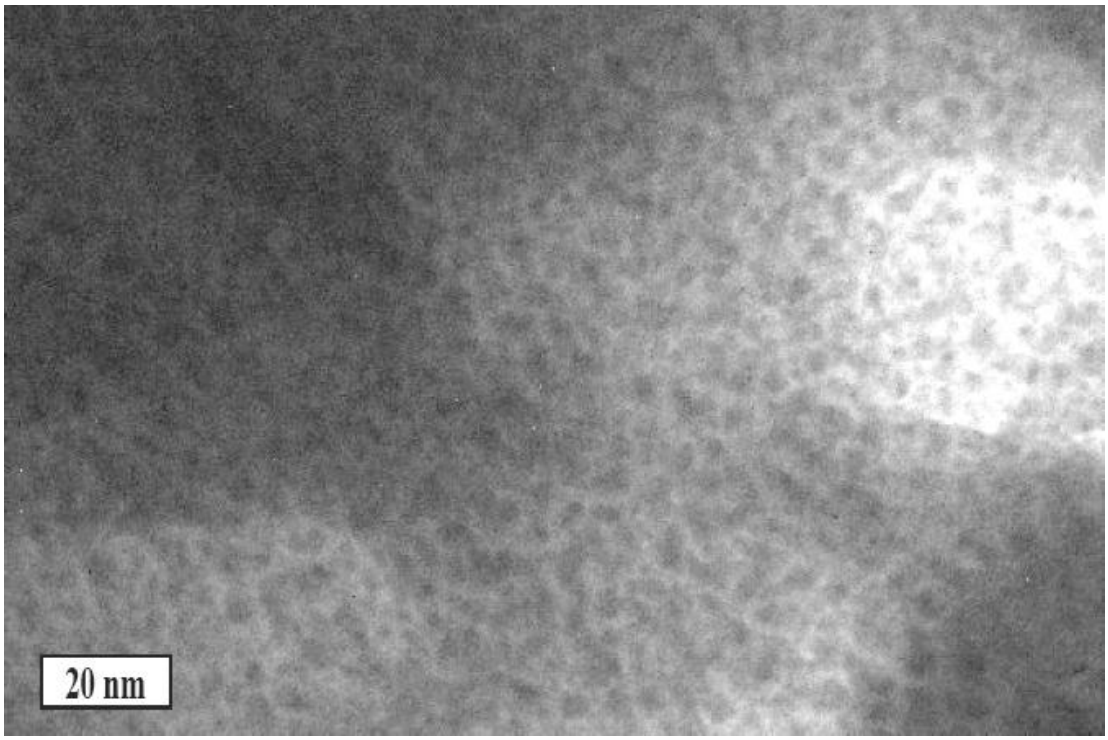

Figure 2-10 Bright field TEM micrograph of a metakaolin geopolymer showing an amorphous, speckled microstructure (Gordon et al., 2005).

2.11 Physical Properties of Geopolymers

Geopolymers have great potential because of their comparable, and often better, physical properties than existing materials (van Jaarsveld et al., 2002). Geopolymers can be designed to exhibit one or more of the following properties; high compressive strength, fast setting time, acid resistance, large working temperature range and low thermal expansion (Davidovits, 1991).

The physical performance of geopolymers is assessed in much the same way as other comparable materials. In concreting applications; compressive strength, flexural strength, tensile strength and durability are important physical properties. In high temperature applications; changes in compressive strength, phase evolution, microstructural evolution, thermal expansion, thermal conductivity and thermo-physical properties are relevant physical properties. The following sections explore the literature about the aforementioned physical properties in relation to geopolymers.

2.11.1 Compressive Strength

Compressive strength is a critical physical characteristic for binding materials as it governs how much load they can support and hence the applications it can be used for. This is very important in construction applications but less relevant in applications where thermal resistance is more important. Many researchers in the geopolymer field use compressive strength as the key physical characteristic to compare with other samples and materials.

The main variables that affect the compressive strength of geopolymers are composition, morphology (including porosity and cracking), curing conditions and reactivity of the aluminosilicate source. The use of additives such as fibre reinforcement or aggregates will also affect the compressive strength.

The Si:Al and Na (or K):Al compositional ratios have a significant effect on the compressive strength of geopolymers. Figure 2-4 and Figure 2-5 illustrate the compressive strength variation as a function of composition ratios for metakaolin and fly ash geopolymers, respectively. If there is not enough alkaline activator, not all the aluminosilicate material undergoes geopolymerisation. Alternatively, if there is too much activator the excess remains in the sample weakening the structure (Rowles and O'Connor, 2003). There is no agreement in the literature on the optimum alkaline activator to aluminium ratio (Na or K:Al), most likely due to different synthesis techniques and curing conditions between studies.

Rowles & O'Connor (2003) reported that insufficient silicon in geopolymer formulations affects the compressive strength due to the Lowenstein/aluminium avoidance principle where Si – O – Al bonding is preferred over Al – O – Al bonding. Hence, high aluminium/low silicon content polymers cannot form large enough polymer networks to have high structural integrity. For this reason, geopolymers are generally synthesised with a Si:Al > 1 in order to produce high strengths.

Sodium alkali activated metakaolin geopolymers synthesised with the following ratios Si:Al = 1.5, Na:Al = 0.6 resulted in compressive strength of 86 MPa in a study

by Subaer (2005). Sodium hydroxide and sodium silicate activated metakaolin geopolymers produced under similar conditions achieved a maximum compressive strength of 64 MPa with ratios of Si:Al = 2.50 and Na:Al = 1.29 in the study by Rowles and O'Connor (2003). Škvára, Jilek & Kopecky (2005) produced sodium hydroxide activated fly ash geopolymers with a compressive strength of 55 MPa, though the composition ratios were not reported. The different composition ratios for maximum strength between the studies are likely due to variances in the reactivity and morphology of the aluminosilicates source material or the conditions used for curing.

The curing conditions affect the compressive strength of the geopolymer because thermal energy is critical in the geopolymerisation reaction. Geopolymers cured at elevated temperatures will gain strength faster than those cured at room temperature (Bakharev, 2006). A longer curing time increases the degree of geopolymerisation in the geopolymer resulting in higher compressive strength (Rangan, 2007). The same study proposed the most efficient curing regime for fly ash geopolymer concrete is a 24 hour pre-curing period at room temperature followed by 24 hours at 60 °C. It was reported that curing for longer times or at higher temperatures did not produce significantly stronger geopolymers. This curing regime is not likely to be optimum for all types of geopolymers as differences in source material reactivity will vary the curing requirements.

The Rangan (2007) study also reported that the compressive strength of geopolymers decreases as the water-to-geopolymer solids ratio increased over the workable range of a concrete mix. The optimum strength fly ash geopolymer concrete was achieved with a water-to-geopolymer solids ratio of 0.16.

2.11.2 Other Mechanical properties

Flexural strength and tensile strength are other mechanical properties often used to characterise geopolymers. One of the major advantages over other binding materials is geopolymers' inherent tensile strength. Geopolymers have a higher tensile strength than equivalent materials such as OPC due to their polymeric framework. Chemical

bonding to silica containing aggregates also contributes to the tensile strength of geopolymer concretes (Gourley and Johnson, 2005). This allows geopolymers to be used without steel reinforcement in some applications which has cost and durability advantages.

Wang et al. (2005) measured the flexural strength of metakaolin geopolymers and found that the strength increased as the pH of the activating solution increased, with samples made with 12 mol/L alkali having the highest flexural strength of over 50 MPa.

The flexural strength and tensile strength of geopolymers can be increased considerably with the use of fibre reinforcement. Hammell et al. (2000) produced geopolymer – carbon fabric composites with a tensile strength of 325 MPa and a flexural strength of 245 MPa.

2.12 Thermal properties of Geopolymers

Owing to their inorganic framework, geopolymers are intrinsically fire resistant and have been shown to exhibit excellent thermal stability, far in excess of that of traditional cements (Barbosa and MacKenzie, 2003a). Geopolymers have been shown to have superior resistance to thermally induced damage at high temperature when compared with OPC based materials (Duxson et al., 2007a, Kong et al., 2005, Mendes et al., 2009, Zhao and Sanjayan, 2011). They have also been shown to have better thermal resistance than available fire resistant composites (Hammell et al., 2000). The potential for geopolymer based materials in high temperature applications has created a lot of interest.

Duxson et al. (2006a) reported that the thermo-physical properties of geopolymers are independent of the alkali cation due to heat energy primarily travelling as phonons along the structural backbone of the polymer, which consists of aluminium, silicon and oxygen. Instead, the thermo-physical properties are influenced by water content, porosity and density, all of which affect the path length of phonons

travelling through a structure (phonon propagation is inhibited by structural boundaries (Kittel, 2005, p. 122). Water content in particular has a strong influence on the thermo-physical properties as it represents a substantial part of the material (up to 30 wt.%) and its presence influences other properties such as density (Duxson et al., 2006a). Geopolymers synthesised from different source material, with everything else being constant (such as density and water content), are not expected to exhibit differing thermo-physical properties.

Extensive research has been done on the thermal properties of metakaolin geopolymers and their composites while the thermal properties of fly ash geopolymers are much less understood. This is largely due to their increased complexity as fly ash geopolymers are a multiphase and highly variable material.

Macroscopic characteristics critical in assessing a material's suitability for high temperature applications include: thermal expansion, thermal conductivity, strength retention, spalling and melting point. Characteristics relevant to the thermal analysis of geopolymers are phase stability, microstructural changes, dehydration and thermodynamics. The following sections review the literature concerning these properties including expected results and influencing factors.

2.12.1 Thermal Expansion of Geopolymers

Thermal expansion is the tendency for matter to increase in volume when heated. The thermal expansion/shrinkage of geopolymers is of particular interest when assessing their potential for high temperature applications. Shrinkage or expansion during heating introduces stresses which can weaken or damage the structure. For coatings, dimensional changes can lead to cracking and spalling from the substrate.

The rate of thermal expansion/shrinkage of geopolymers can be measured *in situ* with a dilatometer. Dimensional changes can be measured directly with a 'push rod' system or remotely using a laser measurement system (Walls, 2006). Repeated thermal cycling can give an indication as to the permanency or reversibility of dilation changes.

Thermal expansion of geopolymers is generally isotropic due to their amorphous structure, however non-uniform expansion can occur due to local variations in composition and temperature, elevating thermal stresses leading to cracking and spalling. Thermal expansion features commonly measured in geopolymers are listed in Table 2.6. A regional breakdown first proposed by Duxson et al. (2007b) and expanded on by Rickard et al. (2010) is detailed in Table 2.6 and shown in Figure 2-11. The temperature range of each region is variable and dependant on sample composition and testing conditions. It should be noted that not all geopolymers will exhibit all the regions defined in Table 2.6 and Figure 2-11.

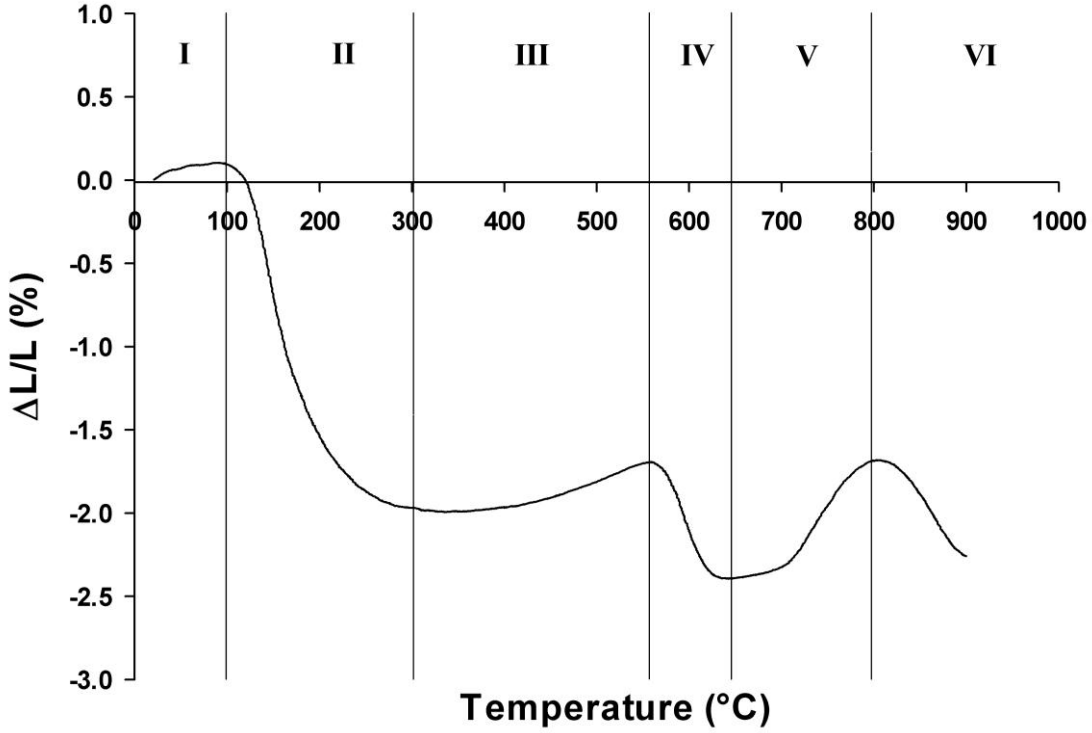

Figure 2-11 Thermal expansion of a fly ash geopolymer showing regional breakdown (see text for details). Si:Al=2.3. Adapted from Rickard et al. (2010).

Geopolymers, like most solid materials, expand upon heating (Region I). However, geopolymers typically contain a high proportion of water either adsorbed in the pores or chemically bound in the structure. Upon heating dehydration causes a loss of water resulting in overall shrinkage. At temperatures less than 100 °C, the dehydration of water is slow and the dominant dilation change is the expansion of the solid geopolymer paste. As the temperature increases, the dehydration rate also increases, and as such the measured dilation is a convolution of the expansion of the

geopolymer and the shrinkage of the water containing pores (Region II). In most geopolymer samples the dominant dilation event in this region is shrinkage and the amplitude of which is proportional to the water content of the sample. However, in very low water content samples and samples containing additives such as vermiculite, there can be a net expansion in this region (Temuujin et al., 2010).

Table 2.6 Thermal expansion characteristics of geopolymers – see Figure 2-11 for depiction of the different regions (Rickard et al., 2010).

Region	Temperature Range (°C)	Description	Effect	Influencing Parameters
I	0-150	Resistive dehydration	Slight expansion	Young's modulus of sample; Heat rate
II	100-300	Dehydration of free water	Significant shrinkage	Water content; Heat rate
III	250-600	Dehydroxylation	Minimal shrinkage	Abundance of hydroxyl groups and chemically bound water
IV	550-900	Densification by viscous sintering of geopolymer gel	Significant shrinkage	Residual water content; Si:Al ratio
V	Above densification temperature	Crystallisation in the geopolymer gel / Expansion due to cracking	Moderate to large expansion	Compositional ratio; Concentration/ Type of impurities
VI	Above densification temperature	Further densification	Large shrinkage	Compositional ratio

The extent of the dehydration shrinkage is dependent on the water content prior to testing, which is different to the synthesised water content as some of this water will dehydrate during curing and storage. The nature of the dehydration shrinkage, such

as onset temperature and duration, is dependent on the structure of the geopolymer and the heating rate during measurement. Duxson et al. (2007b) proposed that geopolymer resistance to dehydration shrinkage is proportional to the Young's modulus of the sample. Geopolymers with a higher Young's modulus can withstand greater capillary strain forces developed during dehydration and as such the onset temperature of the initial shrinkage is increased. The rate of dehydration is controlled by the rate of diffusion of the water from the structure. Thus the pore structure also has a strong influence on the dehydration rate. Duxson et al. (2007b) also reported that increasing the heating rate during thermal expansion tests increased the onset temperature and duration of the dehydration shrinkage event.

Dehydroxylation occurs between 25 °C and 400 °C and is associated with a small mass loss. The dehydroxylation reaction in geopolymers can be generalised by the following reaction (Duxson et al., 2007b);

$$T - OH + OH - T \equiv \rightarrow \equiv T - O - T + H_2O \quad \textbf{2.3}$$

where T is an aluminium or silicon atom.

The thermal shrinkage that occurs in region III, (generally occurring between 300 °C and 600 °C) is due to the physical contraction of the geopolymer gel as the hydroxyl groups are released, creating shorter T-O-T linkages (Duxson et al., 2007b). However, the small amount of shrinkage in this region can be masked by the expansion of solid phases such as the geopolymer gel or secondary phases. This is often the case in fly ash geopolymers due to the relatively high concentration of secondary phases such as quartz, mullite and hematite.

Structural changes such as crystallisation (of the geopolymer gel or secondary phases), oxidation (secondary phases only), sintering and melting affect the thermal expansion of geopolymers at high temperatures (> 500 °C).

The second major shrinkage event occurs between 550 °C and 900 °C (region IV) due to the densification of the geopolymer as the gel sinters and viscous flow fills the voids of the material. Rahier et al. (2007) proposed that the shrinkage in this region is

an indication of the glass transition temperature (T_g) of the geopolymer. Duxson et al. (2007b) found that the onset temperature of the densification reduced with increasing Si:Al ratio. The same study also noted that residual water in the material after dehydration reduces the activation energy for viscous flow of the aluminosilicates.

Beyond the densification region (region V), no consistent trend of thermal expansion has been reported in the literature. Rickard et al. (2010) and Rahier et al. (2007) measured a thermal expansion, whereas Duxson et al. (2007b) and Dombrowski et al. (2007) measured a sharp thermal shrinkage and Barbosa and MacKenzie (2003a) measured the geopolymer to be dimensionally stable. These different observations of thermal expansion in this region are believed to be due to differences in composition and the varying presence of secondary phases. Provis et al. (2009) measured a large expansion in fly ash geopolymers in this temperature region and reported it to be proportional to the liquids to solids ratio. It was suggested the expansion was due to the presence of high silicate phases, which increased in concentration with increasing liquids to solids ratio.

Crystallisation has also been observed to contribute to the thermal expansion in region V. Feldspar-based phases such as kaliophilite (K-activated), leucite (K-activated) and nepheline (Na-activated) have been reported to crystallise from the geopolymer gel and/or secondary phases at high temperatures (Barbosa and MacKenzie, 2003a, Duxson et al., 2007b, Rahier et al., 2007, White et al., 2010). Duxson et al. (2007b) noted that the magnitude of thermal dilation at temperatures above the densification region was influenced by the degree of crystal growth, which is an expansion event. Further details on crystallisation in geopolymers can be found in Section 2.12.4.

Other factors which are believed to influence thermal expansion in region V are crack formation and an increase in porosity. Rickard et al. (2010) found that thermal expansion in this region is dependent on sample size, with bigger samples exhibiting greater thermal expansion. It was suggested that this was caused by increased degree of cracking due to a larger temperature differential between the centre and the surface in the larger samples.

The last characteristic region of thermal expansion is region VI and is identified by large and usually rapid shrinkage. Subaer (2006) reported a sharp shrinkage leading to the failure of the material, whereas Duxson et al. (2007b) observed a slower shrinkage, though the magnitude for both cases was the same. The cause for the shrinkage in this region is due to one or more of the following; continued densification (similar to region IV), destruction of crystalline phases formed in region V, collapse of the pore structure formed in region V, or melting of the sample.

Barbosa and MacKenzie (2003a) reported that minimal shrinkage in subsequent thermal cycling of geopolymers was due to a lack of water in the geopolymer, indicating the permanency of the structural change.

2.12.1.1 Factors influencing the thermal expansion of geopolymers

Water content (w/c ratio)

The thermal expansion of geopolymers is strongly influenced by the water-to-cement ratio (can also be expressed as the water/binder, water/cementitious material or water/solid ratio). The higher the water content, the greater the amplitude of the shrinkage due to dehydration of water. Typical w/c ratios for geopolymers range between 0.15 and 0.4. Geopolymers synthesised for high temperature applications are typically designed with minimal water content; however, they are restricted by the need for the geopolymer slurry to be workable during casting. Kong et al. (2007) reported that a lower w/c ratio can be achieved in fly ash geopolymers than metakaolin geopolymers whilst maintaining a workable mixture. This is due to the spherical shape of fly ash particles allowing a more workable geopolymer slurry than the platy shape of metakaolin particles. Bakharev (2006) was able to achieve lower w/c ratios by compacting the mixture with forces up to 10 MPa prior to curing. Walls et al. (2006) used a high speed centrifugal mixer to reduce water content from 15 to 5 wt.% in fly ash-based geopolymers and observed a concomitant increase in compressive strength and Young's modulus.

Alkali activator

Duxson et al. (2006b) investigated the effect the alkali cation (Na, K or a mix) had on the thermal expansion of metakaolin geopolymers of 1.15 < Si:Al < 2.15. The study found that the choice of alkali had a significant effect on the thermal expansion (see Figure 2-12). Thermal shrinkage of the various alkali based geopolymers was measured to be in the order Na > Na + K > K. The magnitude and the rate of dehydration shrinkage (region II) were most affected by the change in alkali source. This effect was more significant in geopolymers of Si:Al ≤ 1.4. The onset temperature of region IV also changed with alkali source in the order K > Na + K ≈ Na.

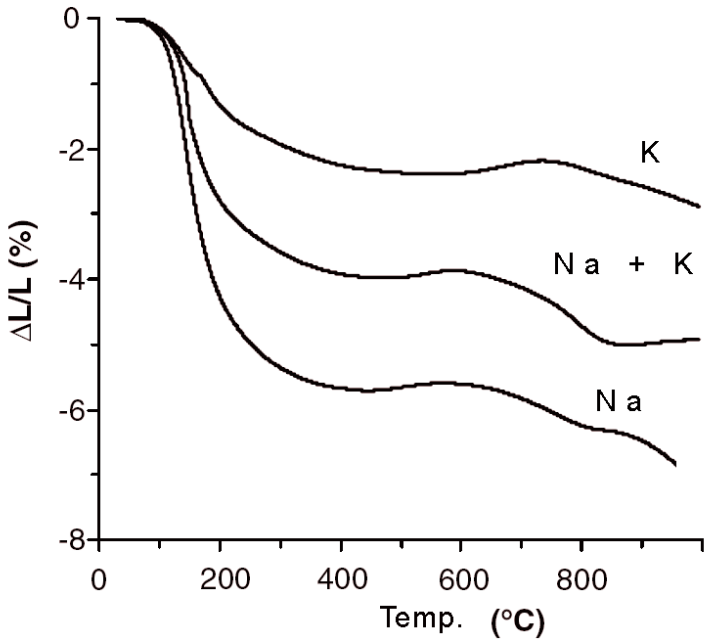

Figure 2-12 Thermal shrinkage of Na, Na+K and K activated metakaolin-based geopolymers with Si:Al ratio of 1.15 (Duxson et al., 2006b).

Compositional ratio

Duxson et al. (2006b, 2007b) investigated the variation of Si:Al (1.15 ≤ Si:Al ≤ 2.15) on the thermal expansion of metakaolin geopolymers. The study found that the total shrinkage upon heating to 1000 °C increased with increasing in Si:Al. The amplitude of dehydration and dehydroxylation shrinkage was not observed to be influenced by Si:Al ratio. The onset temperature for densification of the geopolymer paste (region IV) was found to reduce with increasing Si:Al ratio. It was proposed by Duxson that the reduced onset temperature was due to the incomplete incorporation of aluminium

from the source material, leaving free sodium atoms in the system, which reduces the glass transition temperature (T_g) of aluminosilicates.

Source material type

The following section describes the effect of the source material type on the thermal expansion of geopolymers.

Thermal properties of metakaolin geopolymers have been studied by a number of researchers (Barbosa and MacKenzie, 2003a, Duxson et al., 2006b, Duxson et al., 2007b, Liefke, 1999, Rahier et al., 1997, Subaer, 2005). The trend observed in each study was similar, though the amplitude and temperature of the thermal shrinkage events varied between the studies believed to be due to differences in alkali sources and water contents.

Fly ash based geopolymers have been observed to have similar thermal shrinkage characteristics to metakaolin geopolymers, though the magnitude of the shrinkage is typically less due to the lower water content used to synthesise fly ash geopolymers (Bakharev, 2006, Dombrowski et al., 2007, Kong et al., 2005, Rickard, 2007). Other differences in the shrinkage/expansion character are caused by the impurities introduced via the fly ash. Common impurities in fly ash geopolymers are crystalline silica (quartz), unburnt carbon, iron and calcium oxides. Rickard et al. (2010) studied the effect of high iron and quartz content in fly ash-based geopolymers. The study found that a quartz content of 20 wt.% had only minimal effect on the thermal expansion (most notably a small increase in thermal expansion in region III). Increasing the quartz content to 40 wt.% reduced the thermal shrinkage by over 50 % at 500 °C. A thermal expansion event observed to occur at approximately 800 °C (Figure 2-11), was found to be associated with the oxidation and crystallisation of the amorphous iron oxides from the fly ash (Rickard et al., 2010). Dombrowski et al. (2007) studied the effect of calcium content on the thermal expansion of fly ash geopolymers and found that 8 wt.% $Ca(OH)_2$ was the optimum amount for reduced shrinkage up to 1050 °C (Figure 2-13).

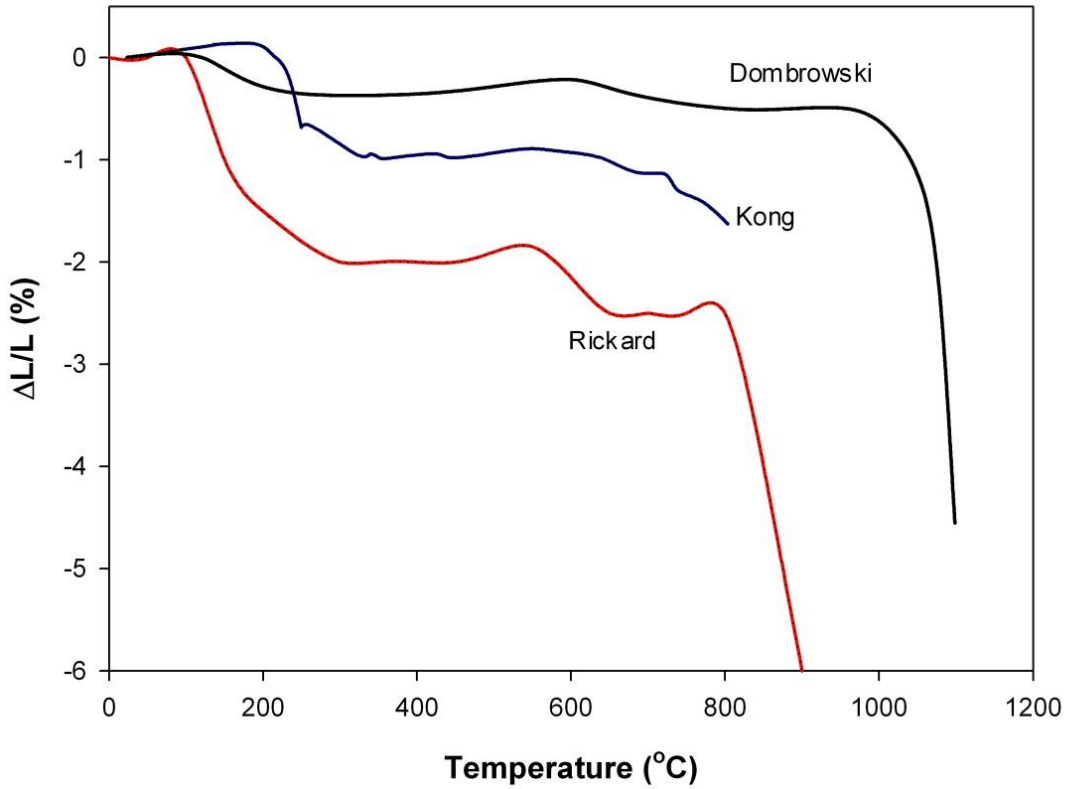

Figure 2-13 Thermal shrinkage of fly ash geopolymers. Figure adapted from Rickard et al. (2010), Dombrowski et al. (2007) and Kong et al. (2005).

2.12.1.2 Thermal expansion of geopolymer concrete

The thermal expansion of concrete, whether Portland or geopolymer cement based, is dominated by the thermal expansion of the aggregates as they usually comprise between 65 and 80 % of the volume (Bazant and Kaplan, 1996). In general, the binding phase shrinks and the aggregates expand during high temperature exposure leading to cracking and reduction in strength. Thermal expansion of geopolymer concrete varies with factors such as aggregate type, aggregate concentration and w/c ratio. Of these, aggregate type has the greatest influence (Bazant and Kaplan, 1996, Kong et al., 2005). Aggregates suitable for use in geopolymer concrete are the same as used in OPC (Rangan, 2007). It is important to note that concretes made with high-quartz aggregates are strongly affected by the rapid expansion due to the α-β quartz phase change occurring at 573 °C (as can be seen the large thermal expansion of siltstone in Figure 2-14).

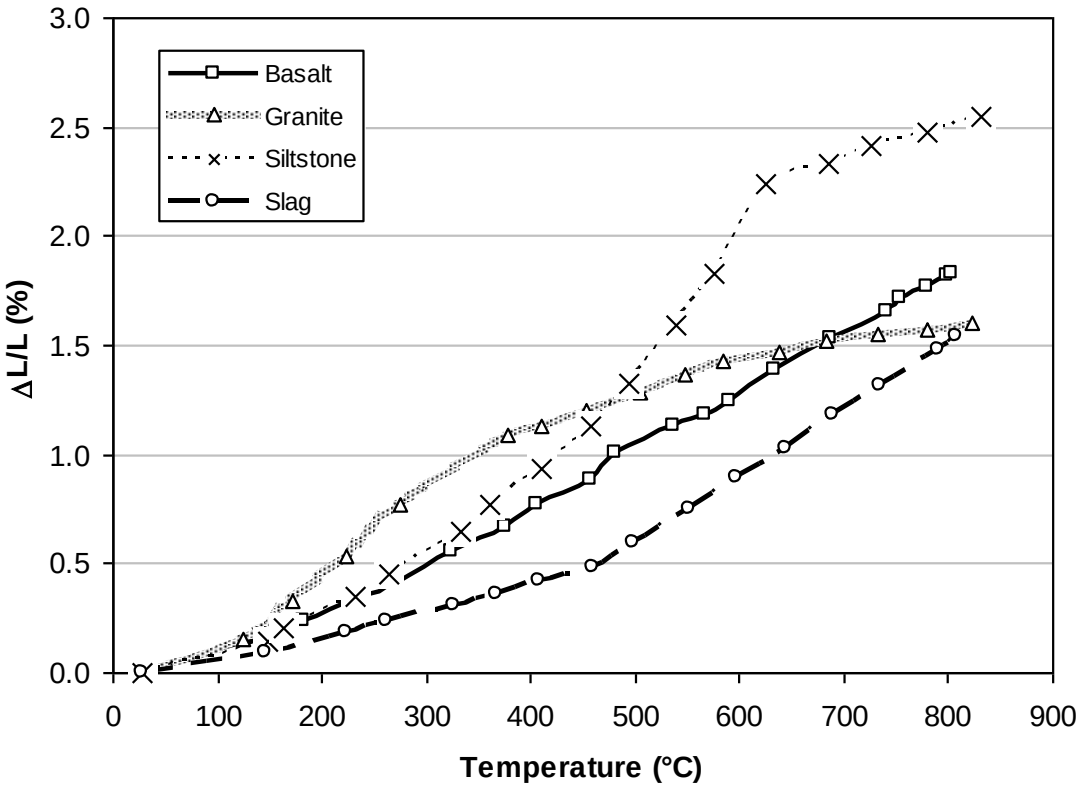

Figure 2-14 Thermal expansion of common coarse aggregates Adapted from Kong and Sanjayan (2008).

A comprehensive study on the thermal expansion of geopolymer concrete has not yet been published, though studies on geopolymer mortars have been reported. Subaer and van Riessen (2006) investigated the thermal expansion of metakaolin geopolymer mortars containing fine quartz and granite aggregates. The study found that the introduction of fine aggregate reduced the thermal shrinkage of the mortar to less than 1 %, half that of the paste only specimen. It was noted that the phase change in the quartz aggregate set the upper value of the dimensionally stable temperature range.

2.12.1.3 Comparison to the thermal expansion of OPC

Thermal expansion data for OPC paste and concrete is widely available in the literature; a thorough investigation was published by Bazant and Kaplan (1996). However, like geopolymers, there is no one thermal expansion curve that is representative for all OPC products. This makes a direct comparison with

geopolymers difficult and somewhat subjective. High temperature (>300 °C) thermal expansion is more significant for comparison between OPC and geopolymers as the dehydration of free water is common to both materials. No noticeable trend in the magnitude of the thermal shrinkage was determined from the literature when comparing OPC and geopolymers. However, it was noticed that OPC continues to shrink throughout the heating cycle (Cruz and Gillen, 1980), whereas geopolymers in many cases exhibited a region of dimensional stability up to 500 °C.

The critical difference between geopolymer and OPC occurs at temperatures greater than 500 °C. The binding phase in OPC is a crystalline calcium silicate hydride (C-S-H) compound containing a large amount of chemically bound water. At high temperatures, this water dehydroxylates causing the destruction of the binding phase, failure of the material and an associated large shrinkage. Geopolymers also have water in their structure but it is weakly bound so that when it dehydroxylates, the binding phase retains its structural integrity and is not associated with significant shrinkage.

2.12.2 Thermo-physical Properties

Thermal conductivity, thermal diffusivity and the specific heat are all properties of interest to scientists studying geopolymers. These characteristics can be determined by analysing data from hot plate or transient hot wire experiments. The transient hot wire method can be performed by either embedding a thermocouple and a heat source into the sample or using a commercially available thermal analysis probe (further details in chapter 3).

2.12.2.1 Thermal conductivity

Thermal conductivity is the ability for a material to conduct heat. The thermal conductivity of geopolymers is measured to assess their potential application as an insulating product or a concrete building material. Insulators require a low thermal conductivity because they are designed to reduce the conduction of heat, whereas it

is preferable for concretes to have a relatively high thermal conductivity as this reduces expansion stresses within the material when exposed to heat (Subaer, 2005).

Low density geopolymer foams designed as thermal insulators have been produced with a thermal conductivity as low as 0.037 W $m^{-1}K^{-1}$ (Liefke, 1999). Duxson et al. (2006a) reported the thermal conductivity of metakaolin geopolymers to range between 0.4 and 0.8 W $m^{-1}K^{-1}$. Subaer (2005) obtained similar results to the Duxson study, with values varying from 0.55-0.65 W $m^{-1}K^{-1}$ (Table 2.7). The thermal conductivity values reported are comparable to that of OPC paste which typically has a thermal conductivity of around 0.5 W $m^{-1}K^{-1}$ (Demiborga, 2003).

The thermal conductivity of geopolymers is reported to be proportional to their bulk density rather their composition (Duxson et al., 2006a, Subaer, 2005). Density is analogous to the distance between various components, thus geopolymers with a shorter distance between the components are likely to exhibit a higher thermal conductivity. This is in good agreement with the phonon transport theory as phonon propagation is reduced by structural boundaries (Kittel, 2005, p. 122). Voids will also reduce the density and the measured thermal conductivity as they are usually filled with low thermal conductivity phases such as air. Low thermal conductivity geopolymers have been synthesised by creating highly porous, low density samples (Prud'homme et al., 2010).

Subaer (2005) reported that the addition of 40 wt.% quartz aggregate increased the thermal conductivity by 40 % in metakaolin geopolymers due to an overall increase in bulk density (Table 2.7). The higher thermal conductivity of quartz (11.1 and 5.9 $Wm^{-1}K^{-1}$ for the c-axis and a-axis, respectively (Weast, 1986)) will also contribute to an overall increase in the thermal conductivity of the geopolymer-quartz composite. Duxson et al. (2006a) investigated the change in thermal conductivity with Si:Al ratio and alkali activator and found no correlation with either Si:Al ratio or alkali activator to the thermal conductivity of the geopolymer.

Table 2.7 Density and thermal conductivity of metakaolin geopolymers of various compositions (Subaer, 2005).

Sample	Density (g cm^{-3})	Thermal Conductivity ($Wm^{-1}K^{-1}$)
Si:Al=1.5, Na:Al=0.6	1.68 ± 0.09	0.65 ± 0.04
Si:Al=1.5, Na:Al=0.8	1.62 ± 0.05	0.64 ± 0.03
Si:Al=2.0, Na:Al=1.0	1.43 ± 0.01	0.55 ± 0.03
Si:Al=1.5, Na:Al=0.6 (+ 40 wt.% quartz aggregate)	1.89 ± 0.02	0.91 ± 0.07

Zuda et al. (2006) investigated the dependence of thermal conductivity on the moisture content of furnace slag based geopolymers. Samples were subjected to preheating at various temperatures, and then water saturated using a humidity chamber. They found that the thermal conductivity increased with moisture content. It was also found that structural changes after pre heating resulted in higher thermal conductivity values due to the increased water capacity.

2.12.2.2 Thermo-analysis of geopolymers (DTA / DSC / TGA)

Thermodynamic processes in geopolymer cements have been measured using differential thermal analysis (DTA) and differential scanning calorimetry (DSC) (Barbosa and MacKenzie, 2003a, Duxson et al., 2007b, Rahier et al., 2007, Rickard et al., 2010, Subaer and van Riessen, 2006). Weight loss during high temperature exposure has been measured using thermo-gravimetric analysis (TGA) (often simultaneously with DTA) (Bakharev, 2006, Barbosa and MacKenzie, 2003a, Duxson et al., 2007b, Kong et al., 2007, Rickard et al., 2010, Subaer and van Riessen, 2006). These testing techniques, as with dilatometry, usually allow a choice of atmosphere during testing. Inert atmospheres such as nitrogen or argon can be used to eliminate atmospheric reactions with secondary phases such as oxidation.

Figure 2-15 contains a typical TGA / DTA curve from a metakaolin geopolymer. Weight loss, due to the dehydration of water, begins above ambient temperatures and the percentage mass loss is proportional to the initial water content of the sample. Water continues to evaporate until approximately 300 °C, where the bulk of the free water has been liberated. A number of studies have shown that at least 80 % of the

weight loss occurs below 200 °C (Barbosa and MacKenzie, 2003a, Duxson et al., 2007b, Kong et al., 2008, Rickard et al., 2010), though this dehydration period can be extended when fast heat rates are applied. Duxson et al. (2006b) commented that water loss up to 300 °C corresponds to evaporation of unconstrained pore water from the geopolymer gel. Weight loss above 300 °C is characteristic of the elimination of water by condensation of silanol or aluminol groups on the surface of the geopolymeric gel (Duxson et al., 2007b). This is a dehydroxylation process as discussed in section 2.12.1.

DTA is used to study the thermodynamics of geopolymers as a function of temperature. Upward trends in DTA curves indicate an exothermic process whereas downward trends indicate an endothermic process occurring at that particular temperature. Dehydration is an endothermic process as the system is losing energy to the water vapour. Mineral phase changes are also endothermic as they draw energy from the system to change phase. Dehydroxylation and crystal destruction events are exothermic processes (Duxson et al., 2007b).

The dehydration endotherm for a metakaolin geopolymer is clearly evident in the minima in the DTA thermogram in Figure 2-15. The temperature of the endothermic minimum and the temperature range of the event has been observed to reduce with increasing Si:Al ratio (Duxson et al., 2007b). Beyond the dehydration endotherm, geopolymers become relatively thermodynamically stable, though slightly exothermic. Geopolymer pastes with compositions conducive to crystallisation may exhibit high temperature endothermic/exothermic activity as the phases form and collapse with increasing temperature. Duxson et al. (2007b) observed an exotherm at approximately 700 °C in metakaolin geopolymers of Si:Al = 1.15 which was attributed to the collapse of a faujasite phase formed at a lower temperature.

Barbosa and MacKenzie (2003a) conducted differential scanning calorimetry (DSC) on metakaolin geopolymers from room temperature to 500 °C. DSC results are comparable with DTA results where geopolymers undergo an endothermic reaction during the rapid dehydration phase between 100 °C and 200 °C. The study also found that geopolymers are slightly exothermic above the dehydration minima.

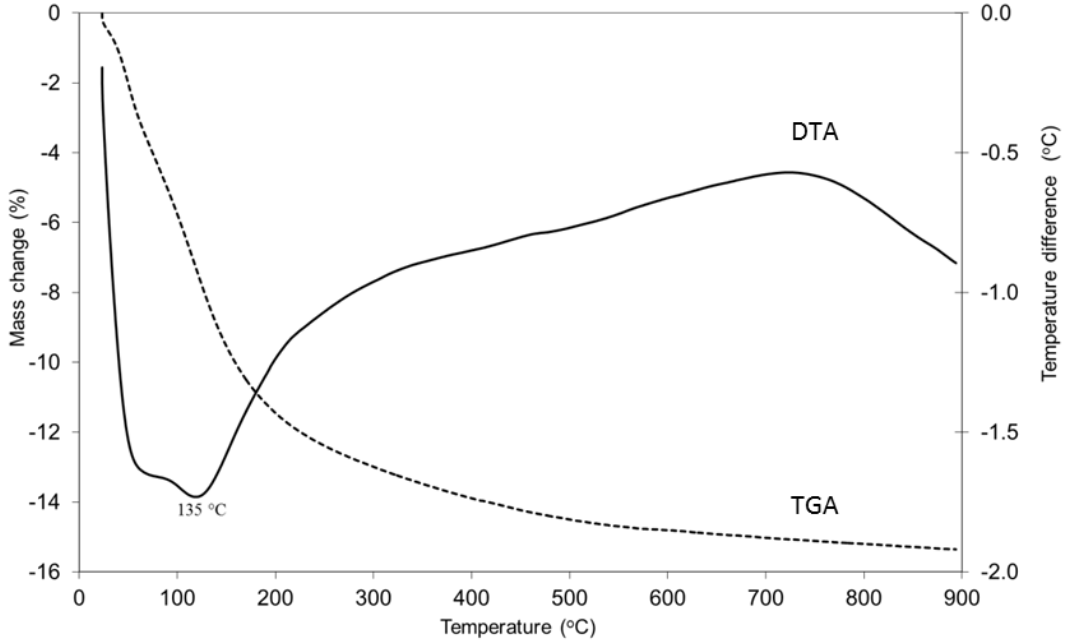

Figure 2-15 TGA–DTA curves for a metakaolin geopolymer prepared with Si:Al = 1.5, Na:Al = 0.6. Adapted from Subaer and van Riessen (2006).

TGA / DTA curves from fly ash geopolymers are more complicated than metakaolin geopolymers due to the presence of impurities. Rickard et al. (2010) obtained TGA / DTA results from a geopolymer, where the precursor fly ash contained 20 wt.% quartz and 15 wt.% iron oxide. An exothermic spike was observed at approximately 400 °C in the DTA curve and a simultaneous weight loss in the TGA curve (Figure 2-16). The exotherm was reportedly caused by poorly ordered iron oxide (possibly ferrihydrite) from the fly ash crystallising to hematite. The associated weight loss resulted from the loss of hydroxyl groups during the phase change. The same study also observed mass gain in fly ash geopolymers heated above 600 °C in air while no mass gain was observed in geopolymer samples heated in flowing nitrogen. The mass gain was thus attributed to the oxidisation of the iron oxides and was exothermic in nature.

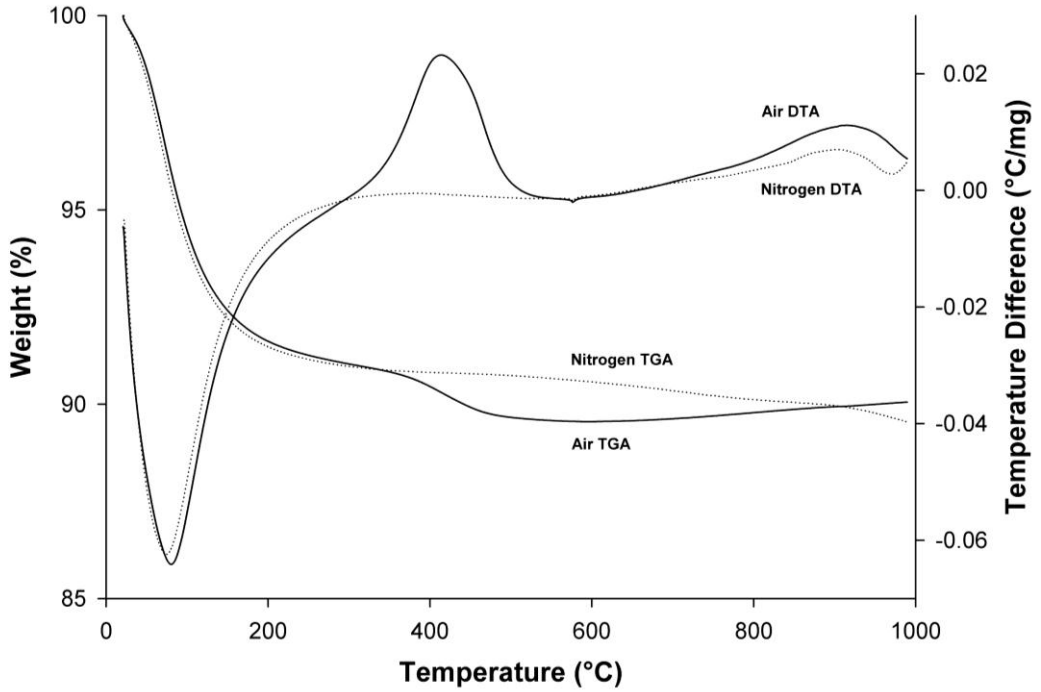

Figure 2-16 TGA / DTA results for a fly ash geopolymer, Si:Al = 2.3, Na:Al =0.85, H_2O:SiO_2 = 2.0 (Rickard et al., 2010).

2.12.3 Mechanical Strength Evolution at High Temperature

Thermal exposure affects the mechanical strength of geopolymers, the extent of which can be used as an indication of the material's thermal resistance. Mechanical strength is commonly measured *ex-situ* (after cooling) by unconfined compressive strength measurements. Young's modulus, splitting and flexural strength measurements can also give an indication as to the change in strength after exposure to high temperature. Testing that involves thermal cycling can be used to demonstrate the long term mechanical performance of the material.

Changes in the mechanical strength, both during and after thermal exposure, are critical in assessing the high temperature performance of geopolymers, especially for materials intended for use in structural applications. Most reported mechanical strength results are derived from ex-situ experiments due to lack of appropriate facilities for *in situ* mechanical testing at high temperatures.

Exposure to high temperatures results in changes to the mechanical strength of geopolymers due to thermally induced structural and phase composition changes in the material. Structural changes include sintering, densification, melting, cracking and pore size/volume/interconnectivity changes. Phase composition changes include crystal growth, crystal destruction, dehydration and geopolymer gel decomposition to release free Si, Al and alkali. Most of the aforementioned changes will reduce the mechanical strength of geopolymers while some will actually promote an increase in mechanical strength.

Densification of the geopolymer gel phase results in fewer voids and allows for more uniform stress gradients during an applied load, leading to greater mechanical strength. Sintering of the un-reacted material, such as crystalline fly ash particles, provides increased mechanical strength due to stronger bonding between the particles. This is especially important in geopolymers containing aggregates. The temperature and extent of the densification and sintering is dependent on the sample's composition and the type of secondary phases.

Pore structural changes have a mixed effect on the mechanical strength of geopolymers. Pores act as defects, and in general, mechanical strength decreases as pore size and volume increases. However, this is not always the case. Increased pore interconnectivity allows for greater water mobility during heating, which reduces structural damages caused by vapour pressure on the pore walls (Kong et al., 2007). Thus geopolymers with a more interconnected pore structure will experience less strength loss than a comparable geopolymer sample with an isolated pore structure. Pore structure is known to vary in geopolymers during thermal exposure (Bakharev, 2006, Duxson et al., 2007b, Perera and Trautman, 2006, Zuda et al., 2006) (see section 2.12.5 for further details) which causes non-linear variations in mechanical strength during heating.

A study by Bakharev (2006) analysed the effect of high temperature exposure on the compressive strength of sodium activated fly ash geopolymers. Figure 2-17 shows the compressive strength evolution of geopolymer samples synthesised with various curing conditions. The samples in Bakharev's (2006) study retained their compressive strength up to 800 °C. Beyond 1000 °C all samples had a significant

drop in compressive strength. Pressure compaction of the very low water content samples of between 1 and 3 MPa during synthesis improved both the as-cured strengths and the strength after exposure to 800 °C, reportedly due to the low water content reducing the dehydration damage on firing (Figure 2-17). The same study also investigated fly ash geopolymers produced using a potassium alkali activator which exhibited lower initial compressive strength, though substantially gained strength up to 1000 °C.

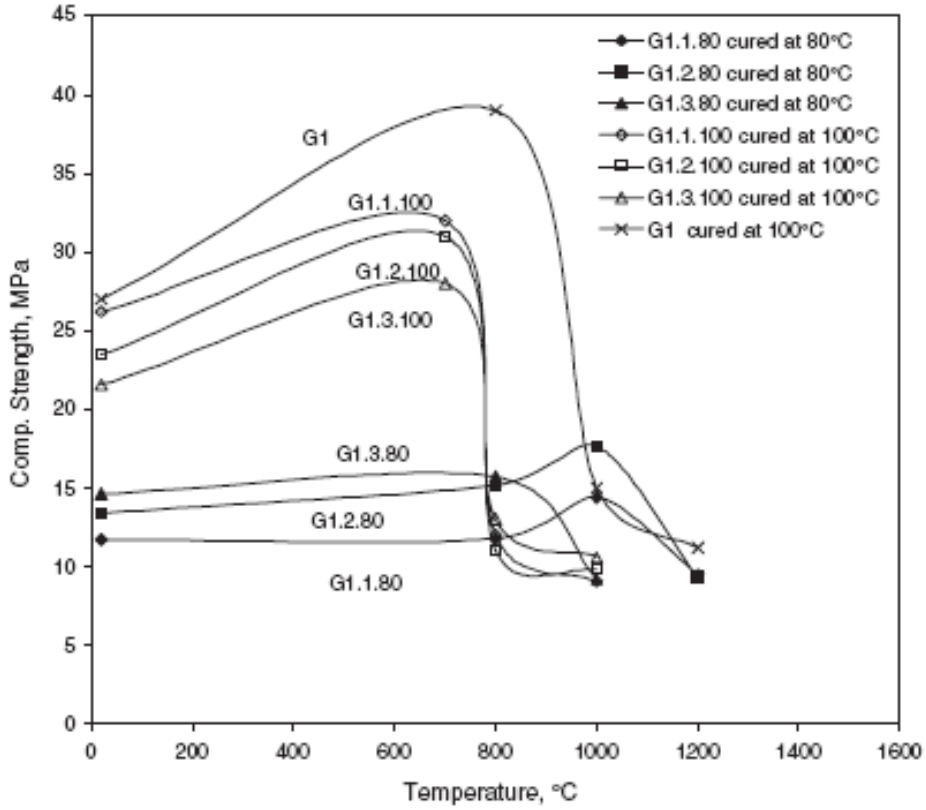

Figure 2-17 Compressive strength of geopolymer materials of w/c = 0.09 prepared using class F fly ash and sodium hydroxide, before and after firing experiments (Bakharev, 2006). Legend denotes compaction pressure in MPa and temperature during curing.

Kong et al. (2005, 2007, 2008) compared geopolymers made with metakaolin and fly ash after exposure to elevated temperatures and found that strength decreased after heating for the metakaolin based samples while the fly ash based samples increased in strength. In addition to SEM analysis, mercury porosimetry was also conducted which revealed that metakaolin geopolymer predominantly had mesopores (2 - 50 nm) whereas fly ash geopolymer had a higher proportion of micropores (<2 nm). This difference in pore size and inferred pore connectivity was reported to be

responsible for retention of strength in the fly ash geopolymers due to the ability of water to escape during heating without damaging the structure. Bakharev (2006) conducted similar experiments and also concluded that changes in porosity due to high temperature exposure directly influenced compressive strength of post fired samples.

Zuda et al. (2006) found increased compressive strength in blast furnace slag based geopolymers (39 wt.% CaO) that exhibited significant crystal growth, suggesting that the crystallisation induced the strength gain. Dombrowski et al. (2007) came to a similar conclusion for fly ash geopolymers with added calcium. Opposing results were observed by Bakharev (2006) who found reduced compressive strength in fly ash geopolymers that exhibited crystal growth. The discrepancies between the studies are most likely due to multiple factors, such as different starting materials and sample composition varying the degree of sintering and cracking. Further details on crystal growth at elevated temperatures are discussed in section 2.12.4.

Provis et al. (2009) correlated mechanical and thermal properties of sodium silicate activated fly ash geopolymers. Some of the geopolymers with moderate strengths also showed a small expansion in the 700 - 800 °C temperature range, which was identified as corresponding to the swelling of a high-silica phase present as pockets within the geopolymer gel structure. Low strength retention was observed for samples where this phase was excessive.

Dombrowski et al. (2007) found that the addition of a small amount of calcium to fly ash geopolymers increased the initial compressive strength, however it reduced the amount of strength gain upon heating to 1000 °C when compared to samples without added calcium.

Comparison to OPC

Compressive strengths of as-cured geopolymers can be tailored to be analogous to the strengths of OPC products, including high strength concrete. The significant difference between the two materials is the change in mechanical strength during and after high temperature exposure. The OPC binding phase (C-S-H gel) is a hydrate and at high temperatures it will dehydrate and subsequently destroy the binding

phase, causing significant strength losses (Neville, 2000). An example of the mechanical strength of OPC based concrete upon elevated temperature exposure can be seen in Figure 2-18. OPC concretes can also lose strength due to explosive spalling as pore water and water liberated from the hydrate phases spalls material from the surface as it exits (Chan et al., 1999).

There are however, specialist cements such as calcium aluminate cement, which exhibit enhanced thermal resistance, though they are much more expensive to produce (up to four times more than standard OPC) (Scrivener et al., 1999). Geopolymers have the potential to out-perform even specialist OPC products due to their intrinsic thermal resistance.

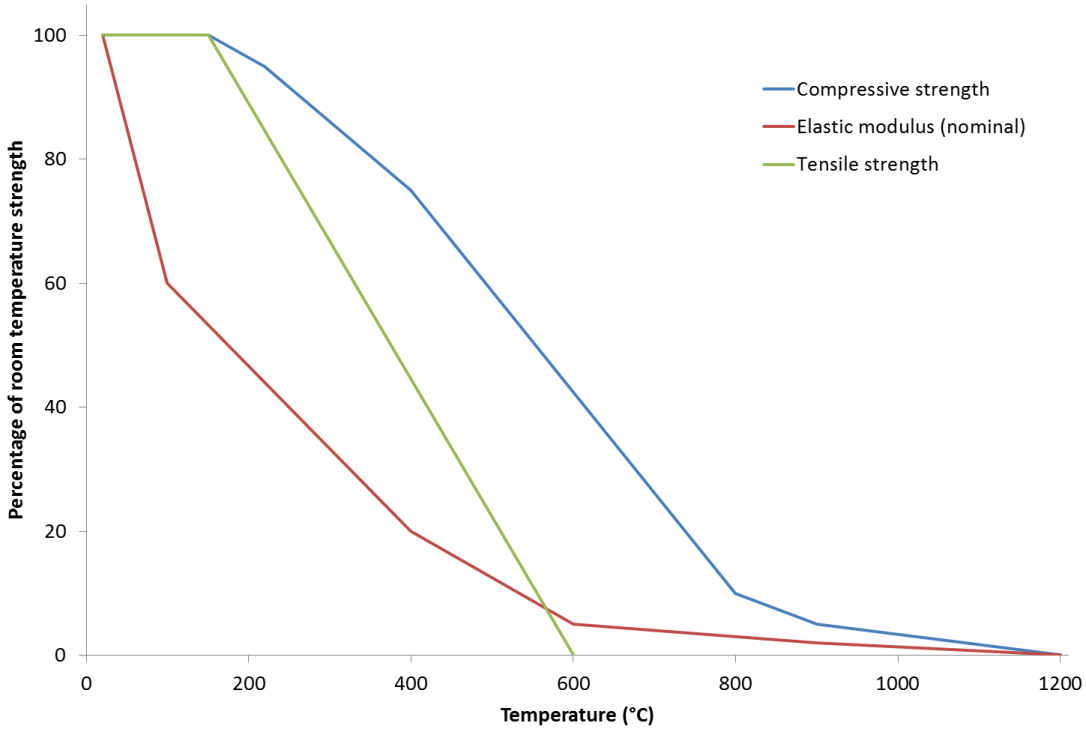

Figure 2-18 Degradation of mechanical properties of Portland cement based concrete (the graph is based on the information provided by Eurocode EN 1992-1-2 (2004).

Geopolymer Concrete

The inclusion of aggregate to form geopolymer concrete drastically alters the thermal properties. At elevated temperatures the geopolymer gel shrinks while the aggregates expand (Kong et al., 2005, Subaer, 2005). The differential expansion between the gel and the aggregate degrades the bulk mechanical properties significantly when compared to paste only samples (Kong et al., 2007). The useful working temperature

for geopolymers containing quartz aggregate is reported to be limited to 500 °C (Subaer, 2005). The use of low thermal expansion aggregates such as basalt is likely to greatly extend the working temperature range.

Kong and Sanjayan (2008) heated fly ash geopolymers to 800 °C and noted that for pastes there was an increase in strength of 53 % while for concrete samples (geopolymer + aggregate) the strength decreased by 65 %. The strength decrease for the concrete sample was attributed to the thermal expansion mismatch: the aggregate expanded by approximately 2 % at 800 °C while the geopolymer contracted by 1.6 %. The thermal expansion mismatch of the different components in concrete remains a challenge yet to be overcome if these materials are to be utilised as construction materials in a fire proofing application.

Geopolymer composites

Research has been undertaken to assess the use of additives, such as vermiculite to make composite geopolymers with improved thermal performance. Zuda et al. (2010) and Zuda and Černý (2009) added both vermiculite and electrical porcelain to slag and alkali activated it to make a light weight composite with impressive properties. Their composite's strength decreased when raised to 800 °C (35 % of room temperature strength) but thereafter the strength increased believed to be due to the growth of ankerite so that by 1200 °C it was 30 % higher than at room temperature. Lin et al. (2009) also manufactured geopolymer composites by adding α-Al_2O_3 to KOH activated metakaolin geopolymers. The presence of the α-Al_2O_3 filler reduced thermal shrinkage which improved the post firing mechanical properties. Lyon et al. (1997) exposed fiber reinforced geopolymer to a high heat flux (50 kWm^{-2}) and found that carbon fiber geopolymer composites can retain up to 67 % of their original flexural strength after exposure.

In situ compressive strength testing

One of the limitations of the research described above is that strength testing and microstructure evaluation is conducted post heating and conclusions drawn are based on ambient measurements. Pan and Sanjayan (2010) directly measured the stress-strain behaviour of geopolymers *in situ* at elevated temperatures to overcome this limitation. They observed that the hot compressive strength of the geopolymer

increased almost two-fold at 520 °C compared with the initial room temperature strength. Beyond 520 °C the glass transition temperature resulted in an abrupt loss of stiffness.

2.12.4 Phase Evolution at High Temperature

Crystallisation and phase changes have been observed to occur in geopolymers exposed to elevated temperatures (Bakharev, 2006, Barbosa and MacKenzie, 2003a, Dombrowski et al., 2007, Duxson et al., 2007c, Kovalchuk and Krivenko, 2009, Rahier et al., 1997, Rahier et al., 2007, Rickard et al., 2010). Phase identification is usually conducted by analysis of XRD data, though electron diffraction can also be used to identify crystalline material.

Geopolymers designed for high temperature applications may be exposed to temperatures in excess of 1400 °C. The high temperatures provide the energy to induce a wide range of changes in the crystal structure and phase abundance in geopolymers. The three main changes are crystal formation, crystal destruction and crystal structural changes. The changes can occur in the geopolymer gel or in the secondary phases. Crystal growth in geopolymers can either enhance the thermal resistance of geopolymers by crystallising to high melting point phases (Barbosa and MacKenzie, 2003b), or reduce the thermal resistance by increasing the thermal expansion mismatch between phases.

2.12.4.1 Phase changes in the geopolymer gel

Geopolymer gel is well known to have only short range order and appear amorphous under Bragg diffraction conditions. During heating to high temperatures, decomposition of the gel frees Na, Si and Al species to crystallise to various zeolitic phases and alkali feldspars. The temperature and extent of the crystal growth varies between studies, for example, Barbosa & MacKenzie (2003a) found that geopolymers remain totally amorphous up to 1200 °C, whereas Duxson observed crystallisation starting as low as 600 °C (Duxson et al., 2007c).

Mineral phases nepheline ($NaAlSiO_4$), leucite ($KAlSi_2O_6$) and kaliophilite ($KAl_4Si_4O_{16}$), have been observed in geopolymers exposed up to 1000 °C (Barbosa and MacKenzie, 2003a, Duxson et al., 2007c, Kong et al., 2007, Rahier et al., 2007). Bell et al. (2008b) formed pollucite ($CsAlSi_2O_6$) from caesium activated metakaolin geopolymers heated above 1000 °C. Higher temperature studies by Barbosa & MacKenzie (2003a) observed corundum (Al_2O_3) and mullite ($Al_6Si_2O_{13}$) forming in metakaolin geopolymers at temperatures greater than 1100 °C. Duxson et al. (2007c) found that initially amorphous geopolymers can contain greater than 80 % crystalline material after heating to 1000 °C.

The degree and type of crystallisation in geopolymers depends on sample composition and heating conditions. Poorly reacted geopolymers have additional Na or K, Si or Al monomers not incorporated in the geopolymer gel and consequently exhibit higher crystal growth during heating (Bakharev, 2006, Barbosa and MacKenzie, 2003a). Sodium based geopolymers have been observed to be more prone to crystallisation than potassium geopolymers (Bakharev, 2006, Duxson et al., 2007b) which has been attributed to sodium's higher diffusion coefficient (Bakharev, 2006).

The Si:Al ratio is once again a strong influence on the behaviour of geopolymers at high temperatures. It has been observed that the extent of crystallisation (the amount of amorphous content that crystallises) decreases with increasing Si:Al ratio (Barbosa and MacKenzie, 2003a, Duxson et al., 2007b). Coupled with this, the onset temperature of crystallisation increases with Si:Al ratio (Duxson et al., 2007b). In general terms, the higher the Si:Al ratio, the greater the phase stability of the geopolymer gel during high temperature exposure.

Crystallisation in geopolymers has been observed to be time dependant (Duxson et al., 2007b, Rahier et al., 2007). Rahier et al. (2007) analysed the diffraction pattern of metakaolin geopolymers held at 1000 °C and found that the small amount of nepheline initially present at 1000 °C increased significantly over a period of 2.5 hours. Similarly, Duxson et al. (2007b) demonstrated that faster heating regimes reduce the amount of crystal growth of certain phases.

2.12.4.2 Phases formed from secondary material

As mentioned previously, geopolymers are a composite material with other phases present amongst the amorphous gel. The secondary material initially present in the geopolymers can either come from the source material or the aggregate. This material is subject to phase changes during high temperature exposure which can affect the bulk thermal properties of the geopolymer.

Rickard et al. (2010) observed increased hematite (Fe_2O_3) peak intensity in fly ash geopolymers after heating to 900 °C. The hematite phase was reported to evolve from the amorphous iron oxides (commonly ferrihydrite) initially present in the fly ash. The ferrihydrite-hematite phase change is reported to be kinetic in the literature (Cornell and Schwertmann, 1996), however it was observed to be dependent on an oxygen containing atmosphere in geopolymers. Bakharev (2006) observed a similar increase in hematite peak intensity in fly ash geopolymers after exposure to 1200 °C.

Quartz is commonly found in geopolymers, not only as part of the aggregate but as a fine impurity in the source material (typically in fly ashes). Quartz undergoes a phase change at 573 °C from low to high quartz (Deer et al., 1996), which is observable in DTA thermograms and dilatometry curves of geopolymers (Rickard et al., 2010, Subaer and van Riessen, 2006). The phase change is accompanied by a volume change which adversely influences the bulk properties such as mechanical strength. There may be other crystalline phases of silica in fly ash geopolymers (formed during the high temperature coal combustion process) such as cristobalite or tridymite which will also undergo phase changes upon heating.

Mullite has been reported to crystallise out of unreacted metakaolin in kaolin based geopolymers heated to 1200 °C (Barbosa and MacKenzie, 2003a). Phase changes in mullite that is initially present in fly ash based geopolymers (up to 20 wt.%) have not been reported in the literature.

Gehlenite ($Ca_2Al_2SiO_7$) has been observed to form at 800 °C in geopolymer samples containing lime ($Ca(OH)_2$) and is produced by the decomposition of calcium-silicate-hydrates (C-S-H) phases (Dombrowski et al., 2007, Perera and Trautman, 2006).

2.12.5 Microstructural Evolution at High Temperature

Changes in geopolymer microstructure have been observed to affect the bulk thermal properties and as such are important to study and characterise. The high resolution capability of electron microscopy has been widely used to analyse microstructural changes in thermally exposed geopolymers. Although usually conducted *ex situ*, *in situ* high temperature microstructural evolution experiments have been conducted on geopolymers using a hot stage in a TEM (Kriven et al., 2003). Thermally induced changes in the pore structure are also of interest to researchers as they have implications for mechanical strength and thermo-physical properties. There are a wide range of pore analysis techniques available including mercury intrusion porosimetry (MIP), nitrogen adsorption/desorption, SEM/TEM and x-ray computed tomography (CT).

Thermal exposure has been observed to alter the microstructure of geopolymers in a number of ways. Sintering, crystallisation and eventual melting alter the morphology of the gel at high temperatures, whilst dehydration and densification affect the size and distribution of the pore structure.

Dehydration causes the first microstructural change, beginning at just above ambient temperature and continuing to above 200 °C. Vapour pressure from the escaping water causes damage to the geopolymer structure and alters the pore connectivity by creating pathways to the surface of the material. Kong et al. (2007) reported that metakaolin geopolymers experience more damage to the microstructure during evaporation than fly ash geopolymers due to the lower interconnectivity of the pore structure.

At higher temperatures, sintering and densification of the geopolymer gel alters the morphology (Figure 2-19). The post exposure geopolymer has fewer inclusions and exhibits a smoother texture than the unexposed geopolymer. This is caused by the viscous sintering of the gel during the high temperature exposure leading to better particle interconnectivity and promoting crack healing (van Riessen et al., 2009, Duxson et al., 2006b). Van Riessen et al. (2009) (Figure 2-19) also noted that the

viscous flow of aluminosilicates out of the undissolved fly ash particles exposed the internal pores that were initially closed.

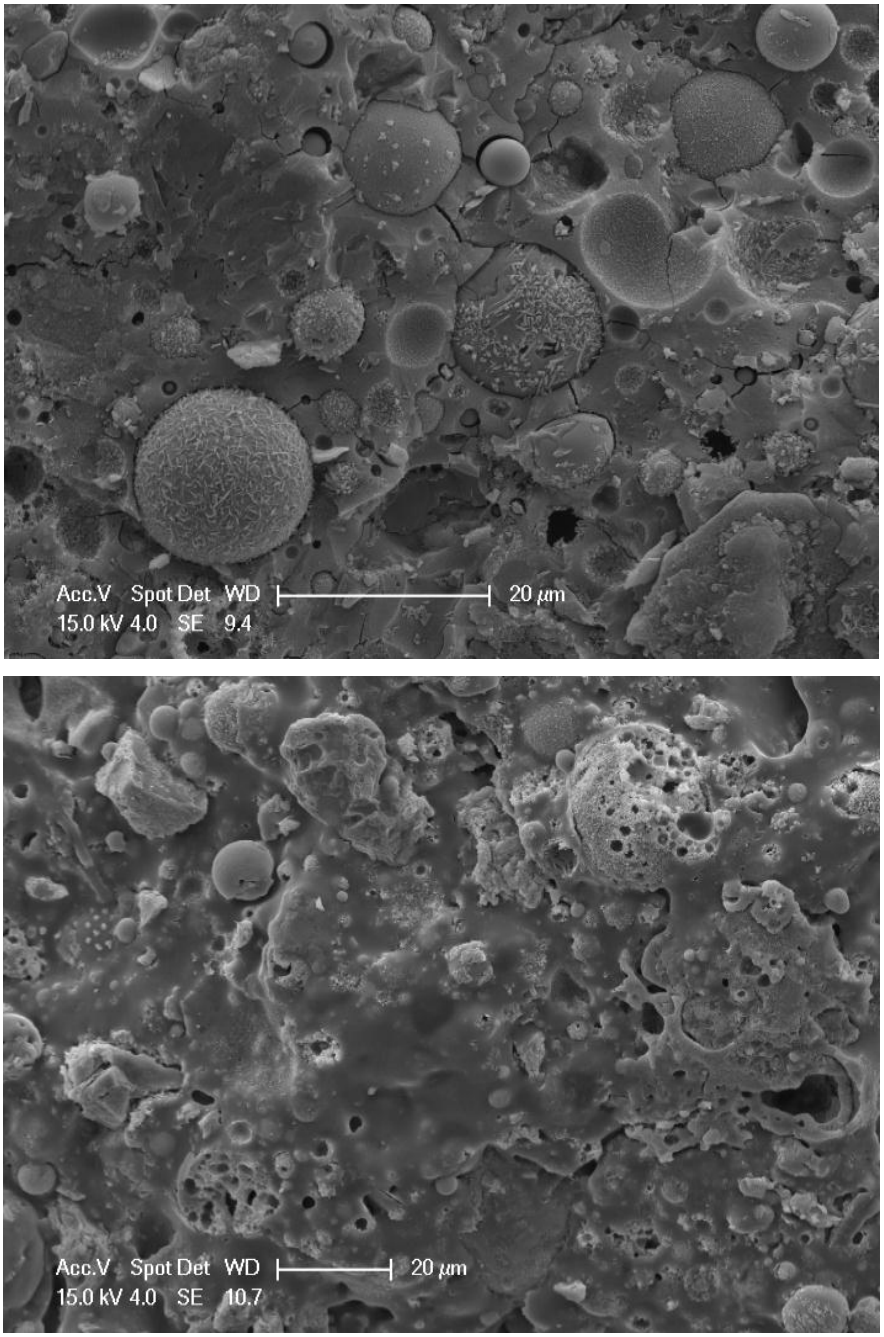

Figure 2-19 SEM micrographs of the fracture surface of a fly ash geopolymer before and after high temperature exposure. Top: Unexposed. Bottom: After exposure to 900 °C (van Riessen et al., 2009).

Geopolymers containing aggregates undergo additional microstructural changes during high temperature exposure. Differential thermal dilation of geopolymer and the aggregate (especially aggregates containing quartz) cause a separation at the

interface. After sintering, viscous flow of the geopolymer gel may re-establish contact with the aggregate (Zuda et al., 2006).

Pore structure evolution

At temperatures just above ambient, pores initially filled with water are emptied due to dehydration. At higher temperatures multiple factors influence the size and distribution of the pores. In fly ash based geopolymers, melting of the amorphous material from unreacted fly ash particles during heating exposes additional pores from within the particles (van Riessen et al., 2009, Kong et al., 2007). The additional porosity from the unreacted fly ash particles increases the porosity of the geopolymer gel.

Bakharev (2006) found that in fly ash geopolymers the cumulative pore volume, when compared to unheated samples, increased by 26 % and 29 % after exposure to 800 and 1000 °C, respectively (Figure 2-20). The same study also found that the average pore size increased significantly from 37.6 nm in the initial specimen to 121 and 1835 nm after exposure to 800 and 1000 °C, respectively (Bakharev, 2006). Duxson et al. (2007b) reported an opposing trend in metakaolin geopolymers, finding that the average pore volume reduced with high temperature exposure due to the densification of the gel after sintering (Figure 2-21).

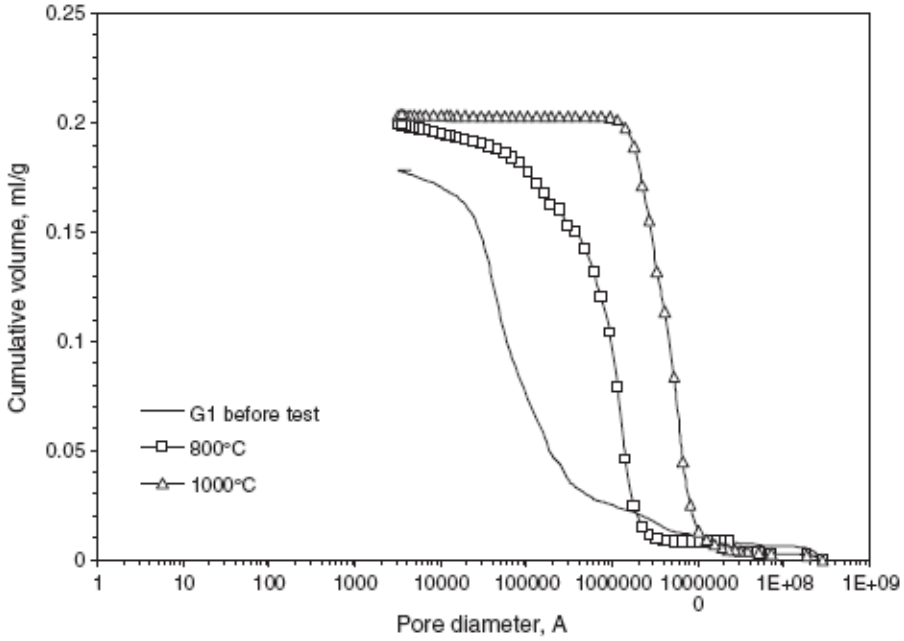

Figure 2-20 Cumulative pore volume versus pore diameter (Å) of geopolymer specimens prepared using Gladstone fly ash and sodium hydroxide at w/c = 0.09 (Bakharev, 2006).

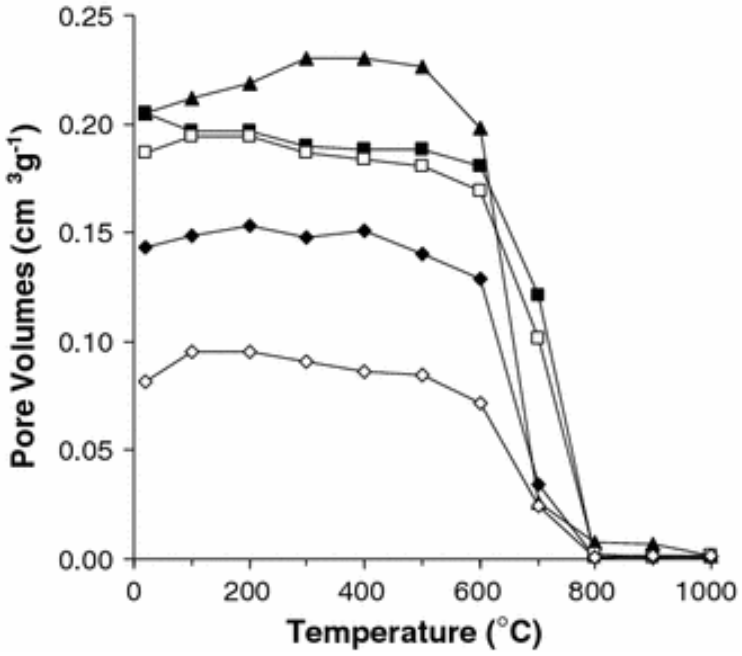

Figure 2-21 Pore volume of Na-geopolymer annealed for 2 h between ambient and 1000 °C with Si:Al of (▲) 1.15, (■) 1.40, (□) 1.65, (♦) 1.90, and (◊) 2.15 (Duxson et al., 2007b).

Degeneration and subsequent crystallisation in the geopolymer gel has also been attributed to an increase in porosity in geopolymers as the freed monomers pack more densely into an ordered structure (Bakharev, 2006). Thus, geopolymers that experience greater crystallisation, such as low Si:Al samples, exhibit a greater

increase in pore volume after high temperature exposure, all else being constant (Duxson et al., 2007b).

2.13 Fireproofing Materials – The Current State of the Art

The following section reviews the current state of the art of fire proofing materials and the relevant national and international standards. Fireproof materials are designed to insulate the heat transfer from a fire to the structure that's being protected in order to minimise the damage and the spread of the fire. There are many types of fireproof materials currently available. The nature of the predicted fire, the building (infrastructure) type and the government regulated design criteria determine what type of fireproofing is used. Economics can also influence material choice as fireproof materials can be very expensive. Most fireproofing materials fit into the following four categories; cementitious materials, intumescent paints, fibrous materials and composite materials.

2.13.1 Fire Protection Standards

Government regulations in most countries require civil structures to adhere to minimum standards of fire protection. This includes active systems (such as alarms and sprinklers) and passive systems (such as insulating panels and coatings). The standards vary from country to country and are also dependant on the predicted fire type (cellulose or hydrocarbon) and structure category.

Standard tests measure the fire performance of fireproofing materials by determining the following properties; insulating properties, flammability, combustibility, flame propagation, heat and smoke release. Failure to meet set criteria in any of these tests will prohibit a product's use in construction applications.

A fire rating is the time that a protected test surface can withstand fire exposure as determined by a standard fire test. The rating is usually specified in terms of time.

Table 2.8 lists selected standards from around the world and some of their comparable criteria.

Table 2.8 Fireproof material standards.

Standard	Country/Region	Description	Maximum temperature of the unexposed surface (°C)
AS1530.4	Australia	Methods for fire tests on building materials, components and structures	140 (average) / 180 (max) above initial temperature
ASTM E-119	U.S.A.	Standard test methods for fire tests of building construction and materials	139 (average) / 181 (max) above initial temperature
ISO 834	International	Fire-resistance tests - Elements of building construction	140 (average) / 180 (max) above initial temperature
BS 476	United Kingdom	Fire tests on building materials and structures	140 (average) / 180 (max) above initial temperature
EN 1991-1-2	Europe	Actions on structures. Actions on structures exposed to fire.	140 (average) / 180 (max) above initial temperature

2.13.2 Standard fire curves

There are many opinions as to what should constitute a standard fire. A typical sequence of a room fire can be expressed in terms of the average air temperature in the room. Figure 2-22 illustrates three stages of such fire (from van Riessen et al., 2009):

(1) the growth or pre-flashover stage, in which the average temperature is low and the fire is localised in the vicinity of its origin;
(2) the fully-developed or post-flashover fire, during which all combustible items in the room are involved and flames appear to fill the entire volume; and
(3) decay or cooling period.

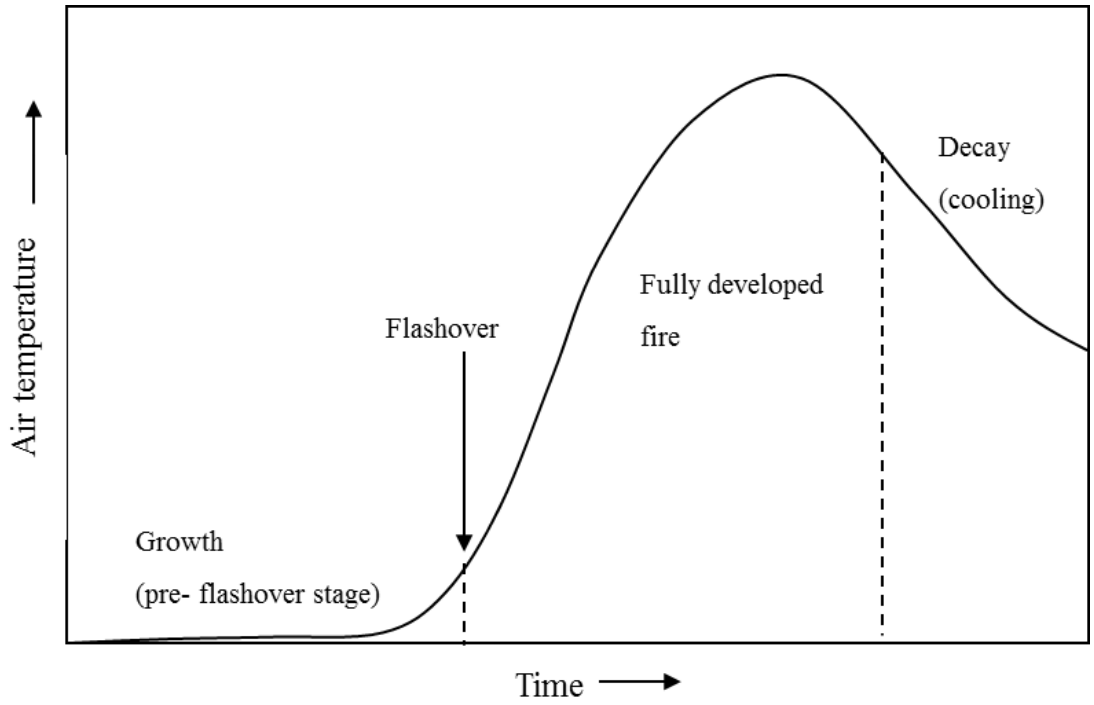

Figure 2-22 Time versus temperature curve of a typical room fire (this is based on the concepts from Fire Engineering for Building Structures) (Institution of Engineers, 1989). Adapted from van Riessen et al. (2009).

Building and structural components are generally required to withstand an accidental fire. For this purpose, it is necessary to adopt a standard fire curve so that there is a common benchmark test to compare different options for the building components. The most commonly adopted fire curve is the ISO 834 (1999), while the ASTM E119 (2011) fire curve is also commonly used which differs slightly from the ISO curve. The ISO 834 (1999) curve is based on a cellulose fire, and is also adopted by the Australian standard AS1530.4 (2005), Norwegian standard NT Fire 046 (1993) standards and Eurocode EN1991-1-2 (2008). The time versus temperature relationship of the standard (cellulose) fire is shown in Figure 2-23. The standard fire curves aim to simulate the temperature versus time curve of Figure 2-22, starting from the flash over stage. Pre-flashover stage of the fire is normally ignored, as it has insignificant impact on building components. For many materials, the performance of the material in a fire can be determined by knowing the maximum temperature exposure of the material. However, materials which are relatively brittle, such as geopolymers and Portland cement-based concretes, are also affected by the thermal gradient developed in the material or building component.

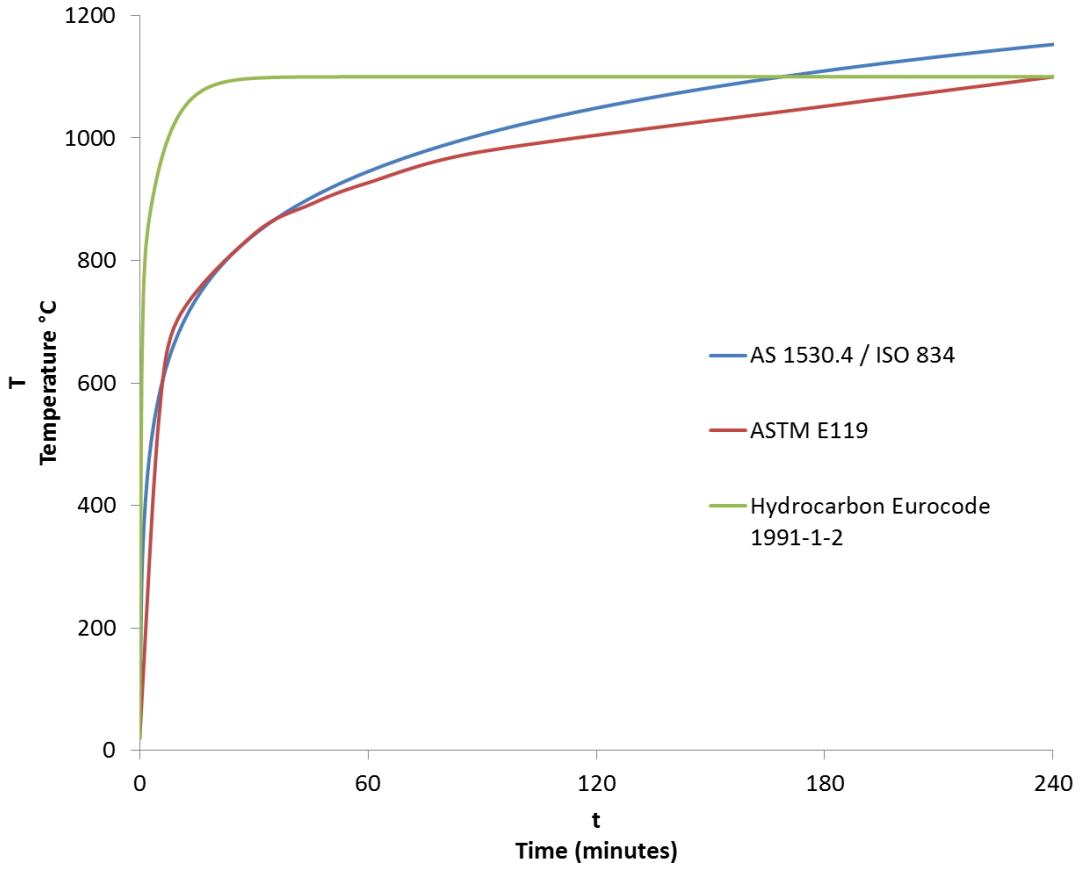

Figure 2-23 Temperature versus time relationship of various standard fire cures (AS 1530.4, ASTM E119, ISO 834, Eurocode EN1991-1-2).

In situations where the probability of occurrence of a hydrocarbon fire exposure is significant, such as road and railway tunnels, offshore and petrochemical industries, the response of the building component to such fire should be considered in the design. Eurocode (EN 1991-1-2, 2008) provides a curve for this purpose and is also shown in Figure 2-23. A hydrocarbon fire is particularly damaging for materials because the rapid temperature rise causes steep thermal gradients and steam pressure build up in the pores which can lead to spalling. Spalling of concrete is an explosive dislodgement of pieces from the surface, reducing mechanical strength and reducing the material thickness (Sanjayan and Stocks, 1993).

Full scale testing of structural components in the same configuration that they will be used in service conditions is required to definitively assess a material for fire resistance. There are few facilities that can conduct these tests and the size and sophistication means that these tests are very expensive. Scaled down tests, such as the apparatus used by Vilches et al. (2003), are available at a number of facilities and

can be used as a cheaper and more convenient alternative prior to more extensive testing.

Details of Australian Standard 1530.4

Figure 2-24 shows the Australian standard fire curve taken from AS 1530.4 (2005). Equation 2.4 details the time – temperature relationship from the standard.

$$T = 345\log_{10}(8t + 1) + 20 \qquad \textbf{2.4}$$

Where T is temperature (°C) and t is time (minutes).

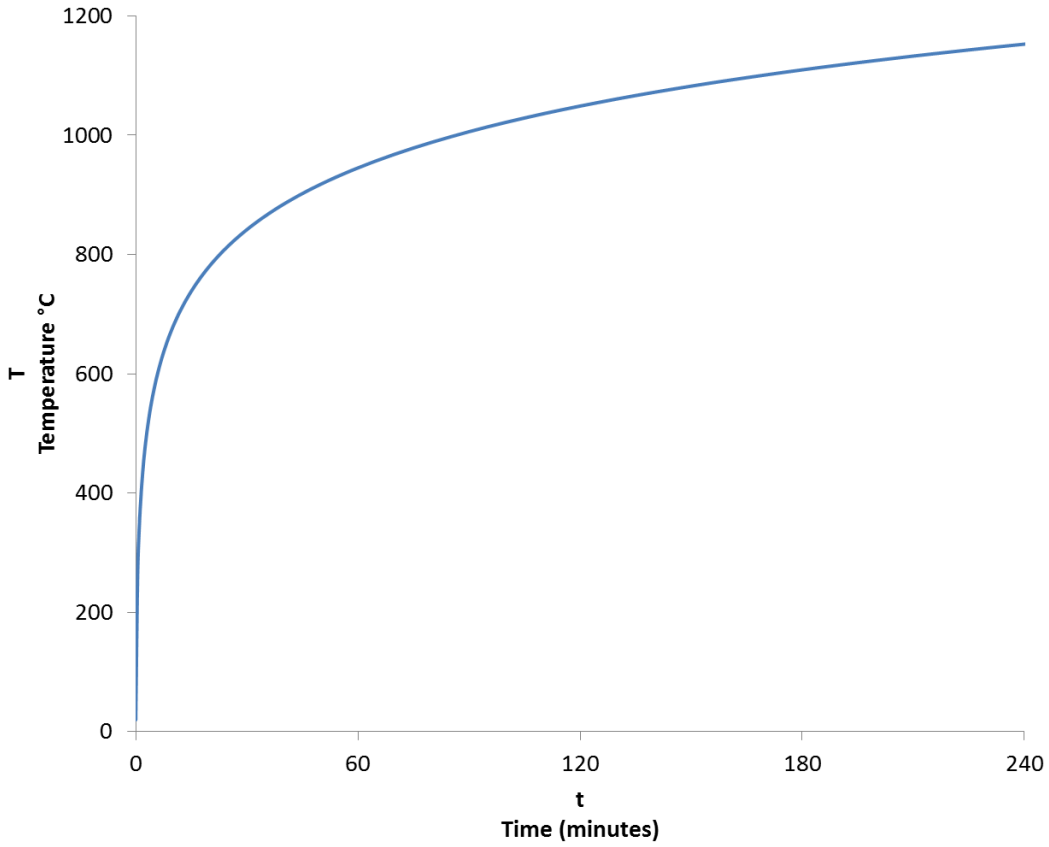

Figure 2-24 Australian Standard time versus temperature curve (AS 1530.4, 2005).

Clause 2.12 of AS1530.4 outlines the criteria of failure. The following excerpt explains the maximum temperature the cold surface (opposing side of heated surface) that an insulating fireproof material can exceed;

"The specimen is deemed to have failed when—

a) the average temperature of the unexposed face of the test specimen, as measured by the thermocouples specified in Clause 2.2.3.1, exceeds the initial temperature by more than 140 K; or

b) the temperature at any location on the unexposed face of the test specimen exceeds the initial temperature by more than 180 K."

Other failure conditions are combustion of the test specimen, loss of structural integrity or exceeding maximum deflection limits.

2.13.3 Cementitious Fire Proof Materials

Cementitious materials are in general inorganic, and as such do not combust during a fire. This makes them an excellent fireproofing material and the reason they have been used extensively for over half a century. Cementitious materials are also good thermal insulators and have the added ability to provide structural support to the building they are fire proofing.

Specialist cements such as vermiculite cements are commonly used as standard OPC cements lose strength and are adversely affected by spalling when exposed to fire. Furthermore, cements with steel reinforcement will fail if the steel is heated above its critical temperature (approximately 500 °C, depending on the type of steel).

Examples

Vermiculite cements, magnesium oxychloride cements, gypsum cements.

Typical applications (thickness, rating, technique)

A number of commercially available cementitious fireproofing materials have been synthesised to achieve a 4 hour fire resistance rating according to ASTM E-119 (2011). The thicker the coating, the better the fire resistance; as such the required fire rating will set the minimum thickness. Cementitious materials require less surface preparation prior to application than other materials, though they typically require a top coat to reduce moisture intrusion. A number of application techniques are used

for fireproofing cementitious materials: shotcrete and gunite spray techniques are commonly used as they are more cost effective than other methods, prefabricated application is also common.

Advantages

- Durable and wear resistant
- Generally low tech
- Can provide structural support
- Low cost source material

Disadvantages

- Requires additives
- Heavy (not always suitable for high rise buildings)
- May cause corrosion of steel substrates
- Thick coatings are generally required
- Cementitious materials are susceptible to spalling and may need to be replaced after a fire due to progressive post fire deterioration.

2.13.4 Intumescent Fire Proof Materials

Intumescent fireproofing materials protect the structure by expanding during a fire to form a porous insulating layer. This is achieved by a thermally activated chemical reaction which releases gas to foam the material, expanding it many times the initial thickness (Bourbigot and Duquesne, 2007).

Examples

Intumescent paints are either water based or solvent based. Water based intumescent paints are better for indoor applications as they do not emit harmful vapours during application.

Typical applications (thickness, rating, technique)

Intumescent paints are typically sprayed using airless spray guns. The surface must be clean, usually by blast cleaning, and commonly primed to ensure good adhesion. Paint on techniques are also widely used. Prefabrication, where the fire proofing layer is applied in a controlled environment, ensures optimum coating thickness and curing conditions. Coating thickness is dependent on the desired fire rating. Typically, a coating of 8 – 10 mm will provide a fire rating of between 1 and 3 hours (Jimenez et al., 2006).

Advantages

- Lightweight
- Thin coatings
- Aesthetic smooth and even coloured finishes achievable.

Disadvantages

- Requires extensive surface preparation and priming
- Often more expensive than other fireproofing materials
- Generally lower fire rating than cementitious fireproofing materials.

2.13.5 Other Fire Proof Materials

Fibrous boards or blankets made from mineral wool or ceramic fibre have been used as a fireproof material (Weil, 2011). Fibrous fireproofing materials are not as effective as other methods, however are adequate in thermally insulating low temperature applications. Fibrous materials can be mixed with an adhesive and sprayed onto the desired surface.

Composite fireproofing materials utilise the benefits of various types of fire resistant materials. For example, a composite panel may consist of two cementitious boards with ceramic fibres sandwiched in between. These materials are prefabricated and have been synthesised to achieve very high fire ratings.

2.14 Fire testing of Geopolymers

Geopolymers have been shown to perform well at high temperatures due to their low thermal expansion and compressive strength increases as described in sections 2.12.1 & 2.12.3, respectively. However, performance of a material after elevated temperature exposure does not necessarily translate into good performance in a fire. In a fire, the materials not only get exposed to elevated temperatures, but also a high rate of temperature increase that needs to be accommodated. There is very little available literature on geopolymers exposed to fire like conditions due to the proprietary nature of the results and the expense of the testing. The following paragraphs review the published literature on geopolymers exposed to fire like conditions with comparisons to OPC based materials.

A comparative test of geopolymer concrete and high strength OPC based concrete carried out at Monash University (Melbourne, Australia) reported that geopolymer concretes have significant advantages (van Riessen et al., 2009, Zhao and Sanjayan, 2011). Comparable geopolymer and OPC samples of strengths 40, 60, 80 and 100 MPa were exposed to fire like conditions. A rapid surface temperature rise test and a standard fire test were conducted on the samples. Observation of the specimens after the fire test revealed moderate to severe spalling of the OPC concretes whereas the geopolymer concretes did not exhibit any spalling (Figure 2-25). It was concluded in Zhao and Sanjayan's (2011) paper that the more porous nature of geopolymer concretes facilitated the release of steam pressure during heating which greatly reduced spalling when compared to OPC concretes of similar initial compressive strength.

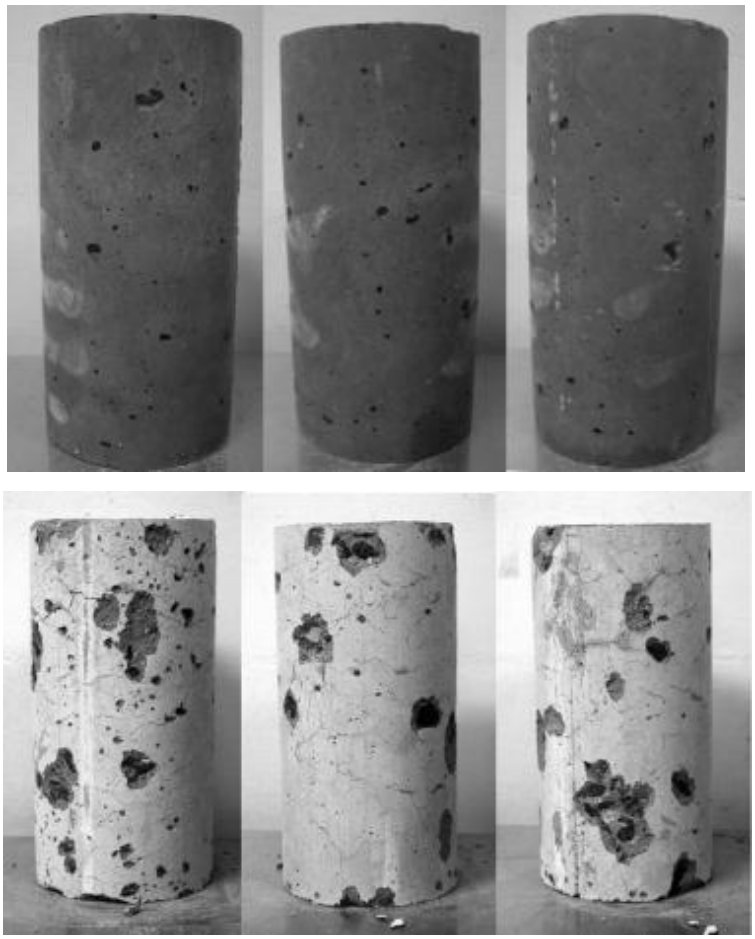

Figure 2-25 Specimens after Fire Test. Top image: 80 MPa geopolymer concrete samples. Bottom image: 80 MPa OPC concrete samples. Note the heavy spalling in the OPC samples (Zhao and Sanjayan, 2011).

Ordinary Portland cement concrete, in particular high strength variants, are highly susceptible to spalling in a fire (Mendes et al., 2008, Mendes et al., 2009, Hertz, 2005, Zhao and Sanjayan, 2011). The high risk of spalling in high strength concretes is reported to be due to the reduced permeability and increased brittleness, compared to normal strength concretes. The risk of spalling is further exacerbated when the concretes are exposed to hydrocarbon fires due to the extremely rapid temperature increases (van Riessen et al., 2009).

Vilches et al. (2003) conducted small scale fire tests on fly ash based geopolymers using a modified furnace. The furnace was simply a regular furnace with the door removed to allow a geopolymer panel of dimensions 28 x 18 cm to be mounted vertically. A temperature controller allowed a standard fire curve to be applied to the sample. The study reported a 33 mm thick sample to have a fire rating of over 60

minutes (Figure 2-26). The period of slow cold side temperature increase (the first 40 mins in the 33 mm sample) was reported to be the evaporation period. Once all the free water evaporated, the cold side temperature was observed to increase rapidly to the failure condition (Tc = 180 K above starting temperature).

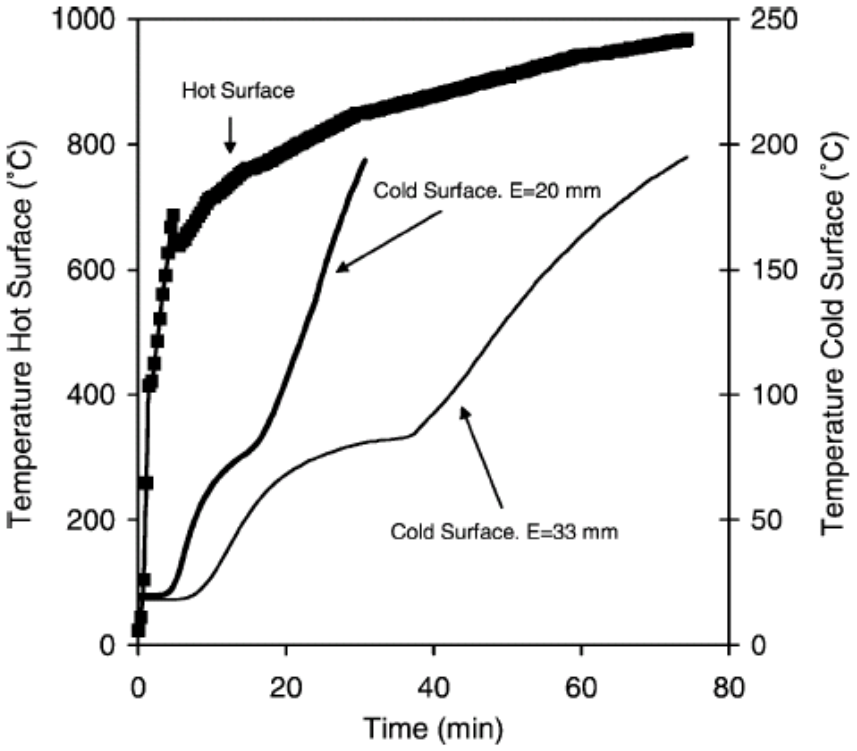

Figure 2-26 Fire test results for 20 mm and 33 mm thick fly ash geopolymer panels (Vilches et al., 2003).

Researchers have also conducted non-standard fire testing by simply applying a flame to their sample (Cheng and Chiu, 2003, Temuujin et al., 2010). This test method applies severe thermal shock to the sample and is useful as a simple test to gauge the fire resistance of a material. However, the results are not comparable between studies and can only be used as a guide due to large variances in flame temperature and incident heat flux. Temuujin et al. (2010) used a gas torch with an estimated flame temperature of 1100 °C and applied it to metakaolin geopolymer coatings on a steel substrate. Samples were observed to retain good structural integrity after the test and no delamination from the substrate was reported. It was noted that the flexibility (plasticity) of the geopolymer during heating was sufficient enough to cater for the thermal expansion mismatch with the steel substrate. Cheng and Chiu (2003) applied a 1100 °C flame to 10 mm thick slag based geopolymer

panels and measured the cold side temperature with time. They found that the temperature of the cold side increased to between 250 °C and 350 °C in the first 10 minutes. After the initial temperature rise a thermal equilibrium was reached and the cold side temperature remained constant until the end of the test (35 minutes). The study also noted that increasing the amount of metakaolin in the samples improved their fire resistance by reducing the cold side temperatures.

2.15 Application of Geopolymers

Geopolymers can be utilised in a wide variety of applications because of their unique properties. Some of these applications include using geopolymers as fire retardant insulation, insulated panels and walls, ceramic tiles, refractory items, concretes and cement, sewerage pipes, toxic waste encapsulation and even as decorative stones (Geopolymer Institute, 2011, Davidovits, 2002). The following paragraphs discuss examples of geopolymers applications.

Geopolymers are most commonly applied as cement or concrete, in the same way as OPC. Geopolymers are ideal for use as cements because of their good mechanical properties and potentially lower cost. As well as conventional concrete applications, geopolymer can be used where rapid strength gain is important such as expedient construction. Some commercial examples of geopolymer concretes are ‘Pyrament® blended cement’ (Geopolymer Institute), Earth Friendly Concrete (Wagners) and E-crete (Zeobond).

Geopolymer cements are ideal for use in sewerage pipes due to their remarkable acid resistance. The bacterium which grows inside sewerage pipes cause small amounts of sulphuric acid to build up on the surface of the pipes which over time can be extremely corrosive. Sewerage pipes made out of Portland cement have a lifetime of approximately 50 years before failing due to corrosion (Gourley, 2005). Geopolymers resist all organic solvents, and consequently sewerage pipes made out of geopolymer cements could last up to 3 times longer than equivalent OPC products (Gourley, 2005).

Geopolymers have been shown to be effective in the encapsulation of toxic waste (Aly et al., 2008, van Jaarsveld et al., 1997). Toxic waste can be added to the geopolymer slurry prior to curing. Once cured, the result is a very hard, impermeable solid containing the toxic waste in an immobilised form. The same method is currently used with Portland cement. The benefits of using a geopolymer cement over Portland cement is the higher immobilisation efficiency and superior physical properties of the concrete (van Jaarsveld et al., 1997). A commercially available geopolymer product used for the encapsulation of toxic waste is Geopolytech® (Geopolymer Institute, 2008).

Geopolymers have been applied to make artificial stone to be used for decorative purposes. Products such as Geopolystone® mimic natural stone or granite. Geopolymers appeal to artists and sculptors because they imitate aged products and can be used in restorative applications (Geopolymer Institute, 2008).

2.15.1 High Temperature Applications of Geopolymers

The following physical characteristics are critically important when considering a material for high temperature, insulating applications: low thermal expansion or compatible thermal dilation with the substrate (coatings only), low thermal conductivity, minimal spalling and a high melting point. In addition, thermally resistant materials must exhibit phase stability and low morphological change. Geopolymers with their intrinsic thermal resistance can be synthesised with these attributes and as such are highly suited to high temperature applications and in particular, fire proofing.

Geopolymers offer an advantage over OPC based materials of significantly reduced spalling and superior mechanical strength retention after exposure to fire (Zhao and Sanjayan, 2011, Kong et al., 2005). Applications for fire-resistant geopolymer products include tunnel linings, high rise buildings, lift doors and marine structures/coatings (Kovalchuk and Krivenko, 2009).

For fire resistant applications there are two clear product types; those that are to be used as structural components (tunnels, walls etc.) and those that will be used as coatings to insulate structural steel beams etc. The first type requires high compressive strength over a wide temperature range so the structure is not compromised while the second type needs high adhesion to a substrate and must be light weight. Wear resistance rather than mechanical strength is important in coating applications.

Geopolymer coatings have been previously shown to be robust on exposure to elevated temperatures. However, there is a tendency to delaminate due to incompatible thermal expansion with the substrate (which usually has a positive thermal expansion, for example steel). The challenge is to modify the geopolymer structure so that it has a thermal coefficient of expansion similar to that of steel leading to a composite that will respond more favourably when heated and thus not delaminate. Temuujin et al. (2009a) prepared metakaolin-based geopolymers with a range of Si:Al and w/c ratios and demonstrated that for Si:Al=2.5 and w/c=0.74 the thermal expansion was positive providing the capacity to adjust this property to match the expansion of steel. This composition consequently exhibited strong adhesion to steel substrates before and after exposure to elevated temperatures. It was reported that the overall performance of these coatings showed that they were well suited to application as fire resistant coatings.

Structures built entirely from geopolymer concrete provide the best fire protection by removing delamination effects caused by the differential thermal expansion of the coating and the structure. Tunnels built from geopolymer concrete will be significantly safer in the event of a fire than ones built just from OPC due to the superior fire resistance and strength retention.

Carbon fibre - geopolymer composites have been used to make fire retardant materials for transportation, military and infrastructure applications (Geopolymer Institute, 2008). At irradiance levels of 50 kWm^{-2} (typical of the heat flux in a well-developed fire), carbon-reinforced polyester, vinylester, epoxy, bismaleimide, cyanate ester, polyimide, phenolic, and engineering thermoplastic laminates all ignite readily and release appreciable amounts of heat and smoke, while carbon-fibre

reinforced geopolymer composites do not ignite, burn, or release any smoke even after extended exposure (Geopolymer Institute, 2008). Geopolymer composites have been reported to retain 67 % of their original flexural strength after a simulated fire exposure (Lyon et al., 1997). These properties make carbon fibre - geopolymer composites suitable for application as fire retardant materials.

Geopolymers composites have been trialled, for use in aircraft due to their fire resistance and comparatively low density (Giancaspro et al., 2006). This technology is still in its infancy; however it has shown great potential. Geopolymer composites have also been used as thermal insulation on the exhaust pipes of Formula 1 race cars (Geopolymer Institute, 2008).

Specialised geopolymer formulations are suitable for refractory applications. Low water content and highly pure geopolymers suit industrial refractory applications where the material may be subjected to temperatures in excess of 1200 ^{o}C. Kriven (2007) demonstrated that caesium and potassium activated geopolymers could be used as precursors to form the ceramic phases pollucite and leucite, respectively. These ceramic phases have high melting points and are suitable for use in high thermal shock applications.

High temperature geopolymer products are on the cusp of production and with further research and development will one day enhance the suite of materials available to industry. However, for these materials to be adopted and incorporated into buildings and engineering infrastructure a more extensive understanding of the effect of high temperature exposure is needed to ensure the materials meet regulatory requirements.

Chapter 3
Experimental Methods

"No amount of experimentation can ever prove me right; a single experiment can prove me wrong."

Albert Einstein

3.1 Introduction

This chapter covers details of the materials used in this study as well as the methods used for synthesising the geopolymers. The techniques used to characterise the geopolymers and source material are also listed. Brief details of the principles behind the techniques are additionally included where considered appropriate.

3.2 Starting Materials

Materials were selected based on their suitability and availability. It was considered important to work on materials that could be utilised in an industrial setting and as such had to be widely available and cost effective. The following information relates to the physical properties and specifications of the starting materials used to produce the geopolymers used in this study.

3.2.1 Fly ashes

This study focussed on the use of fly ash as an aluminosilicate precursor material for the synthesis of geopolymers. Metakaolin based systems are regarded as an 'ideal' system but most researchers would agree that the utilisation of waste precursor materials such as fly ash will enhance the environmental and economic credentials of the end product, improving its likelihood of adoption in an industrial setting. Significantly, this can be achieved without the loss of physical performance, and in many cases, improves the performance when compared to equivalent metakaolin systems (Kong et al., 2007).

Five Australian class F fly ashes were selected for use in this study. The fly ashes were sourced from Collie power station in Western Australia, Eraring and Bayswater power stations in New South Wales, Port Augusta power station in South Australia and Tarong power station in Queensland (Figure 3-1). The fly ash was provided by Fly Ash Australia (FAA) and the Ash Development Association of Australia (ADAA).

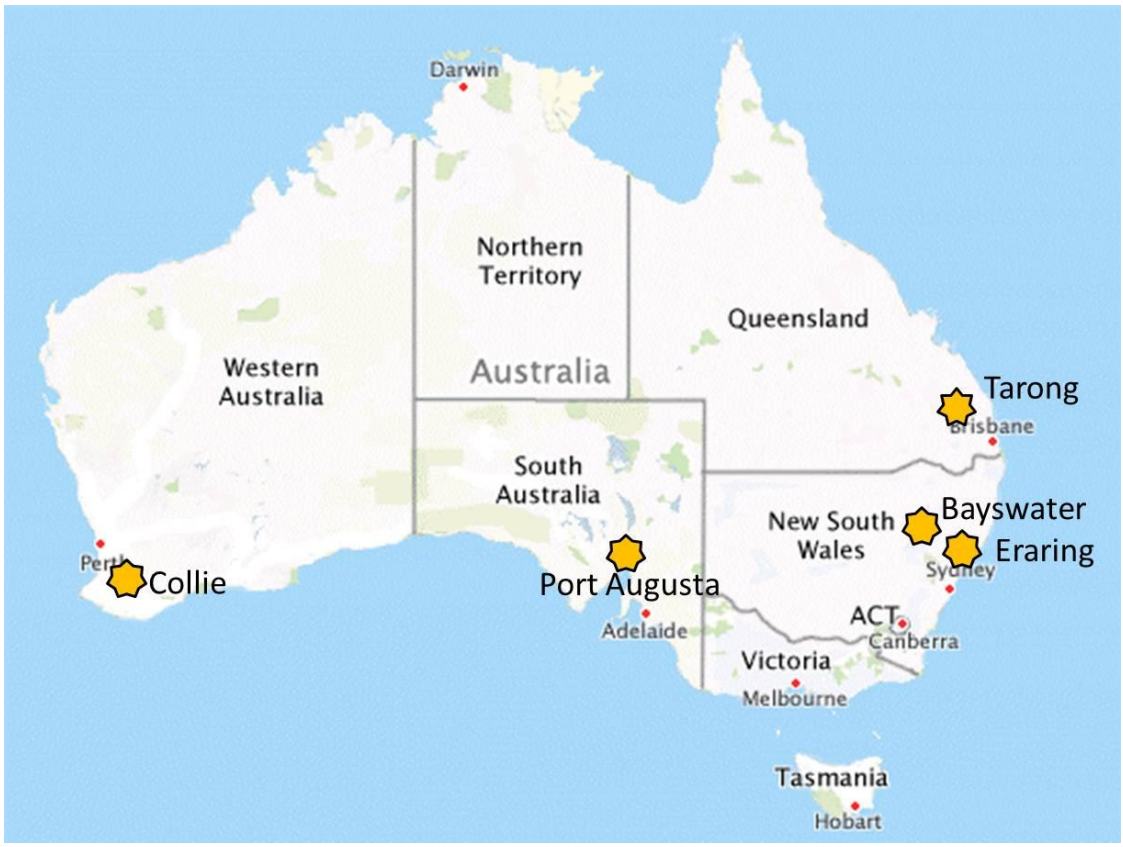

Figure 3-1 Map of Australia showing the locations of the five coal fired power stations that the fly ashes were sourced from. Map of Australia sourced from (Street-directory.com.au).

The fly ashes used for analysis were selected for their diversity in terms of iron content, Si:Al ratio and calcium content based on the composition published by Fly Ash Australia and other researchers. Details of the published composition of the fly ashes can be found in Table 2.3. The composition of the 20 kg batches used in this study was independently measured by XRF (see section 3.6) and is presented in Table 3.1. As expected there were some variances from the published compositions.

A thorough characterisation of the fly ashes was part of this investigation, the results of which are detailed in chapter 4.

Table 3.1 Chemical composition of the fly ashes used in this study as determined by x-ray fluorescence (wt.%). The values in parentheses are the estimated standard deviation of the least significant figure.

Oxide	Collie	Eraring	Tarong	Port Augusta	Bayswater
SiO_2	51.38 (8)	65.47 (8)	73.68 (8)	51.99 (8)	82.25 (8)
Al_2O_3	26.90 (10)	23.00 (10)	22.40 (10)	30.50 (10)	11.90 (10)
Fe_2O_3	13.20 (2)	4.03 (2)	0.64 (2)	2.75 (2)	2.41 (2)
CaO	1.74 (5)	1.59 (5)	0.08 (5)	4.60 (5)	1.37 (5)
K_2O	0.90 (4)	1.68 (4)	0.53 (4)	1.34 (4)	0.55 (4)
TiO_2	1.47 (1)	0.84 (1)	1.28 (1)	2.16 (1)	0.61 (1)
MgO	1.41 (3)	0.51 (3)	0.17 (3)	2.53 (3)	0.29 (3)
Na_2O	0.41 (5)	0.56 (5)	0.09 (5)	2.30 (5)	0.09 (5)
P_2O_5	1.09 (2)	0.27 (2)	0.08 (2)	0.82 (2)	0.15 (2)
SrO	0.23 (1)	0.05 (1)	0.01 (1)	0.06 (1)	0.02 (1)
BaO	0.38 (1)	0.06 (1)	0.03 (1)	0.07 (1)	0.05 (1)
Other	1.15 (6)	1.67 (6)	0.96 (6)	0.39 (6)	0.06 (6)
LOI (1000 °C)	0.44	1.37	0.79	0.49	0.25

3.2.2 Alkaline Solutions

Sodium hydroxide, sodium silicate and sodium aluminate solutions were used as the alkali activators. Some solutions were synthesised in the laboratory whereas others were purchased from commercial manufacturers.

Sodium hydroxide (NaOH) pellets were sourced from Univar Pty Ltd (USA), minimum assay 97.0 wt.%. Sodium hydroxide solutions were synthesised by dissolving the NaOH pellets into specific quantities of deionised water. Evaporation due to the exothermic reaction of the sodium hydroxide and the water was reduced by partially submerging the container in flowing water at ambient temperature. Prior to use, the solutions were stirred until clear to ensure all the pellets had dissolved.

Sodium silicate solutions were sourced from PQ Australia. Grade D (A53) solutions were used which were specified to contain 29.4 wt.% SiO_2, 14.7 wt.% NaOH and

55.9 wt.% H_2O. In order to achieve higher Si:Na ratios than those available in commercial sodium silicate solutions, some solutions were prepared by dissolving sodium hydroxide pellets from Univar Pty Ltd (USA) and fumed silica (Cabosil, Cabot corporation, USA) in deionised water. The solutions were allowed to dissolve for 24 hours at 70 °C prior to use.

Sodium aluminate solutions were supplied by Coogee Chemicals with the specifications of: 19 wt.% Al_2O_3, 25.5 wt.% NaOH and 55.5 wt.% H_2O. In mixes that required higher sodium content, sodium hydroxide pellets were dissolved into the sodium aluminate solution.

3.3 The Synthesis of Fly Ash Geopolymers

The geopolymers used in this study were prepared with a range of compositional ratios as shown in Table 3.2 Only the amorphous component (details in chapter 4) of the aluminosilicates from the fly ashes was used in the calculation as the crystalline material was considered inert in the geopolymerisation reaction. Three mixes were prepared for each fly ash with designed Si:Al ratios of 2.0, 2.5 and 3.0. This Si:Al ratio range was selected as it is known to produce high strength geopolymers (Rowles and O'Connor, 2003). The Na:Al and H:Si compositional ratios were kept reasonably constant and were only varied where workability or solution chemistry demanded it.

The following general procedure was used to prepare the samples;

- The desired quantity of activating solution was prepared as per section 3.2.2
- The fly ash was sieved using a coarse sieve to break up agglomerated particles and weighed into a plastic cup.
- The alkaline solution and then the fly ash were placed in a polypropylene container.

- The sealed container was then placed in a planetary centrifugal mixer (ARE 250, Thinky, Japan). The mixing sequence involved 5 minutes at 1300 rpm and 30 seconds of defoaming at 2100 rpm.
- After mixing the geopolymer slurry was poured into polypropylene moulds.
- The moulds were agitated by hand or on a vibration table to remove the air bubbles in the slurry.
- The moulds were sealed and placed in an oven to cure for 24 hours at 70 °C.
- Samples were kept sealed in their moulds for 7 days before demoulding and storing in zip lock bags prior to testing.

Note: The panels synthesised for fire testing were mixed using a Hobart mixer (Hobart Corp., U.S.A.) as it had a much larger capacity than the Thinky mixer. The mixing speed was set to 1 (low) for 1 minute, then 3 (maximum) for a further 4 minutes for these samples.

Table 3.2 Elemental ratios of the geopolymers prepared in this study.

Fly ash	Si:Al	Na:Al	H:Si	Sample code
Collie	2.0	1.25	5.0	C2B
	2.5	1.25	4.5	C2.5B
	3.0	1.25	6.0	C3B
Eraring	2.0	1.25	5.0	E2B
	2.5	1.25	4.0	E2.5B
	3.0	1.25	4.5	E3B
Tarong	2.0	1.32	6.4	T2B
	2.5	1.25	5.5	T2.5B
	3.0	1.25	5.4	T3B
Port Augusta	2.0	1.25	7.9	P2D
	2.5	1.25	5.5	P2.5D
	3.0	1.25	5.5	P3D
Bayswater	2.0	1.6	6.0	B2C
	2.5	1.47	5.5	B2.5C
	3.0	1.33	5.5	B3C

3.3.1 The Synthesis of Low Density Geopolymers

Low density, fibre reinforced samples were also synthesised in this study. A cellular structure was produced by foaming the geopolymer slurry using a metallic aluminium powder. Aluminium powder was used in this study because it produced a more homogenously foamed material than other foaming agents such as surfactants and hydrogen peroxide, as determined in preliminary experiments. Aluminium powder is highly reactive in an alkaline environment and foams sodium activated geopolymer samples by liberating hydrogen gas according to the following reaction (Aleksandrov et al., 2003);

$$2Al + 2NaOH + 6H_2O \rightarrow 2Na[Al(OH)_4] + 3H_2 \quad \textbf{3.1}$$

The hydrogen gas quickly evolves out of the geopolymer after curing and is replaced by air to form a low density cellular structure. Aluminium powder with a particle size of 50 µm and a purity of 99.5 % (product code AL006020, Goodfellow, U.K.) was used for foaming in this study. Fibre reinforcement was used to stabilise the foamed samples by reducing pore collapse prior to the gel hardening. The addition of fibres is also reported to improve the resistance of binding materials to dehydration damage during high temperature exposure by increasing their permeability (Zeiml et al., 2006). 100 % virgin monofilament polypropylene fibres (Sika Australia Pty Ltd) with specified dimensions of 18 mm (length) and 22 µm (diameter) were used. Polypropylene fibres were selected as they have a low melting temperature (and hence ability to produce evaporation pathways prior to dehydration damage) and good resistance to alkaline environments.

The following general procedure was used to prepare the low density samples;

- The geopolymer slurry was prepared as per section 3.3 with the exception of the use of a Hobart mixer to enable the synthesis of larger mixes. The mixing speed was set to 1 (low) for 1 minute, then 3 (maximum) for a further 4 minutes.
- Polypropylene fibres, with a concentration of 0.25 wt.%, were then gradually added to the slurry with the mixer on a low speed to achieve a uniform dispersion.

- The aluminium powder was then added with a concentration of 0.05 wt.% and the slurry was mixed for a further 30 seconds.
- Immediately after mixing samples were poured into appropriate moulds, sealed and left to cure at 70 ˚C for 24 hours. Moulds were only half filled to allow the slurry to expand unrestricted as the aluminium powder reacted.

3.4 Characterisation Techniques

The samples in this study were characterised with a wide range of testing techniques. Geopolymers are relatively novel and as such there are no standard testing techniques specific to this material. However, due to their similarity to other materials, such as OPC cements, standard test methods from these materials can be adapted and applied to geopolymers. In some cases modified tests were conducted due to sample constraints or equipment availability. Sections 3.6 to 3.16 contain details of the characterisation techniques used in this study.

3.5 Sample Selection

Samples used for analysis were selected to ensure they were representative of the sample suite. Where possible, repeat testing was conducted to determine a mean and identify outliers.

Powders used for XRF, XRD and SEM analysis were sampled from the bulk using a riffle splitter made by Metal Craft. The riffle splitter was utilised to ensure uniform and consistent sampling.

Solid geopolymers intended for mechanical and thermal testing were first visually inspected for large defects such as cracks. Compressive strength samples were additionally checked for bulk density to identify internal voids that can adversely affect the mechanical performance. Samples that failed a visual inspection or had an unexpectedly low density (indicating the presence of internal voids) were not tested.

Geopolymer fracture pieces used for microscopy were selected based on a visual inspection to find a portion that was representative of the rest of the sample.

3.6 X-ray Fluorescence Spectroscopy

X-ray fluorescence spectroscopy (XRF) is a widely utilised analytical technique for the determination of bulk elemental composition. X-ray fluorescence is a phenomenon where an incident photon ionises an inner shell electron of an atom causing an outer shell electron to drop down and simultaneously radiate an x-ray of energy characteristic to that element. Elements are identified by comparing the fluorescence spectra from the sample with known values. Quantitative results are determined by modelling and comparisons to standards with known elemental concentrations.

XRF spectroscopy of the powders in this study was conducted by a commercial laboratory (Ultra Trace Geoanalytical Laboratories). The samples were fused in a silicate glass disc (method code XRF 202) and analysed on a Philips PW 2404 x-ray spectrometer with a 4 kW rhodium tube. Loss on ignition (LOI) was conducted by drying the samples at 105 °C then measuring the mass loss after heating to 1000 °C.

Results were reported as oxides. The report also included details of a number of standards measured during the analysis. Uncertainties were determined by calculating the mean percentage variation from the standards for each oxide.

3.7 X-ray Diffraction

X-ray diffraction (XRD) is a technique used to analyse the crystal structure of a material. XRD occurs when incident x-rays scatter from the electrons bound to atoms of a solid material (Dinnebier and Billinge, 2008). Constructive interference occurs when the difference in path length of two or more scattered rays is equal to a whole number of wavelengths as expressed by Bragg's Law (equation 3.2).

$$n\lambda = 2d \sin \theta \quad \textbf{3.2}$$

where n = is an integer

λ = x-ray wavelength

d = inter-planar distance

θ = scattering angle.

An XRD pattern is formed when the diffracted intensity with respect to diffraction angle in the range of interest is plotted. Crystallographic information can be derived from the pattern through modelling and comparisons to known physical values. XRD can be performed in a laboratory using an x-ray diffractometer or at a synchrotron using a brilliant, highly coherent x-ray source.

XRD measurements were performed for phase analysis of the starting materials and of the resulting geopolymers. Solid geopolymer were crushed to a powder using a ring mill and then prepared as powder samples. Powders were prepared by reducing the particle size in a McCrone micronizer. Three grams of powder and 7 mL of ethanol were placed into a milling vessel with corundum milling media. The powders were milled for 5 minutes to achieve an average particle size of 5 μm.

A fluorite (CaF_2) (Mesh -325, 99.5 % purity, Sigma Aldrich) internal standard (10 wt.%) was used to facilitate quantitative analysis of the fly ash powders. The fluorite was added to the powders prior to micronising to achieve a homogenous distribution and particle size.

3.7.1 Laboratory X-ray Diffraction

XRD patterns were collected on a D8 Advance diffractometer (Bruker AXS, Germany). Approximately 1 g of dried micronised powder was pressed into a plastic sample holder using the pack and tap method. This method was used in order to minimise preferred orientation effects. The data was collected using a nominal 2θ step size of 0.01°, a count time of 0.5 s per step and a 2θ range of 10° – 120°. The operating conditions are listed in Table 3.3.

Table 3.3 Bruker D8 XRD instrumental parameters.

Parameter	Value
Radiation (wavelength-weighted average of Kα1 and Kα2)	Cu (1.5418 Å)
Operating voltage	40 kV
Operating current	40 mA
Detector	LynxEye PSD (3º 2θ)
Filter	Ni filter to eliminate Cu kβ
Goniometer radii	250 mm
Source size	12 mm
Sample length	25 mm
Fixed divergence slit angle	0.3º
Primary Soller slit angle	2.5º
Secondary Soller slit angle	2.5º

3.7.2 Synchrotron X-ray Diffraction

An *in situ* high temperature XRD (HT-XRD) experiment was conducted on the powder diffraction beamline at the Australian synchrotron in Melbourne, Australia. Details of the beamline can be found at Wallwork et al. (2007), though a summary of the instrumental parameters are listed in Table 3.4.

Table 3.4 Operating parameters for the powder diffraction beamline at the Australian synchrotron.

Parameter	Value
Radiation wavelength	0.61992 Å (20.00002 keV)
Source	Bending magnet on a 3 GeV synchrotron
Detector	MYTHEN II microstrip detector
Monochromator	Si (111) flat crystal pair
Goniometer radii	761.2 mm
Source size	5 mm wide, 0.2 mm high
Sample length	Approximately 30 mm
Take off angle	3.0 º

The Mythen II detector used on the powder diffraction beamline is a silicon microstrip detector consisting of 16 modules each having 1280 channels, totalling 20480 channels. The intrinsic angular resolution of the detector is 0.004° covering a solid angle of 80° in 2θ. As the detector is modular, there is a small gap between adjacent modules of 0.2° 2θ (Haverkamp and Wallwork, 2009). To overcome this gap two data sets were collected with a small 2θ offset and subsequently merged using software provided by the beamline, namely Datapro version 2.6. Further details on Mythen detector systems can be found at Schmitt et al. (2003).

The *in situ* HT-XRD experiment was conducted as follows: Micronised powders were suspended in ethanol and deposited onto a platinum strip using a pipette. Repeated applications resulted in a homogenous layer of powder approximately 0.2 mm thick (Figure 3-2). The platinum strip was then placed inside an Anton Paar HTK 16 furnace. The experimental heating profile was set using a 16 stage controller and was configured to closely follow the Australian standard 1530.4 fire curve (Figure 3-3).

Twenty six XRD patterns were collected as the sample were heated to 1050 °C. At each collection period the temperature was held constant and two 60 seconds data sets with a 0.5° 2θ offset were collected to cover the angular gap in the Mythen detector. The collection angle was 5 - 85° 2θ.

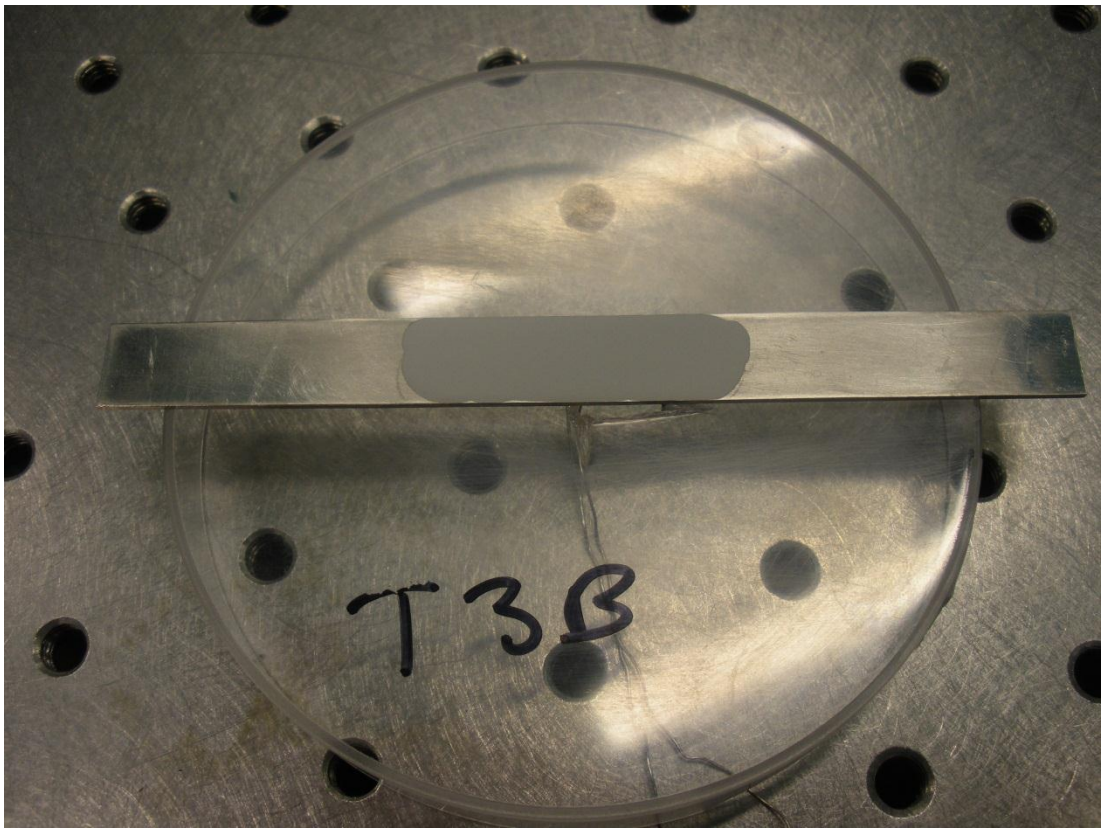

Figure 3-2 Powder layer deposited on a platinum strip as used for the HT-XRD experiment at the Australian synchrotron.

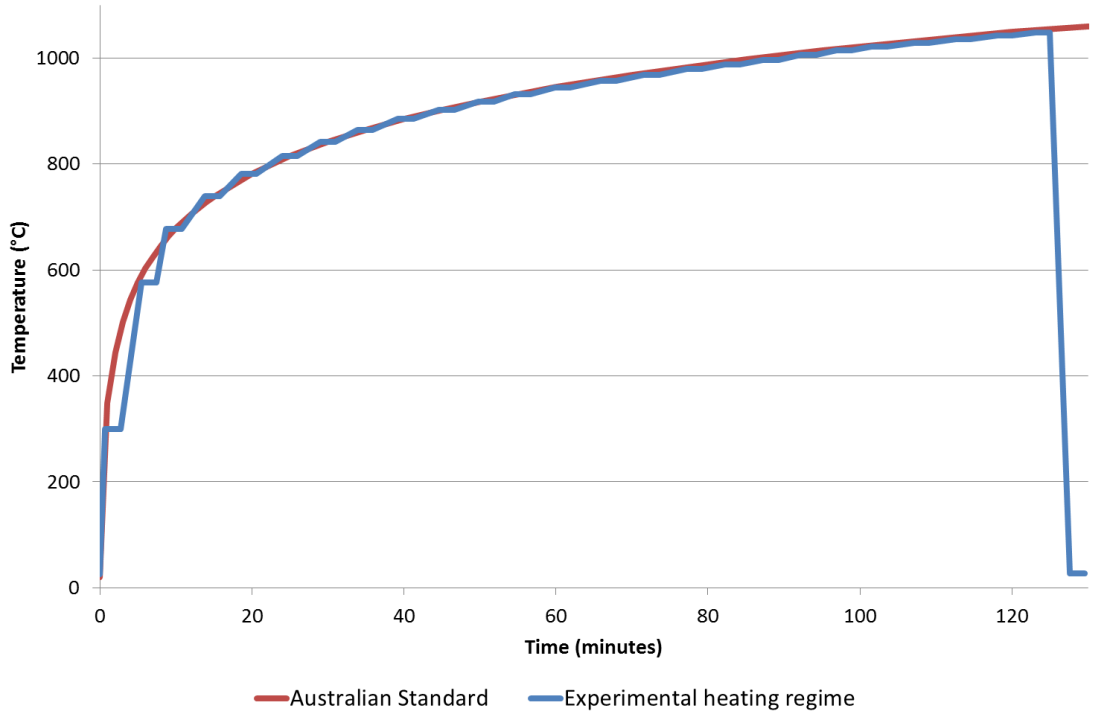

Figure 3-3 Experimental heating profile for HT-XRD experiment. Two minute periods where the temperature is constant represent data collection periods.

3.7.3 Data Analysis

Crystalline phases were identified using Diffrac^{plus} EVA version 16 (Bruker, Germany) to search the Powder Diffraction File (PDF4+ 2009 edition). Peak position and relative peak intensities were used to confirm search/match results. Pattern quality and phase chemistry was also checked to ensure the selection of sensible phases. Crystal structures were then extracted from the Inorganic Crystal Structure Database (ICSD 2009/2) in the form of crystallographic information files (CIF).

The Rietveld method (Rietveld, 1969) was used to model the XRD data and calculate phase concentrations quantitatively. The Rietveld method is a whole pattern method where diffraction patterns can be simulated based on fundamental instrument parameters and crystallographic models for each phase present in the sample. An iterative least squares process allows the input parameters to refine until the simulated pattern closely matches the measured pattern. Rietveld modelling was performed using Topas version 4.2 (Bruker, Germany).

Details of the Cu Kα emission profile that was used are listed in Table 3.5. Instrument settings were as per the values listed Table 3.3. A 5th order Chebychev background function was used to model the background of the patterns. Table 3.6 lists the global and phase parameters that were refined.

Table 3.5 Cu Kα emission profile

Area (%)	Wavelength (Å)	Lorentzian half width (mÅ)
1.59	1.534753	3.6854
57.91	1.540596	0.4370
7.62	1.541058	0.6000
24.17	1.544410	0.5200
8.71	1.544721	0.6200

Table 3.6 Parameters refined in Topas.

Parameter	Global	Standard (fluorite)	Sample phases
Background	Y		
1/X background	Y		
Sample displacement	Y		
Scale		Y	Y
Lattice parameters		N	Y
Crystallite size (Lorentzian)		Y	Y
Site thermals		N	N

Final refinements were checked in terms of the Rietveld weighted profile (Rwp), goodness of fit (GOF), density of calculated phases and R-Bragg values for each phase. The accuracy of the modelled pattern was checked by inspecting the difference curve (Figure 3-4). Uncertainties are reported to 2 estimated standard deviations as generated by Topas (95 % confidence interval).

Additional details of the refinement strategy are listed in appendix A.

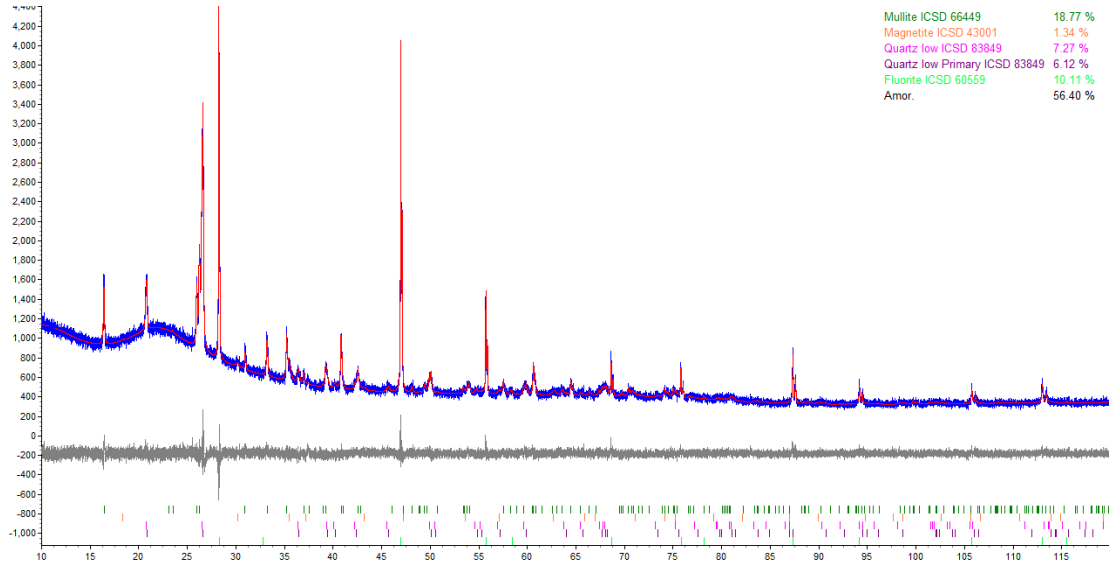

Figure 3-4 Topas screen shot of an Eraring fly ash Rietveld refinement. The quality of the refinement was checked by comparing the measured pattern (blue) to the modelled pattern (red). The difference curve (grey) was used to gauge the magnitude of the variation. The coloured markers below the difference plot represent peak locations for each phase.

3.8 Scanning Electron Microscopy

Scanning electron microscopy (SEM) is a powerful technique used to investigate the microstructure of solid materials. The SEM uses electromagnetic lenses to finely focus an electron beam onto the sample. A range of detectors collect the different signals that originate from the various electron–sample interactions. High resolution grey scaled images are formed by displaying the variations in signal intensity as the beam is rastered over a given area.

Secondary electrons (SE) are produced by inelastic interactions of beam electrons with valence electrons of atoms in the specimen which cause the ejection of the electrons from the atoms (Reimer, 1998). Secondary electrons can be used to create high resolution images of surfaces because they are generated in the first few nanometres of the sample. SE detectors are typically positioned off-axis which gives SE images surface topography contrast due to variances in detected intensity with orientation to the detector. Some modern SEM's have 'inlens' SE detectors which produce high signal, high resolution images though surface topography is less evident due to their on-axis orientation.

Backscattered electrons (BSE) are emitted when beam electrons undergo one or more elastic interactions with sample nuclei and rebound with very little energy loss (Reimer, 1998). BSE intensity is strongly dependant on the atomic number of the scattering atoms. This means that the contrast mechanism in BSE images is elemental contrast, though there will still be some morphology contrast due to surface topography affecting signal intensity.

The high resolution images produced in a SEM enable detailed information of sample microstructure at very high magnifications. Information such as surface morphology, pore size and distribution, crack propagation and phase distribution can be determined from SEM analysis.

Sample surfaces must be conductive for SEM analysis. Thin coatings (2-5 nm) of high atomic number elements such as platinum or gold are used as a conductive layer

on samples. Carbon coatings are used when elemental analysis (section 3.8.2) is required.

SEM's require a moderate to high vacuum to operate in order to reduce air scatter and produce high quality images. The vacuum in the chamber of a SEM causes hydrated samples to outgas which can detrimentally affect their microstructure. This damage can be limited by slow outgassing under a gentle vacuum prior to SEM imaging.

SEM was used to investigate the microstructures of the geopolymers and their precursor material in this study. The analysis was conducted on an Evo 40XVP (Zeiss, Germany) and a Neon 40EsB (Zeiss, Germany) using secondary electrons (SE) as well as backscattered electrons (BSE). The accelerating voltage that was used varied depending on desired information but was predominantly between 5 and 20 kV. Working distances between 2 mm and 10 mm proved sufficient to maintain the balance between resolution and depth of field.

3.8.1 SEM Sample Preparation

Microstructural analysis was performed on polished and fractured geopolymers as well as dispersed fly ash powders. Sample preparation for SEM investigation of polished samples was as follows: The samples were moulded in low viscosity epoxy resin and placed in a desiccator to remove entrained air and facilitate permeation of the resin into the sample. Polishing was conducting using a Struers polishing machine with a magnetic disk system. Coarse polishing (down to 15 µm) was conducted using silicon carbide polishing disks. Fine polishing was conducted using progressively finer diamond suspensions until a 1 µm finish was achieved. The samples were cleaned between each polishing step to remove any residue using deionized water and an ultrasonic bath.

Sample preparation for fractured samples was as follows: Fragments of the order of 2 to 10 mm in width were broken off the bulk sample from various areas using a clean

scalpel. Samples were mounted on aluminium stubs with conductive, double-sided carbon tape.

Fly ash powders were sprinkled onto double-sided carbon tape that was attached to an aluminium sample stub. An even dispersion was achieved by tapping the side of the stub to spread the powder.

Hydrated geopolymer samples were slowly outgassed in a desiccator over a 48 hour period. The desiccator was placed under a mild vacuum and silica gel desiccant was used to remove the moisture from the atmosphere inside the chamber. Once dry, the samples were then coated with 2 nm of platinum (for high magnification analysis) or ~ 10 nm of carbon for elemental analysis.

3.8.2 Energy Dispersive Spectroscopy

Interaction of the primary electron beam in a SEM with atoms in the sample causes atomic shell transitions which result in the emission of fluorescent x-rays, characteristic of that particular element (Reimer, 1998). An x-ray detector placed inside the chamber of an SEM allows for x-ray analysis while simultaneously collecting electron images. If the detector is an energy dispersive type, then the technique is referred to as energy dispersive spectroscopy (EDS)

Elemental analysis in this study was performed using an Oxford Instruments energy dispersive x-ray spectrometer (EDS) connected to a Neon 40EsB (Zeiss, Germany) FE-SEM. Analysis of x-ray spectra was performed using Inca-Analyser software (Oxford Instruments, England). EDS data that was to be analysed for quantitative elemental abundance was collected using spot mode with 10 kV accelerating voltage, a working distance of 7.7 mm (the coincidence point of the e-beam and the EDS detector), a 60 µm aperture and high current on (for maximum signal). The count time was set to 100s (live). Quantitative results are presented as the average of 5 separate measurements at different locations identified as geopolymer gel. The Inca-Analyser software was calibrated with an albite ($Na\ Al\ Si_3\ O_8$) standard.

EDS x-ray mapping was conducted on polished geopolymer samples. The SEM operating conditions were the same as that for the collection of quantitative EDS data with the exception of using spot mode. The magnification was set to 1000x and the x-ray maps for each element were collected simultaneously at a resolution of 512 x 384 pixels. Maps were collected for 500 seconds to achieve an acceptable signal to noise ratio.

3.9 Optical Microscopy

Optical microscopy was performed to analyse the microstructure of samples when a large field of view was required. Optical images offer the benefit of additional contrast from colour differences in the sample.

Optical imaging was performed on the samples using a Nikon SMZ 800 stereo microscope. Sample preparation for optical microscopy was the same as for SEM (section 3.8) except that no conductive coating was required. Images were captured using Image Pro Plus version 4.1.0.

3.10 Thermal Conductivity

Thermal conductivity is a measure of the rate at which heat is transferred through a material (Askeland et al., 2010, page 839). A generic formula for calculating the thermal conductivity of a solid material is shown in equation 3.3 (Askeland et al., 2010);

$$k = Q \times \frac{\Delta x}{A \times \Delta T} \qquad \textbf{3.3}$$

where k = thermal conductivity ($Wm^{-1}K^{-1}$)

Q = heat flow rate (Js^{-1})

Δx = thickness of sample (m)

A = Exposed surface area (m^2)

ΔT = Temperature difference (K)

The measurement of thermal conductivity involves the measurement of the heat flux and temperature difference. Hot wire methods are commonly used to measure the thermal conductivity of refractory's such as insulating bricks and fibrous materials.

The mathematical principle for the hot wire method is based on an infinite line heat source imbedded in an infinite medium. A paper by Glatzmaier and Ramirez (1988) fully derives the mathematical principle of the hot wire method. The following is a summary of their derivation. The time dependent conduction equation in cylindrical coordinates with temperature varying only in the radial direction is given by;

$$\frac{\partial T}{\partial t} = \alpha \frac{1}{r} \frac{\partial}{\partial r}\left(r \frac{\partial T}{\partial r} \right) \qquad \textbf{3.4}$$

Where α is the thermal diffusivity of the sample and r is radial distance from the line source where the temperature is measured. The solution of equation 3.4 for a medium with a constant initial temperature, T_0, and a heat input q per unit length of line source is;

$$T - T_0 = -\frac{q}{4\pi k} E_i\left(\frac{-r^2}{4\alpha t} \right) \qquad \textbf{3.5}$$

Where t is the time elapsed after the heating stared. For $r^2/4\alpha t \ll 1$, equation 3.5 can be expressed as;

$$\Delta T = T - T_0 = \frac{q}{4\pi k} \ln\left(\frac{4\alpha t}{r_w^2 C} \right) \qquad \textbf{3.6}$$

where: r_w = radius of wire

$C = e^y$ where $y = 0.5772$ (Euler's constant)

k = thermal conductivity

Differentiating equation 3.6 with respect to *ln t* and solving for *k* yields;

$$k = \frac{q/4\pi}{d\Delta T / d \ln t} \qquad \textbf{3.7}$$

In order to obtain the values of thermal conductivity (k) from experimental data, the temperature rise is recorded as a function of $ln\ t$ and is fitted using a linear least squares regression. If a is the slope of the fit, then the equation for thermal conductivity (k) is given by;

$$k = \frac{q}{4\pi a} \tag{3.8}$$

As $q = VI / L$ (where L is the length of the wire, V is the applied voltage and I is the applied current), equation 3.8 becomes;

$$k = \frac{VI}{4\pi La} \tag{3.9}$$

3.10.1 Thermal Conductivity Measurements using the KD2 Probe

The thermal conductivity of the geopolymers in this study was measured using a KD2-pro thermal properties analyser (Decagon, USA). The testing technique used by the KD2-pro is analogous to the transient hot wire method though the thermistor is embedded in the heat source rather than separated by a short distance. The KD2-pro complies fully with ASTM D5334-08: Determination of thermal conductivity of soils and rock by thermal needle probe procedure (2008).

Samples prepared for thermal conductivity testing were cylindrical with a length of 90 mm and a diameter of 40 mm. Before curing, a hole 1.3 mm in diameter and 60 mm deep, was moulded into the top of the cylinder using wire. After curing, all samples were left for 28 days at room temperature and 45 % relative humidity to equilibrate. During testing, the probe from the KD2-pro was inserted into the hole and the measurement was taken. UNICK heat transfer compound was used to improve the conduction of heat between the probe and the sample to reduce boundary effects. Samples were left for 1 hour between tests to allow the sample temperature to re-equilibrate. All stated results are the average of 5 repeat measurements.

3.10.2 Thermal Conductivity Measurements using the Embedded Hot Wire Method

Thermal conductivity was also measured using a custom method where the heat source was embedded in the sample during casting. This technique is not limited by boundary effects as there is an intimate contact between the heat source and the sample. A 0.32 mm diameter nickel-chromium heating wire was embedded in a cylindrical sample of dimensions 100 mm (diameter) x 160 mm (height) (Figure 3-5). Temperature changes were measured using an embedded k-type thermocouple. The thermocouple was electrically isolated from the nickel-chromium wire by a thin layer of Teflon tape.

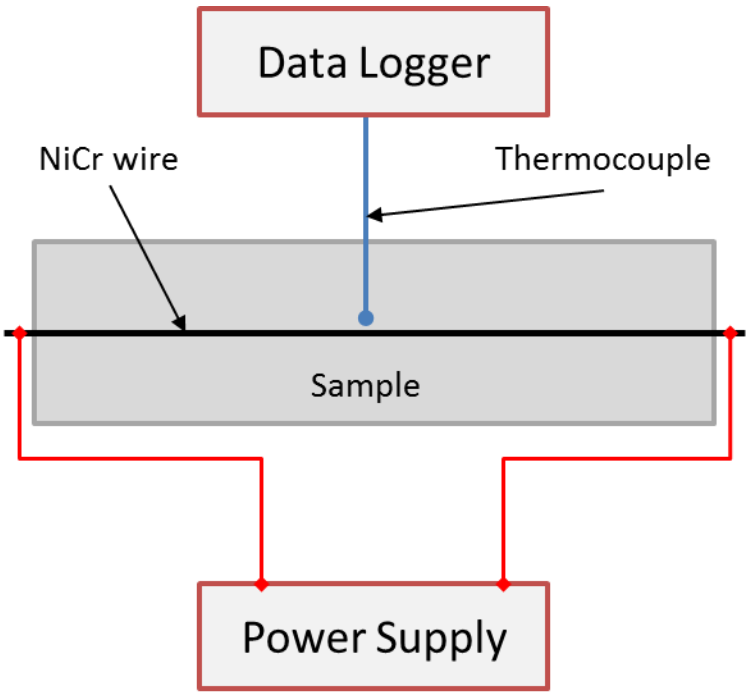

Figure 3-5 Schematic of the embedded hot wire experimental setup.

Voltage and current was set to 2 V and 1 A, respectively. These values were chosen as they provided enough power to increase the sample temperature by at least 10 °C during the 10 minute heating period. The first 300 seconds of data was excluded as the temperature increase was initially non-linear. Thermal conductivity was calculated using equation 3.9 from the linear portion of the graph of temperature versus Ln time.

3.10.3 Thermal Conductivity Measurements using the Guarded Hot Plate Method

High accuracy thermal conductivity measurements were made using a double sided guarded hotplate apparatus, in close accordance with ASTM C-177 (2010) and AS/NZS 4859.1 (2002). The guarded hot plate apparatus is considered an absolute method and is generally interchangeable with the heat flow meter apparatus used in other laboratories.

Two identical samples (of dimensions 50 x 290 x 290 mm) were located between two isothermal cold surface assemblies and a central guarded hot plate composed of a metered section in the centre thermally isolated from a concentric guarded area (Figure 3-6). Heat was applied to one face of each sample as the other side was cooled using a precision temperature controlled recirculated water cooler system.

Once a steady state thermal condition was reached and remained constant for at least 3 hours, power and thermocouple values were recorded in triplicate. The thermal conductivity was then calculated using equation 3.10.

$$k = \frac{\left(\frac{P}{2}\right) t}{(\Delta T) A} \qquad \textbf{3.10}$$

where k = thermal conductivity ($Wm^{-1}K^{-1}$)

P = power (W)

t = sample thickness (m)

ΔT = temperature differential ($T_{hot\ side} - T_{cold\ side}$) (°C)

A = area of metering surface (m^2)

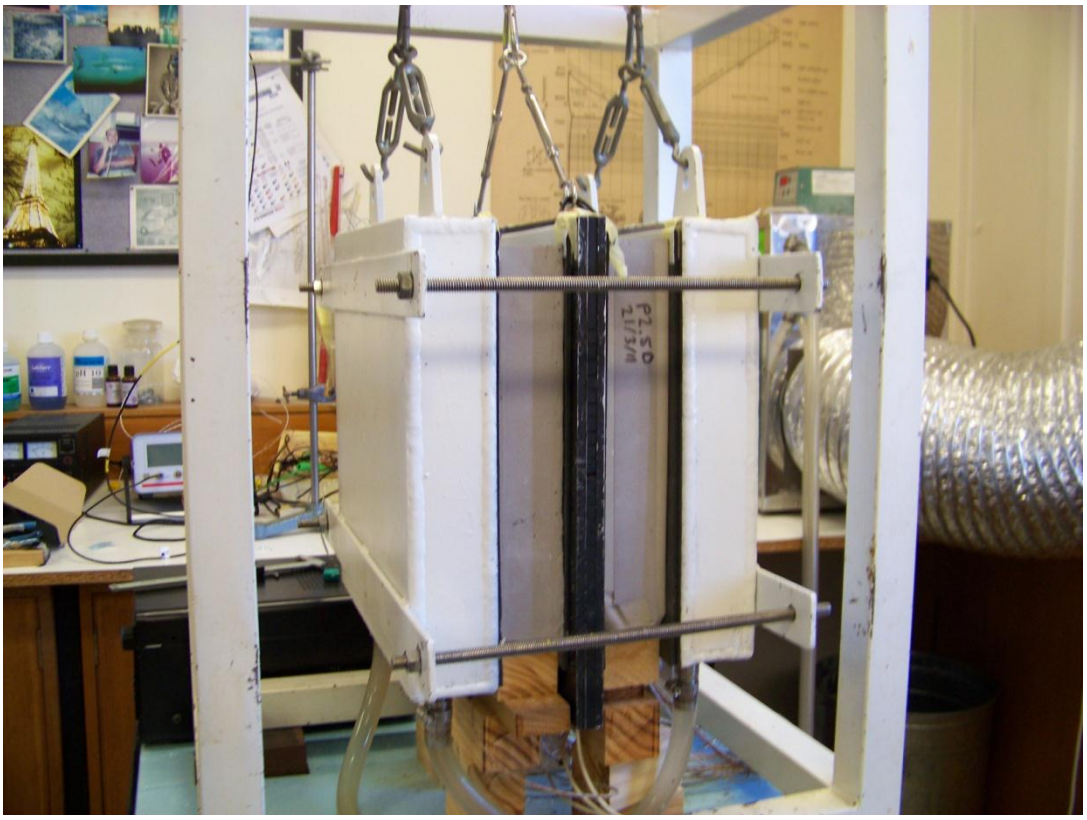

Figure 3-6 Photograph of the guarded hot plate experimental setup. Note: When operating, the apparatus is thermally isolated using an insulating cover (not pictured).

3.11 Thermal Expansion

Thermal expansion is the tendency for matter to increase in volume when heated. Equation 3.11 shows the relationship that is used to calculate the linear thermal expansion of a long thin rod (Nave, 2005).

$$\frac{\Delta L}{L_0} = \alpha \Delta T \qquad \textbf{3.11}$$

Where $\frac{\Delta L}{L_0}$ = the fractional change in length

α = linear coefficient of thermal expansion (K^{-1})

ΔT = temperature difference (K)

Thermal expansion in this study was measured using a DI-24 Adamel Lhomargy dilatometer (France). The dilatometer had to be calibrated prior to sample testing as

the measured thermal expansion from the DI-24 dilatometer was convoluted with the thermal expansion of the sample and the alumina holder it was mounted on. The thermal expansion of the sample was calculated by taking into account the contribution of the alumina holder. Equation 3.12 details the correction applied to the measured data.

$$\left(\frac{\Delta L}{L}\right)_{Corrected} = \left(\frac{\Delta L}{L}\right)_{Measured} + \left(\frac{\Delta L}{L}\right)_{Alumina} = \left(\frac{\Delta L}{L}\right)_{Measured} + (2x10^{-9}T^2 + 7x10^{-6}T - 2x10^{-4}) \quad \textbf{3.12}$$

A copper standard was used to verify the quality of the correction. Copper was chosen because of its linearity of expansion over the working temperature range. Figure 3-7 compares the theoretical expansion of copper as measured using a number of techniques with the corrected and un-corrected thermal expansion of copper as measured using the DI-24 dilatometer.

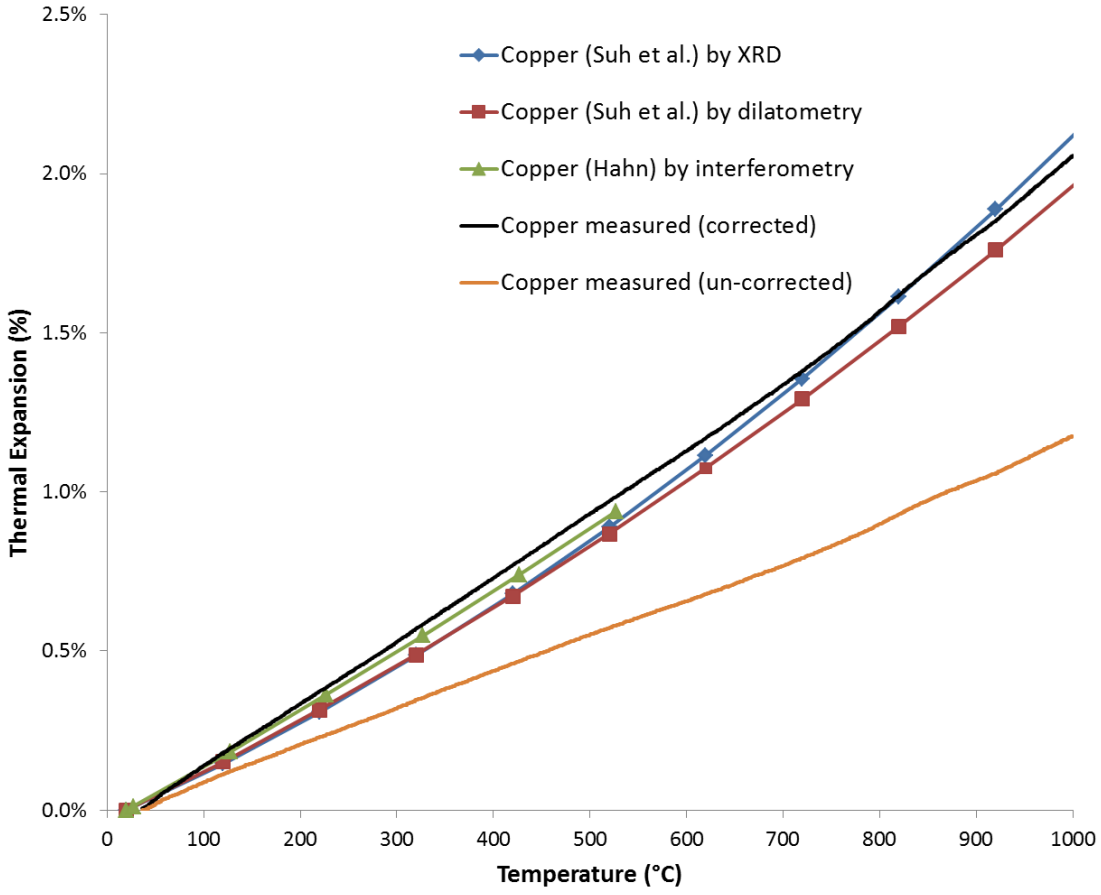

Figure 3-7 Theoretical and measured thermal expansion of copper. Theoretical values taken from (Hahn, 1970) and (Suh et al., 1988).

Dilatometry samples were cast into 1 mL syringes and cut to length to achieve a cylinder of 15 mm length and 5 mm diameter. The measurements were conducted from ambient up to 1000 °C with a heating rate of 5 °C/minute. A preload of 650 μm / 100 mN was set to allow the instrument to record data from shrinking samples. All measurements were done in accordance with ASTM E831: Standard test method for linear thermal expansion of solid materials by thermo mechanical analysis (2006). All presented dilatometry results are an average of the measurements from three samples.

3.12 Particle Sizing

Particle size analysis was performed with a Malvern laser diffraction system at the Commonwealth Scientific and Industrial Research Organisation (CSIRO) laboratories in Waterford, Western Australia. Particle size analysis was used to determine the size range and surface area of the fly ash particles. The dispersing solution was deionised water with a sodium hexametaphosphate dispersing agent. The solution and approximately 1 wt.% of fly ash was sonicated for 10 minutes to break up aggregates prior to analysis.

3.13 Compressive Strength Measurement

Compression tests were conducted to investigate the ultimate strength of the geopolymers in this study. The tests were performed on a Lloyds universal tester EZ50 (United Kingdom) using a 50 kN load cell. The compressive strength was calculated from the maximum load prior to failure according to equation 3.13.

$$\sigma = \frac{F}{A} \qquad \textbf{3.13}$$

where σ = compressive strength (or stress) (MPa)

F = total load on the sample at failure (N)

A = area of the bearing surface of the specimen (m^2).

Cylinders of 15 mm diameter and 30 mm height were prepared for the testing of solid samples. Larger, 50 mm diameter and 100 mm height samples were used for the testing of the low density samples. This was to ensure the sample diameter was at least twice the length of the reinforcing fibres. Samples were sanded to achieve parallel top and bottom surfaces prior to testing. Testing was conducted 28 days after curing. A load rate of 0.25 MPa s^{-1} was used to closely comply with ASTM C39 – Standard test method for compressive strength of cylindrical concrete specimens (2005).

3.13.1 Young's Modulus

The Young's modulus for each sample was derived from the compressive strength test results. Young modulus is a measure of the stiffness of an elastic material and can be determined by calculating the slope of the stress-strain curve during the elastic region of a compressive strength test (equation 3.14) (Askeland et al., 2010, page 211).

$$E = \frac{\sigma}{\varepsilon} \qquad \textbf{3.14}$$

where E = Young's modulus (MPa)

σ = Stress (MPa)

ε = Strain (ΔL / Lo) (change in length / original length)

The reported compressive strength and Young's modulus results are the average of at least 4 repeat tests and the uncertainties are quoted as one standard deviation from the mean.

3.14 High Temperature Exposure of Samples

Samples were heated in a furnace to assess their strength retention after high temperature exposure. Samples of the same dimensions as used for compressive strength testing (15 x 30 mm) were placed in an electric furnace (model 60 SL, Kiln

Manufacturers) on an alumina tray. The heating regime is provided in Table 3.7. After firing, samples were compressive strength tested as per section 3.13.

Table 3.7 Programmed heating regime for firing.

Stage	Time (min)	Temperature (°C)	Heat rate (°C min^{-1})
Stage 0	0	20	0.0
Stage 1	300	105	0.3
Stage 2	180	1000	5.0
Stage 3 (hold)	180	1000	0.0
Stage 4	300	20	3.3

3.15 Density Measurements

3.15.1 Particle Density

Particle density was calculated by measuring the displacement of fluid by fly ash particles in a fixed volume. A known mass of fly ash (approximately 20 g) was placed in a 100 ml specific gravity (SG) bottle. The rest of the volume was filled with ethanol and the mixture was sonicated to remove any entrained air. The bottle was then weighed and the average particle density of the fly ash was calculated from equation 3.15.

$$\rho_{Flyash} = \frac{m_{Flyash}}{(100 - V_{Ethanol})} \quad \textbf{3.15}$$

where

$$V_{Ethanol} = \frac{(m_{Total} - m_{Flyash} - m_{Bottle})}{\rho_{Ethanol}} \quad \textbf{3.16}$$

ρ = density (g cm^{-3})

m = mass (g)

V = volume (cm^3)

All reported results are the average of 5 separate measurements.

3.15.2 Geopolymer Density

The bulk density of solid geopolymer samples was measured by the simple method of dividing the mass by the volume. Cylindrical samples (15 mm diameter, 30 mm high) were used for density measurements. Samples were carefully selected to ensure voids, cracks or shape defects did not skew volume measurements. Sample dimensions were measured using digital Vernier calipers (Kincrome, Australia) and sample mass was measured using a laboratory scale (model AA-200, Denver Instrument Company, USA). All reported results are the average of 10 separate measurements.

3.16 Fire Testing

Fire testing was conducted to assess the performance of geopolymers in simulated fire conditions. The significant difference of fire testing to other thermal testing (as described section 3.14) is the heat rate. Fire testing in this study was conducted to closely comply with the Australian standard fire test AS1530.4: Methods for fire tests on building materials, components and structures - Fire-resistance test of elements of construction (2005). The test involves heating one side of the sample according to the time-temperature relationship in equation 3.17.

$$T = 345\log_{10}(8t - 1) + 20 \qquad \textbf{3.17}$$

where T = temperature (°C)

t = time (minutes)

The standard test requires a sample exposure surface of 3000 x 3000 mm. In order to feasibly test a large number of samples, the sample exposure region was scaled down to 200 x 200 mm (1:15 scale). An electric furnace that was custom designed specifically for this study was used for the fire tests (Figure 3-8).

Figure 3-8 Photo of fire testing furnace.

The furnace had wire wound filaments and the temperature was controlled using a multi stage controller (model PAK-700, Furnace Technologies Pty Ltd). The time-temperature heating regime was programmed to mimic the fire curve in the standard (AS1530.4) (Table 3.8).

Table 3.8 Programmed heating regime for fire testing.

Stage	Time (min)	Δ t (min)	Temperature (°C)
Stage 0	0	0	20
Stage 1	1	1	349
Stage 2	2	1	445
Stage 3	3	1	502
Stage 4	5	2	576
Stage 5	7	2	626
Stage 6	10	3	678
Stage 7	15	5	739
Stage 8	30	15	842
Stage 9	60	30	945
Stage 10	90	30	1006
Stage 11	120	30	1049
Samples allowed to cool naturally back to room temperature			

Three K type thermocouples were placed onto the cold side of the sample. One in the centre of the exposed region and one either side, halfway to the edge of the sample (details in Figure 3-9). Thermocouples were held in constant contact with the specimen by placing a 20 g brass weight onto the insulated casing of the wire (Figure 3-10). Cold side temperatures were recorded individually and as the average of the three thermocouples. A hot side thermocouple was used to check that the furnace temperature was following the standard fire curve. The data for the four thermocouples was logged every 10 seconds using a Vernier LabQuest (U.S.A.).

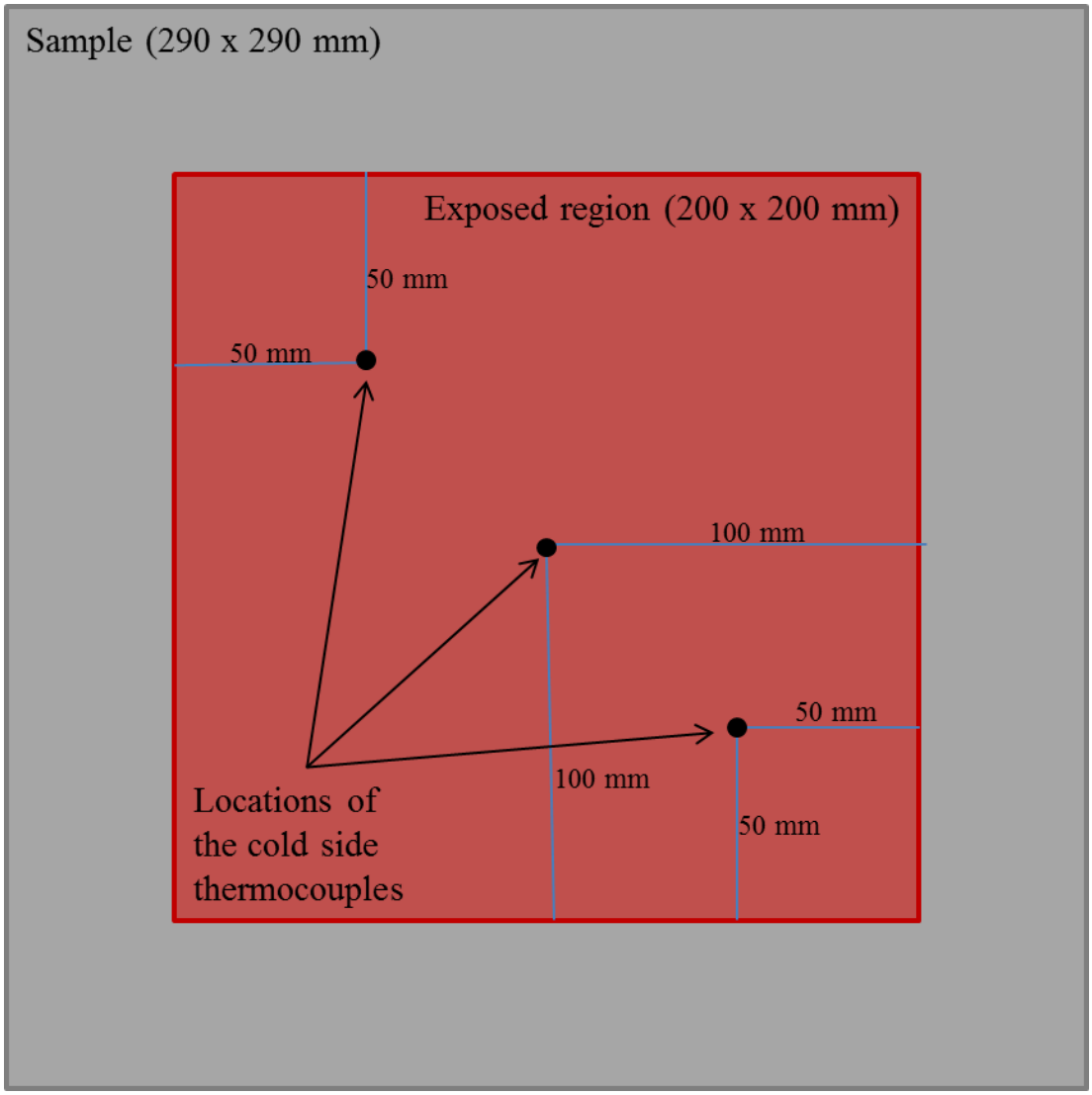

Figure 3-9 Schematic indicating the location of the thermocouples during the fire tests. Note: A fourth thermocouple was also placed on the centre of the hot side approximately 50 mm below the sample (as not to be affected by sample dehydration).

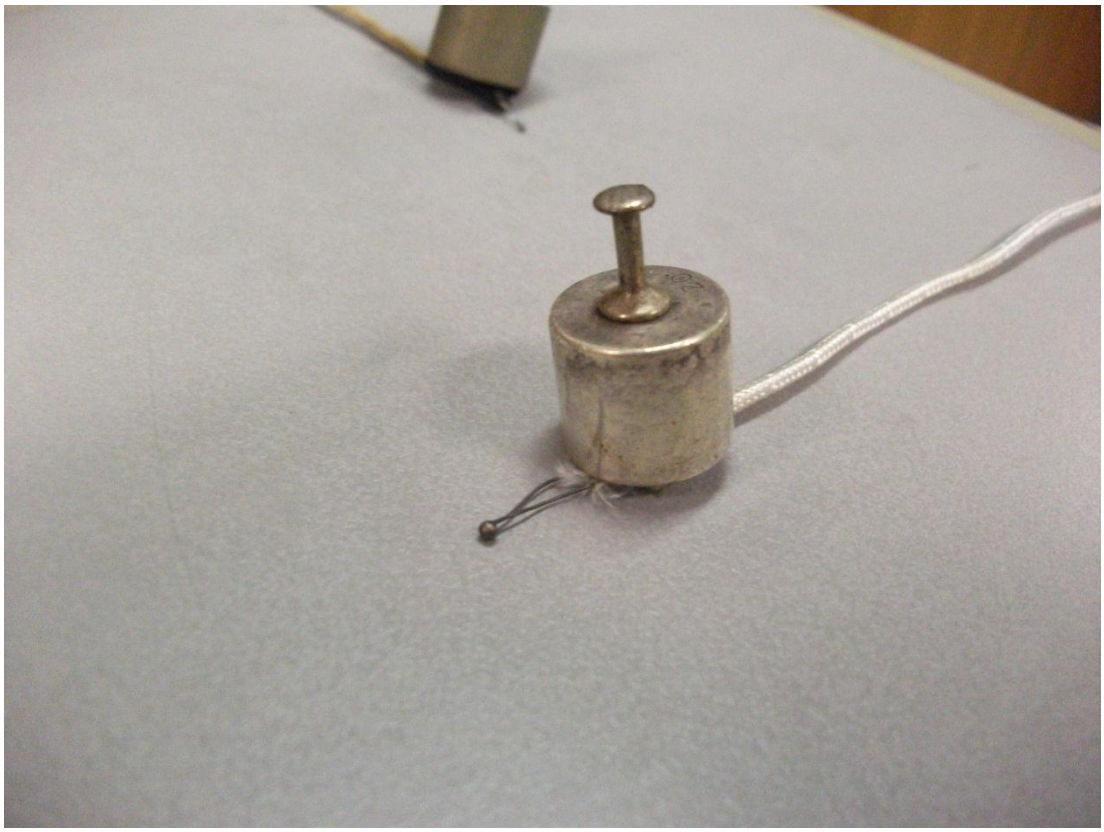

Figure 3-10 Image showing how a brass weight was used to maintain the hot junction of the thermocouple in contact with the sample during the fire testing.

Chapter 4
Precursor Material Analysis

"The important thing in science is not so much to obtain new facts but to discover new ways of thinking about them"

William Lawrence Bragg

4.1 Introduction

In order to fully understand the observed physical properties of the geopolymers produced in this study it was considered critical to fully characterise the materials they were synthesised from. This was particularly important in the case of the fly ashes as their comprehensive composition and physical characteristics were not available from the supplier.

The degree of dissolution of aluminosilicates in high pH alkaline solutions is largely dependent on the particle size, morphology and composition of the source material (van Jaarsveld et al., 2003, Chen-Tan et al., 2009, Fernandez-Jimenez et al., 2005, Bakharev, 2006, Rahier et al., 2003), in particular the amorphous aluminosilicates. Previous research has shown that geopolymers synthesised from aluminosilicate sources with suitable overall chemical composition but lacking an appropriate reactive component will result in incomplete dissolution and consequently be of lower strength (Bakharev, 2006, Rahier et al., 2003).

Fly ash characteristics that are important when considering their use in geopolymers are; particle size (influences reactivity) (Fernandez-Jimenez et al., 2005, Chen-Tan et al., 2009), glass content (determines the amount of reactive material) (Williams and van Riessen, 2010), Si:Al ratio in the glass (controls the mechanical strength and thermal resistance) (Rickard et al., 2011), iron content (important in high temperature applications) and calcium content (affects setting time) (Dombrowski et al., 2007, van Jaarsveld et al., 2003).

This chapter reports on the characterisation of the five fly ashes used in this study in terms of elemental composition, phase composition, particle size, density and morphology.

The contents of this chapter formed the basis of the following publications;
Rickard, W. D. A., Williams, R., Temuujin, J., & van Riessen, A. (2011). Assessing the suitability of three Australian fly ashes as an aluminosilicate source for

geopolymers in high temperature applications. *Materials Science and Engineering: A*, *528*(9), 3390-3397.

Rickard, W. D. A., Temuujin, J., & van Riessen, A. (2012). Thermal analysis of geopolymer pastes synthesised from five fly ashes of variable composition. *Journal of Non-Crystalline Solids*, 358(15), 1830-1839.

Note: Numbers in tables are displayed with their uncertainty in adjacent parentheses. Uncertainties are calculated as the estimated standard deviation of the least significant figure of the measured value. This methodology is used throughout this thesis unless otherwise stated.

4.2 Bulk Compositional Analysis of the Fly Ashes

XRF was performed to assess the bulk chemical composition of each fly ash. As fly ash is known to be a highly variable material, even within batches, a preliminary experiment was conducted to compare the composition of one of the supplied fly ashes from different bags. Table 4.1 reveals there was very little deviation between the different bags of Port Augusta fly ash and as such the average composition can be considered an accurate representation of the composition of the ash in any particular bag. Other fly ashes in this study were delivered in one or two containers and were homogenised by mixing rather than separately analysing each container.

Table 4.2 compares the important compositional oxides from the five fly ashes used in this study (full compositional details in table 3.1). As expected, each fly ash was composed of aluminosilicates, iron oxides and a number of minor oxides. The amount of Al_2O_3 in the fly ashes ranged from 22.4 wt.% to 30.5 wt.%, with the exception of Bayswater fly ash which only had 11.9 wt.% Al_2O_3. The amount of SiO_2 varied from 51.4 wt.% to 82.3 wt.%. The bulk molar silicon to aluminium ratio, varied from 1.6 (Collie) to 5.9 (Bayswater).

Table 4.1 Inter batch compositional comparison of Port Augusta fly ash as determined by XRF (wt.%).

Oxide	Test 1	Test 2	Test 3	Test 4	Test 5	Average	Standard deviation
SiO_2	51.87	52.07	51.96	52.08	51.99	51.99	0.09
Al_2O_3	30.30	30.60	30.60	30.50	30.50	30.50	0.12
Fe_2O_3	2.76	2.78	2.73	2.75	2.75	2.75	0.02
CaO	4.58	4.59	4.62	4.60	4.60	4.60	0.01
K_2O	1.34	1.34	1.34	1.34	1.34	1.34	0.00
TiO_2	2.15	2.16	2.16	2.16	2.15	2.16	0.01
MgO	2.54	2.55	2.52	2.53	2.53	2.53	0.01
Na_2O	2.28	2.29	2.34	2.29	2.29	2.30	0.02
P_2O_5	0.82	0.82	0.83	0.83	0.82	0.82	0.00
SrO	0.06	0.06	0.07	0.07	0.07	0.06	0.00
BaO	0.07	0.07	0.07	0.07	0.07	0.07	0.00
Other	1.74	1.15	1.24	1.29	1.37	1.36	0.23
LOI (1000 °C)	0.51	0.48	0.48	0.50	0.48	0.49	0.01

Table 4.2 Bulk chemical composition (XRF) of the fly ashes and relevant compositional ratios (wt.%). Uncertainties in brackets.

Oxide	Collie	Eraring	Tarong	Port Augusta	Bayswater
SiO_2	51.38 (8)	65.47 (8)	73.68 (8)	51.99 (8)	82.25 (8)
Al_2O_3	26.90 (10)	23.00 (10)	22.40 (10)	30.50 (10)	11.90 (10)
Fe_2O_3	13.20 (2)	4.03 (2)	0.64 (2)	2.75 (2)	2.41 (2)
CaO	1.74 (5)	1.59 (5)	0.08 (5)	4.60 (5)	1.37 (5)
Alkalis (Na_2O & K_2O)	1.31 (6)	2.24 (6)	0.62 (6)	3.64 (6)	0.64 (6)
Other	5.03 (8)	2.30 (8)	1.79 (8)	6.03 (8)	1.18 (8)
LOI (1000 °C)	0.44	1.37	0.79	0.49	0.25
Sum of aluminosilicates	78.28 (13)	88.47 (13)	96.08 (13)	82.49 (13)	94.15 (13)
SiO_2 : Al_2O_3	1.91 (1)	2.85 (1)	3.29 (2)	1.70 (1)	6.91 (2)
Si : Al (molar)	1.62 (1)	2.42 (1)	2.79 (1)	1.45 (1)	5.86 (1)

An important compositional difference between the fly ashes was the amount of iron oxide. Collie fly ash had 13.2 wt.% Fe_2O_3 whereas the other fly ashes had less than 4.0 wt.%. Previous research has shown that volume changes caused by oxidation of the iron detrimentally affects the performance of fly ash geopolymers at elevated temperatures (Rickard et al., 2010). Iron rich fly ash particles have also been observed to inhibit the dissolution of aluminosilicates during geopolymerisation (Chen-Tan et al., 2009).

The sum of the alkali's initially present in the fly ashes is also listed in Table 4.2. Port Augusta fly ash has the highest alkali content with 3.6 wt.%. Alkali's are known to be network modifiers in aluminosilicate glasses (Kovalchuk and Krivenko, 2009) and as such their added presence (as there will be additional alkali in the geopolymer) is likely to reduce the melting point of the geopolymer synthesised from that fly ash.

4.3 Phase Analysis of the Fly Ashes

The XRF data provides a preliminary indication as to the suitability of each of the fly ashes for production of high temperature resistant geopolymers although it is limited by the fact that there is no information about the reactivity of the aluminosilicate component. Research by Chen-Tan et al. (2009) showed that only the amorphous aluminosilicates in the fly ash are reactive in the geopolymerisation reaction that forms a geopolymer.

Figure 4-1 to Figure 4-5, inclusive, contain the XRD patterns for the five fly ashes. Crystalline phases common to all fly ashes were quartz (SiO_2) and mullite ($Al_6Si_2O_{13}$). All fly ashes also exhibited a hump at approximately 22° 2θ which was characteristic of an amorphous phase.

Various iron phases were detected in the fly ashes with the exception of Tarong fly ash. Tarong fly ash contained only 0.64 wt.% of iron oxide in its bulk composition so it was not expected to have detectable crystalline iron phase(s) in the diffraction

pattern. Phase identification of the crystalline iron oxides was inhibited by considerable peak overlap with mullite and quartz phases. Low peak intensity and broad peaks (likely due to low phase concentration and small crystallite size, respectively) also increased the difficulty of iron phase identification. The detected iron phases were hematite (Fe_2O_3), magnetite (Fe_3O_4) and maghemite-C (Fe_2O_3).

Corundum (Al_2O_3) was detected in Port Augusta and Bayswater fly ashes. It was concluded that the corundum phase was introduced during sample preparation when the fly ashes were micronised using corundum milling media. Corundum was not detected in the other fly ashes as they were micronized with a different batch of milling media which was more worn and thus less likely to impart fragments into the sample.

Port Augusta fly ash was the only fly ash to contain a detectable concentration of rutile (TiO_2).

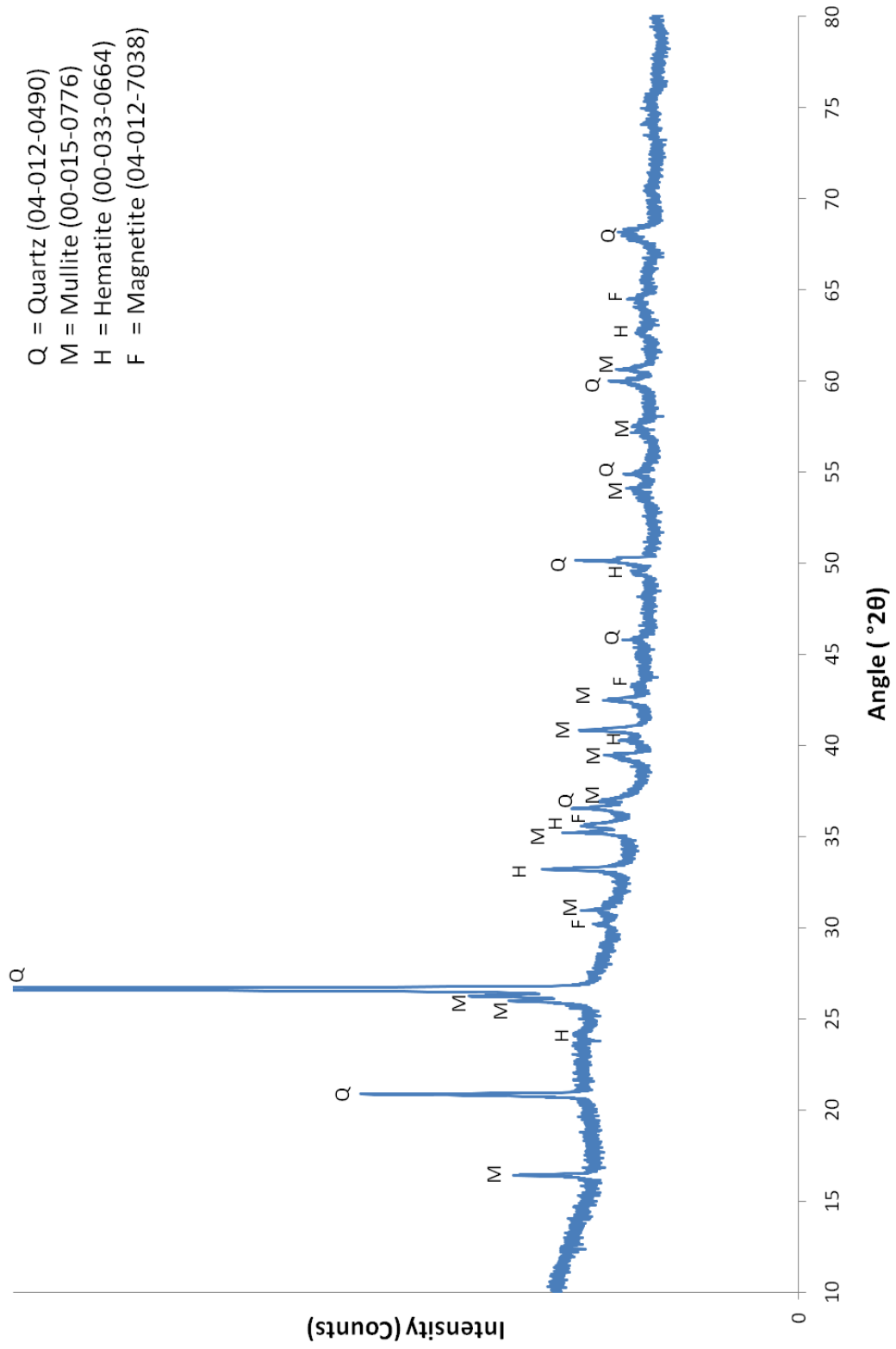

Figure 4-1 XRD pattern for Collie fly ash. High angle data not displayed (80 - 120 °2θ). PDF numbers for each phase in brackets.

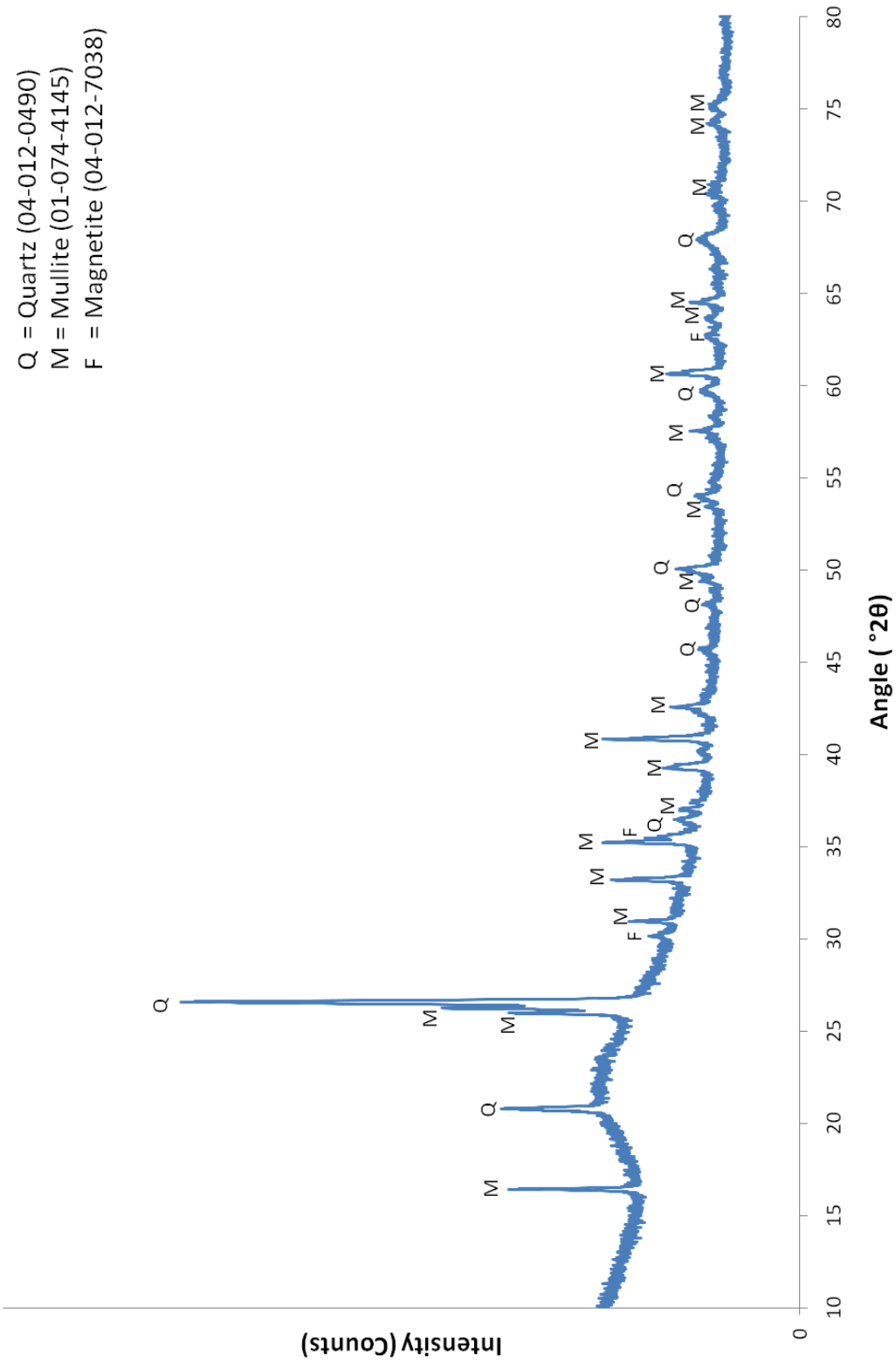

Figure 4-2 XRD pattern for Eraring fly ash. High angle data not displayed (80 - 120 °2θ). PDF numbers for each phase in brackets.

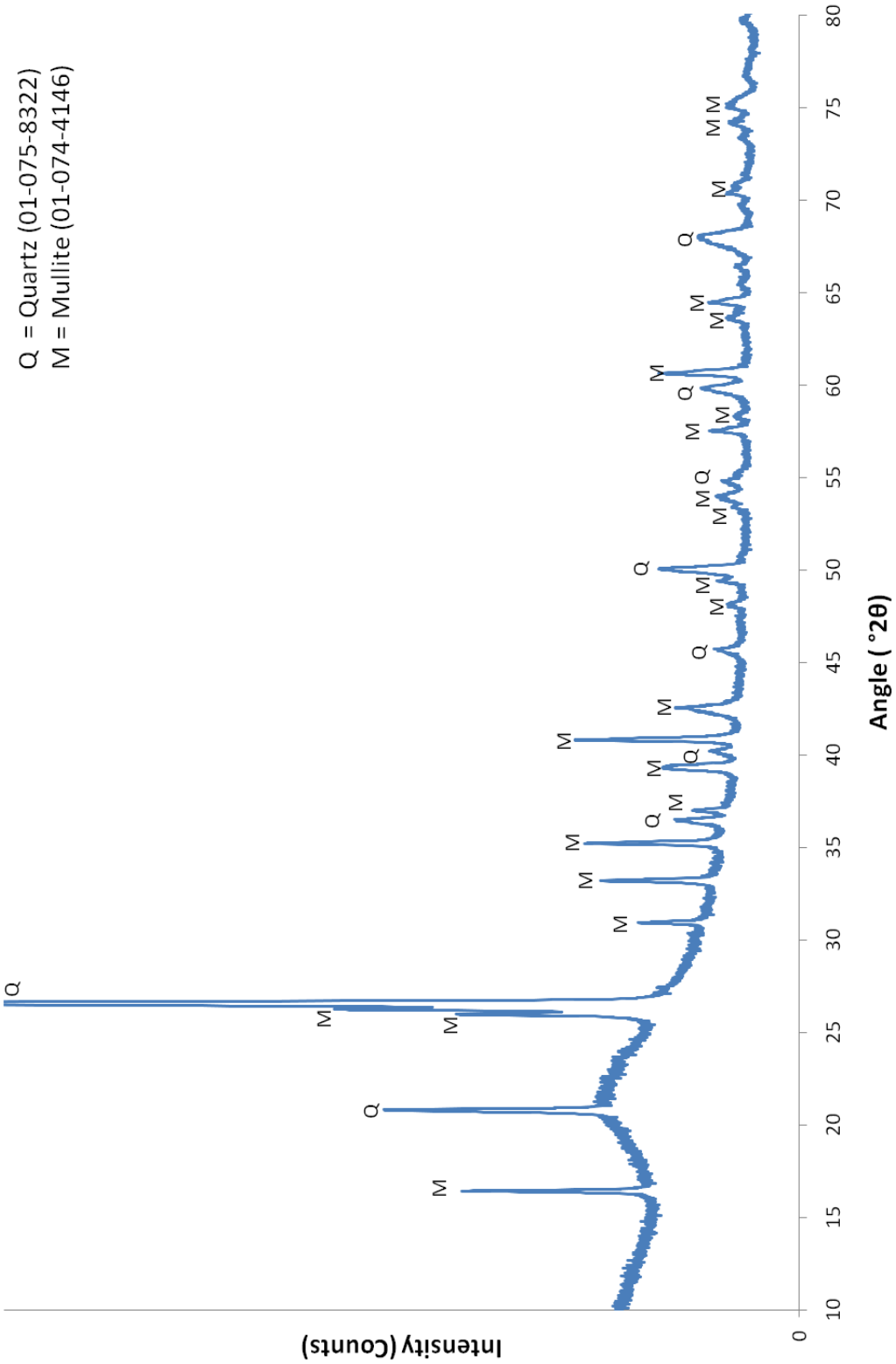

Figure 4-3 XRD pattern for Tarong fly ash. High angle data not displayed (80 - 120 °2θ). PDF numbers for each phase in brackets.

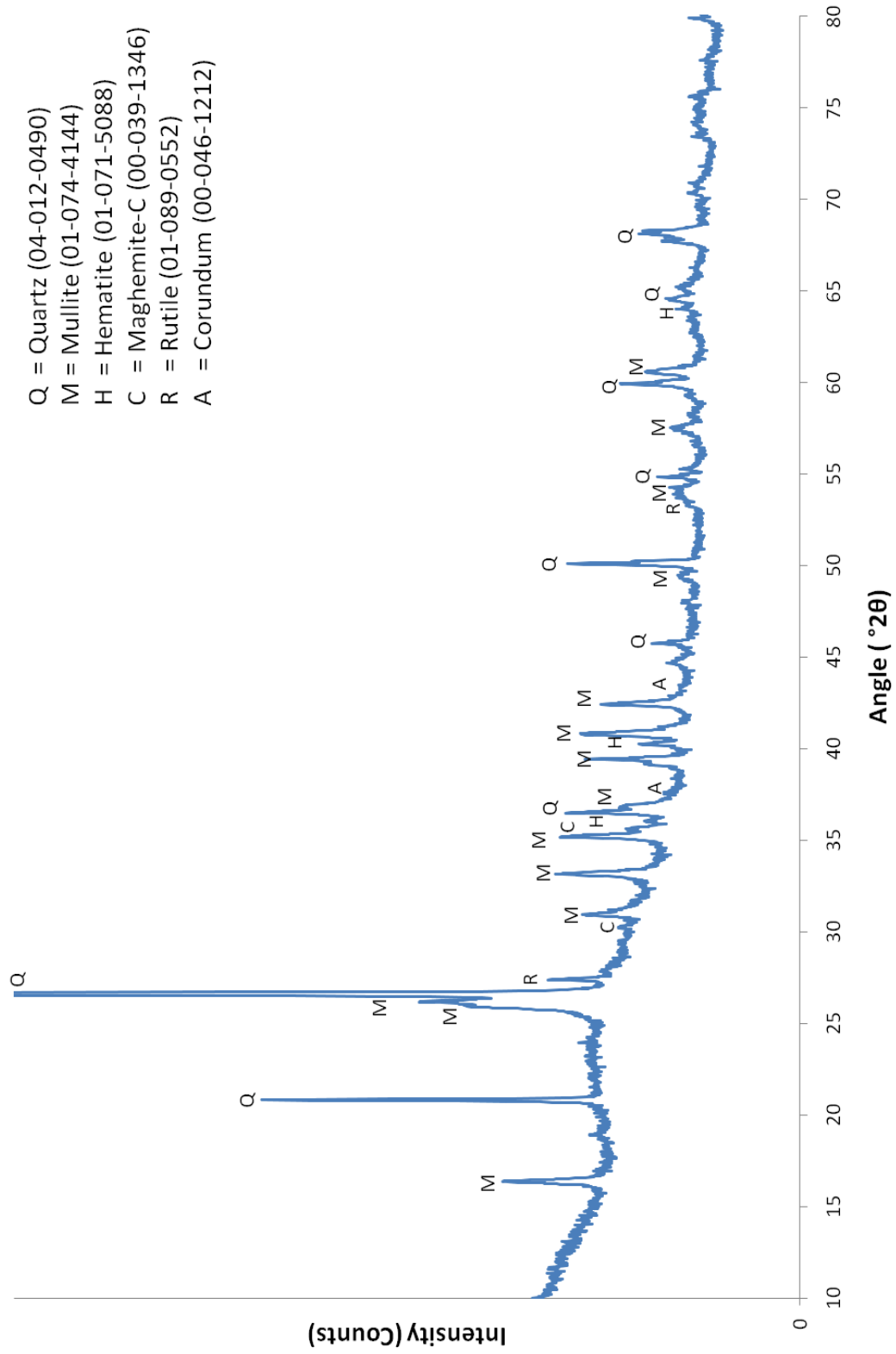

Figure 4-4 XRD pattern for Port Augusta fly ash. High angle data not displayed (80 - 120 °2θ). PDF numbers for each phase in brackets.

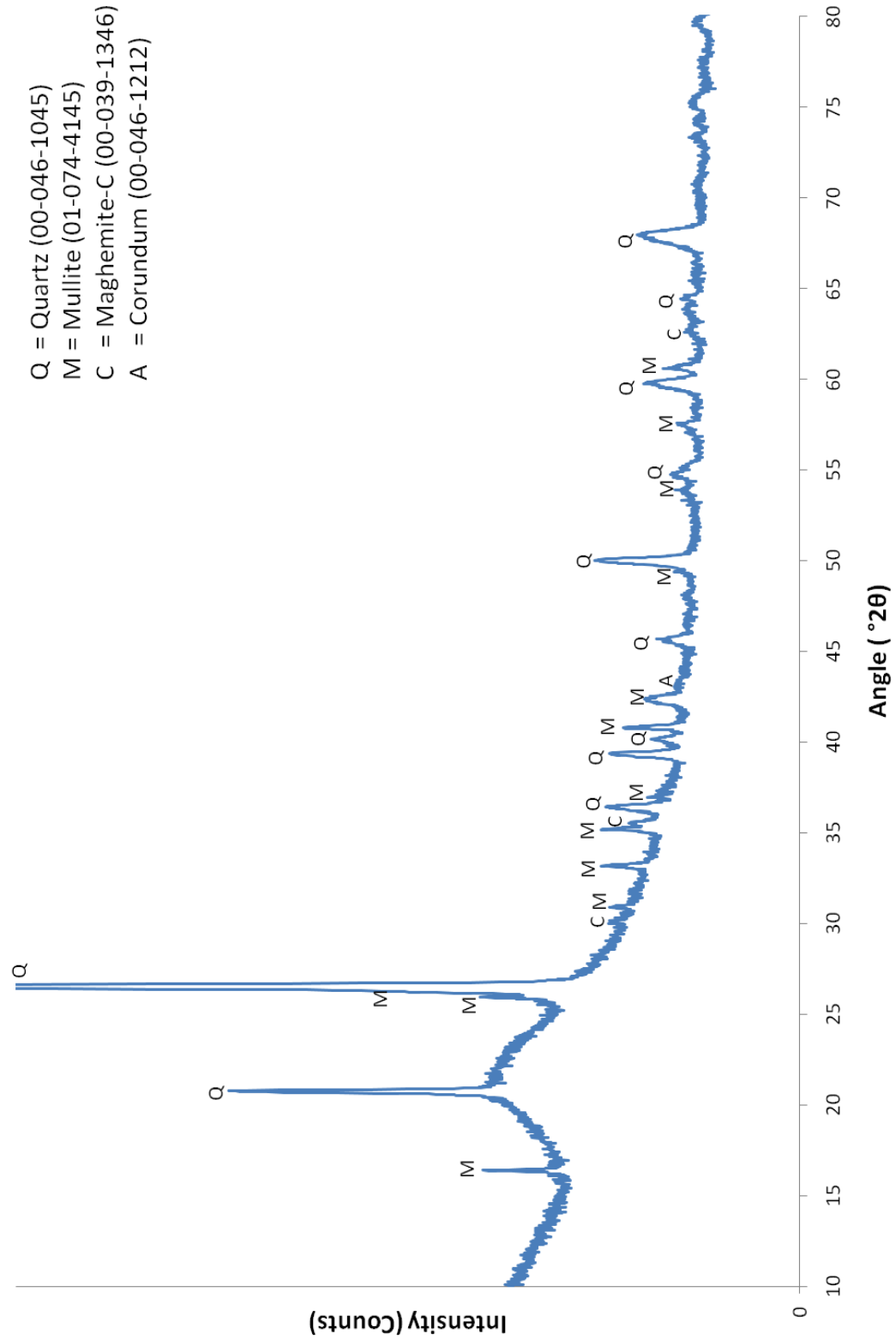

Figure 4-5 XRD pattern for Bayswater fly ash. High angle data not displayed (80 - 120 °2θ). PDF numbers for each phase in brackets.

4.3.1 Quantitative Phase Composition of the Fly Ashes

To quantify the reactive component of each of the fly ashes, the phase composition was determined quantitatively using fluorite as an internal standard (full details of the quantification method are available in chapter 3). Table 4.3 contains a comparison of the phase composition of each of the fly ashes.

The corundum phase as detected in the Port Augusta and Bayswater fly ashes (Figure 4-4 and Figure 4-5) was modelled in the phase quantification but not included in the corrected phase composition (Table 4.3).

Rietveld modelling with the XRD data indicated that there were two populations of quartz with differing crystallite size. It is thought that the quartz phase with the larger crystallite size (> 200 nm), referred to as 'primary quartz', was present prior to the coal combustion process and exists as discreet particles amongst the fly ash spheres. The other quartz population, referred to as 'secondary quartz', had a much smaller crystallite size (< 100 nm) and is thought to have formed during combustion from the decomposition of clay and is present within fly ash spheres. Previous research by Williams and van Riessen (2010) found similar results in an analysis of Collie fly ash. The two quartz phases were modelled separately during the phase quantification and their relative concentrations are listed for each fly ash (Table 4.3).

Various forms of mullite were found to be present in the fly ashes. Mullite crystallises in a solid solution and is known to exist in non-stoichiometric forms with a general formula of $Al_{4+2x}Si_{2-2x}O_{10-x}$ (Gomes and François, 2000). Search-match software was used for the preliminary determination of the form of mullite in each fly ash. A more accurate selection was achieved by refining the mullite lattice parameter, *a*, in Topas for each fly ash, then that value was used to find a corresponding mullite structure in the ICSD database.

Table 4.3 Phase composition of each fly ash as determined by QXRD. Uncertainties in brackets.

Phase	Collie wt.%	Eraring wt.%	Tarong wt.%	Port Augusta wt.%	Bayswater wt.%
Amorphous:	54.00 (45)	62.74 (31)	50.82 (28)	50.63 (73)	68.39 (39)
Crystalline:					
Mullite ICSD 66452	15.80 (18)		25.1 (11)		
Mullite ICSD 66449		20.88 (14)			7.39 (15)
Mullite ICSD 99328				26.83 (33)	
Quartz ICSD 83849					
Primary	15.80 (18)	6.81 (14)	13.77 (13)	11.74 (36)	12.19 (18)
Secondary	11.14 (21)	8.08 (16)	10.31 (14)	8.10 (39)	10.90 (19)
Total	25.19 (39)	14.89 (30)	24.08 (27)	19.84 (75)	23.09 (37)
Magnetite ICSD 43001	2.51 (83)	1.49 (52)			
Hematite ICSD 88417	1.50 (64)			0.87 (38)	
Maghemite-C ICSD 87119				0.85 (27)	1.05 (69)
Rutile ICSD 82081				0.74 (50)	

The concentration of mullite in the fly ashes varied to a greater extent than that of the concentration of quartz. Bayswater fly ash had only 7.4 wt.% mullite, whereas Tarong and Port Augusta fly ashes both had over 25 wt.%. The low concentration of mullite in Bayswater fly ash was consistent with the low amount of alumina in the bulk composition. Mullite has not been reported in the literature to adversely affect the thermal performance of geopolymers but its presence as a crystalline aluminosilicate means there is less amorphous aluminosilicates available for geopolymerisation.

The total concentration of quartz in each of the fly ashes ranged from 19.8 wt.% to 25.2 wt.%. The presence of quartz in a source material is undesirable for geopolymers designed for high temperature applications due to the differential thermal expansion upon heating. This can cause micro cracking which reduces the strength of the material. This problem is more significant where the particle size of the quartz is larger. Kong et al. (2005) observed that the presence of quartz based aggregates significantly reduced the compressive strength of fly ash geopolymers upon heating to 800 °C. Similar results have been observed with quartz based OPC mortars (Subaer and van Riessen, 2006). It is the opinion of the author that the secondary quartz detected in the studied fly ashes is too small to adversely affect the high temperature performance of the resulting geopolymer. Since approximately half the quartz in each fly ash is secondary quartz it can be considered that the concentration of quartz that may adversely affect the thermal performance of a subsequent geopolymer is closer to 10 wt.% rather than 20 wt.%.

The amount of crystalline iron in the fly ashes ranged from a maximum of 4.0 wt.% (Collie fly ash) to 0.0 wt.% (Tarong fly ash). The uncertainties in the iron oxide phases were much larger relative to their concentration than the other modelled phases. This was due to low phase concentration, a high degree of peak overlap and a broad peak shape. Hematite is known to be relatively thermally stable, however the presence of thermally unstable phases such as maghemite-C (known to phase change between 370 ºC and 600 ºC) and amorphous iron (known to crystallise to hematite above 300 ºC) indicate that there are likely to be phase changes upon thermal exposure of the fly ashes (Cornell and Schwertmann, 1996).

Additional details of the QXRD analysis of the fly ashes are listed in appendix A.

4.3.2 Amorphous Composition of the Fly Ashes

The amorphous content of the fly ashes were determined to be; Collie 54.0 wt.%, Eraring 62.7 wt.%, Tarong 50.8 wt.%, Port Augusta 50.6 wt.% and Bayswater 68.4 wt.%. As geopolymerisation involves the dissolution of the amorphous component of the fly ashes, the composition of this phase was determined. The elemental

composition of the amorphous phase was calculated by subtracting the contribution of the crystalline phases from the bulk composition (as determined by XRF). Table 4.4 details the amorphous content of each of the fly ashes. It should be noted that any crystalline phases in the fly ashes below the detection limit of the XRD are unavoidably included in the amorphous content, though their contribution will be minor. The aluminosilicate amorphous phase is considered as the reactive phase during geopolymerisation and as such the values in this table were used to design the geopolymer formulations used in this study.

Table 4.4 Amorphous (glass) composition of each of the fly ashes. Uncertainties in brackets.

Oxide	Collie	Eraring	Tarong	Port Augusta	Bayswater
SiO_2	20.90 (65)	45.03 (65)	42.79 (59)	24.53 (67)	57.15 (77)
Al_2O_3	15.39 (41)	7.67 (32)	4.11 (26)	11.14 (45)	6.47 (29)
Fe_2O_3	9.11 (32)	2.49 (16)	0.64 (2)	1.03 (17)	1.36 (19)
CaO	1.74 (5)	1.59 (5)	0.08 (5)	4.60 (5)	1.37 (5)
K_2O	0.90 (4)	1.68 (4)	0.53 (4)	1.34 (4)	0.55 (4)
TiO_2	1.47 (1)	0.84 (1)	1.28 (1)	1.42 (1)	0.61 (1)
MgO	1.41 (3)	0.51 (3)	0.17 (3)	2.53 (3)	0.29 (3)
Na_2O	0.41 (5)	0.56 (5)	0.09 (5)	2.30 (5)	0.09 (5)
P_2O_5	1.09 (2)	0.27 (2)	0.08 (2)	0.82 (2)	0.15 (2)
SrO	0.23 (1)	0.05 (1)	0.01 (1)	0.06 (1)	0.02 (1)
BaO	0.38 (1)	0.06 (1)	0.03 (1)	0.00 (1)	0.00 (1)
Other	1.15 (6)	1.67 (6)	0.96 (6)	0.46 (6)	0.11 (5)
Sum of amorphous aluminosilicates	36.29 (77)	52.70 (73)	46.90 (64)	35.67 (89)	63.62 (95)
SiO_2 : Al_2O_3	1.36 (6)	5.87 (26)	10.42 (68)	2.20 (7)	8.83 (22)
Si : Al (molar)	1.15 (4)	4.98 (19)	8.84 (49)	1.87 (6)	7.49 (19)
Si : Al (molar) Bulk	1.62 (1)	2.42 (1)	2.79 (1)	1.45 (1)	5.86 (1)
% of bulk Si:Al (amor / bulk)%	71 %	206 %	317 %	129 %	128 %

The amount of reactive alumina in the fly ashes ranged from 4.1 wt.% to a maximum of only 15.4 wt.%. Fernández-Jiménez et al. (2006) reported that alumina is critical in the early stages of geopolymerisation and that low reactive alumina content fly ashes produce low strength geopolymers. The low concentration (and hence high Si:Al ratio) of reactive aluminium in Eraring, Tarong and Bayswater fly ashes requires the use of alkali-aluminate solutions rather than the commonly used alkali-silicate solution to achieve typical Si:Al ratios in geopolymers.

The pie charts in Figure 4-6 present the total phase composition of the fly ashes showing graphically the portion available for geopolymerisation. It can be clearly seen that the amount of reactive SiO_2 varies greatly between the fly ashes with Eraring, Tarong and Bayswater having more than 40 wt.%, whereas Collie and Port Augusta fly ashes have less than 25 wt.%.

The Si:Al ratio of the amorphous content was measured to be significantly different to the bulk (Table 4.2). In all fly ashes except Collie, the Si:Al ratio was higher in the amorphous phase than the bulk. This is likely due to the fact that most of the alumina in the fly ashes is crystalline (in the form of mullite). Eraring and Tarong fly ashes exhibited the greatest difference in Si:Al ratios (see final row of Table 4.4).

The bulk of the iron in each of the fly ashes was observed to be poorly ordered; the highest proportion of crystalline to amorphous iron oxide was measured to be 0.38 (Collie fly ash). The low concentration of crystalline iron oxide may be in part due to the very small crystallite size and/or disordered structure (Norton et al., 1986). Amorphous iron is known to order to phases such as hematite during thermal treatment with concomitant volume changes which have been observed to adversely affect the thermal performance of a fly ash based geopolymer (Rickard et al., 2010).

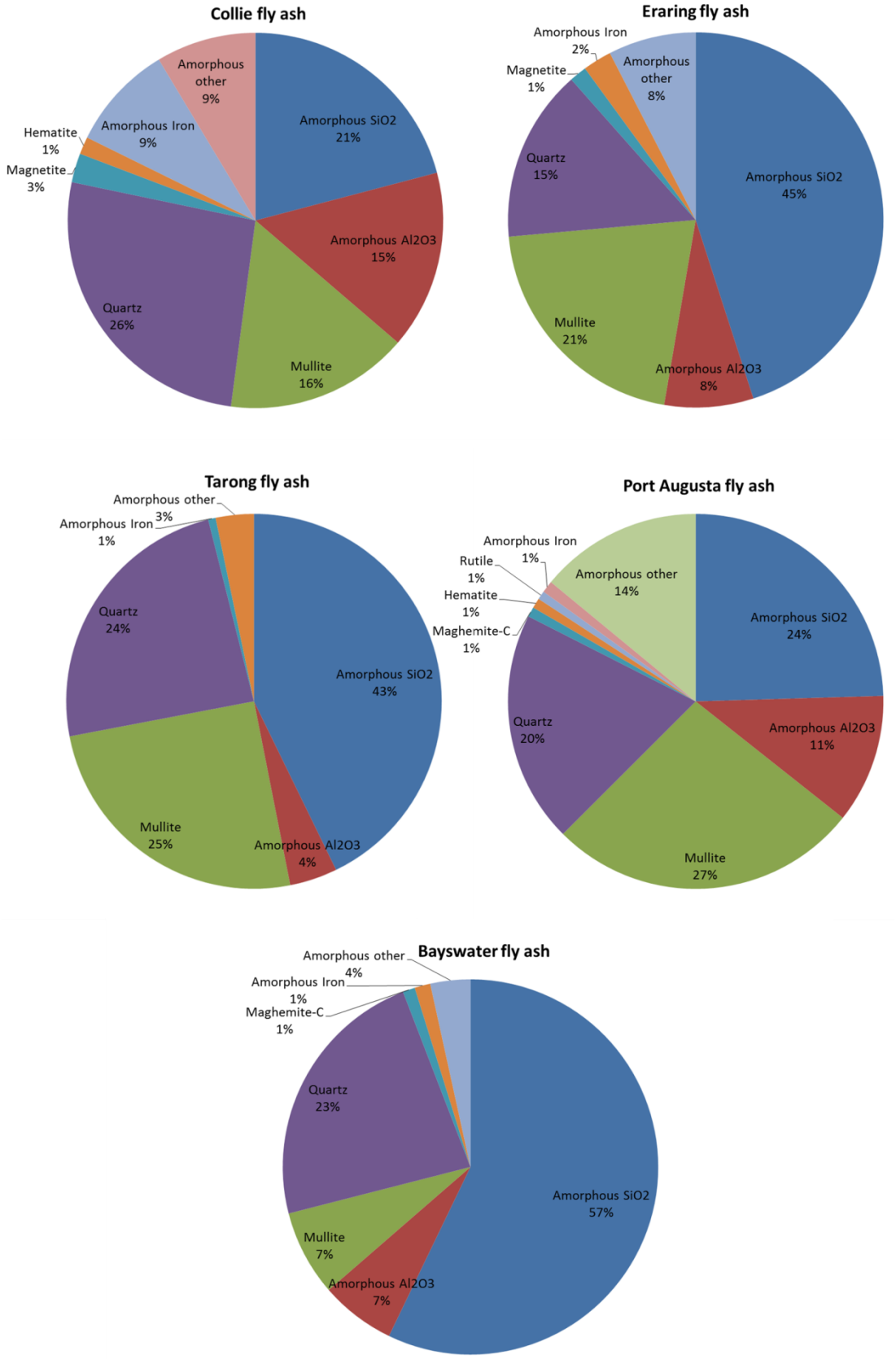

Figure 4-6 Pie charts of the phase distribution for each fly ash.

4.4 Particle Size Analysis of the Fly Ashes

The particle size of the fly ash determines the surface area that is initially available for dissolution by the alkaline solution. It is also known that smaller fly ash particles (< 20 μm) are more likely to have a highly glassy composition (ideal for geopolymerisation), as small particles quench faster than large particles during fly ash formation and as such are less likely to crystallise (Hemmings and Berry, 1987). Figure 4-7 and Figure 4-8 compare the volume passing and particle size distribution for each of the fly ashes in this study, respectively. Each fly ash was found to have a fineness better than the Australian standard for fly ash in cement (AS 3582.1, 1991), where at least 75 % of all particles must be smaller than 45 μm.

The percentage of particles smaller than 45 μm was approximately 80 % for each of the fly ashes with the exception of Bayswater fly ash which had 97 % passing. The bulk of the particles sized were in the range between and 10 μm and 40 μm for each fly ash as seen in Figure 4-8. Port Augusta and, to a lesser extent, Collie fly ash had a bimodal size distribution with a secondary peak in the 1 μm to 5 μm size range.

Significant differences in particle size distribution occurred below 20 μm (Table 4.5). Port Augusta was measured to be the finest of the fly ashes, principally in the sub 5 μm range where it had 40 % by volume passing. Collie and Bayswater fly ashes also had a significant portion of particles passing 5 μm, with 27 % and 26 %, respectively. Eraring and Tarong fly ashes were the coarsest of the ashes with 15 % and 19 % less than 5 μm, respectively.

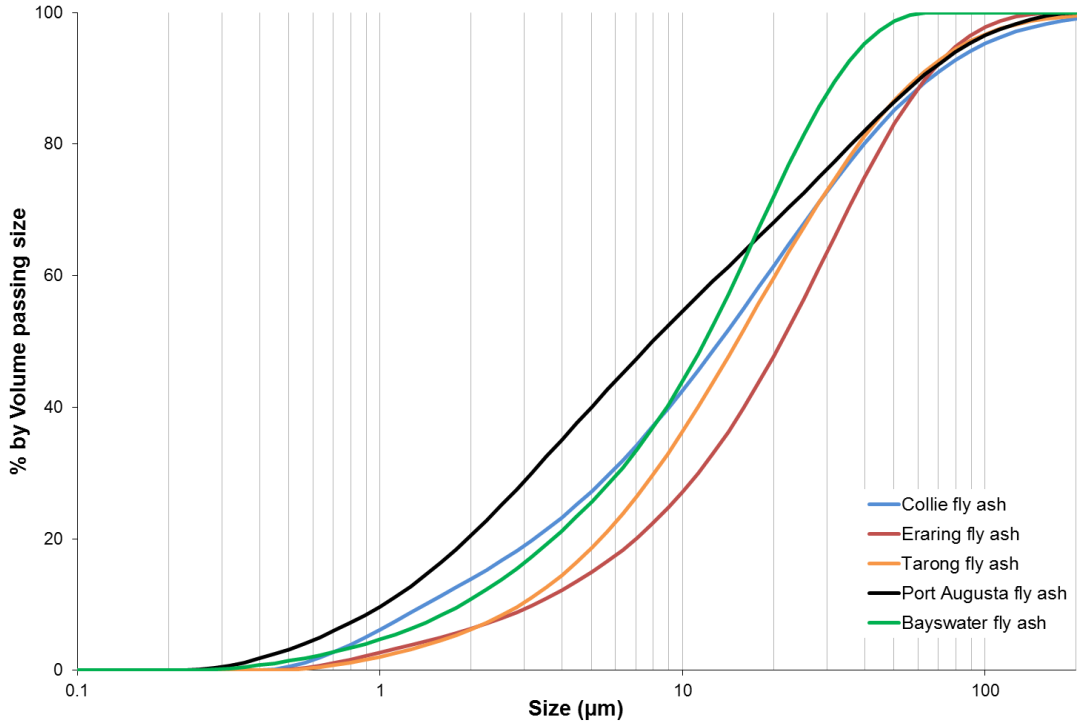

Figure 4-7 Percentage volume passing for each fly ash.

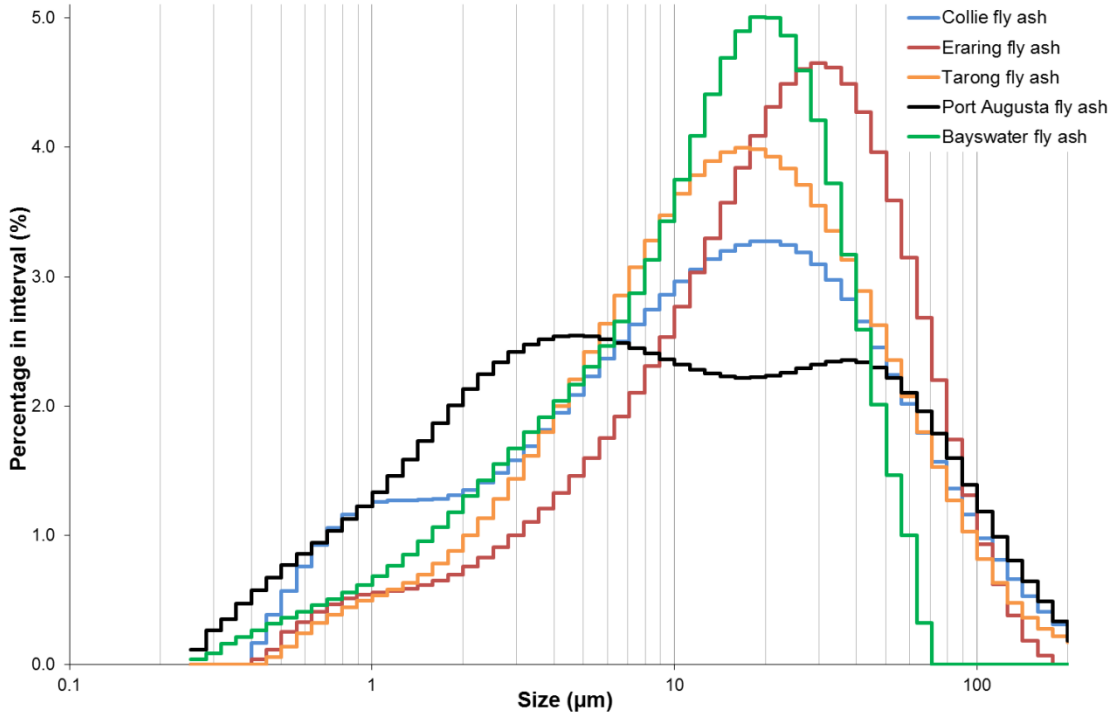

Figure 4-8 Particle size distribution for each fly ash.

If the bulk of the fly ash particles are assumed to be spherical, an estimation of the surface area can be calculated from the particle size data. Due to its high portion of fine particles, Port Augusta had a high specific surface area of 2.14 m^2cm^{-3} (2.14

x 10^6 m^2m^{-3}). Collie and Bayswater fly ashes had specific surface areas of 1.56 m^2cm^{-3} and 1.37 m^2cm^{-3}, respectively. These values were much higher than Eraring and Tarong fly ashes, having specific surface areas of 0.92 $m^2cm^{-3}$and 0.99 m^2cm^{-3}, respectively. A high specific surface area is preferable for fly ashes used for synthesising geopolymers as it promotes expedient dissolution of aluminosilicates in an alkaline solution. However, the phase and inter-particle location of the aluminosilicates will also affect the dissolution rate.

Based on the rankings in Table 4.5, the fly ashes' suitability for geopolymerisation in terms of particle size are as follows (listed from most to least suitable); Port Augusta, Bayswater, Collie, Tarong, Eraring.

Table 4.5 Fly ash particle size comparison. Underlined numbers represent ranking amongst the other fly ashes for each category.

Fly Ash	45 µm fineness (% passing)	20 µm fineness (% passing)	5 µm fineness (% passing)	Specific Surface Area (m^2cm^{-3})
Collie	83 4	61 3	27 2	1.56 2
Eraring	79 5	48 5	15 5	0.92 5
Tarong	84 2	60 4	19 4	0.99 4
Port Augusta	84 2	68 2	40 1	2.14 1
Bayswater	97 1	72 1	26 3	1.37 3

4.5 Morphology of the Fly Ashes

Fly ash morphology is known to affect bulk characteristics of the subsequent geopolymer (van Jaarsveld et al., 2003). Spherical morphology is beneficial to the synthesis of geopolymers as it allows for good workability at low liquids to solids mix ratios (Kong et al., 2007). Low water content is often desirable in high temperature applications as it reduces dehydration shrinkage during heating.

SEM analysis was done to assess fly ash morphology, looking specifically at the particle shape and the location of the aluminosilicate glass within the particles. Glass

that is encapsulated within an un-reactive crystalline material is not available for dissolution during geopolymerisation.

Figure 4-9 to Figure 4-13 give an indication of the typical particle morphology of the five fly ashes. The cross section of the fly ash particles in all samples showed a typical spherical morphology with the bulk of the particles appearing to be glassy (as identified by a smooth surface texture rather than angular crystalline shapes). A high degree of inter-particle and intra-particle heterogeneity was also observed. This has been observed previously (Hemmings and Berry, 1987) and is due to local variations in temperature and composition during the coal combustion and fly ash capture process.

All fly ashes also contained porous and non-spherical particles, though qualitatively it appeared that Tarong fly ash had a greater proportion than the other fly ashes. This morphology has the propensity to reduce the workability of geopolymer slurries made from this fly ash.

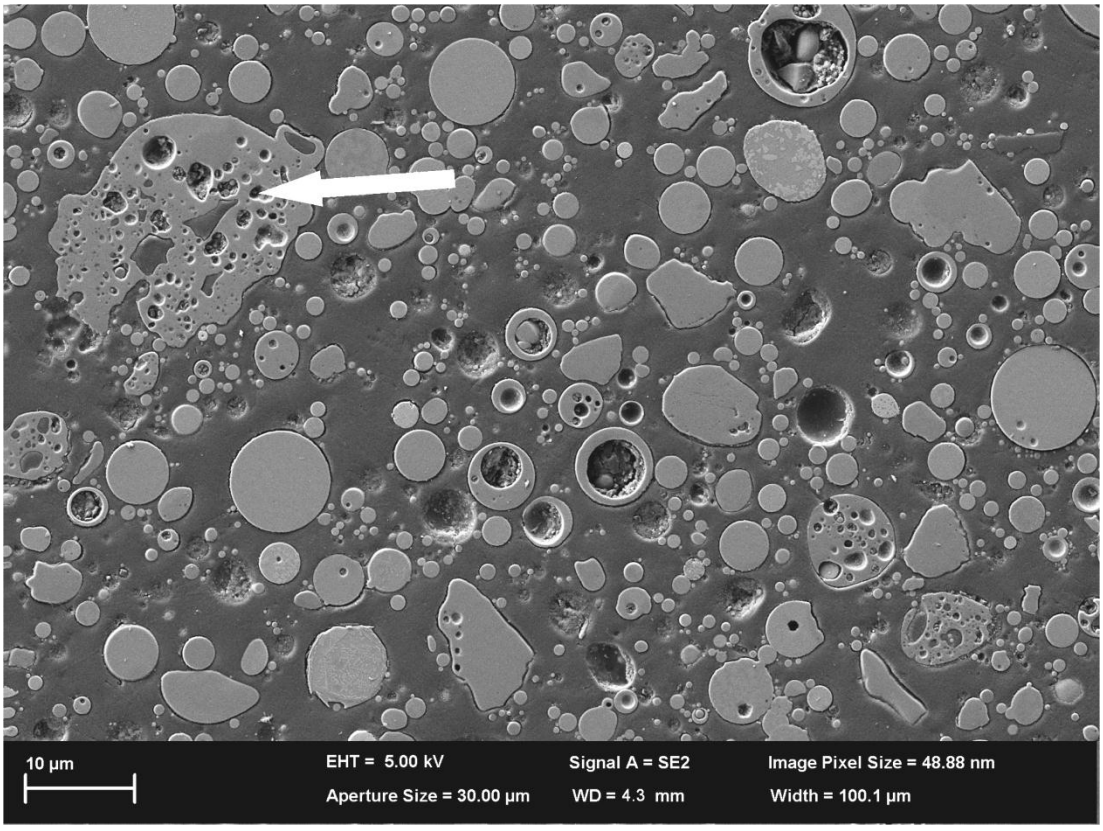

Figure 4-9 SEM micrograph showing the particle distribution for Collie fly ash. The arrow indicates a porous, irregular shaped particle.

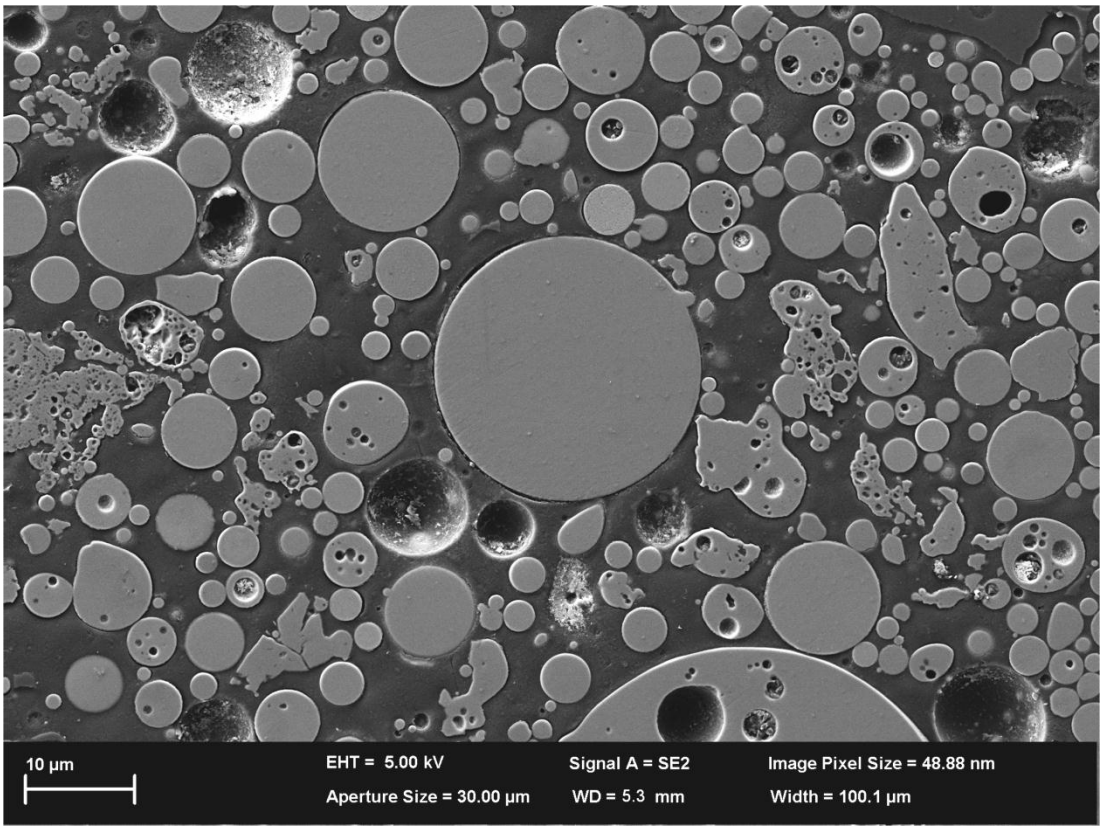

Figure 4-10 SEM micrograph showing the particle distribution for Eraring fly ash.

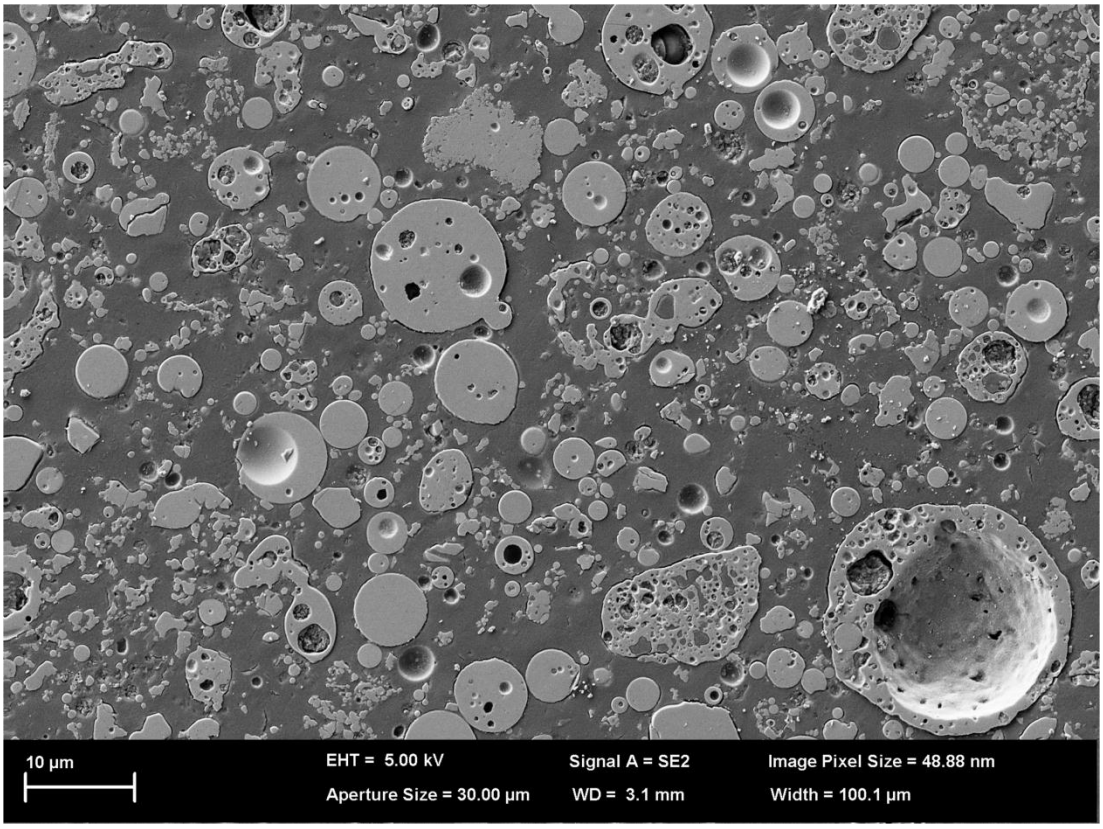

Figure 4-11 SEM micrograph showing the particle distribution for Tarong fly ash.

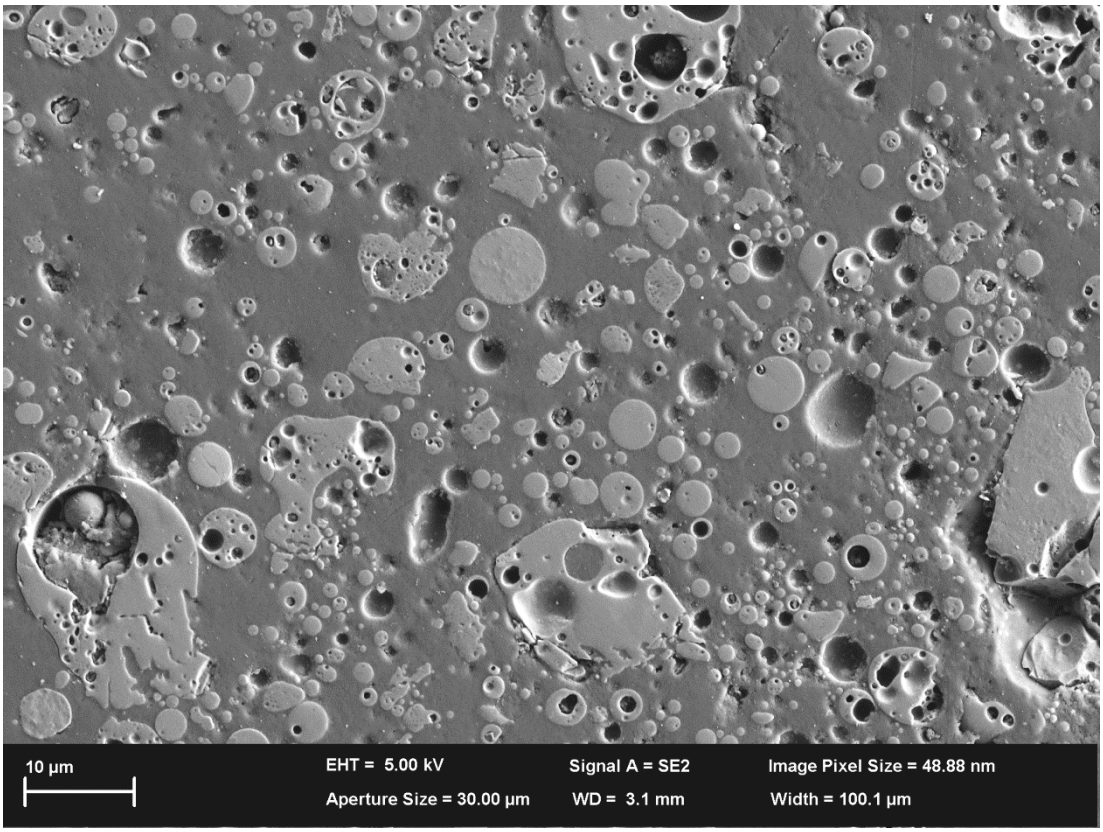

Figure 4-12 SEM micrograph showing the particle distribution for Port Augusta fly ash.

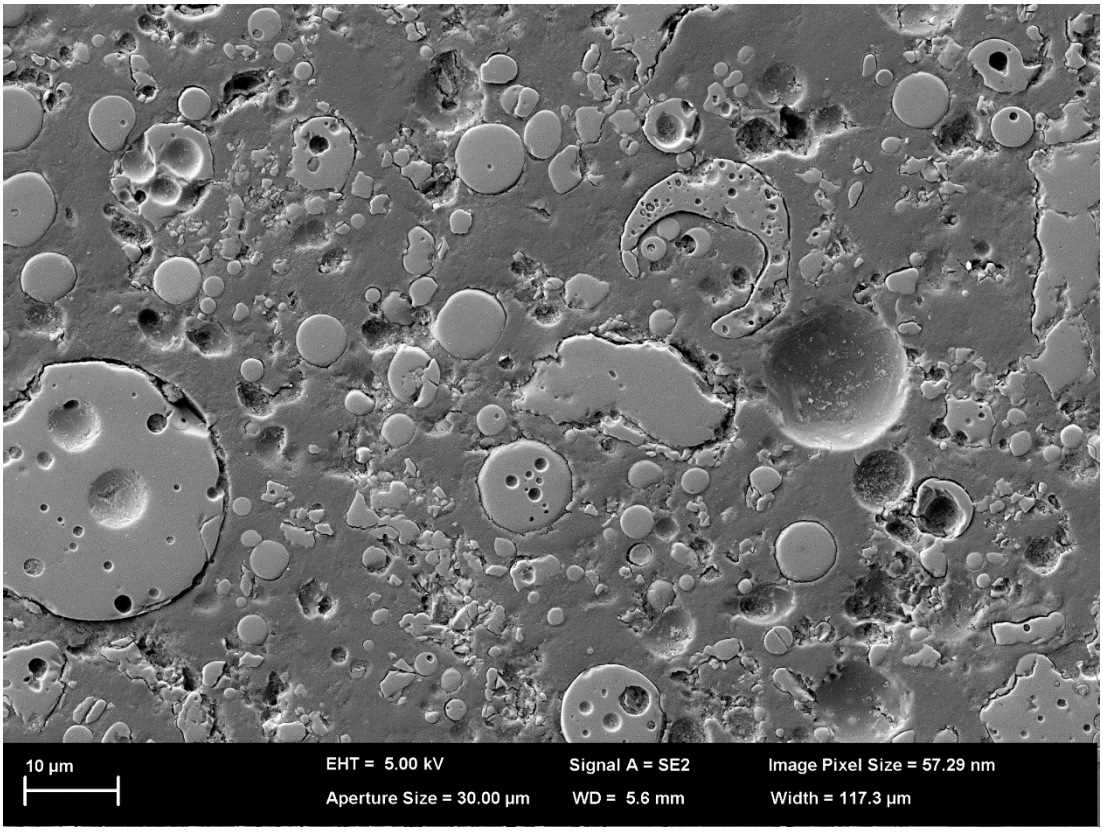

Figure 4-13 SEM micrograph showing the particle distribution for Bayswater fly ash.

Figure 4-14 to Figure 4-17 show examples of the various types of particles observed in the fly ashes. Many of the crystalline phases, detected in the XRD analysis, were observed in the SEM images by identifying characteristic morphology (such as needle shaped mullite crystals or dendritic iron structures) and using EDS for elemental identification. Quartz was typically observed as discrete particles, whereas iron and mullite phases were only observed within glassy particles. There were, however, some blocky crystalline structures observed in some of the glassy particles (Figure 4-14a) which were likely to be secondary quartz phases formed during the coal combustion process. This observation supports the finding of a secondary quartz population of smaller crystallite size identified previously by the XRD analysis (section 4.3). Iron structures were observed with a range of morphologies (Figure 4-14d & Figure 4-16). This was also in good agreement with the XRD analysis where a range of iron phases, including an amorphous phase, were identified.

Figure 4-15 shows an example of a particle that appeared glassy at low magnification, but at a higher magnification was clearly seen to contain a large amount of crystalline material. The needle shaped crystals were approximately 1 μm long and 100-200 nm wide, characteristic of mullite. Observations such as this confirm that even though fly ash particles appear predominantly glassy, they still contain a significant portion of crystalline material and hence the reason why the fly ashes were determined by QXRD to have up to 49 wt.% crystalline material.

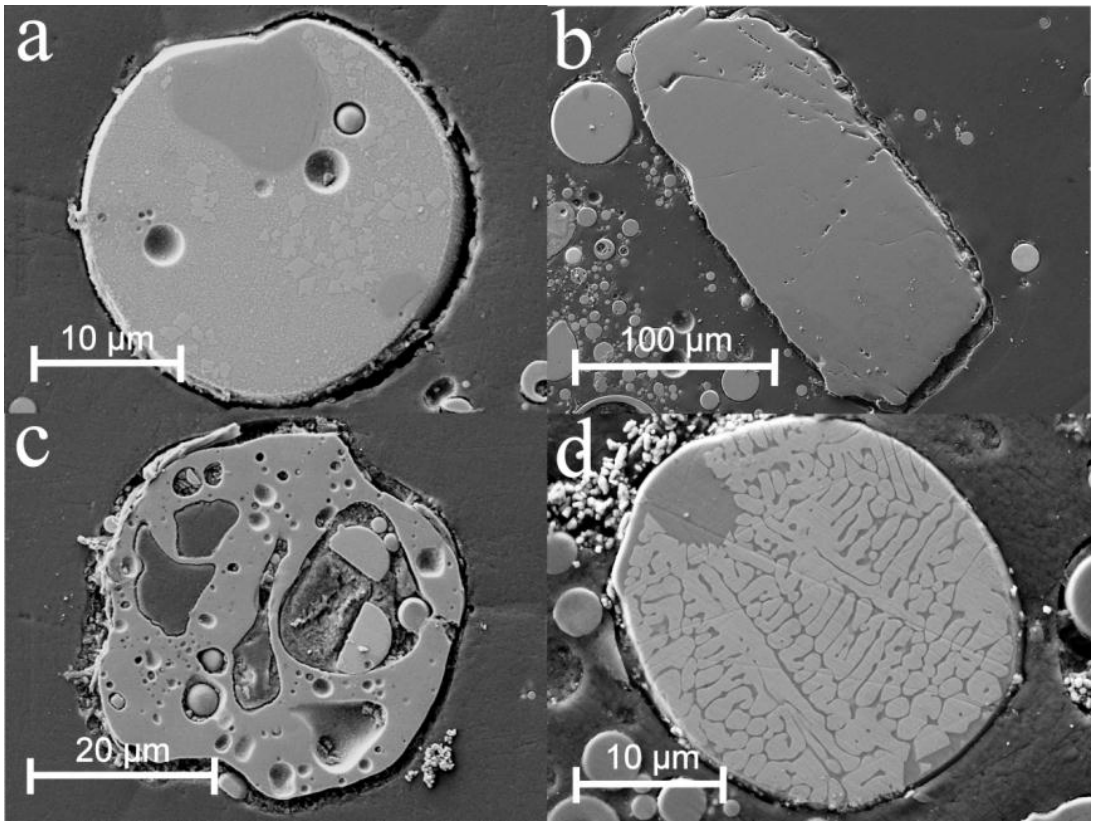

Figure 4-14 SEM micrograph showing different particles observed in Collie fly ash. a) fly ash particle containing blocky crystallites likely to be quartz. b) quartz particle. c) porous fly ash particle. d) fly ash particle containing iron.

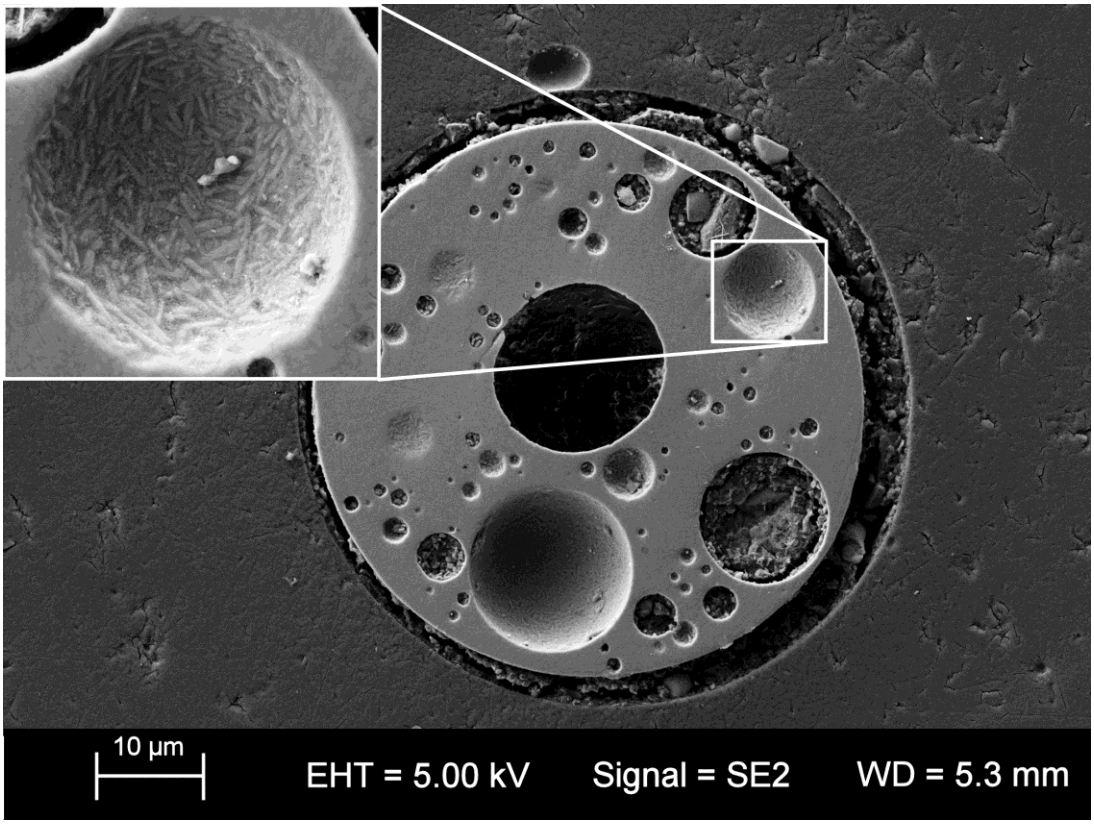

Figure 4-15 SEM micrograph of Eraring fly ash showing a fine mullite structure in a particle that appeared glassy at low magnification.

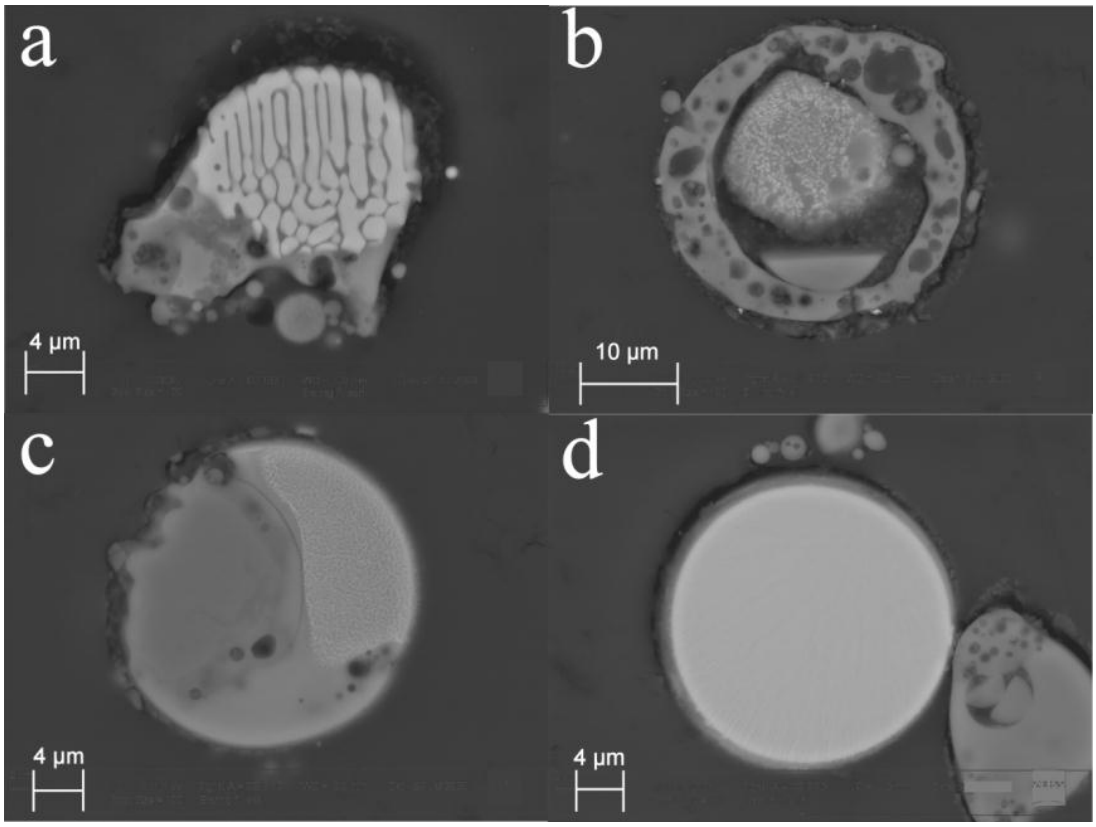

Figure 4-16 SEM micrographs illustrating the variation of iron structures in Eraring fly ash. a) brain like iron structure. b) fine cubic iron structure. c) dispersed iron structure. d) near solid iron structure.

Inter-particle porosity affects the density of fly ashes and resultant geopolymers. Inter-particle porosity is caused by gases released by combusting material and clays during the formation of the fly ash particle (Hemmings and Berry, 1987). Closed porosity was observed in particles from all of the fly ashes. Larger, irregular shaped particles contained a high degree of porosity (Figure 4-14c, Figure 4-17). This was most evident in Tarong fly ash which was observed to have a higher degree of irregular shaped particles. Cenospheres and plerospheres were also observed in all fly ashes.

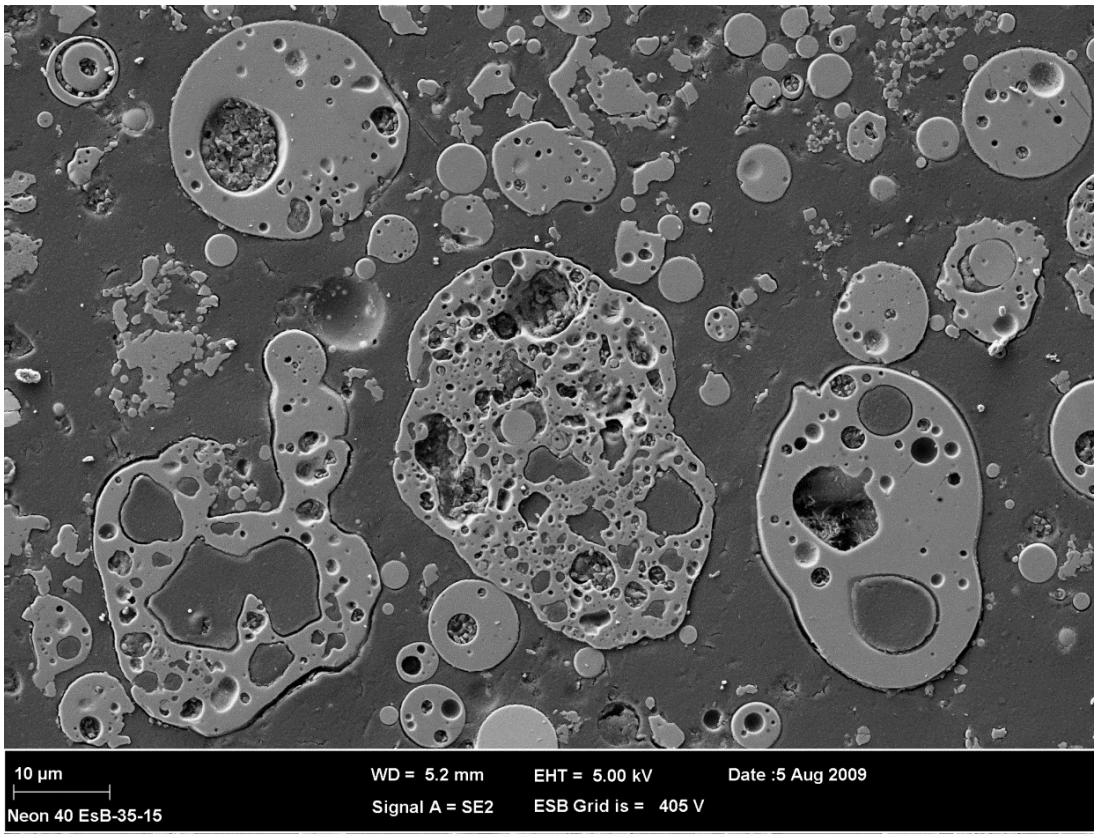

Figure 4-17 SEM micrographs showing a number of porous, non-spherical particles in Tarong fly ash.

4.6 Particle Density of the Fly Ashes

SEM investigations indicated that the particle density of the fly ashes was potentially different due to variations in the observed internal porosity and the concentration of iron. Particle density was measured with the assumption that the particles had closed porosity, as supported by SEM analysis. Table 4.6 details the density results.

Table 4.6 Particle density of each of the fly ashes. Oxide wt.% taken from XRF results.

Fly ash	Iron oxide (wt.%)	Average Particle Density (g cm^{-3})
Collie	13.2 (2)	2.40 (4)
Eraring	4.03 (2)	2.02 (3)
Tarong	0.64 (2)	2.00 (3)
Port Augusta	2.75 (2)	2.12 (2)
Bayswater	2.41 (2)	2.15 (4)

The density results in this study were in good agreement with results in the literature where the density of other ashes was measured between 2 and 2.5 g cm^{-3} (Matsunaga et al., 2002, Lee et al., 1999). As expected, the concentration of iron had a large influence on the average particle density of the fly ashes. Collie fly ash, with the most iron, had the highest density. However, iron was not the only influence on density as the variations in measured density were greater than what is expected by the differences in the iron concentration between fly ashes.

4.7 Conclusions

Fly ash particle size, morphology and the presence of crystalline phases will greatly influence the characteristics of the resulting geopolymer. It is additionally important to fully characterise fly ash that is to be utilised for geopolymers designed for high temperature applications, more so than if the fly ash was used to produce a geopolymer designed for ambient temperature environment. This is because fly ash contains a large portion of secondary phases, such as amorphous iron, which are likely to phase change upon elevated temperature exposure.

Quantitative phase analysis determined that only a portion of each of the fly ashes was available for geopolymerisation and that the reactive Si:Al ratio varied greatly between the fly ashes. Collie and Port Augusta fly ashes had relatively low amorphous Si:Al ratios (1.15 and 1.84, respectively) whereas the Eraring, Tarong and Bayswater fly ashes had high Si:Al ratios (4.98, 8.84 and 7.49, respectively). SEM investigations supported the XRD analysis as identified crystalline phases were observed in the fly ashes. An understanding of the location and morphology of each of the phases was also obtained by observing the interior structure of the fly ash particles in the SEM.

The spherical morphology is preferable to enable low water content geopolymer mixes (due to ease of workability) which is beneficial for reduced shrinkage at elevated temperatures. The presence of free quartz particles in the fly ashes may also

reduce the workability and has the potential to induce expansion cracking at elevated temperatures.

The average particle density of fly ash was found to be largely dependent on the concentration of iron. However, internal porosity was also identified as a contributing factor.

The characteristics of each of the five fly ashes presented in this chapter were used to design the geopolymers in this study and assist in interpreting the results in the following chapters.

Chapter 5
Thermal Properties of Fly Ash Geopolymers

"The science of today is the technology of tomorrow"

Edward Teller

5.1 Introduction

This chapter describes the characteristics of the geopolymers synthesised from the five fly ashes that were described in detail in chapter 4. Geopolymer properties are compared before and after exposure to 1000 °C in a furnace. The samples are characterised in terms of compressive strength, Young's modulus, density, thermal expansion and thermal conductivity.

Geopolymers will be referred to as either 'as-cured' or 'fired'. 'As-cured' denotes samples that were cured and then left in an ambient environment for at least 28 days prior to testing. 'Fired' denotes samples that were cured, left in an ambient environment for at least 28 days and then exposed to 1000 °C in a furnace.

The contents of this chapter formed the basis of the following publications;
Rickard, W. D. A., Williams, R., Temuujin, J. & van Riessen, A. (2011). Assessing the suitability of three Australian fly ashes as an aluminosilicate source for geopolymers in high temperature applications. *Materials Science and Engineering: A*, *528*(9), 3390-3397.

Rickard, W. D. A., Temuujin, J., & van Riessen, A. (2012). Thermal analysis of geopolymer pastes synthesised from five fly ashes of variable composition. *Journal of Non-Crystalline Solids*, 358(15), 1830-1839.

5.2 Compressive Strength

Geopolymeric materials designed for high temperature applications do not necessarily require high mechanical strength. For instance, high compressive strength is not essential for applications such as fireproof coatings or insulating panels, whereas it is required for structural applications such as columns and tunnels. A more significant property of a high temperature resistant material is its strength stability during and after high temperature exposure.

To get an indication of their suitability for synthesising high temperature resistant materials, the fly ashes in this study were used to produce a range of geopolymers and then these samples were subjected to elevated temperature exposure. Table 3.2 (chapter 3) details the elemental ratios of the geopolymer samples made in this study. The main compositional variable was the Si:Al ratio, which varied from 2.0 to 3.0. The other ratios were varied by a small amount in certain cases to achieve workable slurries during synthesis. Only the amorphous aluminosilicates, as determined by quantitative XRD (Table 4.8), were used in the compositional calculations.

Each of the fly ashes required the activating solution to contribute a portion of either the aluminium or silicon to the mixture. Collie and Port Augusta fly ashes had reactive Si:Al ratios less than 2 (1.2 and 1.9, respectively) and as such were activated with sodium silicate solutions to achieve the desired geopolymer Si:Al ratios of 2.0, 2.5 and 3.0. Eraring, Tarong and Bayswater fly ashes had reactive Si:Al ratios greater than 3 (5.0, 8.8 and 7.5, respectively) and as such were activated using sodium aluminate solutions to achieve the same set of compositional ratios.

Soluble amorphous silica was added to the activating solutions where the silica content of the available commercial sodium silicate solutions was insufficient. No soluble aluminate was used in this study; instead the amount of sodium aluminate solution was increased to increase the alumina content in mixes that required it. This forced the water content and Na:Al ratio in some samples, notably the Bayswater fly ash geopolymers, to be slightly higher than the rest of the samples. Figure 5-1 demonstrates the magnitude of the shift from reactive Si:Al ratio in the fly ashes to the designed Si:Al ratio in the geopolymers for each fly ash.

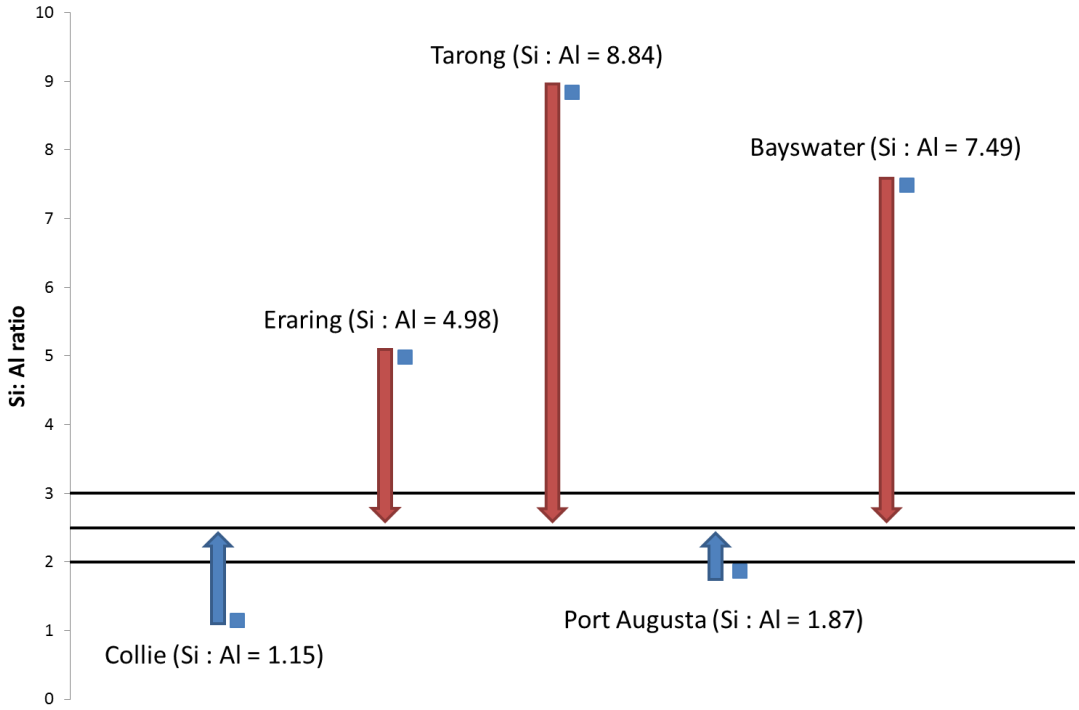

Figure 5-1 Fly ash reactive Si:Al ratios relative to designed ratios for the samples synthesised in this study.

The intention of the mix design was to produce geopolymers from each of the fly ash sources with comparable compositional ratios. It is noted that the samples will only achieve the designed compositional ratios if 100 % of the reactive components convert to the geopolymer phase. It is therefore accepted by the author that incomplete dissolution of the fly ash may occur in the samples in this study and accordingly the analyses of the results have taken this into account.

The as-cured compressive strengths varied greatly between the fly ashes (Table 5.1). Initial compressive strengths ranged from an impressive 143 MPa to a very low 6 MPa. Collie and Port Augusta fly ashes produced the strongest samples. In particular, Collie fly ash samples with a Si:Al of 2.0 and Port Augusta fly ash with a Si:Al ratio of 2.5 produced samples with compressive strengths over 100 MPa. Tarong and Eraring fly ashes produced moderate strength samples, whereas Bayswater fly ash produced comparatively weak geopolymers. As a general trend, the as-cured compressive strengths varied with Si:Al ratio according to 2.0 & 2.5 > 3.0. With the exception of Bayswater fly ash geopolymers, the compressive strength of all samples was at least 25 MPa, sufficient for most high temperature applications where thermal resistance rather than mechanical strength is most critical.

Table 5.1 Compressive strength of geopolymers made from each of the fly ashes. Note: The sample listed as '<<1' indicates that it was too weak to be tested. Note: The data for Collie, Eraring and Tarong fly ashes was published in (Rickard et al., 2010). Uncertainties in brackets.

Fly ash	Si:Al	28 day compressive strength (MPa)	Compressive strength after firing to 1000 °C (MPa)	% of as-cured strength
Collie	2.0	128 (9)	24 (9)	19 %
	2.5	53 (10)	15 (4)	29 %
	3.0	29 (3)	<< 1	0 %
Eraring	2.0	31 (2)	78 (11)	249 %
	2.5	33 (8)	132 (19)	396 %
	3.0	28 (5)	126 (20)	457 %
Tarong	2.0	26 (2)	13 (8)	49 %
	2.5	26 (4)	73 (17)	277 %
	3.0	25 (2)	99 (24)	396 %
Port Augusta	2.0	82 (3)	44 (3)	54 %
	2.5	143 (22)	17 (1)	12 %
	3.0	67 (3)	6 (1)	9 %
Bayswater	2.0	10 (1)	27 (4)	267 %
	2.5	6 (1)	21 (3)	320 %
	3.0	6 (1)	29 (3)	455 %

It is believed by the author that the variation in compressive strength between the geopolymer mixes was largely due to differing levels of geopolymerisation (or degree of reaction) between the mixes. The greater the conversion of the amorphous aluminosilicates from the fly ash into geopolymer gel, the closer the sample was to achieving the deigned compositional ratios, and hence the stronger the sample. The degree of conversion of fly ash glass to geopolymer gel was analysed by SEM with results presented in chapter 6.

Bayswater fly ash geopolymers were much weaker than the rest of the samples with a maximum strength of 10 ± 1 MPa. It is thought that the low strengths of these samples were due to a low level of geopolymerisation, likely due to the low amount of reactive alumina in the fly ash (6.47 wt.%) and higher water content of the mixes.

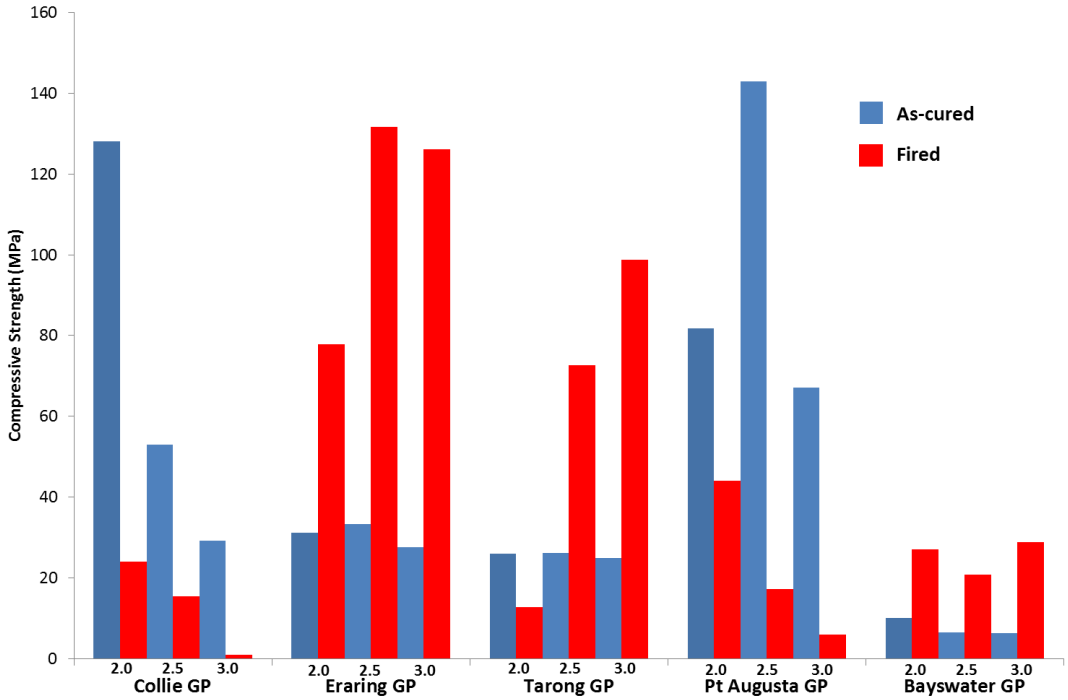

Figure 5-2 Compressive strength before and after firing to 1000 °C for geopolymers made from each of the fly ashes.

The compressive strength of geopolymers exposed to 1000 °C is also included in Table 5.1. The variation in strength before and after firing is further demonstrated in Figure 5-2. Post firing compressive strengths varied dramatically between the fly ash precursors. In general, Eraring, Tarong and Bayswater fly ash geopolymers exhibited compressive strength increases after firing whereas Port Augusta and Collie fly ash geopolymers exhibited strength losses. Eraring fly ash geopolymers had the most significant strength gains with up to a 5 fold increase in strength. Geopolymers with initial compressive strengths greater than 40 MPa exhibited strength losses after firing, whereas samples with lower initial compressive strength exhibited strength gains. Similar effects have been observed to occur in OPC based materials, where high strength mixes have been found to be much more susceptible to strength losses after firing than low strength mixes (Li et al., 2004).

Post firing compressive strengths were observed to be influenced by the Si:Al ratio in the geopolymer and the iron content of the fly ash precursor. Collie fly ash geopolymers exhibited the greatest strength loss after exposure. Visual inspection of the Collie fly ash samples after firing revealed a colour change from grey to red and a high degree of surface cracking (images and further details of the colour change are

included in chapter 6). This has been observed previously (Rickard et al., 2010) and is characteristic of the oxidation of the iron from the precursor fly ash, causing cracking and subsequent strength losses. Port Augusta fly ash geopolymers also exhibited significant compressive strength losses though there was only 2.75 wt.% of iron oxides in the fly ash compared to the 13.2 wt.% in Collie fly ash. Additionally, Eraring geopolymers with an iron oxide content of 4.0 wt.% in the fly ash exhibited strength gains. This suggests that in at least the samples with low concentrations of iron oxides, other strength reducing structural changes are occurring that have a greater impact on the samples than the presence of the iron. Microstructural changes such as dehydration damage, crystallisation and shrinkage cracking are likely to contribute to compressive strength losses after firing in these samples.

For samples that exhibited strength gains, the higher the Si:Al ratio of the geopolymer, the greater the percentage strength gain after high temperature exposure. Eraring geopolymers in particular exhibited exceptional strength increases after firing. The Tarong geopolymers with Si:Al of 2.5 and 3.0 and all of the Bayswater geopolymers also increased in strength. It was also noted that the fired geopolymers had wider strength variability and thus a corresponding larger uncertainty than the as-cured geopolymers. This was indicative of cracks or flaws of varying prominence introduced by the firing affecting the load bearing capacity of the samples.

5.2.1 Young's Modulus

The Young's modulus of the tested samples provided information about the stiffness of the samples. The Young's modulus was generally observed to increase with increasing compressive strength (Table 5.2). This indicates that the stronger samples were also 'stiffer' which was expected.

Table 5.2 Young's moduli of geopolymers made from each of the fly ashes. Note: The sample listed as '<<1' indicates that it was too weak to be tested.

Fly ash	Si:Al	Young's modulus (GPa)	Young's modulus after firing to 1000 °C (GPa)	% of as-cured Young's modulus
Collie	2.0	3.73 (6)	2.04 (36)	55 %
	2.5	1.81 (10)	1.54 (15)	85 %
	3.0	0.30 (3)	<< 1	0 %
Eraring	2.0	1.92 (8)	3.41 (10)	177 %
	2.5	1.47 (12)	3.69 (32)	252 %
	3.0	1.67 (8)	3.83 (27)	229 %
Tarong	2.0	1.76 (2)	1.08 (12)	61 %
	2.5	1.68 (13)	3.30 (9)	196 %
	3.0	1.69 (17)	3.40 (37)	201 %
Port Augusta	2.0	3.47 (5)	2.98 (19)	86 %
	2.5	3.29 (18)	1.99 (19)	60 %
	3.0	2.37 (39)	0.92 (16)	39 %
Bayswater	2.0	1.12 (15)	2.10 (23)	176 %
	2.5	0.77 (13)	1.80 (15)	233 %
	3.0	0.96 (5)	2.44 (34)	254 %

It is difficult to compare the results in this study with others in the literature as very few studies have reported the Young's modulus of fly ash geopolymers and those that have were either concerned with concretes or composites rather than fly ash geopolymer pastes. Comparisons with studies on metakaolin geopolymer pastes indicate that the samples in this study generally had a lower Young's modulus of the order of 2 - 5 GPa (Duxson et al., 2005, Kirshner and Harmuth, 2004). This was not unexpected as the lower homogeneity of fly ash geopolymers, due to the greater presence of secondary phases, is likely to reduce the stiffness.

Figure 5-3 compares the stress-strain curves for a sample with a relatively high Young's modulus to a sample with a low Young's modulus. It can be seen the Port Augusta 2.5 sample had an extended period of elastic deformation up until the point of failure with no evidence of plastic deformation. Conversely, the Collie 3.0 sample

with a very low Young's modulus had a brief period of elastic deformation before an extended period of plastic deformation.

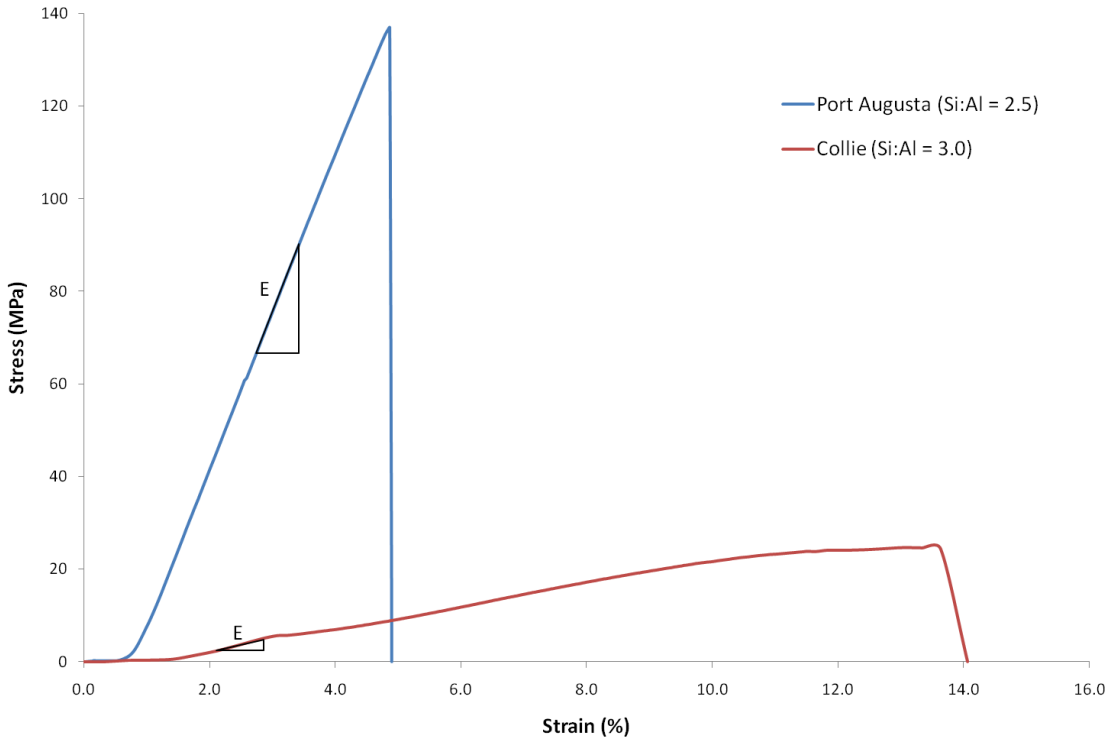

Figure 5-3 Stress – Strain curve for as-cured Port Augusta 2.5 and Collie 3.0 geopolymers showing the variation in failure behaviour under load. The right angled triangle denotes the location on the curve where the Young's modulus was determined (i.e. region of elastic deformation).

Post firing Young's modulus results were commensurate with the compressive strength changes after firing. Most samples that gained exhibited compressive strength gains after firing also exhibited a higher Young's modulus, though the percentage change was less. Graphing the Young's modulus versus the compressive strength for each sample (Figure 5-4) revealed some additional information. Comparing the trend lines for the as-cured and fired results indicates that the samples had a higher Young's modulus after firing across the compressive strength range. Thus, for a given compressive strength the samples were stiffer after firing. This effect was more pronounced in samples with compressive strengths less than 70 MPa. It is acknowledged that the fit of the trend lines are tenuous and as such these findings are regarded as indicative only.

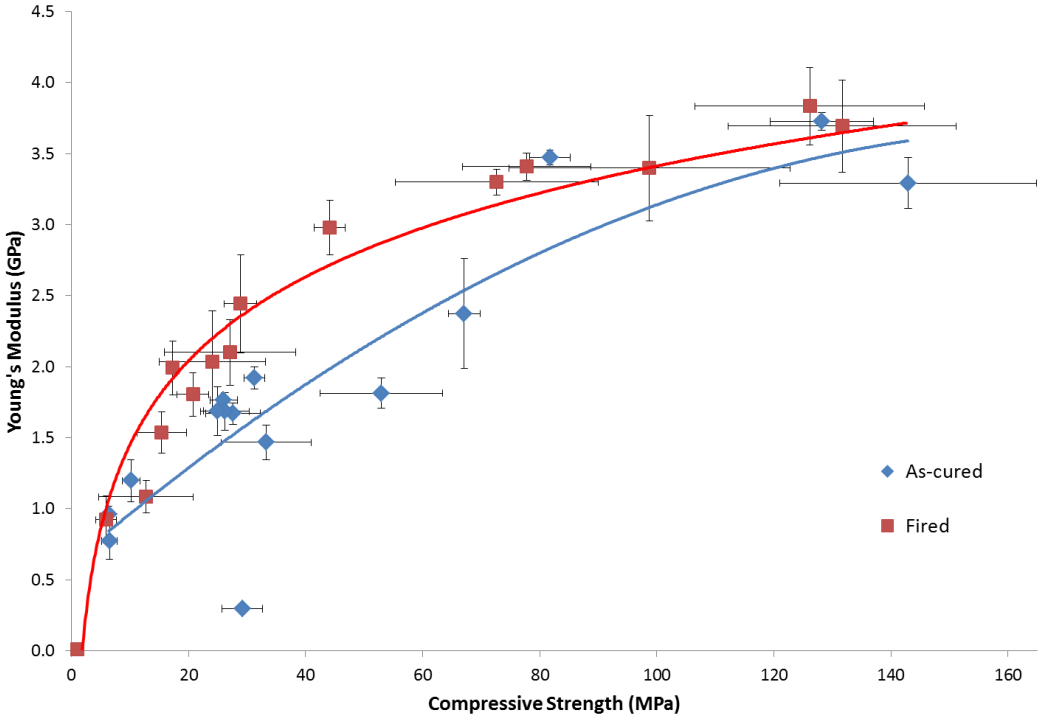

Figure 5-4 Comparison of Young's modulus versus compressive strength before and after firing to 1000 °C.

5.2.2 Effect of the Activating Solution

The compressive strength results suggest the post firing strength retention could be related to the activating solution used to synthesise the sample. Collie and Port Augusta fly ashes had reactive Si:Al ratios less than 2 and as such were activated with sodium silicate solutions to achieve the desired geopolymer Si:Al ratios of 2.0, 2.5 and 3.0, producing high strength geopolymers. Eraring, Tarong and Bayswater fly ashes had reactive Si:Al ratios greater than 3 and as such were activated using sodium aluminate solutions to achieve the same set of compositional ratios, producing geopolymers with low to moderate compressive strengths. The post firing compressive strength testing of the geopolymers produced opposite results where the sodium aluminate activated samples exhibited moderate to high compressive strengths and the sodium silicate activated samples exhibited low compressive strengths.

The amount of the silicon or aluminium in the final geopolymer added via the activating solution was found to influence the compressive strength of the samples

before and after firing. In the sodium silicate activated samples it was found that increasing the amount of silicon added via the activating solution led to a reduction in as-cured and post firing compressive strengths. It is possible that the samples with a large portion of Si added via the activating solution did not incorporate all the added material into the geopolymer structure, reducing the strength and leaving residual silicates. The amount of aluminium added via the activating solution had little effect on the as-cured compressive strengths in the sodium aluminate activated samples. This may be due to the fact that the concentration of aluminium in the activating solution didn't change between mixes (as no soluble alumina was used), only the amount of solution varied between samples.

After firing, however, the amount of aluminium (and silicon) in the activating solution was observed to influence the compressive strength in the samples. Figure 5-5 compares the post firing compressive strengths as a percentage of the room temperature strength with the percentage of Si or Al introduced via the activating solution. The trend lines in Figure 5-5 suggest that reducing the amount of Si or Al added via activating solution improved the compressive strength gain / retention after firing. The effect was more pronounced in the sodium aluminate activated samples which exhibited strength gains of almost five fold where 40 % of the total Al was added via the activating solution. Given there is no indication that the trend has reached a maxima, it is likely that lower Al concentrations would result in even greater strength increases, though this would require high Si:Al ratio samples which may have lower as-cured compressive strengths.

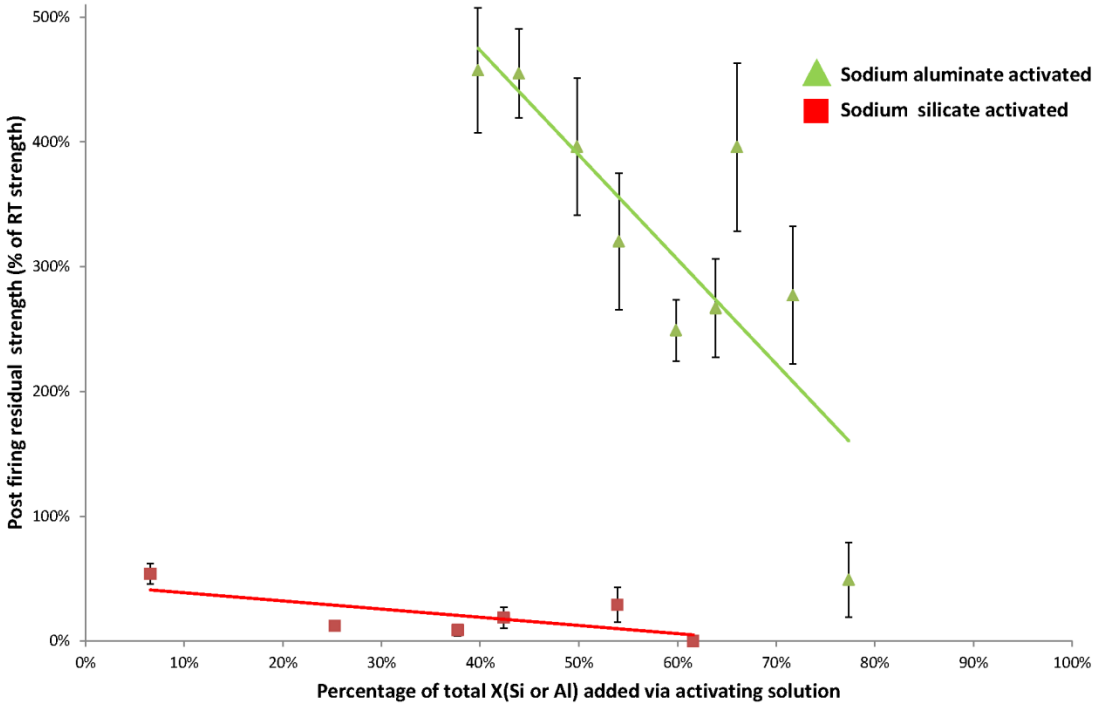

Figure 5-5 Comparing the effect of the amount of the X (Si or Al) added via the activating solution on the post firing compressive strengths (as a percentage of room temperature strengths).

5.3 Mass Loss on Firing

The mass loss of each sample upon to exposure to 1000 °C is presented in Table 5.3. Mass loss at elevated temperatures is primarily due to the evaporation of free and chemically bound water from the geopolymer. The combustion of the residual carbon in the fly ash will also cause mass loss though this is likely to be minimal as the concentration (as determined by LOI, Table 4.2) was very low, nominally less than 1 wt.% of the geopolymer. Mass gain of the order of 1 wt.% due to the oxidation of iron species in fly ash geopolymers that has been previously reported (Rickard et al., 2010) will also contribute to the measured mass change, though this will also be a minor contribution.

The measured mass loss after firing of the samples in this study ranged from 10 to 17 wt.%. As the other effects mentioned above are likely to contribute to mass changes of less than 1 wt.%, it can be assumed that the bulk of this mass loss was due to the dehydration of water.

Water is initially present in the geopolymers as a component of the activating solution during synthesis. The samples in this study were made with between 18 and 27 wt.% water, with the sodium aluminate activated samples generally having more water than the sodium silicate activated samples. After curing and demoulding pore water dehydrates at ambient temperatures until equilibrium with the surrounding atmosphere is achieved. After this period, given a constant humidity, the concentration of water in the sample should remain constant. Upon exposure to 1000 °C, all the remaining water in the geopolymer will dehydrate. Assuming that all mass loss is due to the dehydration of water, then the mass lost on firing can be equated to the equilibrium water content of the geopolymer. Water loss at ambient conditions can also be calculated by subtracting the mass loss on firing from the initial water content during synthesis (Table 5.3).

Table 5.3 Mass loss on firing for each of the samples with comparisons to water content.

Fly ash	Si:Al	Initial water content (wt.%) ± 0.05	Mass loss on firing (wt.%) ± 0.1	Ambient dehydration (calculated) (wt.%) ± 0.15
Collie	2.0	17.63	14.07	3.56
	2.5	18.35	11.68	6.67
	3.0	25.21	13.07	12.14
Eraring	2.0	23.00	13.04	9.96
	2.5	18.47	12.04	6.43
	3.0	20.93	11.48	9.45
Tarong	2.0	26.03	16.98	9.05
	2.5	22.51	14.80	7.71
	3.0	22.82	13.33	9.49
Port Augusta	2.0	18.40	14.27	4.13
	2.5	17.94	12.92	5.02
	3.0	20.65	10.96	9.69
Bayswater	2.0	26.83	14.09	12.74
	2.5	26.57	16.33	10.24
	3.0	27.73	10.08	17.65

For all samples except the Bayswater 3.0 geopolymer, the bulk of the dehydration occurred on firing with only about a third of the original water dehydrating at

ambient conditions (Figure 5-6). The samples that exhibited the lowest ambient dehydration (i.e. retained the bulk of their water after curing), such as the Collie 2.0 and Port Augusta 2.0 samples, also exhibited high compressive strengths (Table 5.1). This suggests that their structures were less permeable as the sample required elevated temperatures to release the water. Conversely, the samples that had a high portion of dehydration at ambient conditions, such as the Bayswater geopolymers, had low compressive strengths. This suggests that their structures were much more permeable.

There was no apparent correlation of mass loss (dehydration) after firing to strength changes after firing. This suggests that the amount of water that dehydrates does not determine the strength variation. Thus the dehydration of a small amount of water was as likely to damage the geopolymer structure as it exited the sample as that of a large amount of water.

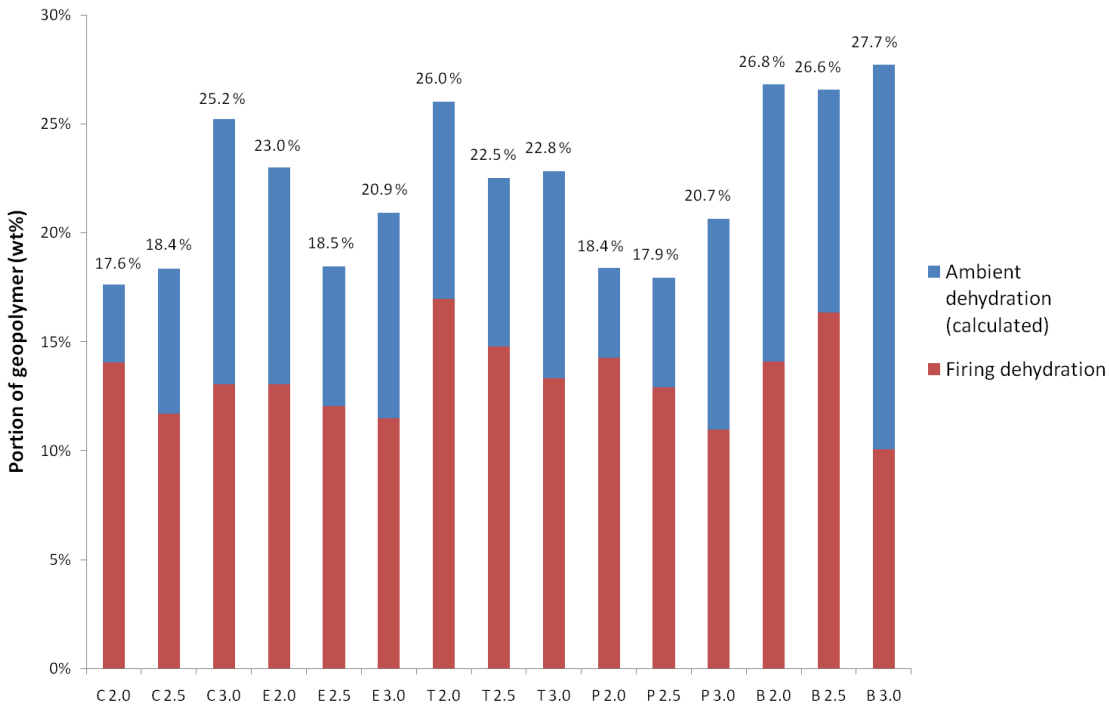

Figure 5-6 Total water content for each sample (number at the top of each column) as well as the proportion due to dehydration at ambient and upon firing.

5.4 Density Evolution

Viscous flow of aluminosilicates and subsequent sintering in geopolymers at high temperatures is known to increase their density after firing (Duxson et al., 2007b). Other effects, such as the dehydration of water in the sample and the swelling of the high silicate phases (see section 5.5) will reduce geopolymer density by reducing the mass or expanding the volume. Thus the measured changes in density after high temperature exposure are a convolution of the simultaneous effects. Density is known to affect the mechanical strength of geopolymers (Wang et al., 2005) and as such its assessment provides useful additional insight into the thermally induced changes of samples after heating to 1000 °C.

Table 5.4 lists the density of the samples in this study before and after firing to 1000 °C. The as-cured densities were observed to be consistent with the compressive strength results. The lower strength, sodium aluminate geopolymers (from Eraring, Tarong and Bayswater fly ashes) were measured to have densities ranging from 1.51 to 1.71 g cm^{-3}, whereas the higher strength sodium silicate activated geopolymers (from Collie and Port Augusta fly ashes) had higher densities, ranging from 1.86 to 2.11 g cm^{-3}. The density results for Eraring, Tarong and Bayswater fly ashes were consistent with a comparable study by Andini et al. (2008) that reported the density of fly ash geopolymers to be between 1.48 and 1.74 g cm^{-3}.

The post firing densities were consistent with the measured changes in compressive strengths after firing, though the percentage change was much smaller. For example, the densities of the Port Augusta fly ash geopolymers only reduced by a few per cent after firing, while the compressive strengths after firing reduced by more than 50 %. This suggests that other strength reducing (but not density reducing) effects, such as cracking, were more dominant in these samples. Bayswater fly ash geopolymers were once again an anomaly with a slight reduction in density even though they exhibited increased post firing compressive strengths.

There was no obvious trend of initial water content with changing as-cured densities, though there was some correlation of decreasing density after firing with increasing

initial water content. This was expected as during firing all the water in the sample evaporates leaving voids which reduces the density. Thus samples with a greater concentration of water should exhibit a greater density reduction upon firing, though this effect is convoluted with other effects such as shrinkage of the geopolymer gel.

Table 5.4 Density of the geopolymers before and after exposure to 1000 °C.

Fly ash	Si : Al	Cured density ($g\ cm^{-3}$)	Post firing density ($g\ cm^{-3}$)	% of cured density
Collie	2.0	1.99 (5)	1.69 (6)	85 %
	2.5	2.11 (10)	1.56 (4)	74 %
	3.0	2.04 (7)	1.45 (3)	71 %
Eraring	2.0	1.58 (6)	1.67 (3)	106 %
	2.5	1.61 (12)	1.71 (4)	106 %
	3.0	1.57 (4)	1.71 (3)	109 %
Tarong	2.0	1.55 (7)	1.55 (1)	100 %
	2.5	1.58 (5)	1.64 (2)	104 %
	3.0	1.51 (5)	1.80 (2)	119 %
Port Augusta	2.0	1.86 (8)	1.80 (3)	97 %
	2.5	1.89 (7)	1.86 (1)	98 %
	3.0	1.86 (4)	1.75 (17)	94 %
Bayswater	2.0	1.70 (6)	1.51 (2)	89 %
	2.5	1.71 (16)	1.58 (11)	93 %
	3.0	1.68 (2)	1.68 (4)	100 %

5.5 Thermal Expansion

Figure 5-7 to Figure 5-11 show the thermal expansion versus temperature plots for the geopolymers synthesised from each of the fly ashes. In each plot there is the thermal expansion curve for geopolymer Si:Al ratios of 2.0, 2.5 and 3.0. A marked difference can be observed between the different fly ashes and also in some cases, with changing Si:Al ratio. Eraring, Bayswater and to a slightly lesser extent Tarong fly ash geopolymers exhibit impressive thermal stability up to almost 800 °C by having minimal dimensional change after the initial shrinkage due to the dehydration of free water (noted by a shrinkage of 1 - 2 % between 50 °C and 200 °C). The Si:Al

ratio had very little effect on the thermal shrinkage of the samples in this study which was consistent with results obtained by Duxson et al. (2007c) who found that the Si:Al ratio had little effect on the thermal shrinking of metakaolin geopolymers of Si:Al ≥ 1.65. Above 800 °C, all samples exhibited a sharp shrinkage indicating the onset of sintering and densification.

Collie and Port Augusta geopolymers exhibited far less dimensional stability upon heating. Notably, Collie fly ash exhibited increased thermal expansion with increasing Si:Al ratio. The activating solutions to make these geopolymers contained additional silicate as they had low Si:Al ratios in their fly ashes. It is possible that some of the activating solution remained unreacted or only partially reacted during the formation of the geopolymer leaving residual silicates in the sample. The thermal expansion observed in the Collie fly ash geopolymer samples is consistent with the swelling of unreacted silicates, with the magnitude proportional to the amount of added silica. Thermal expansion in geopolymers due to the swelling of high silicate secondary phases has been observed previously in the literature (Fletcher et al., 2005, Provis et al., 2009, Temuujin et al., 2010). There was considerably less swelling in the Port Augusta samples than the Collie samples due to the much lower concentration of added silica in the activating solutions (as the Si:Al ratio of the Port Augusta fly ash glass was closer to the target Si:Al range).

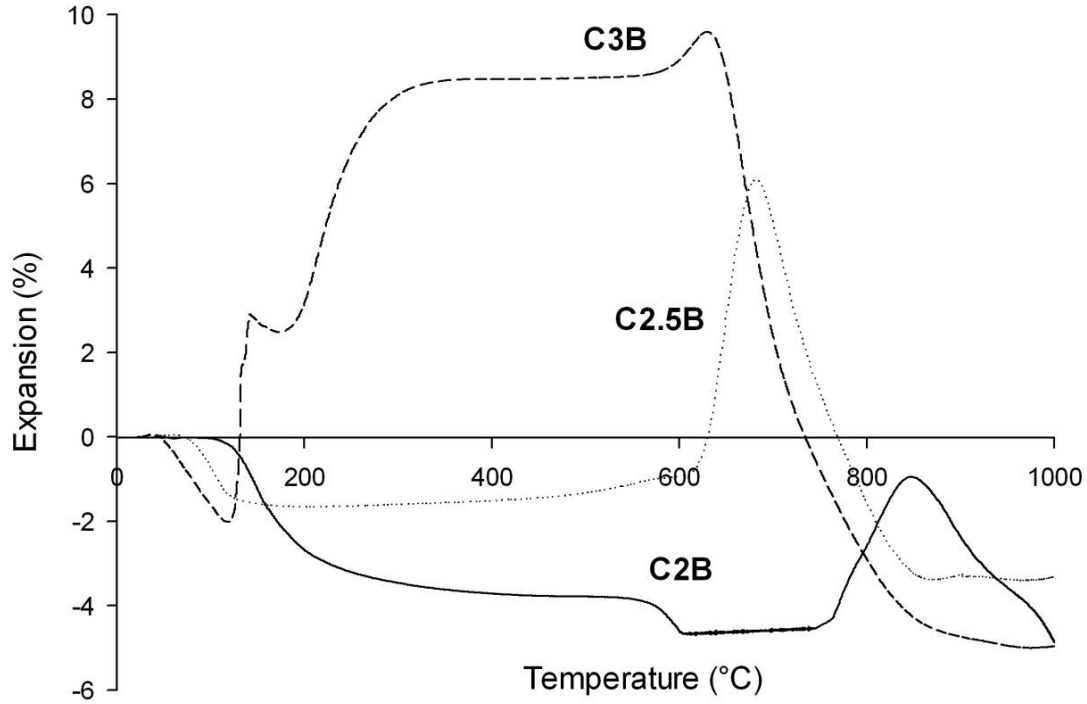

Figure 5-7 Thermal expansion of geopolymers made from Collie fly ash with Si:Al = 2.0, 2.5 and 3.0. The flat region between 600 and 750 °C in the curve for sample C2B is due to sharp shrinkage caused by a temporary loss of contact with the dilatometers push rod.

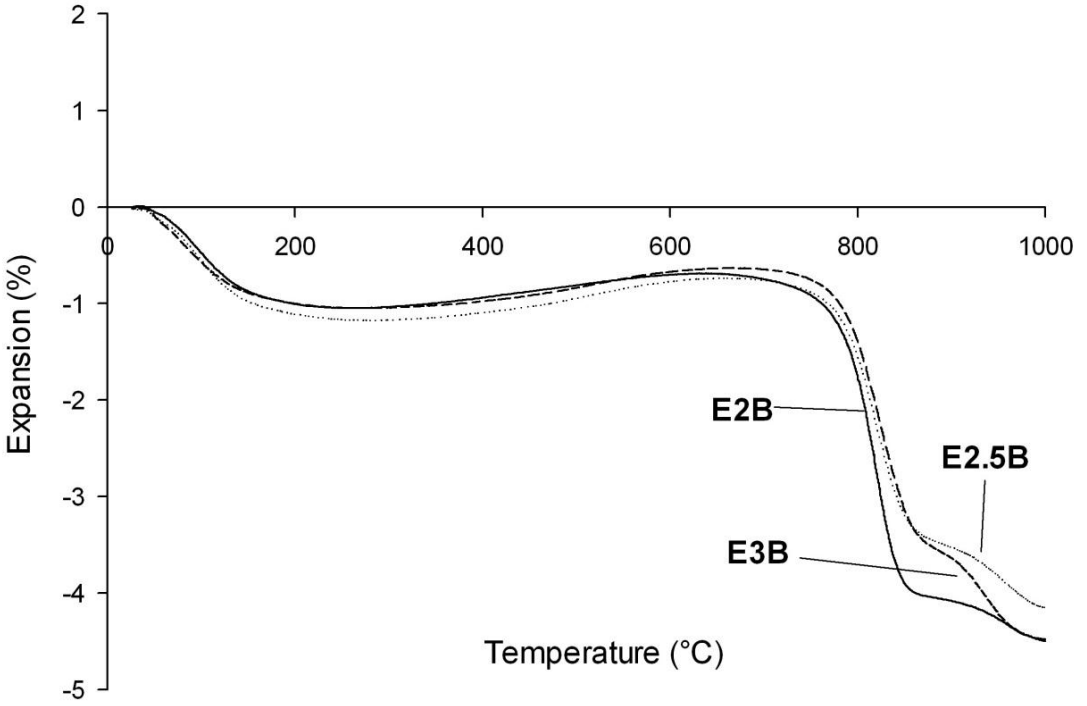

Figure 5-8 Thermal expansion of geopolymers made from Eraring fly ash with Si:Al = 2.0, 2.5 and 3.0.

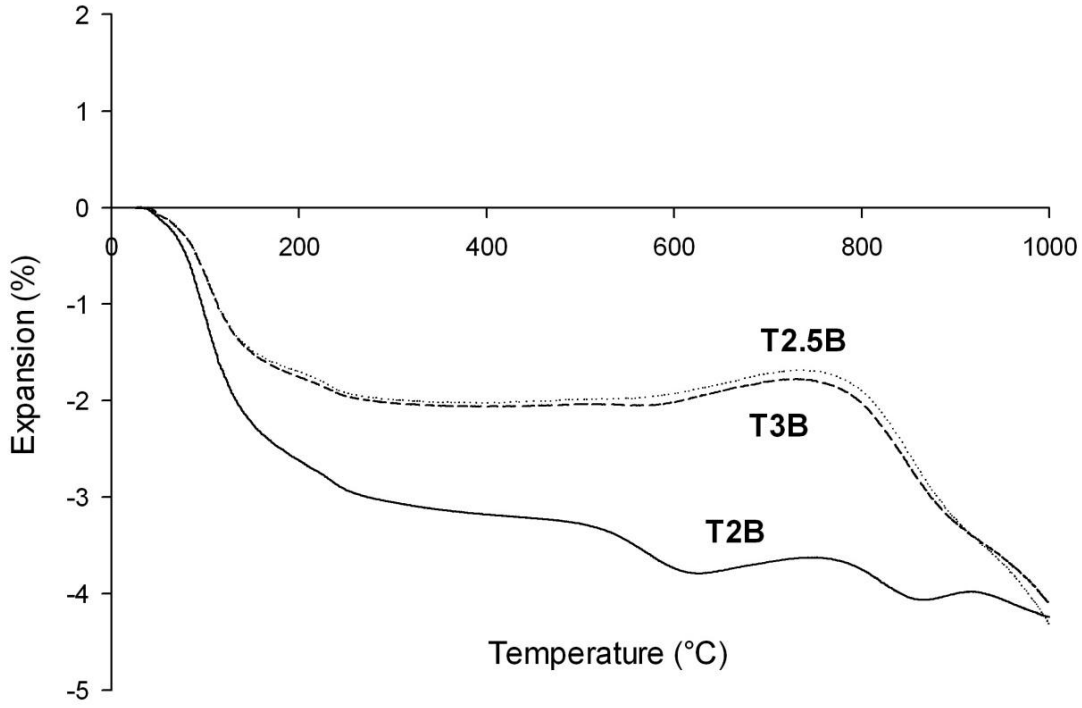

Figure 5-9 Thermal expansion of geopolymers made from Tarong fly ash with Si:Al = 2.0, 2.5 and 3.0.

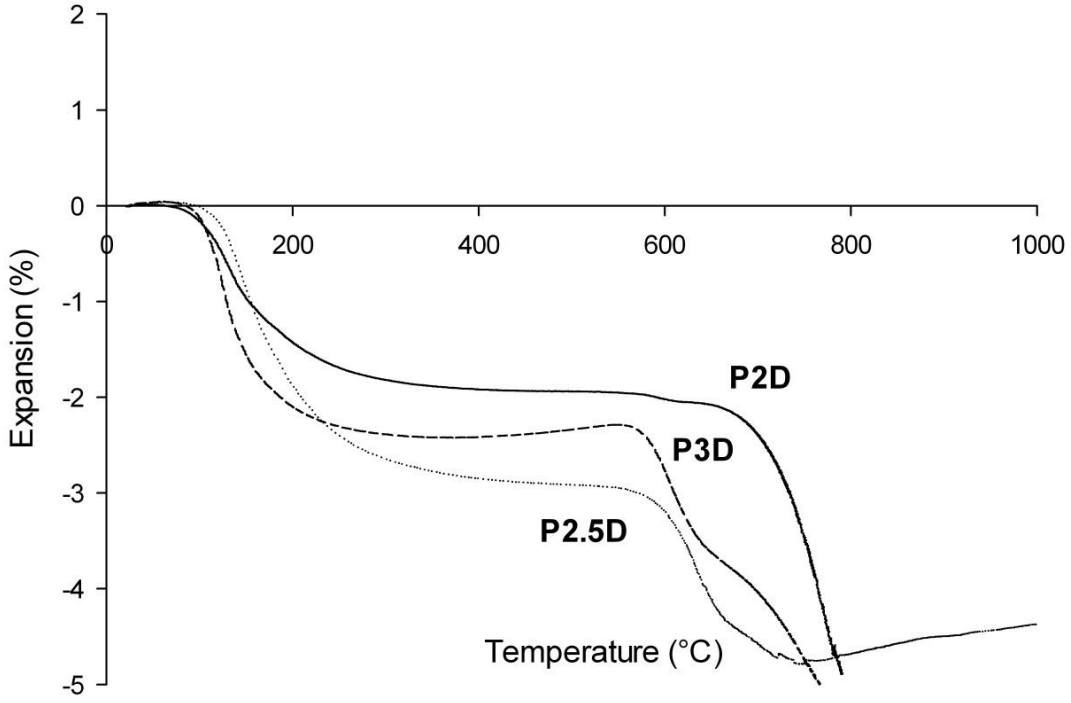

Figure 5-10 Thermal expansion of geopolymers made from Port Augusta fly ash with Si:Al = 2.0, 2.5 and 3.0.

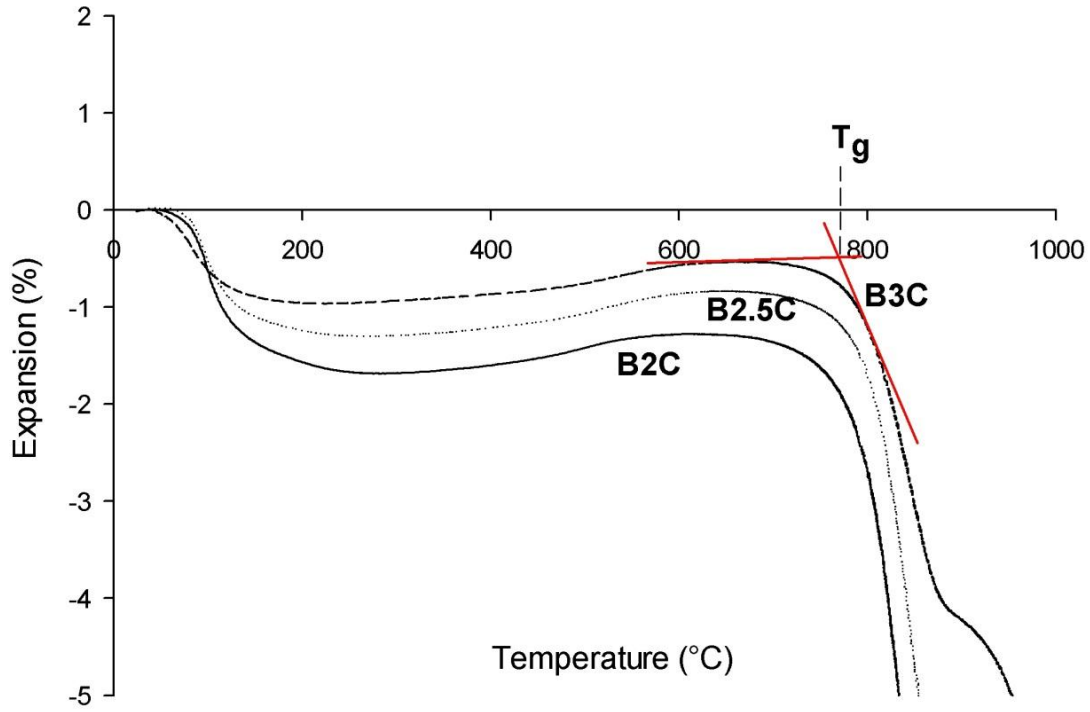

Figure 5-11 Thermal expansion of geopolymers made from Bayswater fly ash with Si:Al = 2.0, 2.5 and 3.0. The red lines demonstrate the method used to identify transition temperatures (see text for details).

Rahier et al. (2007) proposed that the major shrinkage event that generally occurs between 500 °C and 800 °C is an indication of the glass transition temperature (T_g) of the geopolymer. The T_g (otherwise known as the softening temperature or onset temperature of densification) of each sample was identified as the intersection of the extended lines following the slope before and after the major shrinkage event as illustrated by the red lines in Figure 5-11. This method for determining the glass transition temperature of geopolymers has been previously used by Pan and Sanjayan (2011). Similarly, the temperature for the onset of dehydration shrinkage (T_s) and the temperature of the expansion peaks after densification (T_{e1} and T_{e2}) were determined for all samples (Table 5.5). The causes for the observed thermal expansion features are discussed in the following paragraphs.

Table 5.5 Transition temperatures derived from the thermal expansion data. Total alkali content for each sample is also included. Dashes indicate the transition didn't occur or was not distinguishable.

Fly ash	Si : Al	Total alkali content	Shrinkage onset temperature T_s (°C)	Glass transition temperature T_g (°C)	High temperature expansion T_{e1} (°C)	2nd High temperature expansion T_{e2} (°C)
Collie	2.0	8.89	118	563	840	-
	2.5	8.32	75	589	676	-
	3.0	7.33	40	-	627	-
Eraring	2.0	11.11	34	772	925	-
	2.5	10.18	35	761	926	-
	3.0	8.91	40	772	908	-
Tarong	2.0	9.02	33	524	774	910
	2.5	7.66	34	-	778	945
	3.0	6.68	34	-	766	959
Port Augusta	2.0	9.79	90	700	-	-
	2.5	9.53	117	591	-	-
	3.0	9.07	95	573	708	-
Bayswater	2.0	10.19	74	776	-	-
	2.5	8.22	75	781	-	-
	3.0	6.57	38	777	-	-

The shrinkage onset temperature ranged from just above ambient to almost 120 °C. Duxson et al. (2007b) reported that geopolymers with a higher Young's modulus can withstand greater capillary strain forces developed during dehydration and as such the onset temperature of shrinkage increases. The results in this study were consistent with this observation as samples with a high Young's moduli such as the Collie 2.0 and Port Augusta 2.5 geopolymers had the highest shrinkage onset temperatures. Figure 5-12 and Figure 5-13 compare the shrinkage onset temperature to the compressive strength and Young's moduli of the geopolymers, respectively. A general trend of increasing mechanical strength with increasing shrinkage onset temperature can be observed, though the correlation with the trend line is low in both graphs.

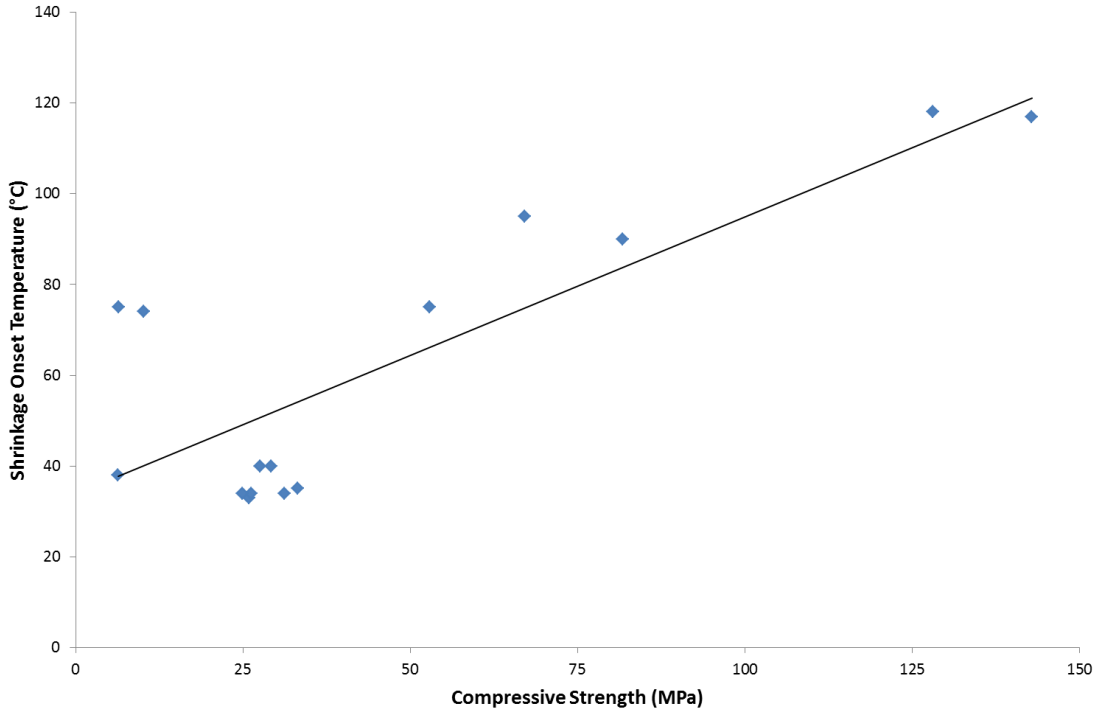

Figure 5-12 Compressive strength versus shrinkage onset temperature for the geopolymers in this study.

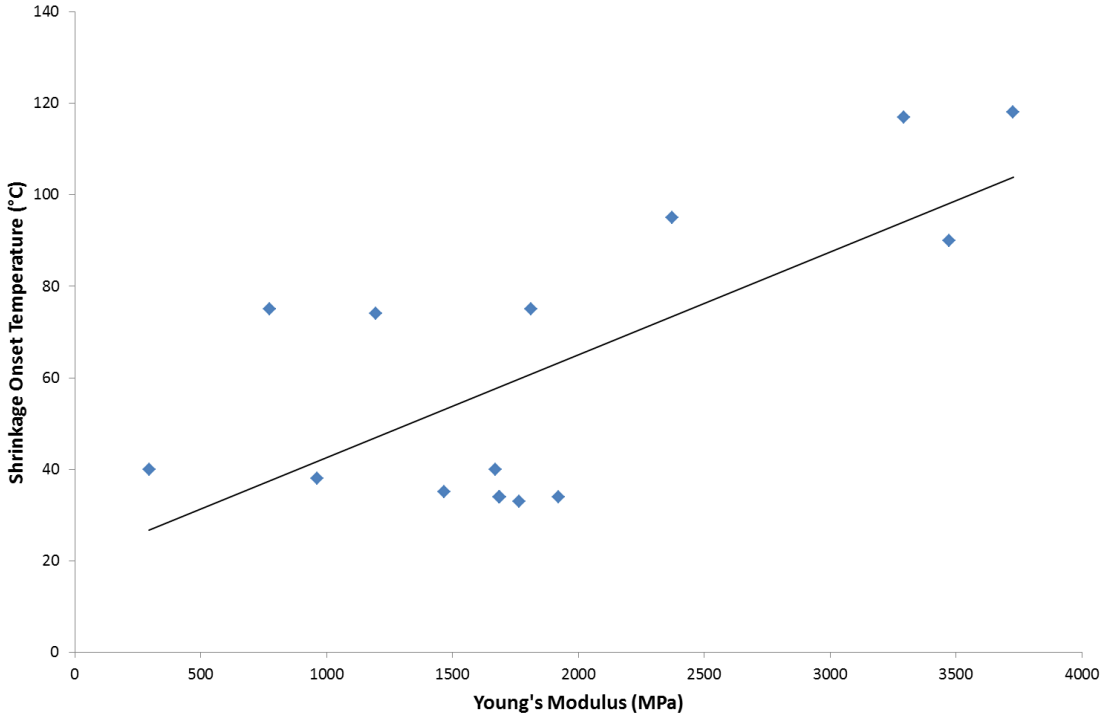

Figure 5-13 Young's Modulus versus shrinkage onset temperature for the geopolymers in this study.

The first shrinkage event in geopolymers is due to the dehydration of water and as such it was expected that the samples with higher water content after curing would

exhibit greater shrinkage during this stage. However, the amplitude of the dehydration shrinkage of the samples in this study did not appear to be proportional to water content. For example, the dehydration shrinkage of the Bayswater 2.5 and 3.0 geopolymers were similar even though the 2.5 sample had over 6 wt.% more mass loss due to dehydration (from Table 5.3).

The glass transition temperature (T_g) ranged from 524 °C to 781 °C. In some samples, such as the Collie 3.0 sample, the shrinkage event indicating the T_g was convoluted with a high temperature expansion event and as such was unable to be distinguished. Duxson et al. (2007b) found that T_g reduced with increasing Si:Al ratio though in this study there was no such trend observed. Alkalis are also known to be a sintering agent in aluminosilicate glasses (Kovalchuk and Krivenko, 2009) and thus are likely to influence T_g. The total alkali content, comprising the alkali initially present in the fly ash as well as the alkali used for activation was determined for each sample (Table 5.5). Comparing the T_g for each sample to the total alkali content did not show any clear trend and as such the presence of alkali was not observed to be a major influence of the high temperature behaviour in these samples. The cause for the variance in the T_g between the samples wasn't clear based on previous observations from the literature though it was noted that the sodium aluminate activated geopolymers (Eraring, Taring and Bayswater) generally exhibited higher T_g than the sodium silicate activated geopolymers (Collie and Port Augusta).

Some samples exhibited one, or in some cases two, expansion peaks above the glass transition temperature (listed in Table 5.5 as T_{e1} and T_{e2}). The expansion peaks in the Collie fly ash geopolymers were much greater that the other samples. The cause of the high temperature expansion in these samples was likely due to the swelling of a high silicate phases. However, as high temperature expansion peaks were also observed in the sodium aluminate activated samples, though to a much lesser degree, it is likely that there were multiple causes for these expansion events. The expansion in the sodium aluminate samples could be caused by crystallisation of the geopolymer gel or that the densification due to sintering had completed or slowed and the measured dilation was due to the expansion of the solid geopolymer phase. Fly ash geopolymers are highly inhomogeneous as they contain numerous phases

such as unreacted fly ash, geopolymer gel and residual activating material, each with different thermal expansion and sintering temperatures. As such multiple shrinkage events are likely to occur as the phases that sinter do so at different temperatures rather than at a single temperature as would be expected in a single phase material.

5.6 Thermal Conductivity

Thermal conductivity of the geopolymers from this study was measured to determine their propensity to transfer heat. Materials with high thermal conductivity can conduct heat more readily and are thus less likely to be severely affected by internal thermal stresses during high temperature exposure. However, a low thermal conductivity is beneficial in insulating applications to reduce heat flow. Table 5.6 contains the thermal conductivity values for the geopolymers from each of the fly ashes as measured using a KD2-pro thermal properties analyser. The density for each sample is also included as it is known to strongly influence the thermal conductivity of geopolymers (Duxson et al., 2006a).

During data collection it was noted that the measured values were sensitive to boundary effects between the probe and the sample, even though a thermal transfer compound was used. As such, a comparative measurement of the thermal conductivity of the Port Augusta 2.5 sample was made using the highly accurate steady state guarded hot plate method (refer to section 3.10.3 and ASTM C177 (2010) for details). This technique requires two large panels (300 x 300 x 50 mm) and a single measurement is taken over a period of days as the sample is allowed to equilibrate. This technique was not considered practical for the analysis of all the samples in this study due to a limited supply of fly ash and as such the result for the Port Augusta 2.5 sample was used as a comparison to the KD2-pro result. The thermal conductivity of the Port Augusta 2.5 sample using the guarded hot plate method was 0.79 ± 0.06 $Wm^{-1}K^{-1}$ which was 16 % higher than the value obtained using the KD2-pro. It is believed that the lower thermal conductivity as measured by the KD2 pro (measurement time 90s) was due to boundary effects between the sample and the probe, exacerbated by the short measurement time. There is the

potential for boundary effects to affect measured values in guarded hot plate experiments though they are greatly reduced as it is a steady state method where the sample has more than 48 hours to equilibrate. Thus it is considered that the measured values in Table 5.6 are likely to be marginally lower than the true value.

Table 5.6 Thermal conductivity and density of the samples prepared in this study. Samples were aged for 28 days at ambient conditions with a relative humidity of 45% prior to testing. Uncertainties in brackets.

Fly Ash	Si:Al	As-cured sample density (g cm^{-3})	Thermal conductivity (W m^{-1} K^{-1})
Collie	2.0	1.99 (5)	0.81 (4)
	2.5	2.11 (10)	0.66 (3)
	3.0	2.04 (7)	0.63 (3)
Eraring	2.0	1.58 (6)	0.46 (2)
	2.5	1.61 (12)	0.46 (2)
	3.0	1.57 (4)	0.47 (2)
Tarong	2.0	1.55 (7)	0.46 (2)
	2.5	1.58 (5)	0.54 (3)
	3.0	1.51 (5)	0.40 (4)
Port Augusta	2.0	1.86 (8)	0.64 (3)
	2.5	1.89 (7)	0.66 (3)
	3.0	1.86 (4)	0.44 (2)
Bayswater	2.0	1.70 (6)	0.33 (2)
	2.5	1.71 (16)	0.40 (2)
	3.0	1.68 (2)	0.34 (2)

Given the possible errors in the measured values, the results in this study remained consistent with other results in the literature on metakaolin geopolymers of similar density. Duxson et al. (2006a) reported thermal conductivity values between 0.4 and 0.8 W $m^{-1}K^{-1}$, and Subaer and van Riessen (2006) obtained values between 0.55 and 0.65 W $m^{-1}K^{-1}$. Ordinary Portland cement paste has been reported to have a thermal conductivity of 0.53 W $m^{-1}K^{-1}$ (Demiborga, 2003). The thermal conductivity of the samples in this study ranged from 0.33 to 0.81 W $m^{-1}K^{-1}$. It was observed that increases in the thermal conductivity of the samples were weakly correlated with increasing sample density (Figure 5-14). Samples with lower density are likely to

have more air voids than higher density samples and as air has a very low thermal conductivity it was expected that the total thermal conductivity will reduce.

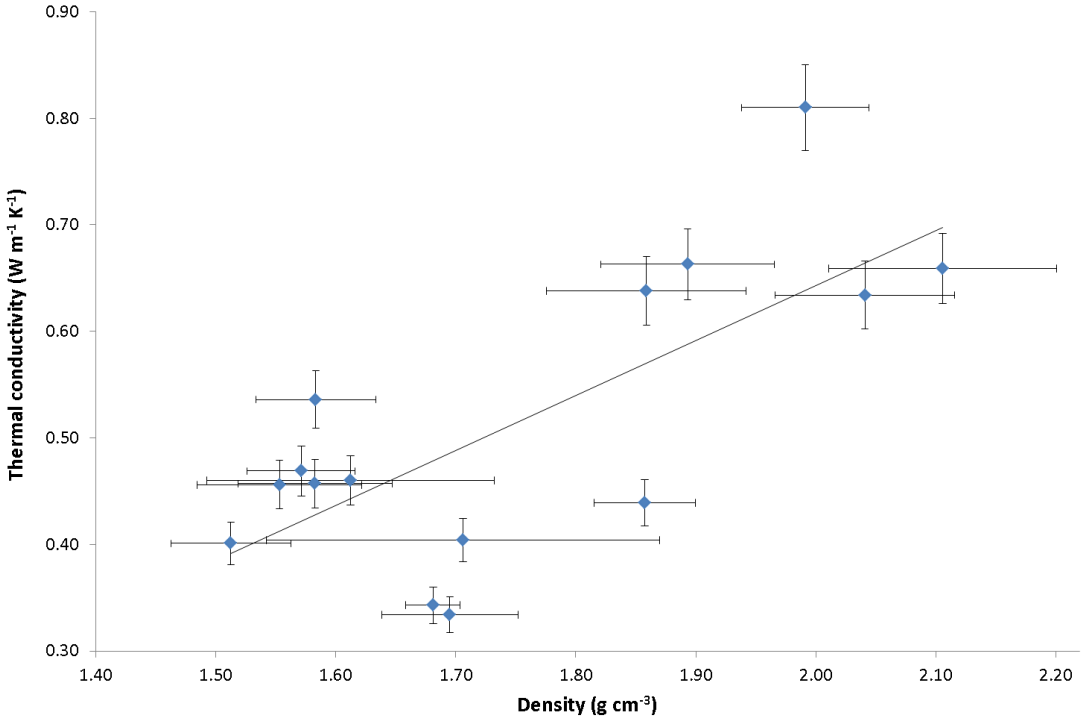

Figure 5-14 Thermal conductivity versus density for fly ash geopolymers in this study.

5.7 Conclusions

Fly ash based geopolymers are a highly complex material due to their many phases and inhomogeneous structure. Physical measurements on these samples are convoluted by the varying influence of each of these phases and as such the interpretation of the results was inherently difficult. In some cases the trends in the results were good and the causes for the measured characteristics were easily interpreted, though in other cases the results were scattered and difficult to interpret.

Physical characteristics of geopolymers synthesised from five different fly ashes before and after firing to 1000 °C have been presented in this chapter. The results varied greatly with fly ash source and the most influential fly ash characteristic was the reactive Si:Al ratio (amorphous Si:Al ratio) as it influenced the composition and type of the activating solution. Fly ashes with a high reactive Si:Al ratio (≥5) were

sodium aluminate activated and produced geopolymers with low to moderate as-cured compressive strengths but exhibited excellent dimensional stability during heating and greater compressive strengths after heating. Fly ashes with a low reactive Si:Al ratio (<2) were sodium silicate activated and produced geopolymers with high as-cured compressive strengths but exhibited poor dimensional stability during heating and greatly reduced compressive strengths after heating.

Previous studies (Rickard et al., 2010) have suggested that a high iron content in the source fly ash can cause cracking and subsequent strength losses in geopolymers. The results in this study suggest that there is little effect in geopolymers made with fly ashes containing low iron concentrations (< 3 wt.%) as there was no observable correlation of thermal performance with iron concentration in the fly ashes other than Collie. Collie fly ash has 13.2 wt.% iron oxide and exhibited the worst strength retention and dimensional stability of the samples suggesting that high concentrations of iron in the fly ash precursor are detrimental to a geopolymer's thermal performance.

Thermal expansion results indicated the swelling of unreacted silicates during heating in the low reactive Si:Al ratio (sodium silicate activated) fly ash geopolymers. It is likely that swelling of the unreacted silicates caused the loss of compressive strength during heating in these samples. This is supported by the fact that for both the Collie and Port Augusta geopolymers the post firing compressive strengths reduced as the silica content in these samples increased (i.e. as the Si:Al increased from 2.0 to 3.0).

Other measurements on the samples before and after heating indicated general trends though the correlation was not always high due to the convoluted results obtained from multiphase materials. The post firing densities were consistent with the measured changes in compressive strengths after firing, though the percentage change was much smaller. There was no apparent correlation of mass loss due to dehydration after firing to strength changes. The as-cured thermal conductivity of the samples in this study ranged from 0.33 to 0.81 W $m^{-1}K^{-1}$ which weakly correlated with sample density.

Chapter 6
Microstructural Evolution of Fly Ash Geopolymers

"We see past time in a telescope and present time in a microscope. Hence the apparent enormities of the present"

Victor Hugo

6.1 Introduction

This chapter reports on the microstructural changes in the geopolymers described in chapter 5 before and after exposure to 1000 °C in a furnace. Global physical changes, such as variation in compressive strength, are indicative that the thermal exposure induced changes in the microstructure. The changes in sample morphology were characterised by optical and electron microscopy whereas changes in the elemental and phase composition were analysed by EDS and XRD, respectively.

In a few instances throughout this chapter, images of only the most representative samples have been included. To have included the images from every sample in the body of this chapter would have made the chapter impractically long. There is a selection of additional images and micrographs included in appendix B.

A conceptual model for the microstructural changes in fly ash geopolymers exposed to elevated temperatures is also included in this chapter.

The contents of this chapter formed the basis of the following publication;
Rickard, W. D. A., Temuujin, J., & van Riessen, A. (2012). Thermal analysis of geopolymer pastes synthesised from five fly ashes of variable composition. *Journal of Non-Crystalline Solids*, 358(15), 1830-1839.

6.2 Microstructural Evolution

The as-cured geopolymers all had a brownish-grey colour (Figure 6-1). After firing, all samples were observed to ‘redden’ to a varying degree (Figure 6-2). This is caused by the oxidation and liberation of iron species initially contained inside fly ash particles during high temperature exposure. The degree of ‘reddening’ was observed to be proportional to the iron content in the fly ashes, with Collie fly ash geopolymers (iron oxide content 13.2 wt.%) the reddest and the Tarong fly ash geopolymers (iron oxide content 0.6 wt.%) the whitest after exposure. A similar

character of colour change and cracking was observed in the Si:Al = 2.5 and 3.0 series geopolymers.

Structural changes after firing were noticeable with the naked eye. Collie geopolymers exhibited extensive surface cracking after firing, whereas Eraring and Tarong geopolymers exhibited very few observable cracks. Port Augusta and Bayswater geopolymers exhibited a moderate amount of cracking. In addition it was noted that the Bayswater geopolymers also showed signs of melting (Figure 6-2).

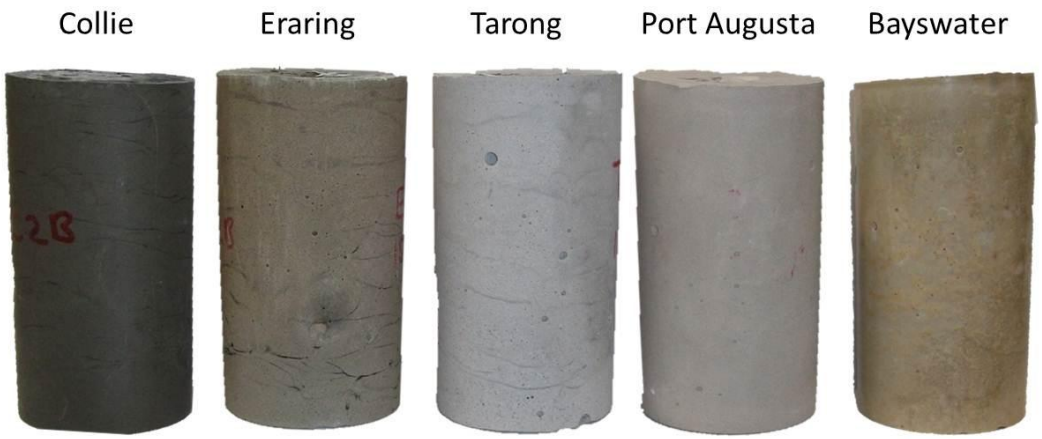

Figure 6-1 Fly ash geopolymer samples (Si:Al 2.0) as-cured.

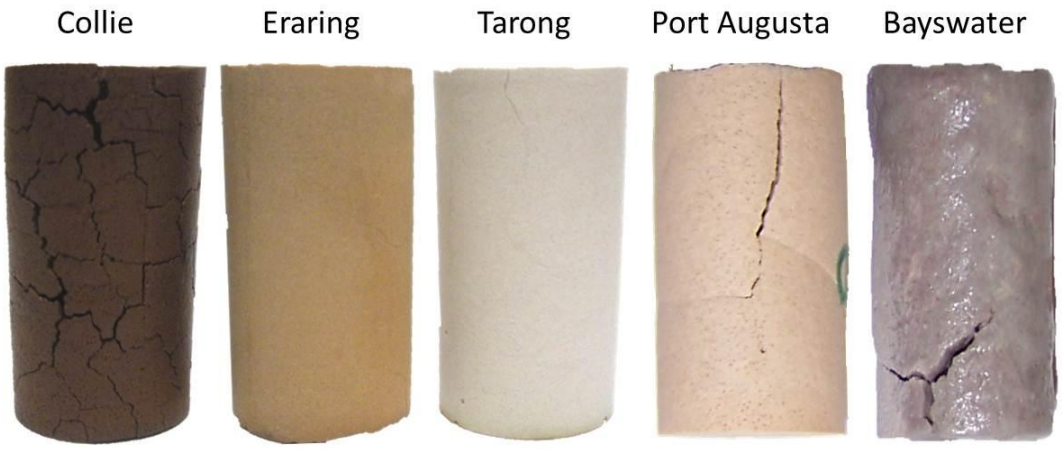

Figure 6-2 Fly ash geopolymer samples (Si:Al 2.0) after firing to 1000 °C. Note the variation in colour change and degree of cracking.

Interestingly, samples that exhibited extensive cracking still had moderate compressive strengths, and conversely, some samples with very little observable cracking had low compressive strengths after firing. If sintering and viscous flow of the aluminosilicates happens after crack formation then, to a certain degree, the cracks will ‘heal’ and thus compressive strength can be maintained. However, in samples where the cracking occurred after the sintering phase, then the cracks remain as weak points during strength testing.

6.2.1 Optical Microscopy

Low magnification, large field of view, microscopy was conducted to observe changes in the microstructure at moderate length scales. Figure 6-3 compares polished fragments of Collie and Tarong fly ash geopolymers (Si:Al= 2.5) before and after firing to 1000 °C. The Collie fly ash geopolymer can be seen to have reduced homogeneity after firing with local variation in the degree of iron oxidation observable; noted as red veins running along the fine cracks in the sample. There was also a visible pore structure that was not present in the as-cured sample. In contrast, the Tarong fly ash geopolymer exhibited a homogenous structure with no visible porosity after firing. This is consistent with the mechanical strength results as the Tarong sample, with less thermally induced defects, exhibited greater strength retention / increase than the Collie sample. Analogous observations, where samples that exhibited compressive strength gains also exhibited a more homogenous microstructure, were found with the other samples.

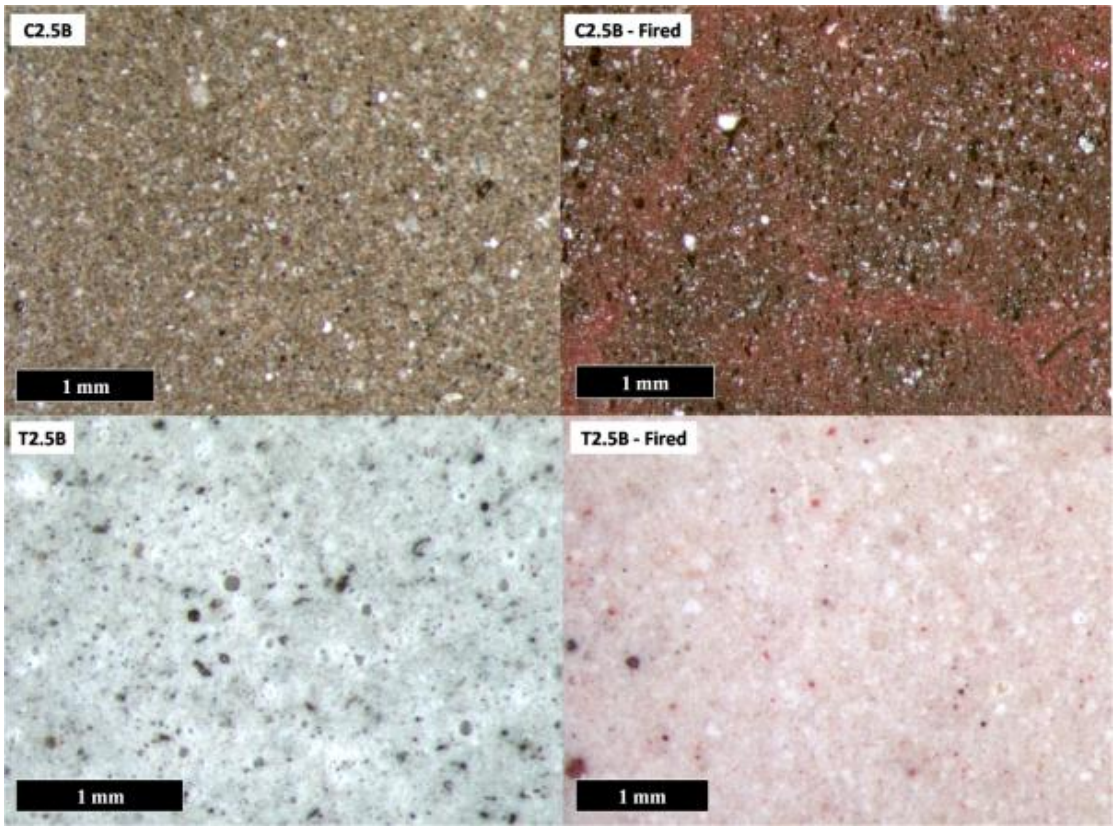

Figure 6-3 Optical microscope images comparing Collie (top) and Tarong (bottom) geopolymers before and after firing to 1000 °C.

6.2.2 Scanning Electron Microscopy

SEM was performed on the geopolymers synthesised in this study to analyse the microstructure using fractured and polished surfaces (Figure 6-4 to Figure 6-13). The as-cured microstructure was typical for fly ash geopolymers consisting of geopolymer gel amongst unreacted fly ash particles. Collie and Port Augusta fly ash geopolymers were observed to have the highest proportion of geopolymer gel indicating a higher degree of fly ash was converted into the geopolymer phase. These fly ashes had the finest particle size distribution and largest surface area of the fly ashes investigated (Figure 4-8, Table 4.5) so it was expected that there would be greater dissolution of the amorphous aluminosilicates to form geopolymer gel.

SEM imaging of some of the Collie and Port Augusta fly ash geopolymers revealed surface cracking. It is believed that this was an artefact of sample preparation rather than an existing sample characteristic. The higher density (from Table 5.4) and greater portion of geopolymer gel in these samples reduced their permeability and as

such inhibited the dehydration of free water when placed in a vacuum, causing the cracking. This effect was further exaggerated in the polished samples (Figure 6-10 and Figure 6-11) as they were additionally subjected to numerous wet-dry cycles during preparation. This was not the case in the lower density samples where water was able to escape without damaging the structure.

Eraring, Tarong and Bayswater fly ash geopolymers were observed to be primarily composed of partially reacted fly ash particles bonded by geopolymer gel. The majority of the un-reacted fly ash particles were larger than 5 μm in all geopolymer samples.

The morphology of the geopolymers changed significantly after firing to 1000 °C. In all samples there was a significant reduction in the number of unreacted fly ash particles and better inter-particle bonding. This was due to the high temperature sintering and viscous flow of aluminosilicates out of the amorphous unreacted fly ash particles and into the geopolymer gel. This resulted in a more homogenous and better connected microstructure in all samples. This was likely to be the main mechanism that leads to increases in compressive strength after firing. The effect of the additional aluminosilicates on the composition of the geopolymer gel is discussed in section 6.3.

Despite having a more homogenous and better connected microstructure, Collie and Port Augusta geopolymers exhibited significantly reduced compressive strength after firing. The strength reduction is believed to arise from the extensive cracking in these samples which was more influential than the strength gained from sintering. It is proposed that high temperature sintering caused localised strength increases, though bulk cracking caused by phase changes (details in section 6.4) and dehydration damage resulted in the overall strength losses.

The pore size distribution was observed to change significantly after firing. There was an apparent increase in porosity in the size range of 5 to 20 μm in all samples. The sub-micron pores within the geopolymer gel (Figure 6-12) as observed in the as-cured geopolymers were not present in the fired samples. This change in pore size is likely due to the collapse of the small pores as sintering causes the geopolymer gel to

densify. The commensurate reduction in geopolymer gel volume increases the volume of the voids in between the gel and as such the inter-gel pores increase in size. The viscous flow of material out of un-reacted fly ash particles during firing also affected the porosity of the samples as pores initially trapped within the fly ash particles were liberated.

The following pages contain SEM micrographs from the three geopolymer mixes (Si:Al = 2.0, 2.5 and 3.0) from each of the fly ashes before and after firing to 1000 °C.

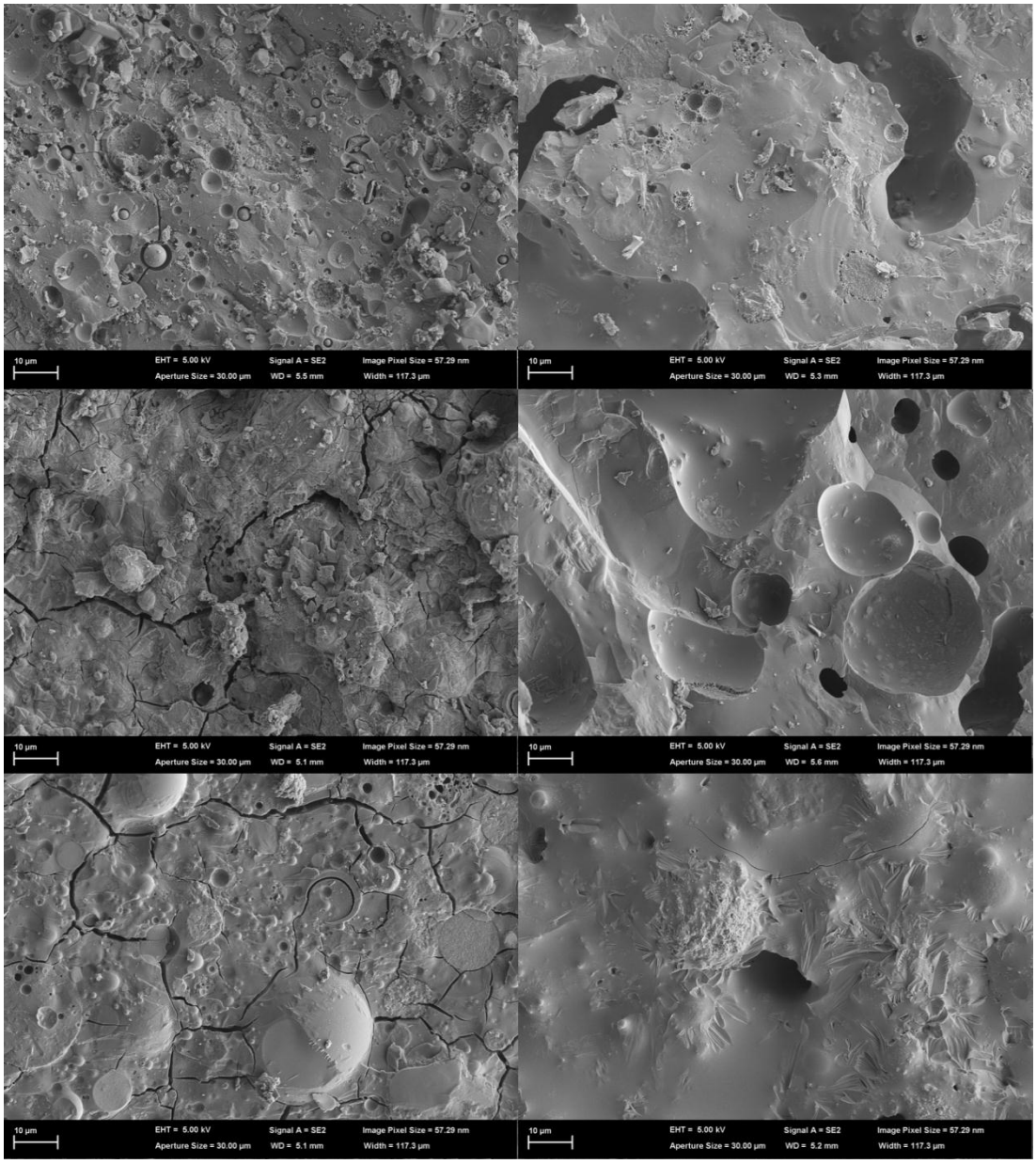

Figure 6-4 SEM micrographs comparing the microstructure of the Collie fly ash geopolymers before (left images) and after (right images) heating to 1000 °C (Top Si:Al = 2.0, middle Si:Al = 2.5 and bottom Si:Al = 3.0).

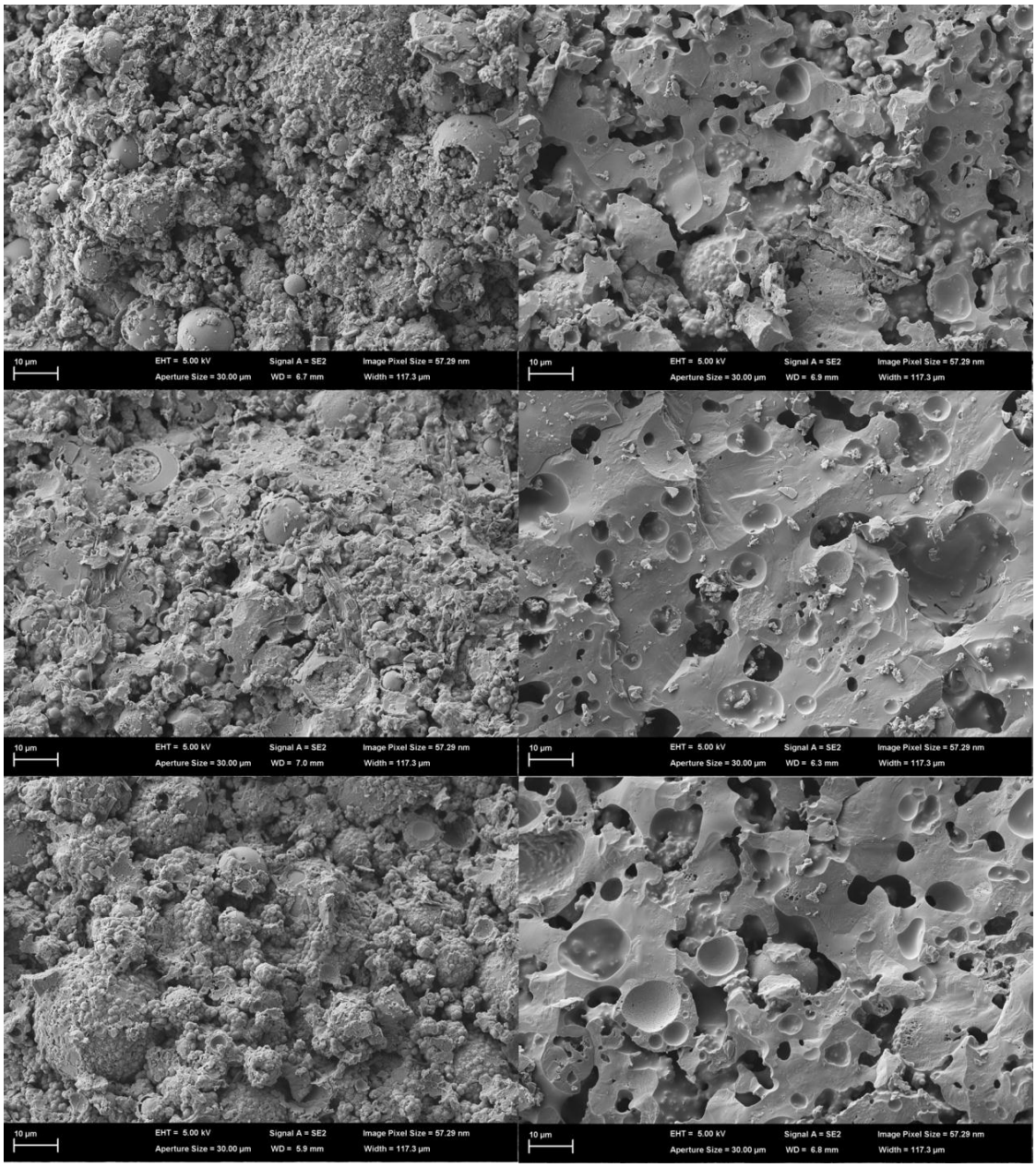

Figure 6-5 SEM micrographs comparing the microstructure of the Eraring fly ash geopolymers before (left images) and after (right images) heating to 1000 °C (Top Si:Al = 2.0, middle Si:Al = 2.5 and bottom Si:Al = 3.0).

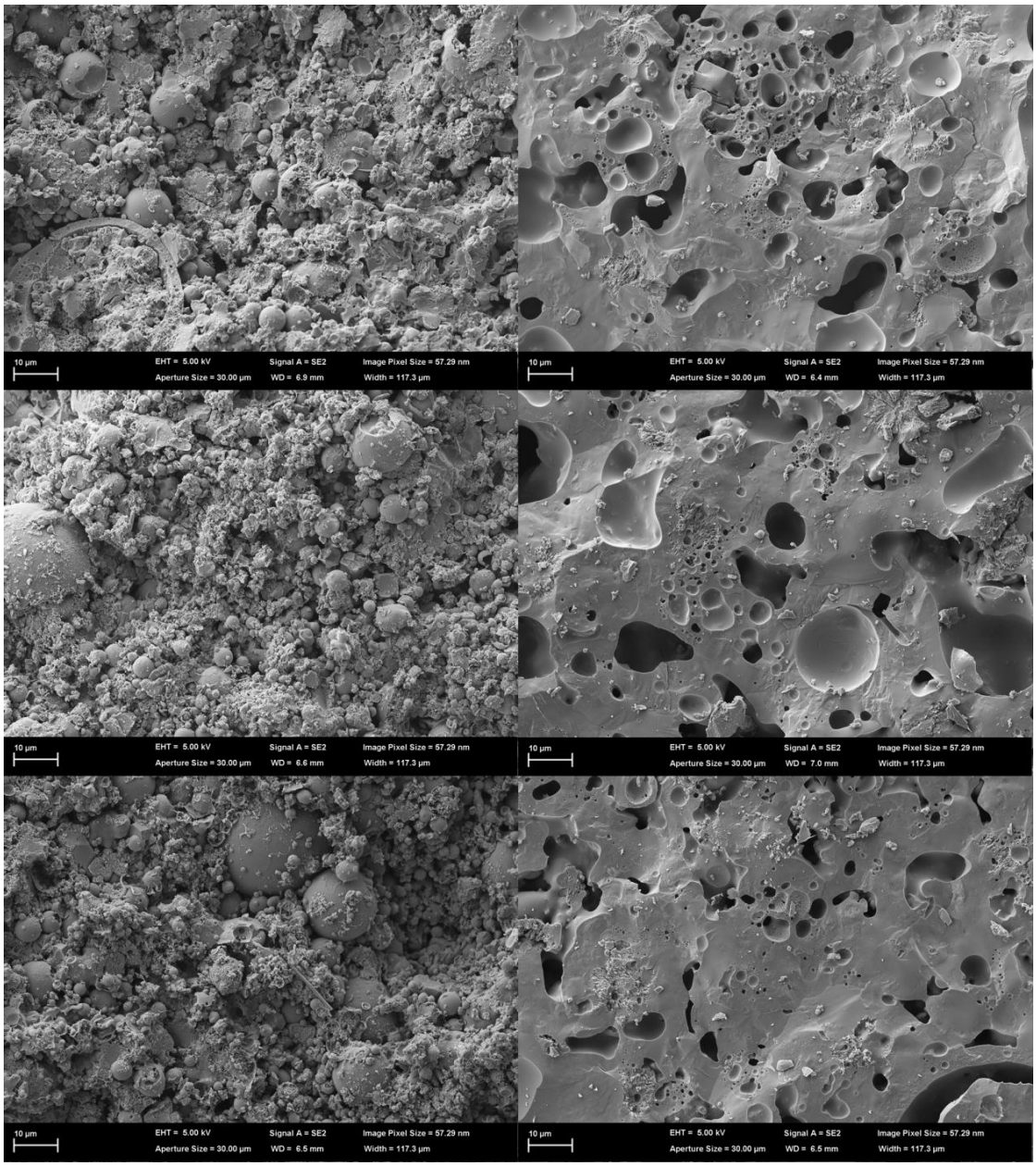

Figure 6-6 SEM micrographs comparing the microstructure of the Tarong fly ash geopolymers before (left images) and after (right images) heating to 1000 °C (Top Si:Al = 2.0, middle Si:Al = 2.5 and bottom Si:Al = 3.0).

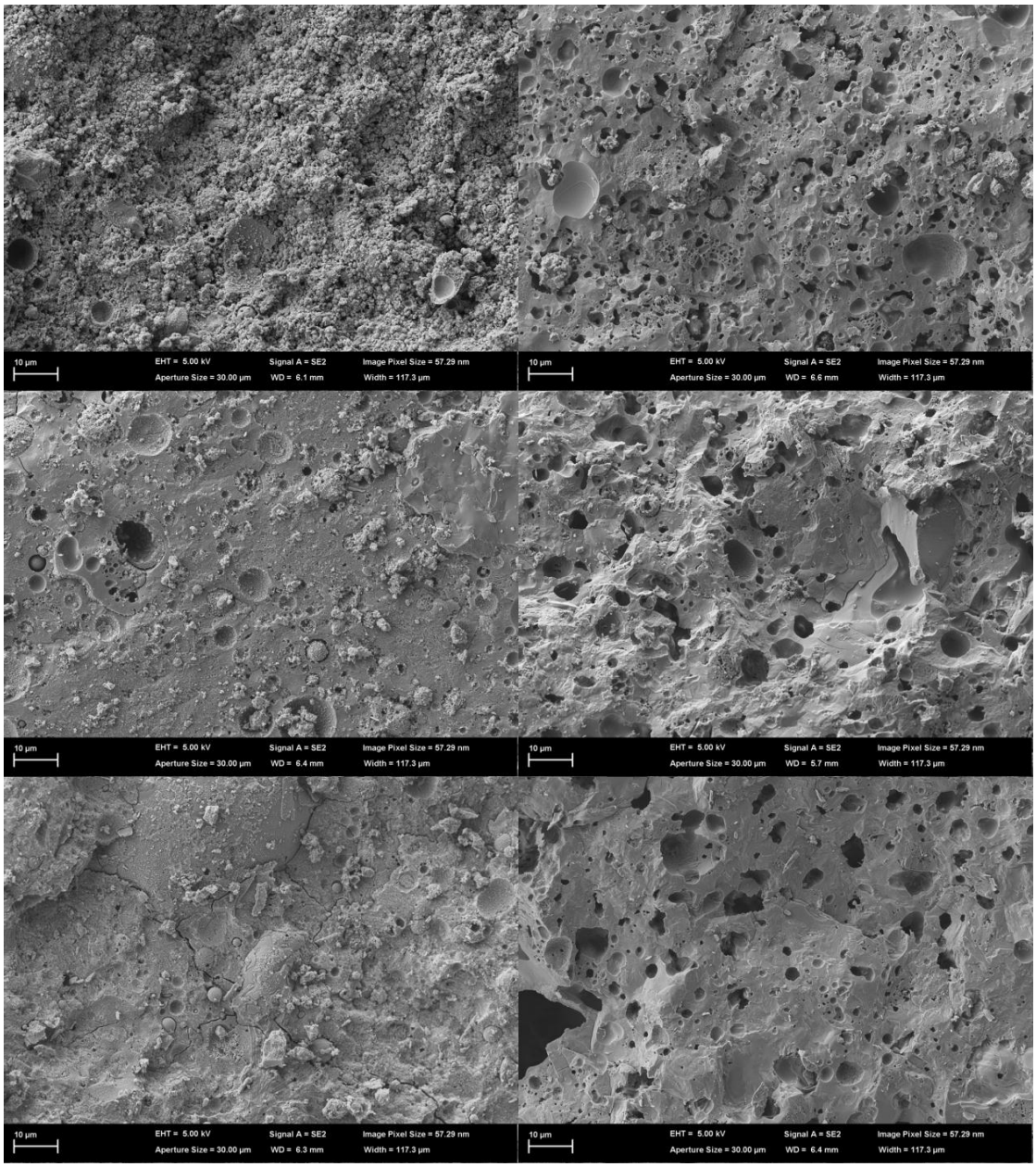

Figure 6-7 SEM micrographs comparing the microstructure of the Port Augusta fly ash geopolymers before (left images) and after (right images) heating to 1000 °C (Top Si:Al = 2.0, middle Si:Al = 2.5 and bottom Si:Al = 3.0).

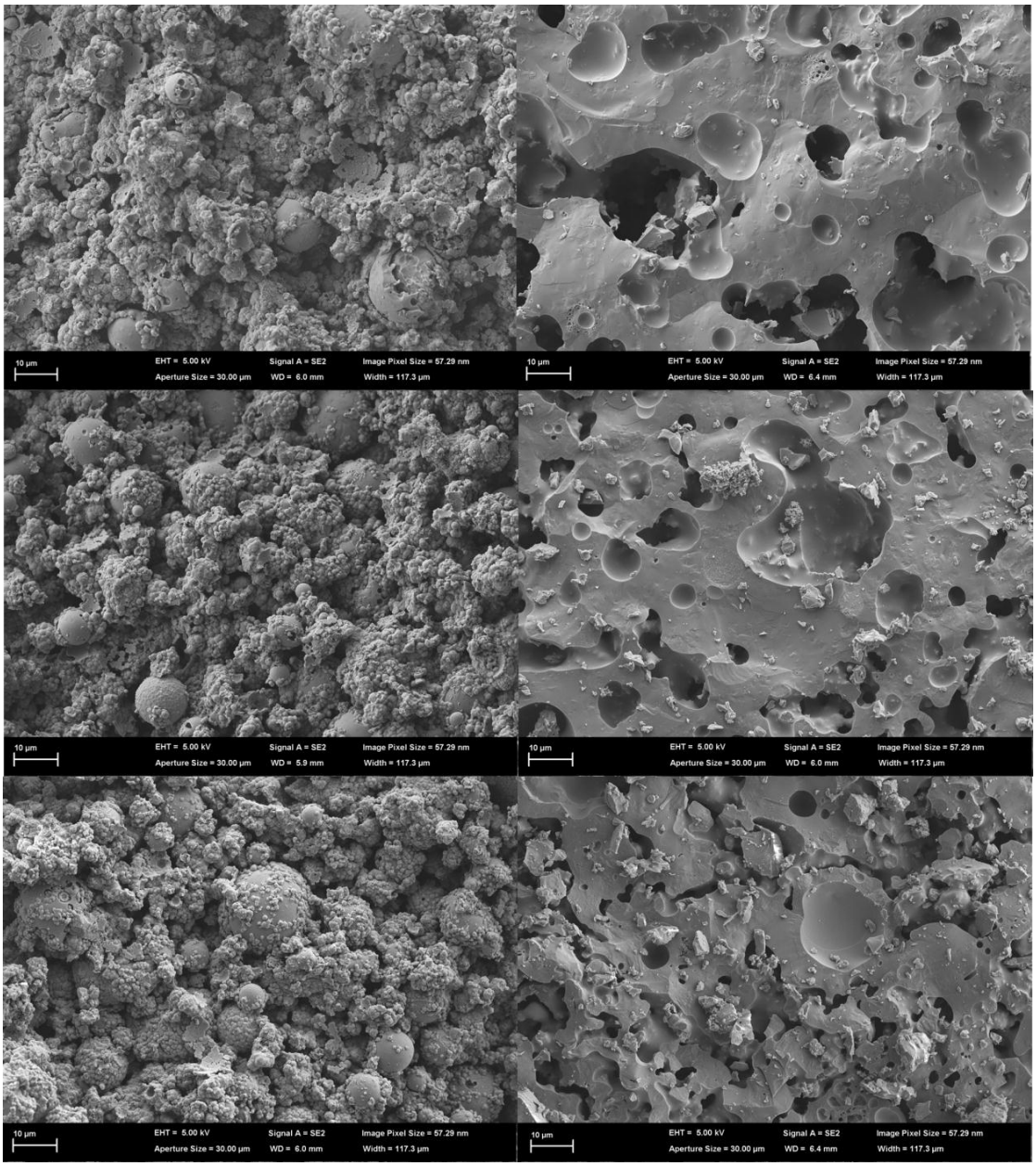

Figure 6-8 SEM micrographs comparing the microstructure of the Bayswater fly ash geopolymers before (left images) and after (right images) heating to 1000 °C (Top Si:Al = 2.0, middle Si:Al = 2.5 and bottom Si:Al = 3.0).

The size of the pores in the post fired Bayswater samples were observed to vary with distance from the surface of the sample (Figure 6-9). An outer layer (~1000 µm thick) containing pores up to 200 µm in diameter was followed by a region of reduced porosity (~500 µm thick). A homogenous and consistent pore size was then observed in regions greater than 1500 µm from the surface. This effect was likely caused by the Bayswater samples sintering so extensively that partial melting occurred, an affect observed in the post firing images of these samples (Figure 6-2).

The melting and subsequent liquefaction of the geopolymer gel when the sample was heated above its Tg (~780 °C) would have facilitated the near surface pores to coagulate and migrate towards the surface, explaining the observed affect.

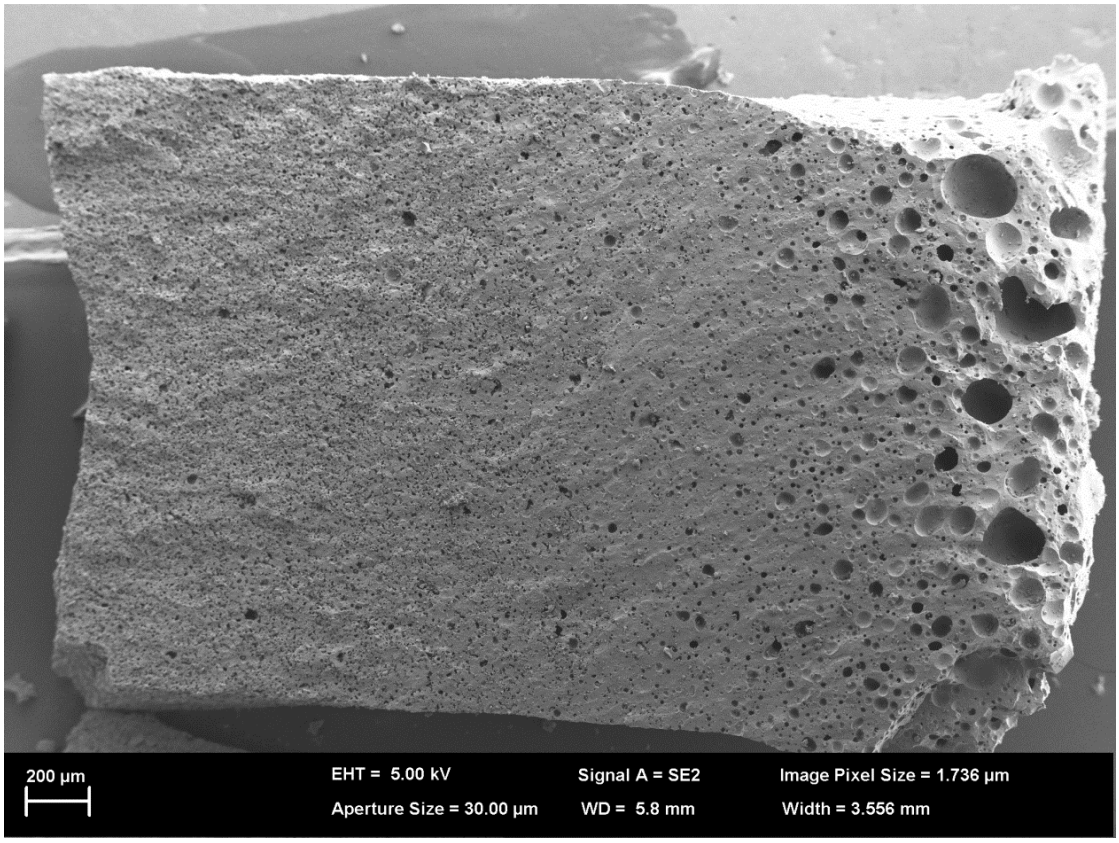

Figure 6-9 SEM micrograph of a Bayswater fly ash geopolymer (Si:Al = 2.5) after firing showing the pore size variation from the outside (right) to the centre (left).

Samples were polished to assess the connectivity of the pores. Figure 6-10 and Figure 6-11 compare the polished cross sections of the Si:Al = 2.5 geopolymer for each fly ash as imaged with a backscattered electron (BSE) detector. The cracks in the Collie and Port Augusta fly ash samples are believed to be caused by exposure to high vacuum in a SEM as explained previously. High atomic number material (identified as bright regions in BSE micrographs), such as iron or titanium oxides, was observed to exist within unreacted fly ash particles and not within the geopolymer gel in all the samples. After firing, the high atomic number material was observed to remain predominantly in discrete regions rather than being distributed throughout the geopolymer gel. This suggests that there was minimal incorporation of the metal oxides into the geopolymer gel during firing.

The polished cross sections gave an indication as to the pore connectivity of the samples before and after firing. It was observed that all of the pores in the micrographs for the Collie and Port Augusta fly ash geopolymers (before and after firing) were isolated, whereas many of the pores in the other geopolymers were connected to other pores. As the connectivity of the pores influences the permeability of the samples, the SEM results indicate that the Collie and Port Augusta fly ash geopolymers were less permeable than the Eraring, Tarong and Bayswater fly ash geopolymers.

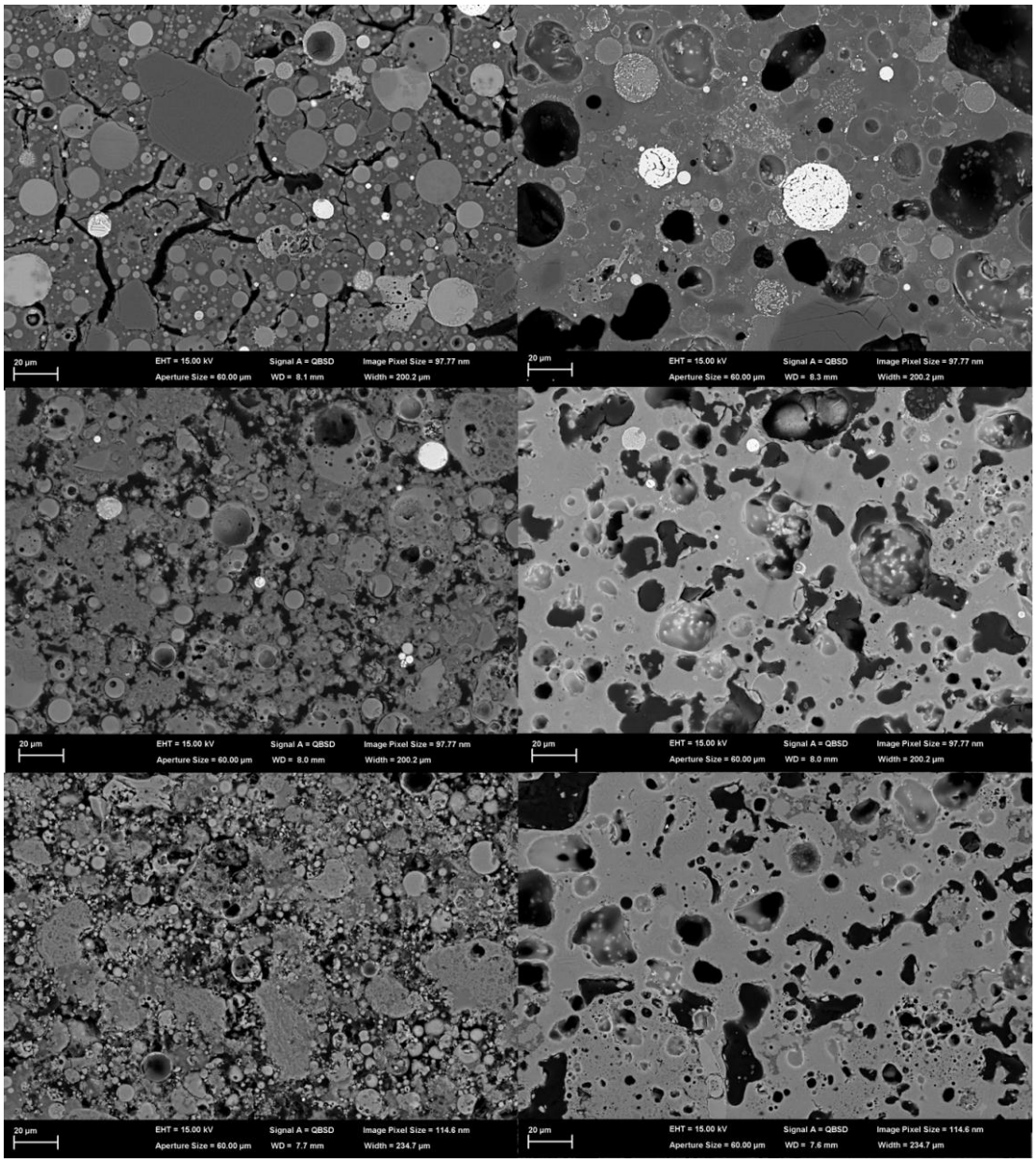

Figure 6-10 Backscattered SEM micrographs of the Si:Al = 2.5 geopolymers (polished) before (left images) and after firing to 1000 °C (right images). Top: Collie, middle: Eraring, bottom: Tarong fly ash geopolymers.

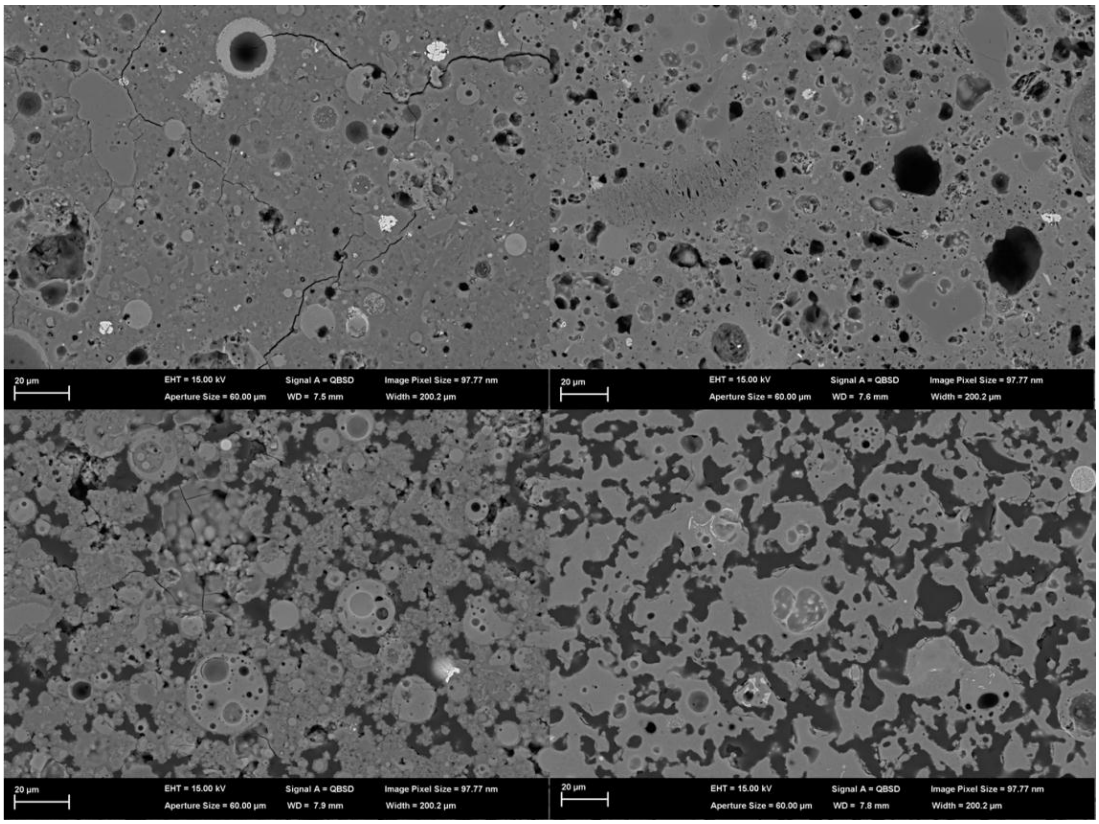

Figure 6-11 Backscattered SEM micrographs of the Si:Al = 2.5 geopolymers (polished) before (left images) and after firing to 1000 °C (right images). Top: Port Augusta fly ash geopolymer, bottom: Bayswater fly ash geopolymer.

The above micrographs were taken at too low a magnification to be able to discern finer pores such as micro (<2 nm) and meso (2-50 nm) pores which, in addition to the larger pores, are known to play a role in the transport of water in geopolymers (Lloyd et al., 2009). Figure 6-12 contains a high magnification (25,000x) micrograph of the Port Augusta 2.5 sample that shows the geopolymer gel containing a network of fine pores (<100 nm). It is expected that the geopolymer gel in the other samples would also have contained fine pores in addition to the large pores observed in the low magnification images. As such, it is likely that these fine pores also played a role in the movement of water during firing, though this has not been quantified in this work.

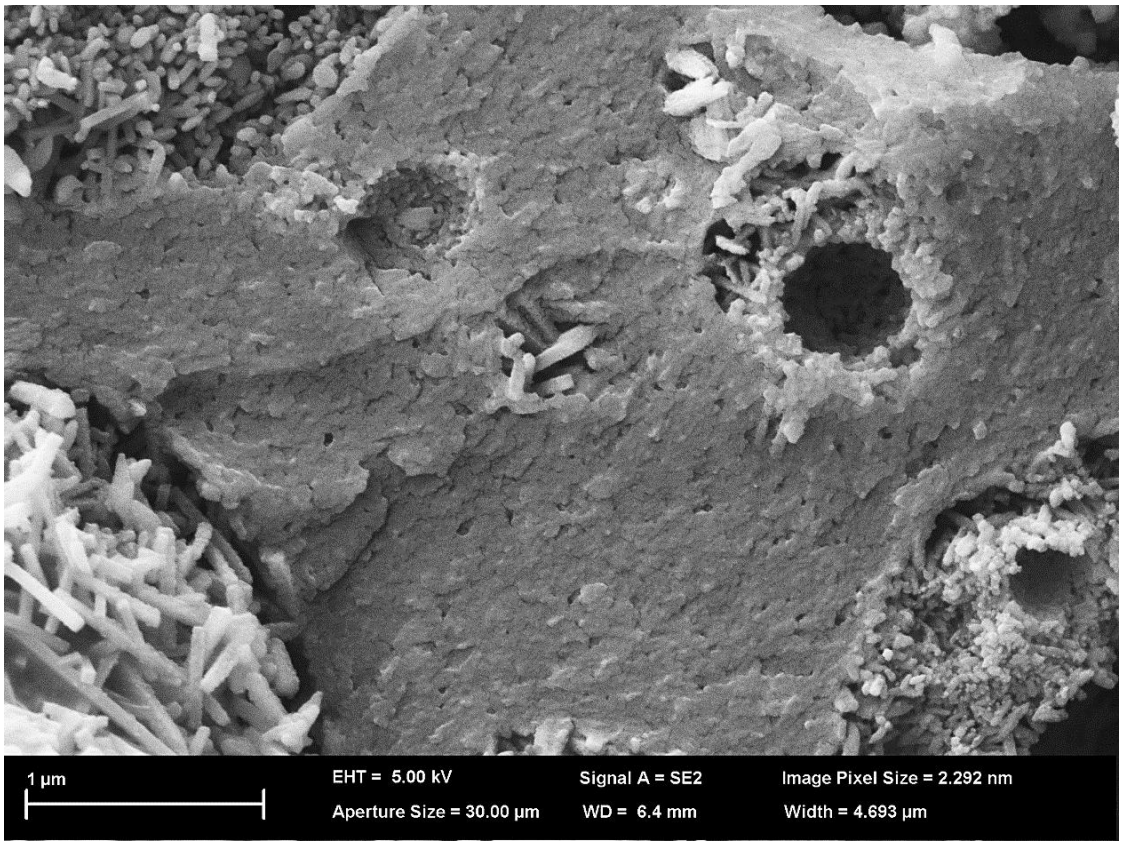

Figure 6-12 Fine pores (< 100 nm) within the geopolymer gel in an as-cured sample. Needle shaped mullite crystals can also be seen. Sample: Port Augusta 2.5.

The resistance to alkaline dissolution of the crystalline material from the fly ashes is demonstrated in Figure 6-13 (top) where concentrated bundles of mullite needles can be seen in the as-cured geopolymer. During geopolymerisation much the amorphous aluminosilicates are dissolved out of the fly ash particles to form the geopolymer gel, leaving the crystalline material. This is consistent with the assumption in this study that the crystalline aluminosilicates in the fly ashes were not available for geopolymerisation. Mullite needles and quartz particles were also observed in the post fired samples indicating that the crystalline phases were not destroyed upon firing (Figure 6-13, bottom).

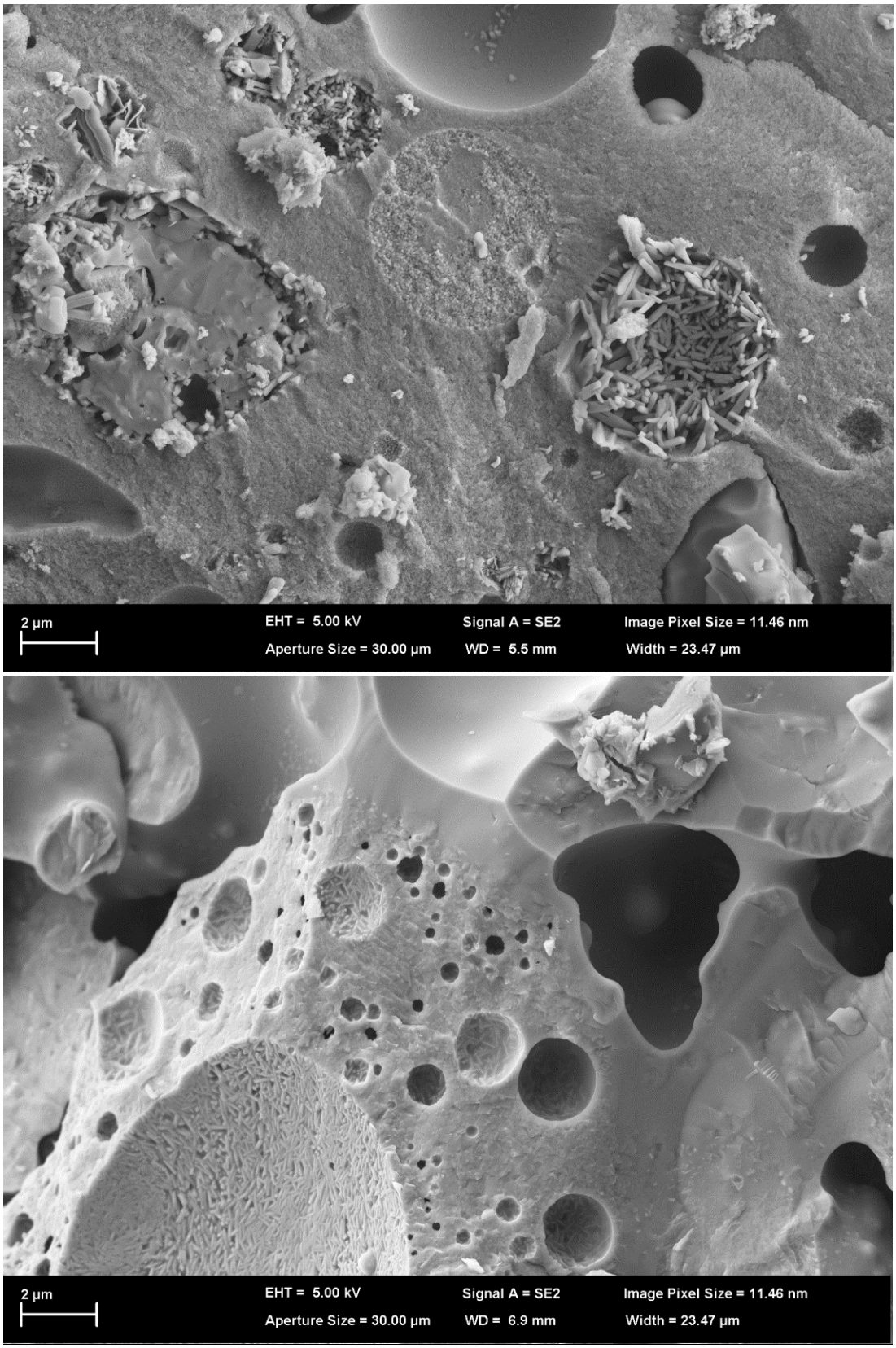

Figure 6-13 SEM micrographs showing the presence of crystalline material (mullite needles) in the as-cured geopolymer (top) and in the fired geopolymer (bottom). Sample: Port Augusta 2.5.

6.3 Energy Dispersive X-ray Spectroscopy

Energy Dispersive X-ray Spectroscopy (EDS) was performed on the geopolymers to assess their elemental composition and distribution before and after firing.

6.3.1 Elemental Composition of the Geopolymer Gel

EDS analysis was restricted to just the geopolymer gel. However, because the x-ray interaction volume was larger than the electron interaction volume is it possible that some of the spectra included information from secondary phases such as unreacted fly ash particles. The contribution of the secondary phases was diminished by using a 10 kV accelerating voltage to reduce the interaction volume whilst maintaining enough energy to cause iron and titanium to fluoresce. Figure 6-14 contains typical EDS spectra from the geopolymer gel before and after firing.

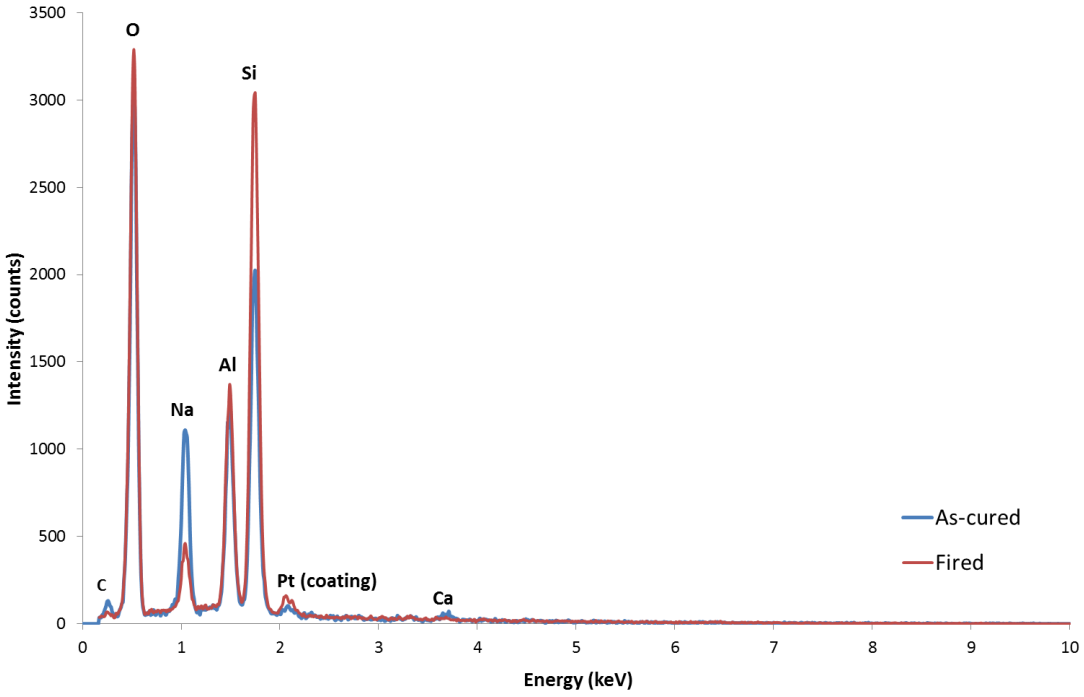

Figure 6-14 EDS spectra from the geopolymer gel of the Bayswater 2.5 sample before and after firing.

The geopolymer gel of the samples in this study was composed of Si, Al, Na and O with a small concentration of impurities such as Ca, K, Mg, Ti and Fe (Table 6.1,

Si:Al= 2.5 only). It was not possible to discern if the impurities were substituted into the short range structure of the geopolymer gel; existed as fine particles within the gel; or existed within subsurface unreacted fly ash particles that contributed to the collected spectra.

Table 6.1 Elemental concentration of the geopolymer gel of the Si:Al = 2.5 geopolymer from each fly ash as determined by EDS. All results are the average of at least 5 measurements collected at different locations identified as geopolymer gel. Uncertainties in brackets.

Fly ash		Si	Al	Na	O	Other
Collie	As-cured	24.6 (3.1)	7.1 (1.2)	12.5 (2.8)	51.9 (5.1)	3.9 (0.6)
	Fired	27.3 (1.2)	9.4 (0.5)	3.3 (0.8)	52.9 (4.6)	7.1 (2.1)
Eraring	As-cured	18.0 (2.2)	11.9 (3.1)	19.8 (2.1)	49.7 (6.3)	0.6 (0.3)
	Fired	32.5 (1.9)	11.3 (0.8)	3.4 (0.6)	50.9 (4.8)	1.9 (0.5)
Tarong	As-cured	22.5 (1.1)	10.1 (1.6)	20.4 (3.2)	46.1 (6.1)	0.9 (0.4)
	Fired	37.6 (4.2)	11.9 (1.5)	1.9 (0.5)	47.8 (3.7)	0.7 (0.3)
Port Augusta	As-cured	28.1 (2.4)	10.1 (3.1)	5.6 (1.1)	51.7 (5.4)	4.5 (1.1)
	Fired	32.1 (3.7)	13.3 (2.2)	5.2 (0.9)	46.3 (7.0)	3.1 (1.3)
Bayswater	As-cured	20.4 (1.8)	11.5 (3.7)	13.0 (3.4)	54.5 (3.9)	0.6 (0.2)
	Fired	26.9 (3.5)	8.1 (0.9)	2.7 (0.6)	61.3 (5.4)	1.0 (0.2)

The measured composition of the geopolymer gel phase varied greatly, both between samples and within individual samples. The inter-sample compositional variability indicated that there was a high degree of in-homogeneity in the gel. This suggests that there was little movement of the aluminosilicates after dissolution in the geopolymerisation process causing the gel to have a composition that reflected the composition of neighbouring fly ash particles rather than that of the average composition of all the fly ash particles. Thus, most of the dissolution of aluminosilicates must have occurred in a solid or highly viscous state rather than a liquid state.

Thermal expansion measurements in chapter 5 indicated there was likely to be high silica regions in the sodium silicate activated samples, in particular in the Collie fly ash geopolymers. EDS analysis of the Collie fly ash geopolymers indicated presence of small regions that were predominantly composed of silicon, sodium and oxygen with only a minor concentration aluminium (Figure 6-15). This supports the thermal

expansion findings that high silica regions were present sodium silicate activated samples.

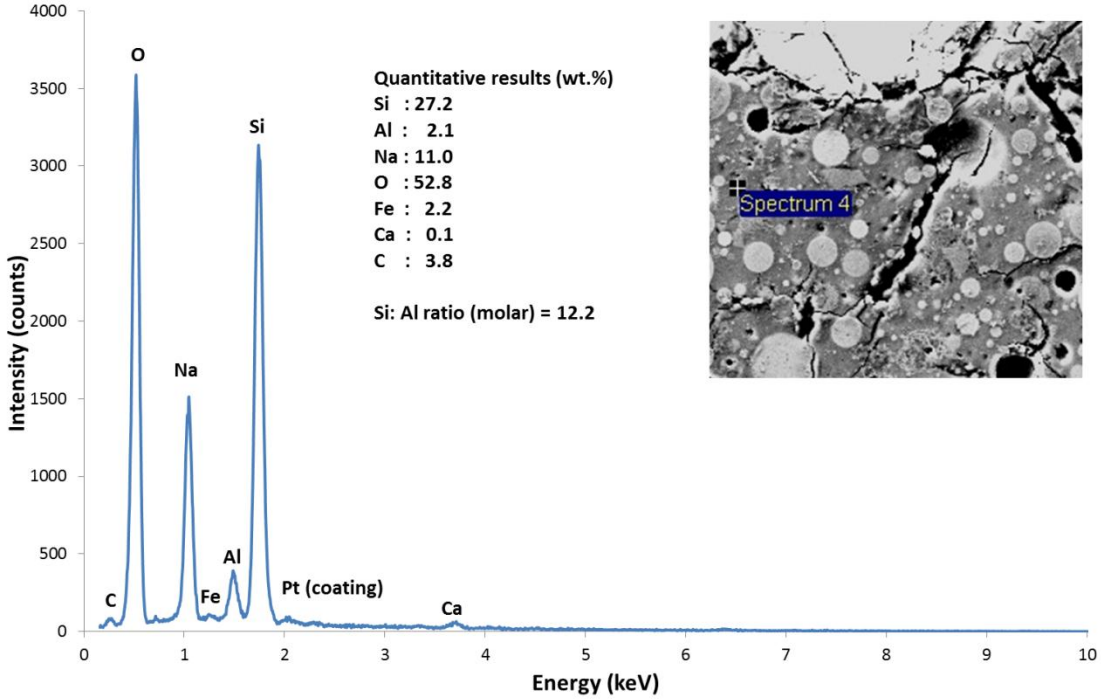

Figure 6-15 EDS spectrum of a high silicon region in the geopolymer gel of the Collie 2.5 sample. Inset: Micrograph shows where the spectrum was collected from.

The relative concentrations of the elements were considered more significant than their measured wt.%. The elemental ratios (molar) in the geopolymer gel before and after firing were compared to the designed compositional ratios (Table 6.2). If there was 100 % dissolution of the amorphous aluminosilicates from the fly ashes, it would be expected that the Si:Al ratio in the as-cured samples would reflect the designed ratios. However, SEM investigations indicated the presence of unreacted fly ash particles which appeared to be amorphous in all geopolymer samples. Thus not all the reactive aluminosilicates in the ashes were dissolved into the geopolymer gel and as such the composition of the gel was expected to differ to that of the designed composition.

Table 6.2 Elemental ratios of the geopolymer gel of the geopolymers from each fly ash as determined by EDS. Uncertainties are in the brackets.

Fly Ash	Si:Al			Na:Al		
	Design	As-cured	Fired	Design	As-cured	Fired
Collie	2.0	2.6 (3)	3.0 (3)	1.3	1.7 (2)	0.5 (1)
(Glass Si:Al = 1.2)	2.5	3.3 (5)	2.8 (3)	1.3	2.1 (1)	0.4 (1)
	3.0	5.2 (4)	4.2 (3)	1.3	2.2 (3)	0.6 (1)
Eraring	2.0	1.3 (1)	2.6 (3)	1.3	1.0 (1)	0.5 (1)
(Glass Si:Al = 5.0)	2.5	1.4 (4)	2.8 (3)	1.3	2.0 (2)	0.3 (1)
	3.0	2.0 (4)	2.5 (2)	1.3	1.7 (1)	0.5 (1)
Tarong	2.0	1.4 (5)	2.0 (2)	1.3	2.2 (2)	0.3 (1)
(Glass Si:Al = 8.8)	2.5	2.1 (2)	3.0 (2)	1.3	2.4 (3)	0.2 (1)
	3.0	2.1 (2)	3.4 (7)	1.3	2.3 (3)	0.3 (1)
Port Augusta	2.0	1.5 (1)	1.8 (3)	1.3	1.2 (1)	0.5 (1)
(Glass Si:Al = 1.9)	2.5	2.7 (3)	2.3 (3)	1.3	0.6 (1)	0.5 (1)
	3.0	3.2 (2)	2.4 (4)	1.3	0.9 (1)	0.5 (1)
Bayswater	2.0	1.7 (2)	2.8 (2)	1.6	2.5 (2)	0.5 (1)
(Glass Si:Al = 7.5)	2.5	1.7 (2)	3.2 (2)	1.5	1.3 (1)	0.4 (1)
	3.0	1.9 (3)	3.2 (2)	1.3	1.3 (1)	0.4 (1)

All of the geopolymers had Si:Al ratios that varied from their designed ratios. Interestingly the direction of the deviation from the designed ratio reflected their activating solution. The sodium aluminate activated samples exhibited aluminium rich geopolymer gel and as such their as-cured Si:Al ratio was lower than designed. The sodium silicate activated samples exhibited silicon rich geopolymer gel and as such their as-cured Si:Al ratio was generally higher than designed.

After firing, the mixing of aluminosilicates from the previously unreacted fly ash particles into the geopolymer gel resulted in the Si:Al increasing or decreasing depending on the Si:Al of the amorphous aluminosilicates it each particular fly ash. For example, the Si:Al ratio in the Eraring 2.5 geopolymer increased from 1.4 to 2.8 after firing due to the contribution of amorphous aluminosilicates with a Si:Al ratio of 5.0. For the Collie 2.5 geopolymer, the Si:Al reduced from 3.3 to 2.8 due to the contribution of aluminosilicates with a Si:Al ratio of 1.2. Figure 6-16 contains graphs that show the shift in the measured Si:Al of the geopolymer gel for each sample

before and after firing. It can be seen that the measured Si:Al ratio moved towards the designed Si:Al ratio in all samples except the Collie 2.0 sample. In some instances the measured Si:Al passed the designed ratio suggesting that some of the unreacted crystalline aluminosilicates also were entering the geopolymer gel phase upon firing (more details in section 6.4).

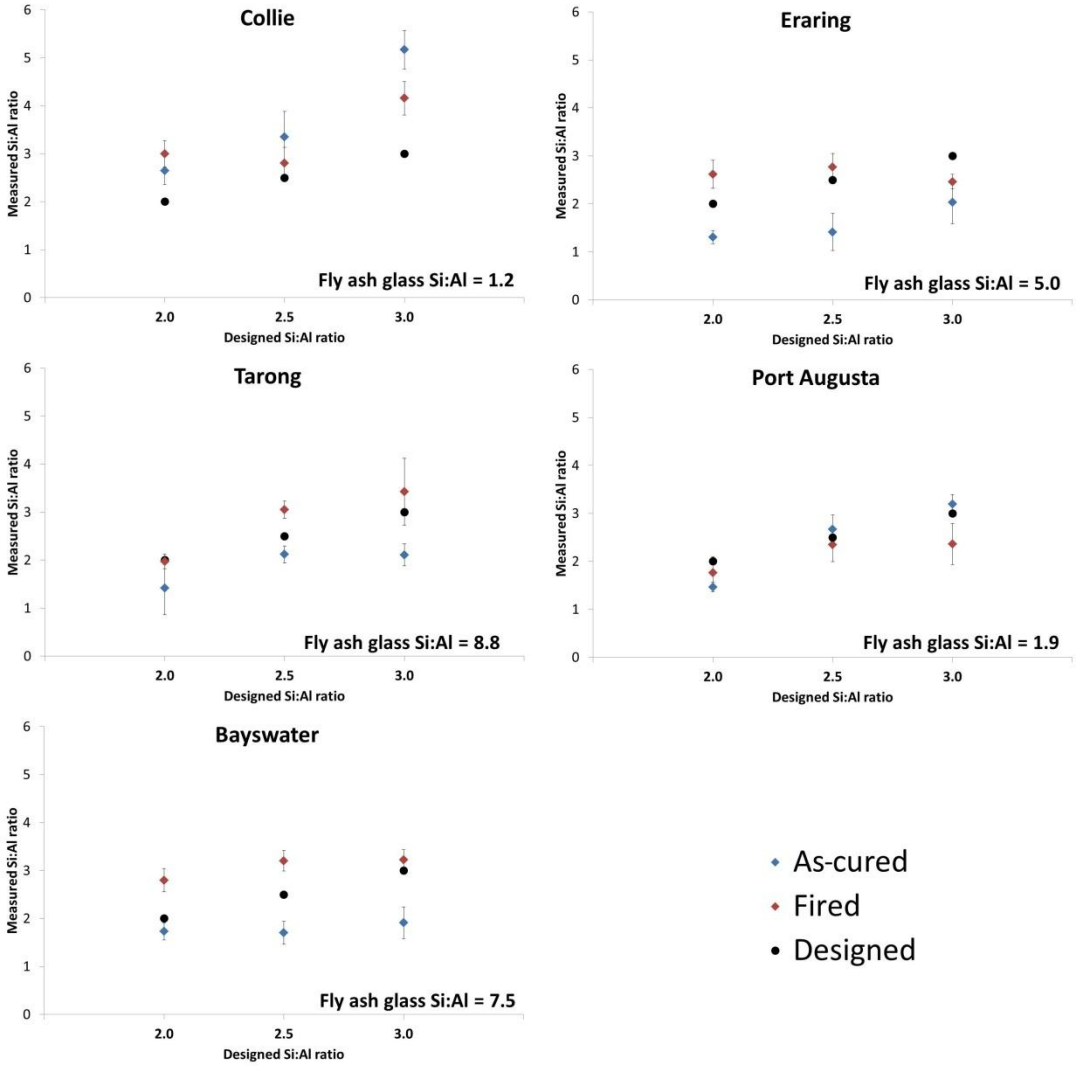

Figure 6-16 Graphs of measured versus designed Si:Al ratio of the geopolymer gel for all samples before and after firing (molar ratios).

The Na:Al ratios in the as-cured samples were expected to be higher than the designed ratios due to the incomplete dissolution of aluminosilicates during the geopolymerisation reaction, leaving excess sodium in the structure. The measured Na:Al ratios for the as-cured samples from most of the geopolymers reflected this expectation, though for some of the samples, in particular the Port Augusta

geopolymers, the ratios were equal or lower than the designed ratios. It is likely that some of the excess sodium would remain dissolved in the pore water and as such it would not necessarily contribute to the measured sodium content in a vacuum dried sample as used for EDS analysis. This effect would be more pronounced in the completely dehydrated samples after firing, explaining why their measured Na:Al ratios were less than expected.

6.3.2 Elemental Distribution in the Geopolymer Gel

EDS mapping was performed to assess the migration of the various elements after firing and to obtain an "average" distribution that point analysis (section 6.3.1) was unable to provide. Figure 6-17 and Figure 6-18 compare the elemental distribution of the as-cured and fired sodium silicate activated Collie fly ash geopolymer and the sodium aluminate activated Eraring fly ash geopolymer (Si:Al = 2.5), respectively.

The clear change after firing in both samples was a more homogenous distribution of the geopolymer gel phase elements. Some differences in the magnitude of the redistribution of silicon and aluminium were observed between the sodium silicate activated geopolymer and the sodium aluminate activated geopolymer. The aluminium in the as-cured, sodium silicate activated geopolymer was predominantly concentrated in the unreacted fly ash particles (Figure 6-17). After firing, the distribution of aluminium was significantly more homogenous. Conversely, the silicon in the sodium aluminate activated geopolymer was initially concentrated in the unreacted fly ash particles. After firing, the distribution was much more homogenous (Figure 6-18). The distribution of the sodium in all samples was, as expected, observed to be solely located in regions identified as geopolymer gel.

As was also indicated by the point analysis and observed in the SEM micrographs, the microstructure of fly ash geopolymers becomes more homogenous after firing due to the sintering and viscous flow of aluminosilicates out of previously unreacted fly ash particles into the geopolymer gel phase.

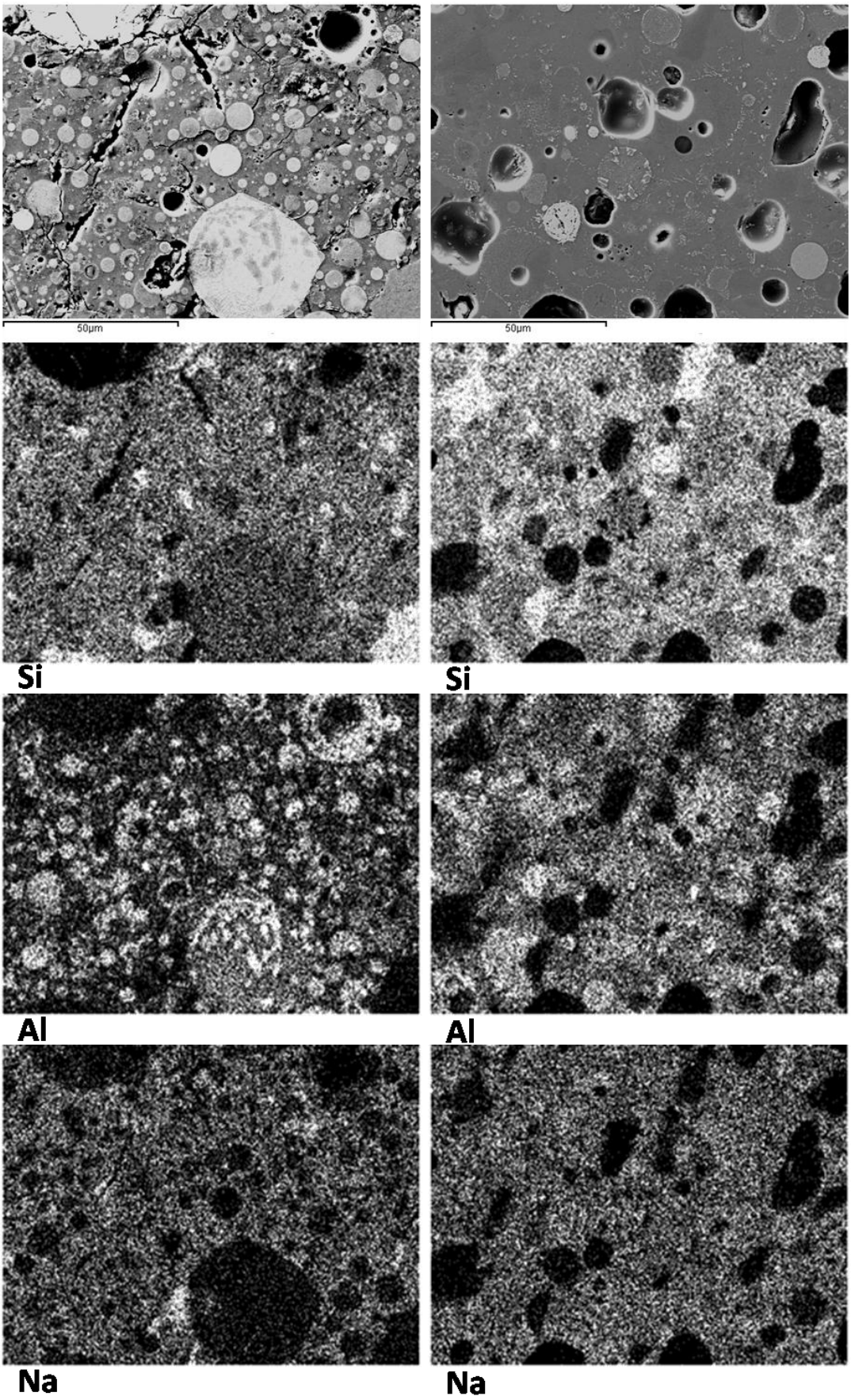

Figure 6-17 SEM micrograph and corresponding EDS elemental maps for the Collie Si:Al = 2.5 geopolymer. Left: As-cured, right: Fired. The maps for Fe, O, Ti and Ca are not shown.

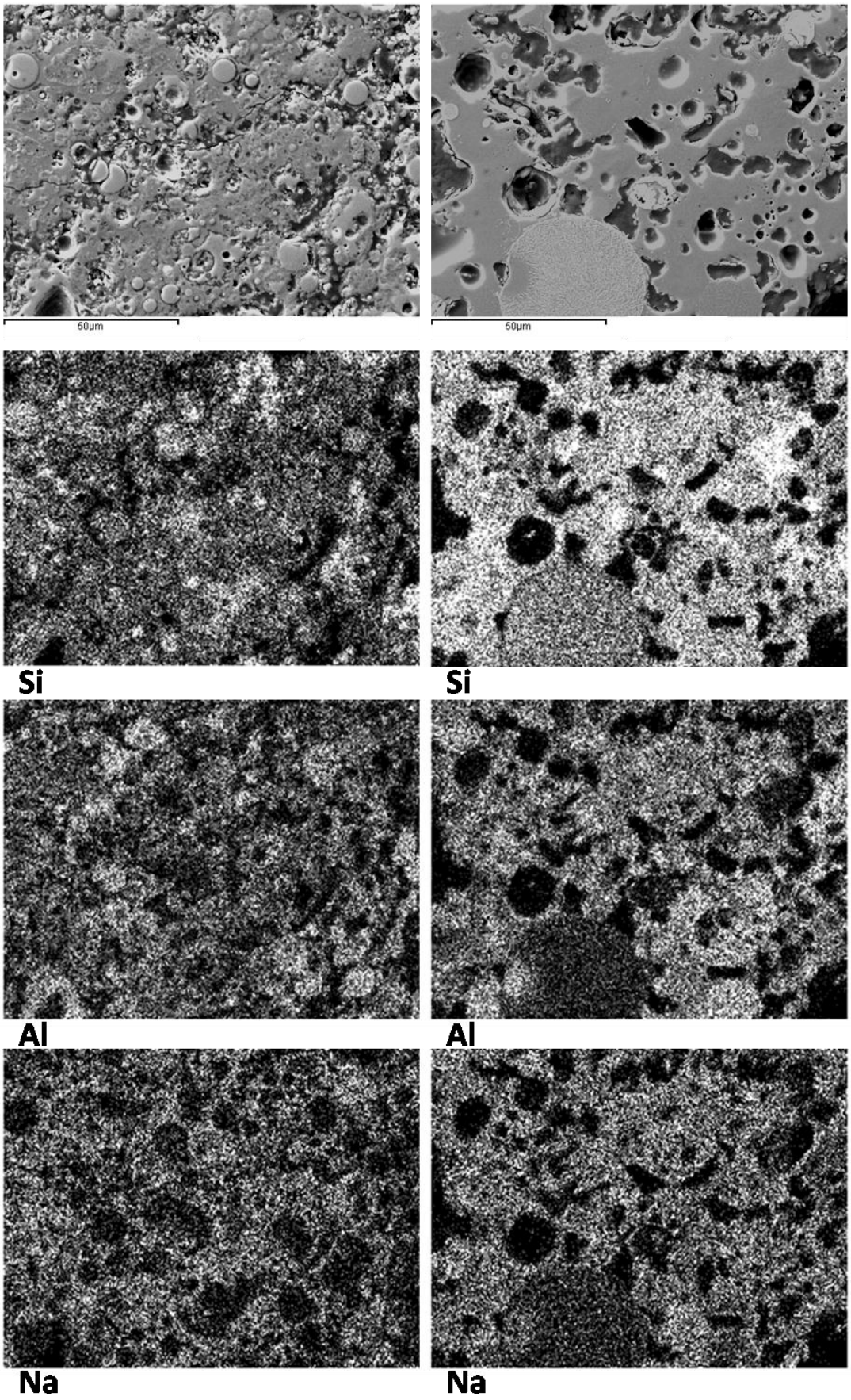

Figure 6-18 SEM micrograph and corresponding EDS elemental maps for the Eraring Si:Al = 2.5 geopolymer. Left: As-cured, right: Fired. The maps for Fe, O, Ti and Ca are not shown.

6.4 Phase Analysis

Figure 6-19 to Figure 6-23, inclusive, contain the XRD patterns for the geopolymers from each fly ash before and after firing. The crystalline phase composition of the as-cured geopolymers reflected their source fly ash by containing the same phases. XRD is generally not able to distinguish between the amorphous glass in the fly ash and the amorphous geopolymer gel. Previous research by Williams et al. (2011) has shown that it is possible to distinguish between the amorphous phases in metakaolin geopolymers by modelling the two humps though this was not achievable in the samples in this study as the amorphous fly ash and the amorphous geopolymer humps were not distinguishable.

In addition to the crystalline material from their source fly ash, the sodium aluminate activated geopolymers (Eraring, Tarong and Bayswater) also contained various hydrated zeolitic phases such as hydrosodalite ($Na_6(AlSiO_4)_6$ $8(H_2O)$) and faujasite-Na ($Na_{1.88}Al_2Si_{4.8}O_{13.54}9H_2O$). These samples were observed by SEM to have a low concentration of geopolymer gel which suggests there was incomplete activation and incorporation of the activating solution into the geopolymer phase. The zeolitic phases found in these samples were likely to have crystallised out of the residual activating solution and the dissolved aluminosilicates that did not geopolymerise. The broad diffraction peaks for these phases suggests that the degree of order was low. The peak intensity of the zeolitic phases was detected to increase as the Si:Al ratio reduced indicating that there was a greater concentration of these phases in the samples with more aluminate added via the activating solution.

Tarong fly ash geopolymers were found to contain gibbsite ($Al(OH)_3$). Gibbsite is likely to have precipitated out of the sodium aluminate activating solution either prior to sample synthesis or during the geopolymerisation process when the pH of the solution dropped as the sodium was consumed by the geopolymer phase.

After firing the samples retained their characteristic amorphous hump though there were changes in the crystalline phase composition. The hydrated zeolitic phases that were detected in the as-cured geopolymers were destroyed upon firing. The samples

were instead found to contain sodium based feldspars. Nepheline ($NaAlSiO_4$) was detected in all of the geopolymers after exposure to high temperature. Other phases formed were albite ($NaAlSi_3O_8$) (Collie and Port Augusta geopolymers) and tridymite (SiO_2) (all except Port Augusta geopolymers). These high temperature phases are reported to improve the thermal resistance of the geopolymers due to their high melting points (nepheline 1257 °C, albite 1118 °C (Schairer and Bowen, 1956) and tridymite 1670 °C (Deer et al., 1996, Barbosa and MacKenzie, 2003b, Kovalchuk and Krivenko, 2009).

It was not possible to determine if the new phase(s) derived from changes in the original crystalline material or crystallisation of amorphous material either from the unreacted fly ash or the geopolymer gel. Previous research has found the geopolymer gel phase remains totally amorphous when fired up to 1200 °C (Barbosa and MacKenzie, 2003a), whereas other studies have observed crystallisation starting as low as 600 °C (Duxson et al., 2007c). It is believed by the author of this study that the bulk of the crystallisation observed in the samples derived from the free Na, Si and Al species after the decomposition of the poorly ordered zeolitic phases that were present in the as-cured samples. This is supported by the amorphous hump in the diffraction patterns remaining largely the same after firing. However, as the EDS analysis revealed, the composition of the geopolymer gel phase was highly variable and as such there were likely to be regions where chemistry was favourable for crystallisation. Thus, a portion of the phases formed after high temperature exposure could have resulted from the decomposition of the geopolymer gel, though the retention of an amorphous hump in the post fired samples suggests this was a minor contribution.

The peak intensity of the mullite and the quartz phases were found to reduce in all geopolymers after firing. Mullite has a melting point of approximately 1830 ºC, varying slightly with mullite composition (Schneider et al., 2008). As such it was not expected that the mullites would melt or be destroyed during firing to 1000 ºC. It is believed that the presence of free sodium in the geopolymers caused the low temperature melting of the mullite into the geopolymer phase as alkali's are known to be excellent sintering agents (Kovalchuk and Krivenko, 2009). The reduction of quartz peak intensity was likely due to the partial phase change to tridymite which

occurs above 870 ºC. (Deer et al., 1996). Tridymite reverts back to quartz when cooled slowly however in regions of the sample where the cooling was rapid, such as the exterior, tridymite is likely to remain at room temperature.

Phase changes were also observed in the iron oxides though they were difficult to analyse due to their low peak intensity and extensive peak overlap with other phases. In most of the samples, maghemite-C (Fe_2O_3) was destroyed or detected with reduced peak intensity after firing. Magnetite (Fe_3O_4) (Collie and Eraring geopolymers) peak intensity was not observed to change after firing. Hematite (Fe_2O_3), however, exhibited increased peak intensity, especially in the Collie fly ash geopolymers (due to their higher concentration of iron). Hematite is likely to have crystallised from the amorphous iron oxides in the fly ash as well as from the phase transformation of maghemite-C, known to occur between 370 ºC and 600 ºC (Cornell and Schwertmann, 1996). Port Augusta and Bayswater fly ash geopolymers were found to still contain small maghemite-C peaks after firing. It has been reported that Al substitution in maghemites, as is likely in fly ash phases, can retard the phase transformation (Sidhu, 1988), explaining their presence after firing.

The phase composition after firing was largely independent of Si:Al ratio as the phases for the three samples for each fly ash geopolymer were the same. However, it was observed that the peak intensity of the formed phases varied with Si:Al ratio. In all samples the peak intensity of the nepheline phase reduced with increasing Si:Al ratio. This suggests that a low silicon content was more favourable for nepheline crystallisation (consistent with Si:Al of 1 for nepheline) in geopolymers fired to 1000 ºC. The trend for the albite was not consistent across the fly ashes. In the Collie fly ash geopolymers the peak intensity of the albite phase decreased with increasing Si:Al ratio, whereas in the Port Augusta geopolymers the peak intensity increased. Albite was not detected in the geopolymers from the other fly ashes.

The following paragraphs contain a summary of the phase changes detected for the geopolymers from each of the five fly ashes:

Collie fly ash geopolymers: As-cured – Amorphous, crystalline phases reflect source fly ash phases. After firing – Decreased mullite peak intensity, maghemite-C destroyed, increased hematite peak intensity; nepheline, albite and in the Collie 3.0 sample, tridymite formed.

Eraring fly ash geopolymers: As-cured – Amorphous, crystalline phases reflect source fly ash phases with the inclusion of various poorly ordered zeolitic phases. After firing – Decreased mullite and quartz peak intensity, maghemite-C destroyed, slightly increased hematite peak intensity, zeolitic phases destroyed; nepheline and tridymite formed.

Tarong fly ash geopolymers: As-cured – Amorphous, crystalline phases reflect source fly ash phases with the inclusion of faujasite-Na and gibbsite. After firing – Decreased mullite and quartz peak intensity, faujasite-Na and gibbsite destroyed; nepheline and tridymite formed.

Port Augusta fly ash geopolymers: As-cured – Amorphous, crystalline phases reflect source fly ash phases. After firing – Decreased mullite and quartz intensity; nepheline and albite formed.

Bayswater fly ash geopolymers: As-cured – Amorphous, crystalline phases reflect source fly ash phases with the inclusion of various poorly ordered zeolitic phases. After firing – Decreased mullite and significantly reduced quartz intensity (most particular in the Si:Al = 2.0 sample), zeolitic phases destroyed; nepheline and tridymite formed.

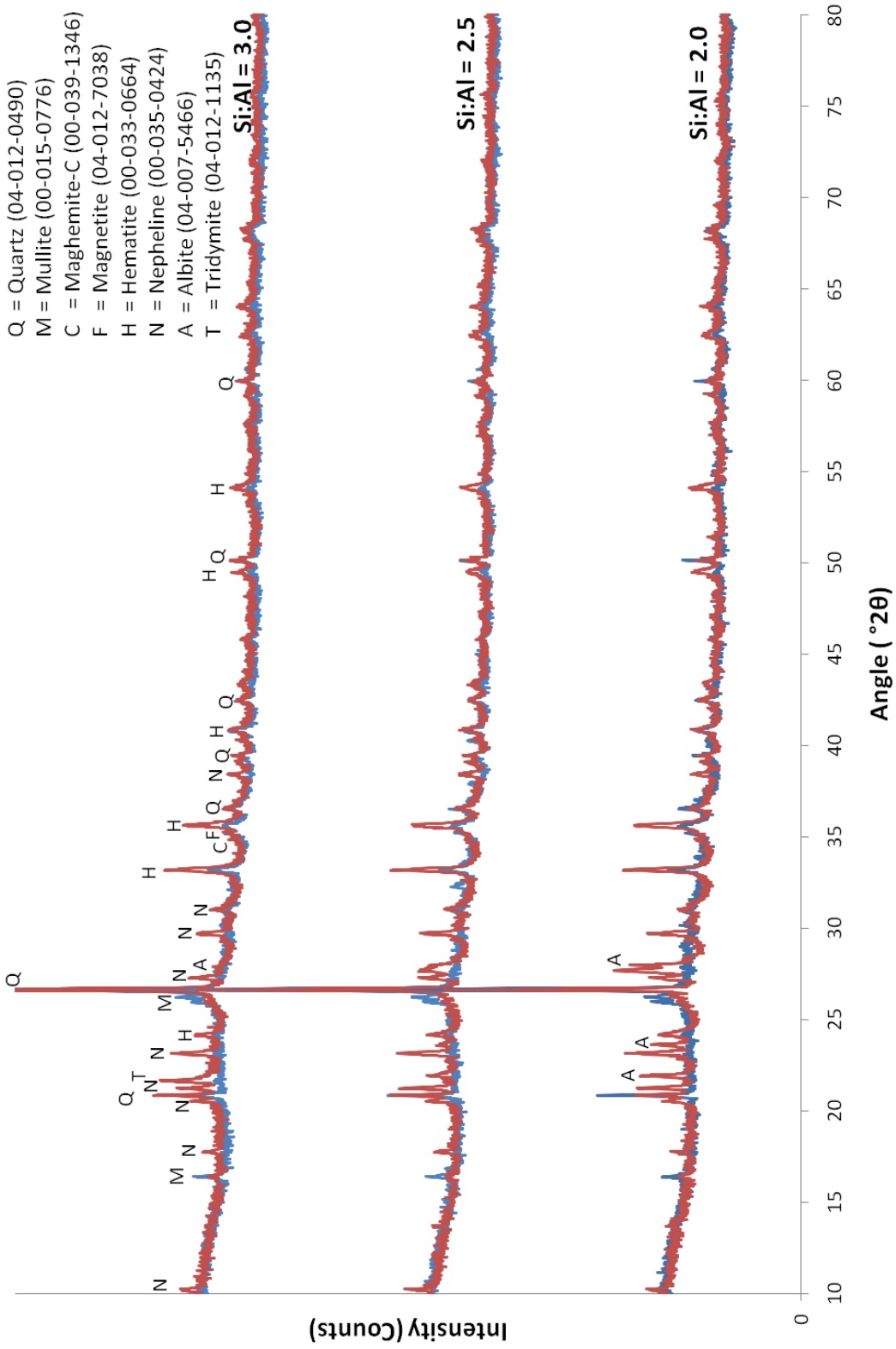

Figure 6-19 XRD patterns for the Collie geopolymers before and after firing. Blue = as-cured, red = fired.

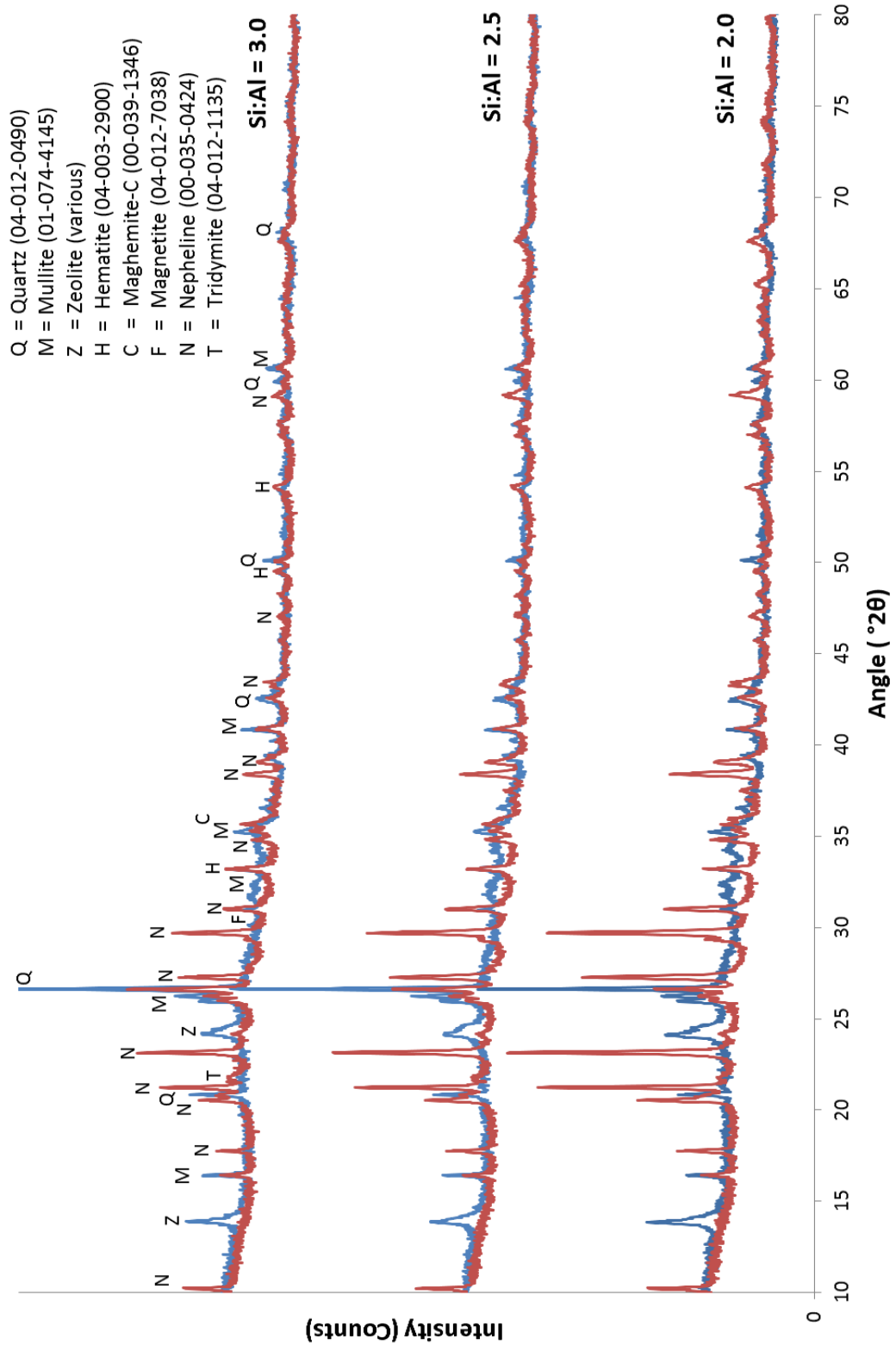

Figure 6-20 XRD patterns for the Eraring geopolymers before and after firing. Blue = as-cured, red = fired.

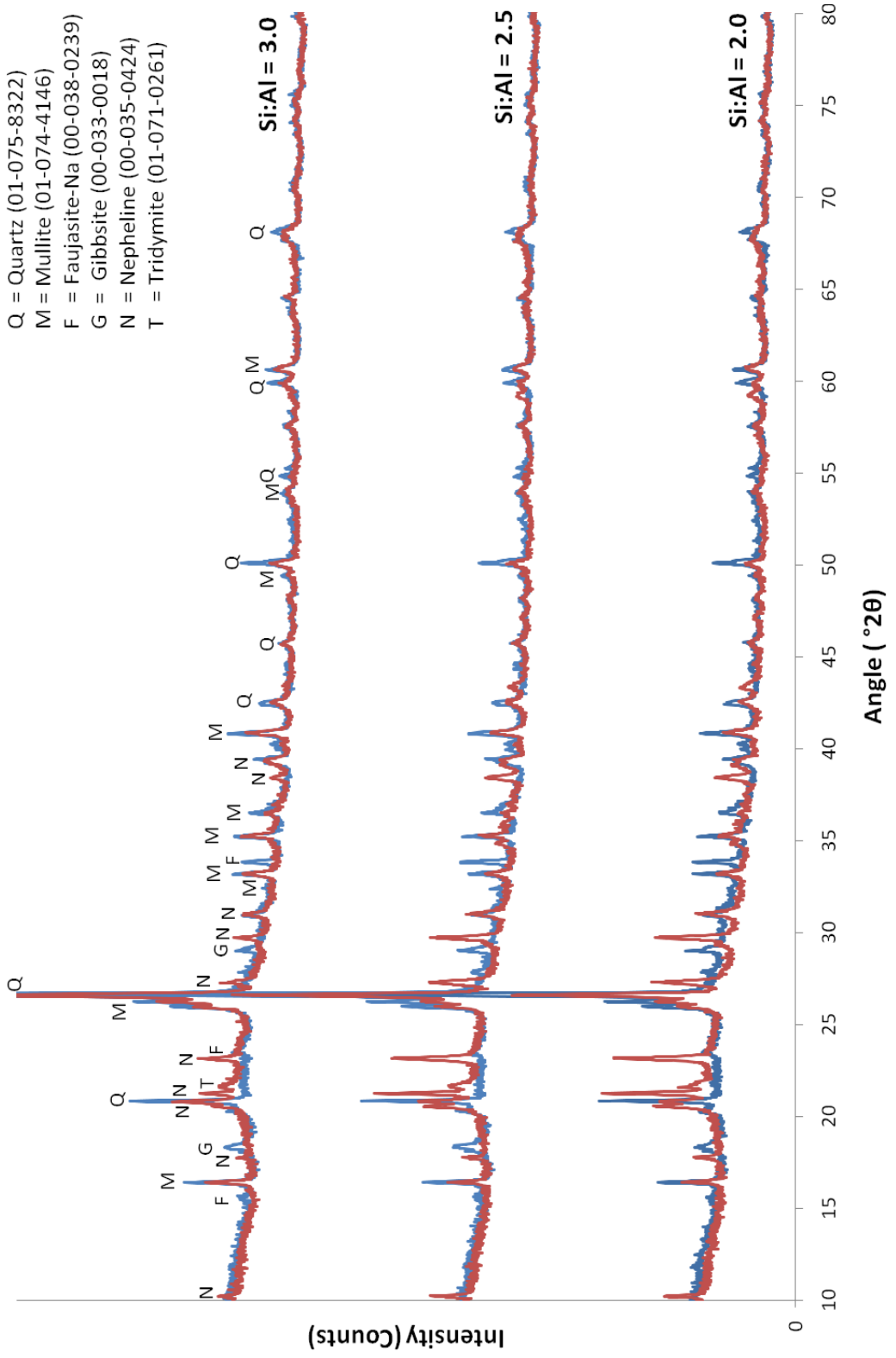

Figure 6-21 XRD patterns for the Tarong geopolymers before and after firing. Blue = as-cured, red = fired.

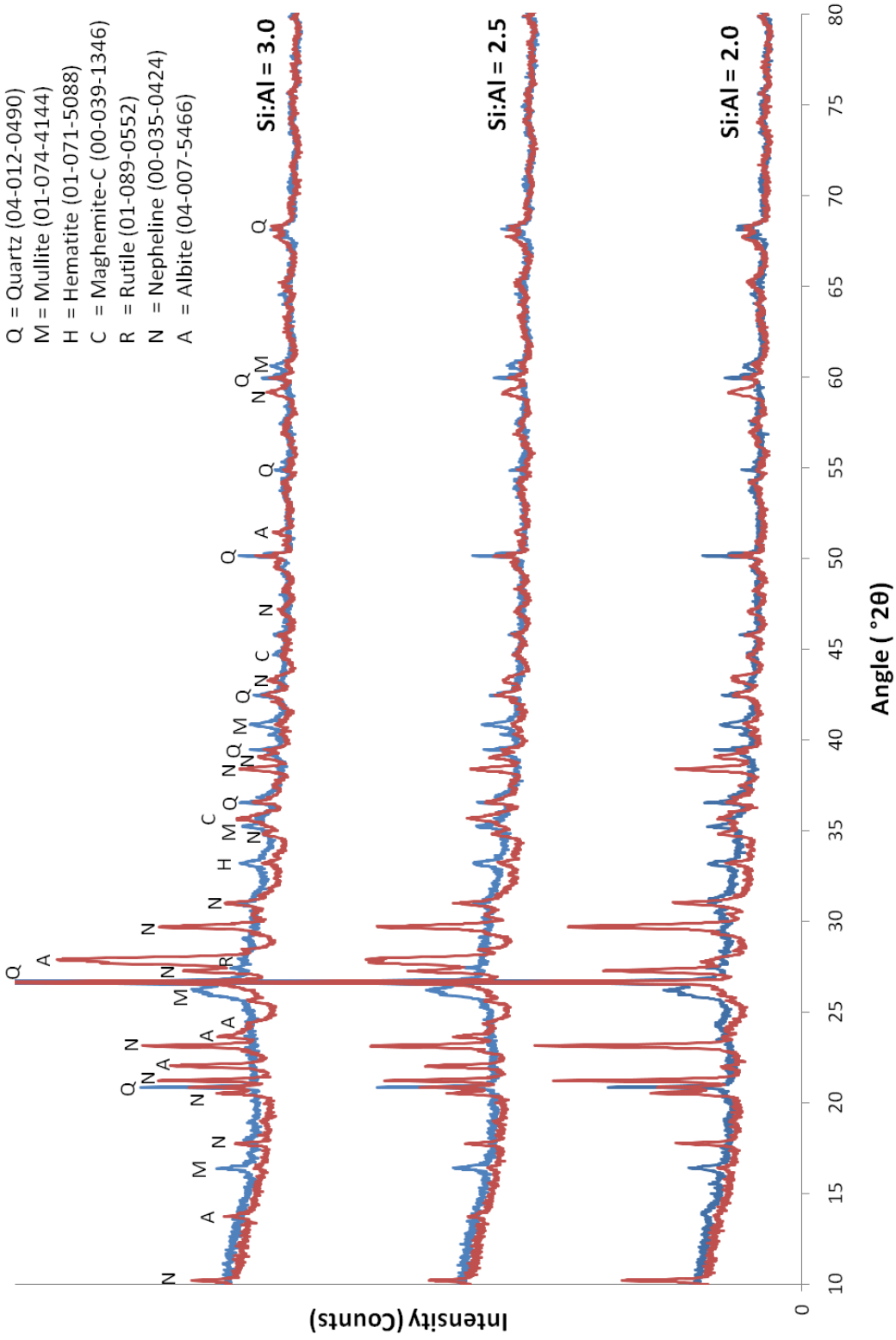

Figure 6-22 XRD patterns for the Port Augusta geopolymers before and after firing. Blue = as-cured, red = fired.

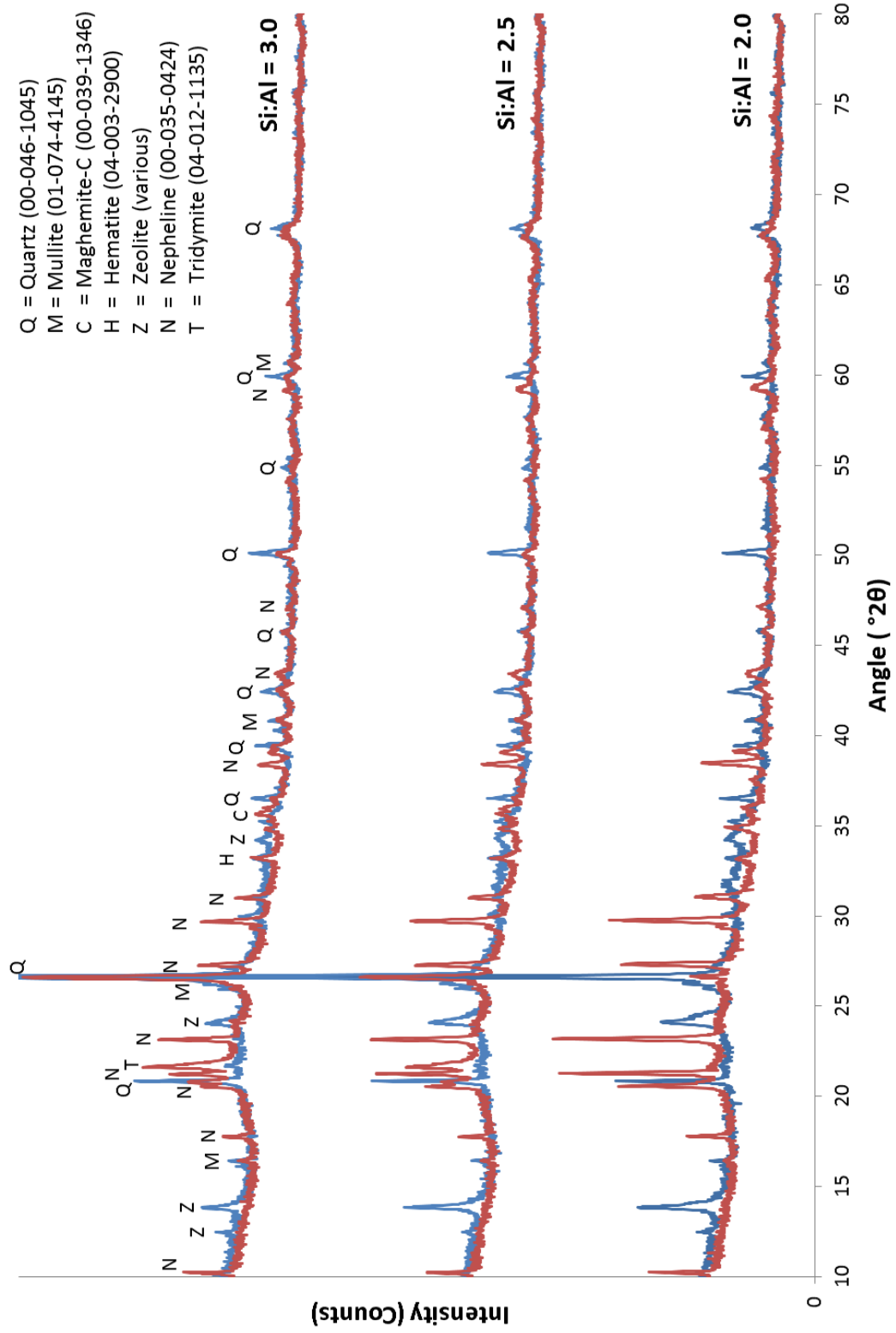

Figure 6-23 XRD patterns for the Bayswater geopolymers before and after firing. Blue = as-cured, red = fired.

6.5 A Conceptual Model for Microstructural Changes after Firing

A model for the microstructural changes in high and low strength geopolymers is proposed in this section. The model was derived from the microstructural observations in this chapter and results from the physical testing in chapter 5. Fly ash geopolymers were divided into four major phases in this simplified model, namely; geopolymer gel, unreacted fly ash particles, crystalline material, and voids / pores. The following behaviour for the four phases is proposed:

- During firing, the geopolymer gel dehydrates its pore and chemically bound water and shrinks as a result.
- At elevated temperatures the amorphous aluminosilicates from the unreacted fly ash particles diffuse into the geopolymer gel.
- The initial crystalline material remains inert during high temperature exposure (XRD results suggested that some of the crystalline material was not inert, however this was not considered in this proposed model).
- New crystalline phases (such as nepheline) form from the decomposed zeolitic phases and the residual activating material.
- Pores are consolidated and become voids in spaces vacated by other phases.

The proposed behaviour of these phases was then applied to the microstructures of high and low strength geopolymers.

6.5.1 Case 1: High strength fly ash geopolymers

'As-cured' geopolymer morphology:

High strength fly ash geopolymers have a microstructure consisting primarily of geopolymer gel. The observable pores range in size from 100 nm to 5 µm and are predominantly isolated. Many of the pores contain water. There are some unreacted fly ash particles, generally greater than 10 µm in diameter. There is some crystalline material, such as quartz, mullite and iron oxides, both within the unreacted fly ash particles and amongst the geopolymer gel. An

example of a fly ash geopolymer with this morphology is the Port Augusta 2.5 sample (Figure 6-7 and Figure 6-11) which had a 28 day compressive strength of 143 MPa.

Behaviour during exposure to 1000 °C:

- The low permeability and isolated pores of the geopolymer forces the dehydrating pore and chemically bound water to create fractures in the geopolymer gel as it is driven out of the structure.
- Volume expansion of the crystalline material causes some localised cracking in the geopolymer gel.

'Fired' geopolymer morphology:

After firing there are much less discernible unreacted fly ash particles. The remaining unreacted fly ash particles are intimately bonded to the geopolymer gel. The geopolymer gel is denser, less porous and also contains some small nepheline crystallites. Cracks can be found throughout the structure, particularly in the vicinity of large crystallites. The increase in gel density is more than offset by the presence of larger pores (5 to 20 µm in diameter) and air voids caused by the cracking, and as such the bulk density reduces.

A schematic of the as-cured and fired morphologies of high strength geopolymers can be found in Figure 6-24 (top left and right, respectively).

6.5.2 Case 2: Low strength fly ash geopolymers

'As-cured' geopolymer morphology:

Low strength fly ash geopolymers have a much lower portion of geopolymer gel and a much greater portion of unreacted fly ash particles than high strength fly ash geopolymers. The geopolymer gel is located on the surface of partially dissolved fly ash particles that range in size from 5 to 20 µm in diameter. The density of the structure is about 20 % lower than the high strength geopolymers as the unreacted fly ash particles prevent close packing of the structure. Well-connected pores / voids fill the space between the geopolymer coated fly ash particles creating a permeable pore structure. Some of these pores / voids contain water. There is some crystalline material, such as quartz and iron oxides, both within the unreacted fly ash particles and as discreet particles. An example of a fly ash geopolymer with this

morphology is the Bayswater 2.5 sample (Figure 6-8 and Figure 6-11) which had a 28 day compressive strength of 6 MPa.

Behaviour during exposure to 1000 °C:

- Dehydrating water is able to evaporate out of the structure relatively uninhibited creating much less fractures in the geopolymer gel when compared to the high strength case.
- Volume expansion of the crystalline material causes less cracking than high strength samples as there are more voids to compensate for the expansion.

'Fired' geopolymer morphology:

After firing there are much less discernible unreacted fly ash particles with the majority of the particles less than 10 μm in diameter now incorporated into the geopolymer gel. The remaining unreacted fly ash particles are intimately bonded to the geopolymer gel. The geopolymer gel is denser, and also contains some small nepheline crystallites. There are fewer pores / voids though they are larger in size than they were prior to firing.

A schematic of the as-cured and fired morphologies of low strength geopolymers can be found in Figure 6-24 (bottom left and right, respectively).

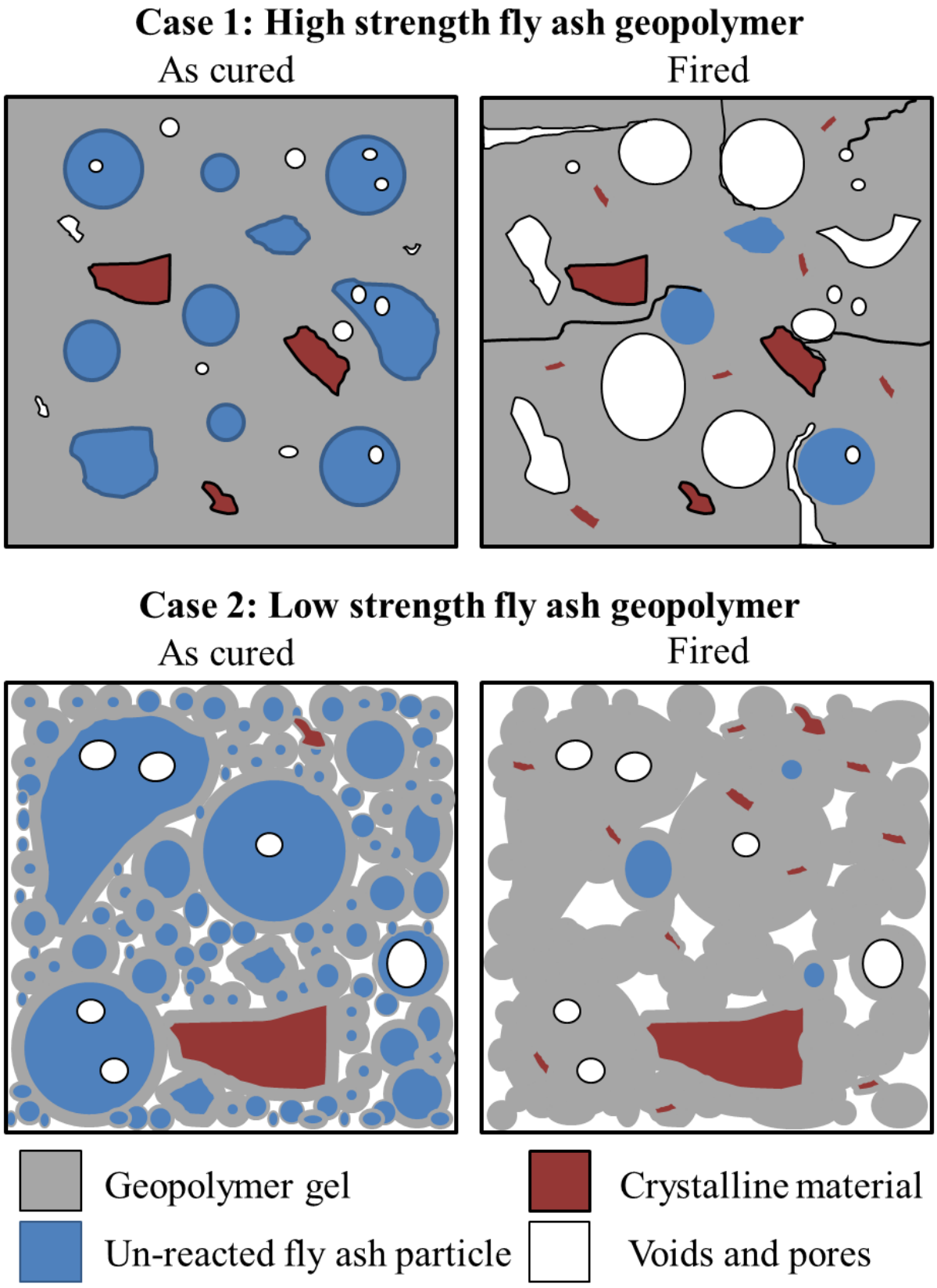

Figure 6-24 Schematic of the proposed microstructural changes upon firing for high and low strength fly ash geopolymers. The field of view for each schematic is 100 x 100 µm.

The proposed model for the behaviour of fly ash geopolymers at elevated temperature is a model for two specific morphologies and as such does not necessarily apply to all geopolymers. For instance, medium strength geopolymers or geopolymers made from a fly ash with a high concentration of quartz are likely to behave differently to the proposed model.

Given these limitation this model can be used to predict the changes in morphology after firing of a fly ash geopolymer if the as-cured morphology matches either the described high or low strength cases.

6.6 Conclusions

The microstructural changes of geopolymers synthesised from five different fly ashes before and after firing have been presented in this chapter. The following paragraphs contain an overall summary of the conclusions from this chapter and chapter 5 (thermal properties of fly ash geopolymers) on the analysis of fly ash geopolymers exposed to 1000 °C in a furnace.

Microstructural investigations of the as-cured geopolymers showed that the sodium silicate activated samples had a greater proportion of geopolymer gel than the sodium aluminate activated samples suggesting that this activating solution was more successful in converting the amorphous aluminosilicates in the fly ashes to form the binding phase. The sodium silicate activated geopolymers were also found to be denser than the sodium aluminate samples. This was partially due to the sodium silicate activated samples being able to be synthesised with marginally lower water content, as a soluble silicate was used to concentrate the activating solutions. The greater portion of binding phase and higher density of the sodium silicate activated geopolymers lead to them having greater compressive strengths than the sodium aluminate activated geopolymers.

After firing, geopolymer compressive strength was affected by microstructural changes in the non geopolymer phases and damage due to dehydration. Sintering was the main factor that lead to increased compressive strength in the geopolymers after firing as it released more of the aluminosilicate material from the unreacted fly ash particles into the binding phase and improved inter-particle connectivity. This effect was evident and reasonably consistent in all

samples and as such the cause for the variable post firing strengths was due to the varying influence of other strength reducing effects.

The magnitude of the difference between the reactive Si:Al ratio in the fly ash to the designed Si:Al ratio of the geopolymers (between 2.0 and 3.0) affected the compressive strength of the samples as it influenced the composition of the activating solution. In the sodium silicate activated samples it was found that increasing the amount of silicon added via the activating solution lead to reduced post firing compressive strengths. It is likely that these samples had silicates from their activating solution that were not incorporated into the geopolymer structure, leaving residual material. A high silicate phase in the sodium silicate activated samples was detected by EDS but not by XRD, indicating that the phase was amorphous.

Thermal expansion measurements indicated that there was swelling of the high silicate phase at high temperatures in the sodium silicate activated samples. It is likely that the swelling of this phase contributed to the strength losses in the sodium silicate activated samples. This is supported by the fact that the post firing compressive strengths of the Collie and Port Augusta fly ash geopolymers reduced significantly as the silica content in the activating solution increased (i.e. as the Si:Al increased from 2.0 to 3.0). SEM analysis also indicated that the sodium silicate activated samples were susceptible to dehydration damage, due to their high concentration of geopolymer gel and isolated pore structure, which would have also contributed to strength loss in these samples.

The amount of aluminium added via the activating solution had little effect on the as-cured compressive strengths of the sodium aluminate activated samples, though it did influence the post firing strengths. It was found that reducing the amount of aluminium added via the solution increased the post firing compressive strength gain. XRD analysis of these samples found that the sodium aluminate activated samples contained crystalline zeolitic phases, with increasing peak intensity with reducing Si:Al ratio in the geopolymer (i.e. increasing aluminium added via the activating solution). These phases were destroyed upon firing which may have had a similar effect on the strength of the geopolymers as the destruction of the high silicate phase in the sodium silicate activated geopolymers, though to a much lesser extent as it was not associated with any significant volume changes in the thermal expansion measurements.

XRD analysis confirmed the as-cured geopolymers were largely amorphous though they still contained the crystalline phases that were initially present in the fly ash precursor. Some of the geopolymers, in particular the low strength geopolymers, contained poorly ordered zeolitic phases as well. After firing the geopolymers remained largely amorphous though they all contained feldspars that likely crystallised from the non-geopolymer phases.

In summary, fly ash geopolymers in this study exhibited strength improving micro structural changes due to sintering after firing. However, the instability of non geopolymer phases during high temperature exposure led to strength losses in some samples depending on the type and composition of the activating solution. The sodium silicate activated geopolymers were more susceptible to damage by non geopolymer phases, such as high silicate phases, as these phases were associated with a volume expansion which subsequently caused cracking and strength losses.

Chapter 7
Performance of Fly Ash Geopolymers Under Simulated Fire Conditions

"Most institutions demand unqualified faith; but the institution of science makes scepticism a virtue."

Robert K. Merton

7.1 Introduction

This chapter reports on the effects of simulated fire exposure on solid and low density, foamed geopolymers. Three mixes were selected from the mixes evaluated in chapters 5 and 6. Eraring and Tarong fly ash mixes with a designed Si:Al ratio of 2.5 were chosen due to their strength gains after firing to 1000 °C and relative thermal stability during thermal expansion testing. The Port Augusta 2.5 mix was also chosen so a comparison with a sodium silicate activated sample could be made. This sample also had high as-cured compressive strength which made it suitable for forming a moderate strength foamed material.

Low density samples were produced by adding a small amount of metallic aluminium to the geopolymer slurry which reacted with the free NaOH to produce a cellular structure. Cellular structured materials are commonly used in fire proofing applications for their insulating capability during high temperature exposure. Fibre reinforcement was used to stabilise the foamed samples by reducing pore collapse prior to the gel hardening. The addition of fibres is also reported to improve the resistance of binding materials to dehydration damage during high temperature exposure by increasing their permeability (Zeiml et al., 2006).

The chapter begins by evaluating the physical properties of the low density geopolymers. The results, along with the results in chapters 5 and 6, were then used to aid in the interpretation of the fire test results from 50 mm thick panels exposed to a simulated fire.

When a sample is referred to in this chapter as ‘fired’ it indicates the sample has been gradually heated in a furnace (with the same heating regime as used in chapter 5 and 6) and not exposed to a simulated fire. Samples that were exposed to a simulated fire are referred to as ‘fire tested’.

The contents of this chapter formed the basis of the following publication;
Rickard, W. D. A. & van Riessen, A. (submitted 2012). Performance of solid and cellular structured fly ash geopolymers exposed to a simulated fire. *Cement and Concrete Composites*.

7.2 Properties of Low Density Geopolymers

Prior to simulated fire testing, the low density geopolymers were characterised. Figure 7-1 is a photo of the low density samples from the three mixes that were analysed. Figure 7-2 shows an example of the cellular structure that was typically formed by the addition of aluminium powder to the geopolymers. The macropores, as formed by the addition of aluminium powder, were observed to range between 1 and 10 mm in diameter. In some regions, as visible on the side of the Eraring 2.5 sample (Figure 7-1), large pores were observed which were due to the coalescence of smaller pores prior to gel hardening.

Figure 7-1 Low density fly ash geopolymer cylinders, 50 mm (diameter) x 100 mm (height). Port Augusta 2.5 (left), Eraring 2.5 (centre) and Tarong 2.5 (right).

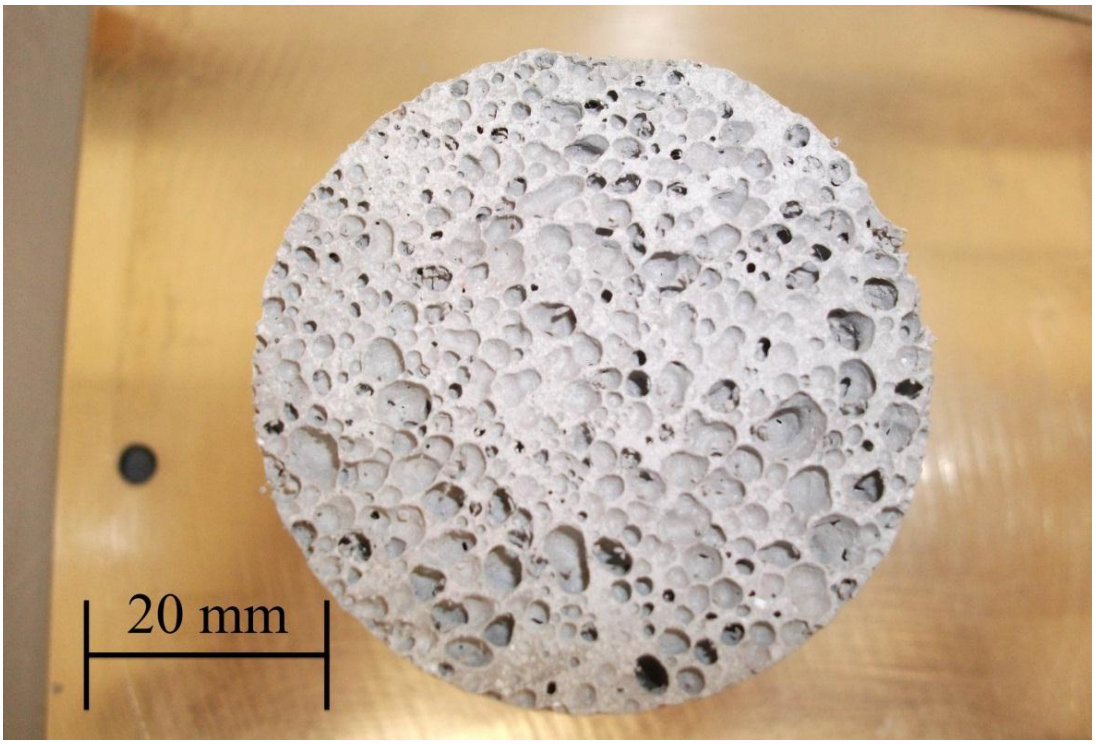

Figure 7-2 An example of the pore size and distribution typically observed in the low density geopolymers foams. Sample: Port Augusta 2.5 geopolymer foamed by the addition of 0.05 wt.% Al powder.

The concentration of the foaming agent (aluminium powder) and the reinforcing fibres (100 % virgin monofilament polypropylene) was kept constant for all the low density samples. This enabled comparisons to be made between the different geopolymer matrices. The concentration of the additives was chosen based on preliminary experiments where slurry workability (reduced by the addition of fibres) and cured density were optimised in order to produce homogenously foamed samples with a density less than 1 g cm^{-3}.

The workability or viscosity of the geopolymer slurry was noted to be highly influential on the mixes' ability to form a homogenous low density sample. If the mix was too easily workable (i.e. low viscosity) then there was a tendency for pores to collapse before curing. Adding fibres reduced the workability of the slurries which in turn reduced pore collapse. When the fibre concentration was too high, however, the workability of the mix was very poor and as such there was poor dispersion of the fibres. It was found that a fibre concentration of 0.25 wt.% produced the best results for each of the three mixes. The addition of 0.05 wt.% aluminium powder

produced samples with as-cured densities close to 0.90 g cm^{-3} (Table 7.1), approximately half the density of the solid mixes.

The Port Augusta 2.5 mix produced the strongest low density geopolymer with a compressive strength of 10.9 MPa. The compressive strengths of the low density Eraring 2.5 and Tarong 2.5 geopolymers were 6.0 and 5.5 MPa, respectively (Table 7.1). The strength of these samples was, as expected, much lower than the strength of the solid geopolymers though they were comparable with other low density geopolymer foams in the literature. A study by Svingala and Varela (2009) on metakaolin and slag based geopolymer foams produced samples with compressive strengths ranging between 2.9 and 9.5 MPa at densities between 1.0 and 1.2 g cm^{-3}.

Table 7.1 Compressive strength and densities of the low density geopolymers before and after firing to 1000 °C. Low density refers to samples foamed with aluminium powder and stabilised with polypropylene fibres. Uncertainties in brackets.

Sample	Compressive Strength (MPa)			Density (g cm^{-3})		
	As-cured	Fired	% of as-cured	As-cured	Fired	% of as-cured
Eraring 2.5 (low density)	6.0 (9)	10.3 (8)	172 %	0.93 (4)	0.90 (3)	within uncertainty
Tarong 2.5 (low density)	5.5 (8)	3.3 (1)	60 %	0.89 (6)	0.87 (5)	within uncertainty
Port Augusta 2.5 (low density)	10.9 (9)	2.5 (3)	23 %	0.92 (6)	0.79 (5)	86 %

The mode of failure during compressive strength testing of the low density geopolymer samples was different to the solid samples due to the fibre reinforcement. Instead of a sharp drop in the stress-strain graph at the point of maximum load, the low density samples exhibited an extended period of plastic deformation (Figure 7-3). The fibre reinforcement allowed the samples to continue to support some load after the initial failure created extensive cracking in the structure (Figure 7-3, image). This characteristic was not observed in the low density samples after firing as the fibre reinforcement vaporises on heating above the melting point of polypropylene, between 160 and 175 °C (Zhang and Horrocks, 2003).

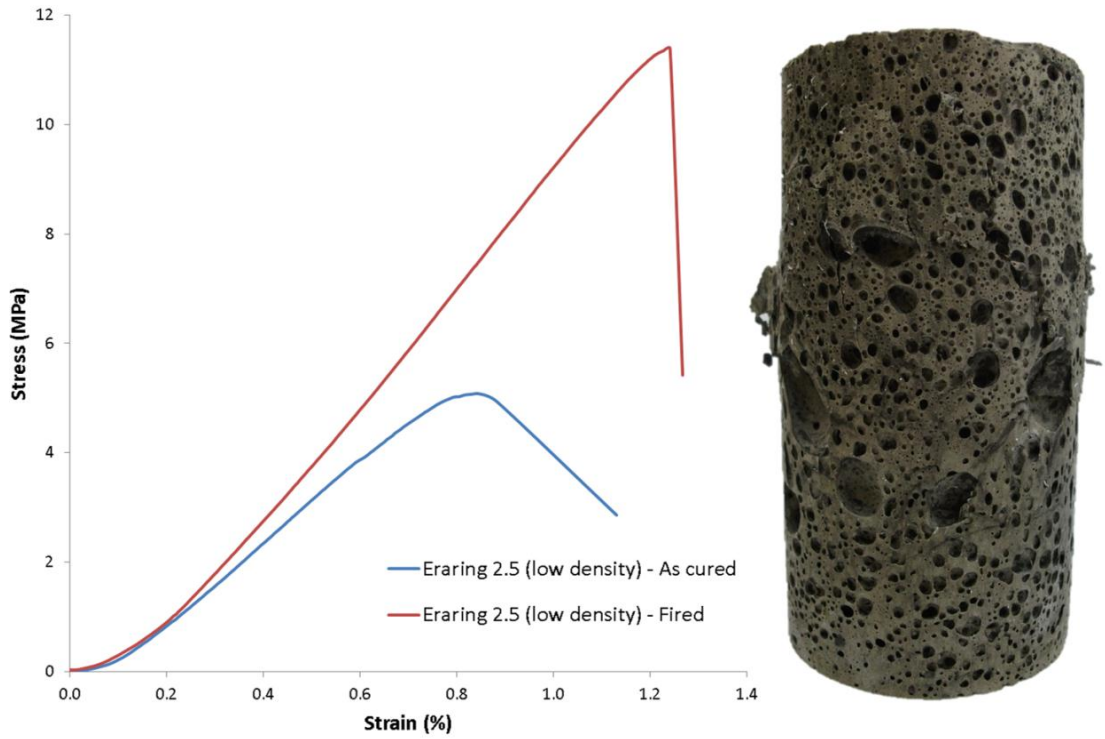

Figure 7-3 Typical stress-strain curve exhibited by the low density geopolymers before and after firing. Image: Photo of an as-cured Eraring 2.5 low density geopolymer after compressive strength testing. Note: The fibres hold the sample together after failure.

After firing the compressive strengths varied with fly ash in a similar manner to the equivalent solid samples as reported in chapter 5. The residual compressive strengths ranked the fly ashes as Eraring > Tarong > Port Augusta, which was the same for the solid samples (with Si:Al = 2.5). However, the percentage strength change on firing for the low density samples differed from the solid samples. The solid Eraring and Tarong 2.5 geopolymers more than doubled their as-cured strength after firing (396 % and 277 % of their as-cured strengths, respectively), whereas the low density equivalent samples exhibited more moderate post firing gains / losses (172 % and 60 %, respectively).

The density change on firing also varied between mixes (Table 7.1). The density of the Eraring and Tarong samples was within the measurement uncertainty, whereas the density of the Port Augusta samples exhibited a density reduction of 14 %. The Eraring and Tarong 2.5 low density geopolymers shrank in volume sufficiently to offset the mass loss from the dehydration of water (and the vaporisation of the polypropylene fibres in the low density samples) (Table 7.2). The low density Port

Augusta 2.5 geopolymer exhibited negligible volume change on firing and as such the density reduced proportional to the mass loss. The reason as to why this sample did not shrink on firing is not clear from the results in this study.

The percentage mass loss on firing for the low density geopolymers was greater compared with the solid equivalent (which exhibited 12.0, 14.8 and 12.9 wt.% mass loss for Eraring, Tarong and Port Augusta 2.5 samples, respectively) (Table 7.2). The percentage change was much greater than the contribution from the loss on ignition of the fibres (0.25 wt.%). This indicated that the low density geopolymers retained more water in their as-cured structure than their solid equivalents. This is counter intuitive given their presumably higher surface area. However it can be explained by the fact that the low density samples were much larger than the solid samples (50 x 100 mm cylinders compared with 15 x 30 mm cylinders) meaning the path length for water to evolve out was longer and as such there was a lower percentage of ambient dehydration.

Table 7.2 Mass and volume changes in the low density geopolymers before and after firing to 1000 °C. Uncertainties in brackets.

Sample	Mass change on firing (wt.%)	Volume change on firing (wt.%)
Eraring 2.5 (low density)	-16.22 (6)	-13.80 (2)
Tarong 2.5 (low density)	-19.80 (6)	-17.90 (2)
Port Augusta 2.5 (low density)	-13.81 (6)	within uncertainty

7.3 Microstructural Evolution of Low Density Geopolymers Fired to 1000 °C

The microstructure of the low density geopolymers was analysed before and after firing to assess the effect of the fibres and macropores (Figure 7-4). The microstructure of the low density samples as observed with a SEM was almost identical to the microstructure of the solid samples. The main difference was the presence of polypropylene fibres in the as-cured samples and hollow tubes in the fired samples where the fibres once were. Some of the smaller macropores were observable in the SEM though the optical images in Figure 7-1 and Figure 7-2 give a better indication as to the pores created by the aluminium foaming agent.

Micrographs of the as-cured samples (Figure 7-4, left images) show that the polypropylene fibres were sparsely spread throughout the geopolymer matrix. The fibre concentration was not considered great enough to create a significant number of dehydration pathways on firing (left after the fibres vaporise) to strongly influence the degree of dehydration damage in the samples. However, the fibres were observed to pin cracks which reduces their propagation, improving the mechanical properties of the material. Fibres are not present in the fired samples as they vaporised on heating (Figure 7-4, right images). As such, the fibres' most significant influence at a concentration of 0.25 wt.% was during sample synthesis (by reducing pore collapse) and crack pinning in the as-cured samples.

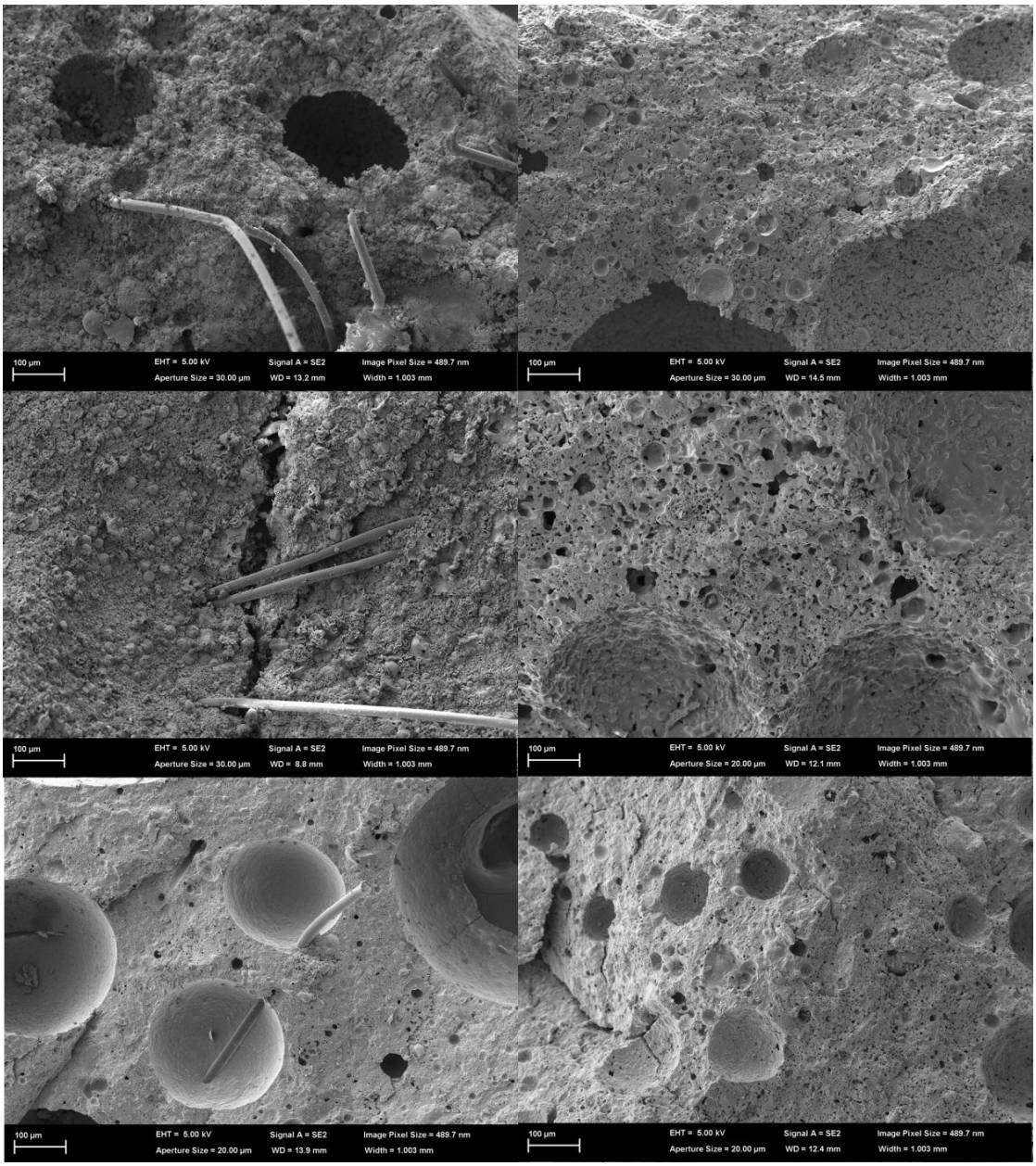

Figure 7-4 SEM micrographs comparing the morphology of the low density geopolymers before (left images) and after firing (right images). Top: Eraring 2.5, middle: Tarong 2.5 and bottom: Port Augusta 2.5.

7.4 Thermal Conductivity of Low Density Geopolymers

The thermal conductivity of the low density geopolymers was evaluated as this property influences the ability of a sample to reduce the transfer of heat from a fire. Thermal conductivity testing of the low density samples was conducted using an embedded hot wire technique (details in chapter 3) so measurements could be

collected over an extended time period (5 - 10 minutes) compared with the KD2 thermal probe that was used to analyse the solid samples (measurement time of 1.5 minutes). The advantage of collecting over an extended period of time was that a greater volume of sample contributes to the measured result as more of the sample has time to be heated. The length of the heating element was also greater in the embedded wire samples further increasing the precision of the measurements. The low density samples have a variable pore structure and as such a larger test volume was considered critical to produce representative results. Figure 7-5 displays typical test results as a sample was heated by the embedded wire over a period of 10 minutes.

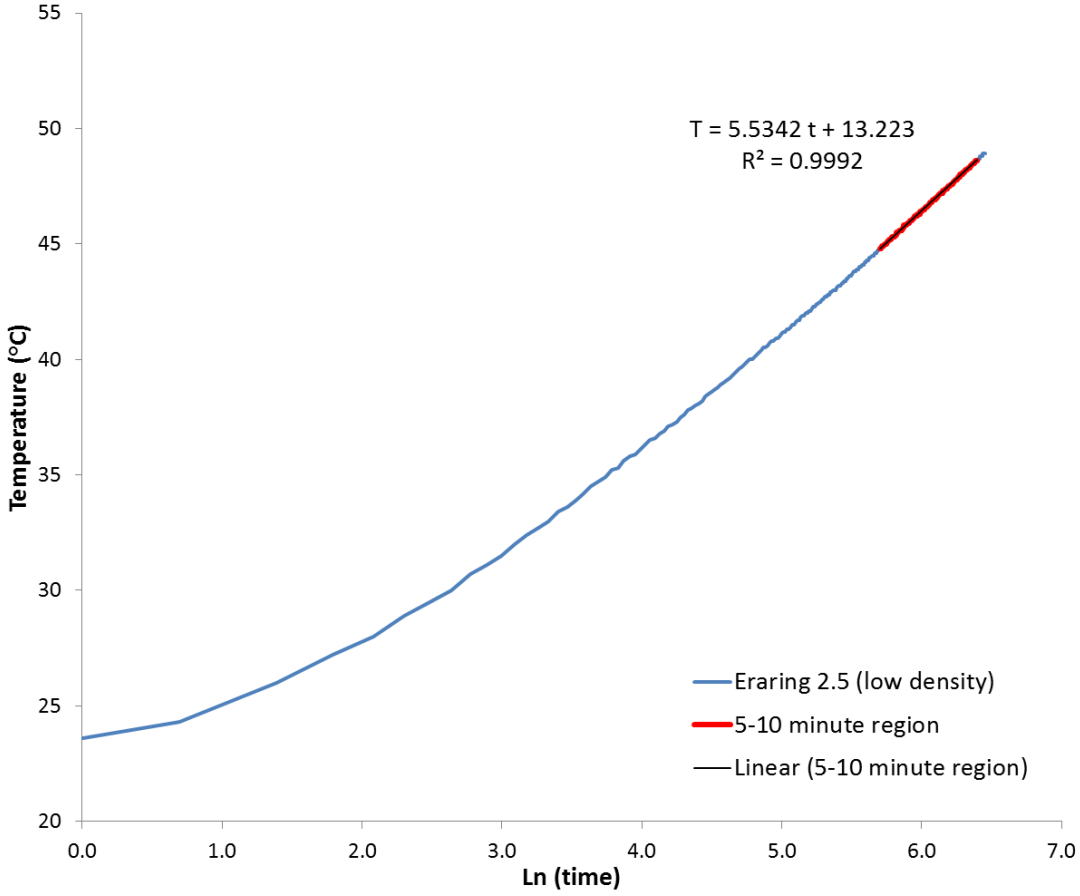

Figure 7-5 Sample temperature versus natural log time (s) for the low density Eraring 2.5 sample as it was heated by an embedded nichrome wire with a voltage of 2 V and a current of 1 A. Thermal conductivity was calculated using the gradient of the curve during the 5 to 10 minute period of the test.

Table 7.3 lists the thermal conductivity of the low density geopolymers as well as including comparisons with the solid equivalent samples described in chapter 5. It was observed that there was an almost direct relationship between reduction in density and reduction in the thermal conductivity of the sample. Prud'homme et al. (2009) measured the thermal conductivity of foamed geopolymers with a density of 0.53 g cm^{-3} to be 0.22 W $m^{-1}K^{-1}$ whereas Vaou and Panias (2010) measured thermal conductivities of between 0.03 and 0.06 W $m^{-1}K^{-1}$ for foamed geopolymers with densities ranging from 0.30 to 0.65 g cm^{-3}. The thermal conductivities of the samples in this study were higher than other foamed geopolymers reported in the literature, though the sample densities in this study were higher than samples in the compared studies.

Table 7.3 Thermal conductivity and density of the low density geopolymers.

Sample	Thermal conductivity (W $m^{-1}K^{-1}$)	% of solid equivalent	Density (g cm^{-3})	% of solid equivalent
Eraring 2.5 (low density)	0.25 (3)	54 %	0.93 (4)	58 %
Tarong 2.5 (low density)	0.31 (5)	57 %	0.89 (6)	56 %
Port Augusta 2.5 (low density)	0.39 (4)	59 %	0.92 (6)	49 %

7.5 Effect of Simulated Fire Exposure on Solid and Low Density Geopolymers

Testing was conducted to assess the performance of geopolymers under simulated fire conditions. Fire tests involve very rapid heating of one side of a sample (hot side) as the temperature on the opposite side (cold side) is measured. This test assesses the ability of the sample to insulate the heat of the fire. Other indicators as to a sample's performance during a fire test are combustibility, smoke release and the retention of sample integrity during and after exposure. In this study combustibility (defined as the ability of a material to ignite) was not required to be assessed as geopolymers are inorganic and do not burn. Similarly for smoke release as the only

smoke producing volatile was the polypropylene fibres in the low density samples and the concentration was too low to produce significant volumes. Insulating performance was measured by three thermocouples on the cold surface and sample integrity was assessed qualitatively by observing the extent of cracking on both sides of the sample.

50 mm thick panels were synthesised from each of the three mixes. An example of the panels can be seen in Figure 7-6. The solid and the low density equivalent of each mix were tested to analyse the effect of reducing the density. Testing was conducted for 120 minutes as this was enough time for all samples to exceed the maximum temperature increase allowable by the Australian standard 1530.4. The justification for continuing the tests after the sample exceeded the failure condition was so that all samples were subjected to the same thermal history and as such phase and microstructural comparisons could be made.

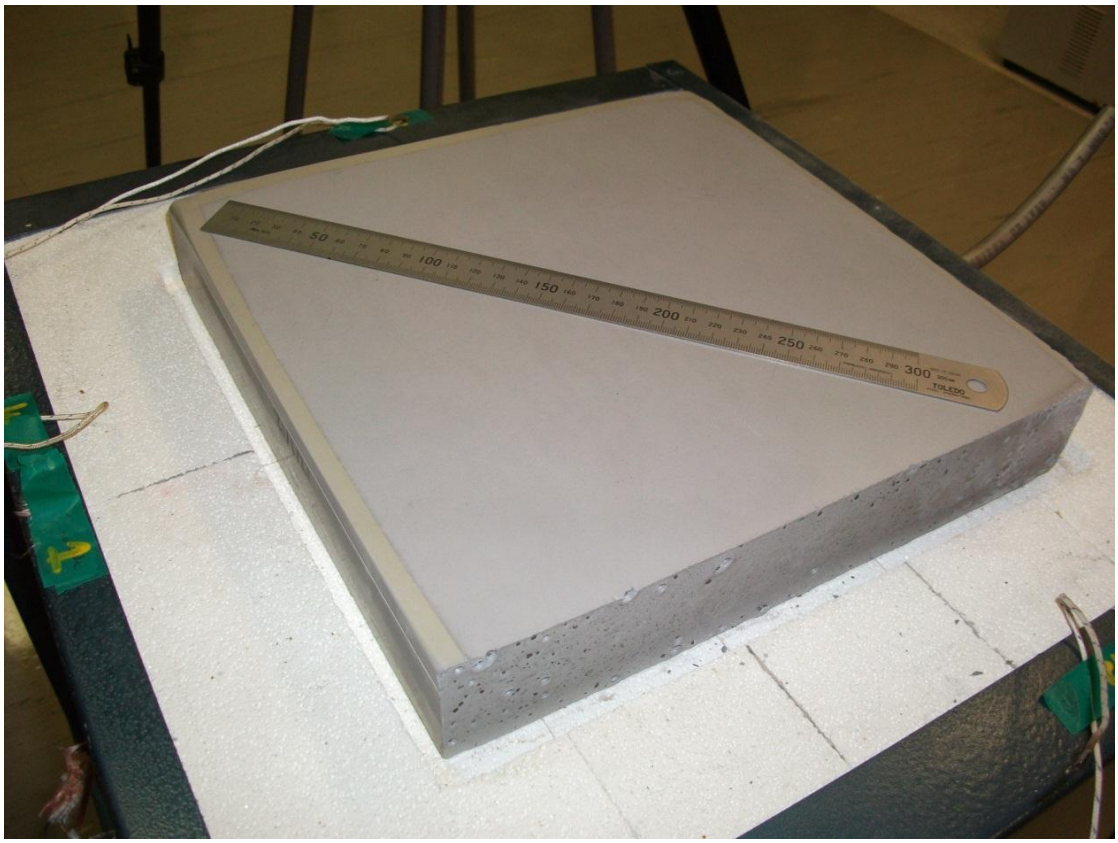

Figure 7-6 A 50 mm thick (290 x 290 mm) geopolymer panel mounted on top of the fire testing furnace (thermocouples yet to be attached). Sample: Port Augusta 2.5 solid geopolymer.

The following three conditions were used to determine the time at which the sample failed (as per AS1530.4, text in italics is directly quoted from the standard);

- Failure condition 1 – "*the average temperature of the unexposed face of the test specimen exceeds the initial temperature by more than 140 K"*
- Failure condition 2 – "*the temperature at any location on the unexposed face of the test specimen exceeds the initial temperature by more than 180 K"*
- Sample integrity – *"failure in relation to integrity shall be deemed to have occurred upon collapse, the development of cracks, fissures, or other openings through which flames or hot gases can pass"*. The standard notes that a crack that is more than 6 mm wide and / or can be measured to be 25 mm deep using a gauge constitutes a failure of the sample's integrity.

Figure 7-7 shows a graph of the typical results collected during the fire testing (full graphs from all the samples are listed in appendix B). In all tests the measured temperature of the furnace lagged behind the temperature required by the standard for the first 10 to 20 minutes. This was largely due to the evaporation of water from the sample which consumed a lot of the energy radiated by the heating elements. This is permissible by the standard which states that a deviation of 15 % from the temperature required is allowable in the first 30 minutes of the test. After the 20 minute mark the furnace was able to remain within a few degrees of the required temperature and well within the deviation allowable by the standard.

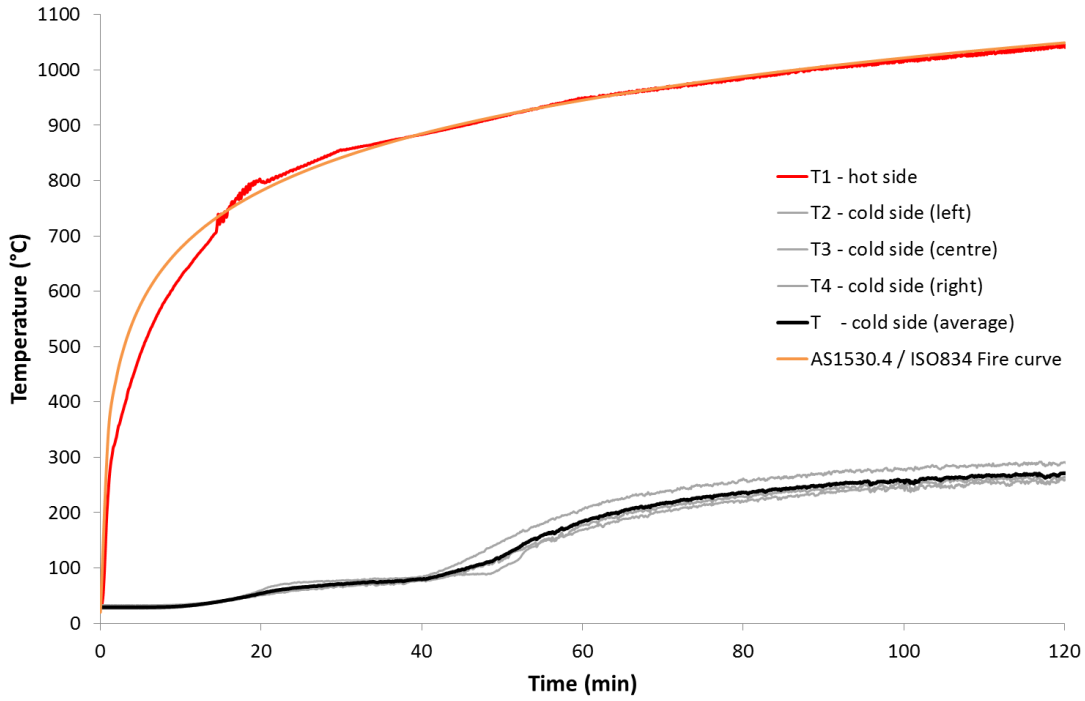

Figure 7-7 Temperature change with time of each of the four thermocouples during a 120 minute fire test on the low density Eraring 2.5 geopolymer. The average temperature of the three cold side thermocouples and the standard fire curve is also plotted on the graph.

All of the samples exhibited common features in the cold side temperature curves during the fire tests, though the gradient and duration of the features varied between the samples. During the initail part of the test (t < 10 minutes) the cold side temperatures remained at ambient. After this period the heat from the furnace conducted through the sample and the cold side temperatures began to increase. The gradual temperature increase during this period was due to the evaporation of water in the sample absorbing much of the energy from the furnace. After this, there was a period when the cold side temperature approached 100 °C where the rate of temperture increase slowed markedly to form a brief plateau in the time-temperature curve. This was due to the passage of the boiling front through the top of the sample and is a common feature in fire tests on hydrated materials. The reason why the temperature recorded by the thermocouples was marginally less than 100 °C as the boiling front passed was due to the thermocouples not being embedded into the sample and as such not all of the hot junction of the thermocouple was in contact with the sample resulting in some heat loss to the air. After the boiling front traversed the sample and the bulk of the water had evaporated, the cold side temperature rose rapidly. The last characteristic of the test curves was the

progression towards equilibrium as the energy dissipated by the sample neared the energy radiated by the furnace. None of the samples achieved equilibrium but all samples showed a destinctive slowing of temperature increase towards the end of the test, most notably in the low density samples.

Figure 7-8 and Figure 7-9 compare the average cold side temperatures from the solid and low density samples from each of the tested geopolymers. Table 7.4 lists the times when the samples exceeded the failure conditions as well as the cold side temperature at the end of the test. For both the solid and low density samples the mixes ranked Tarong 2.5 > Port Augusta 2.5 > Eraring 2.5 in terms of ability to insulate.

None of the samples exceeded the second failure condition or the sample integrity failure condition prior to the first failure condition. As such, the fire ratings for the samples were equal to the time that it took for the average temperature of the cold side to exceed 170 °C (2nd column, Table 7.4).

All samples exhibited varying degrees of cracking during the fire testing, though only the Port Augusta 2.5 sample exhibited cracks that would have caused the sample to fail the integrity criteria (by developing a crack 6 mm wide, see Figure 7-13). The crack initially occurred at the 87 minute mark of the test (4 minutes after the sample exceeded the first failure condition).

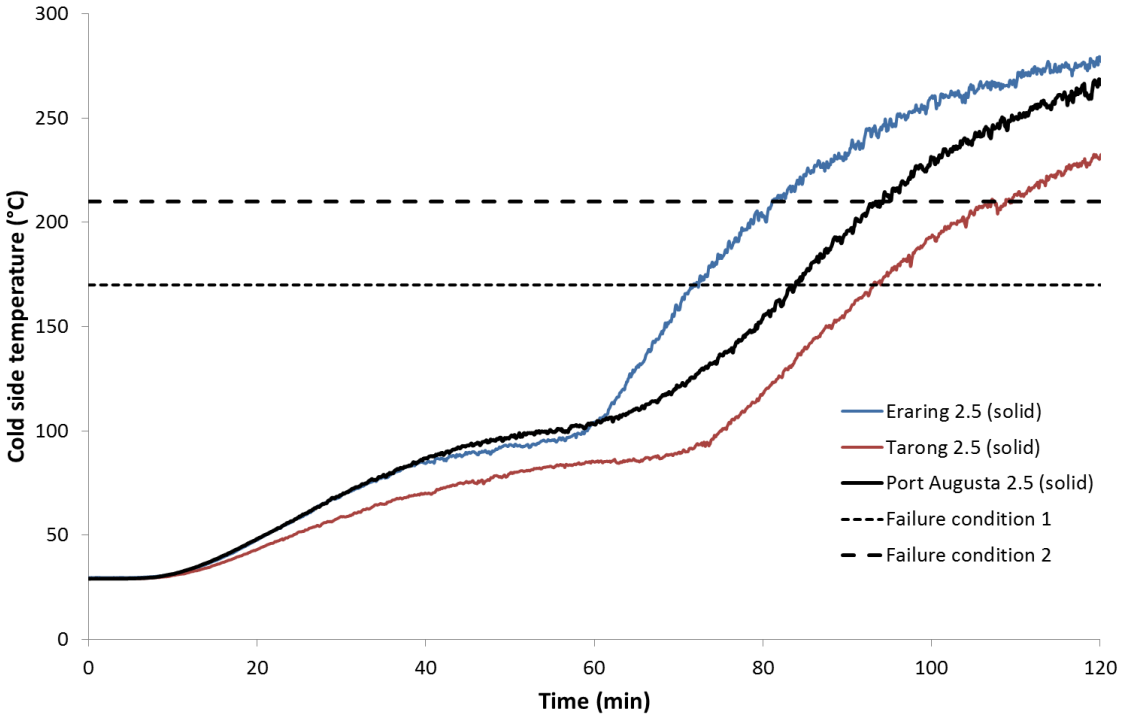

Figure 7-8 Evolution of the average cold side temperature from the three solid geopolymers during a 120 minute fire test.

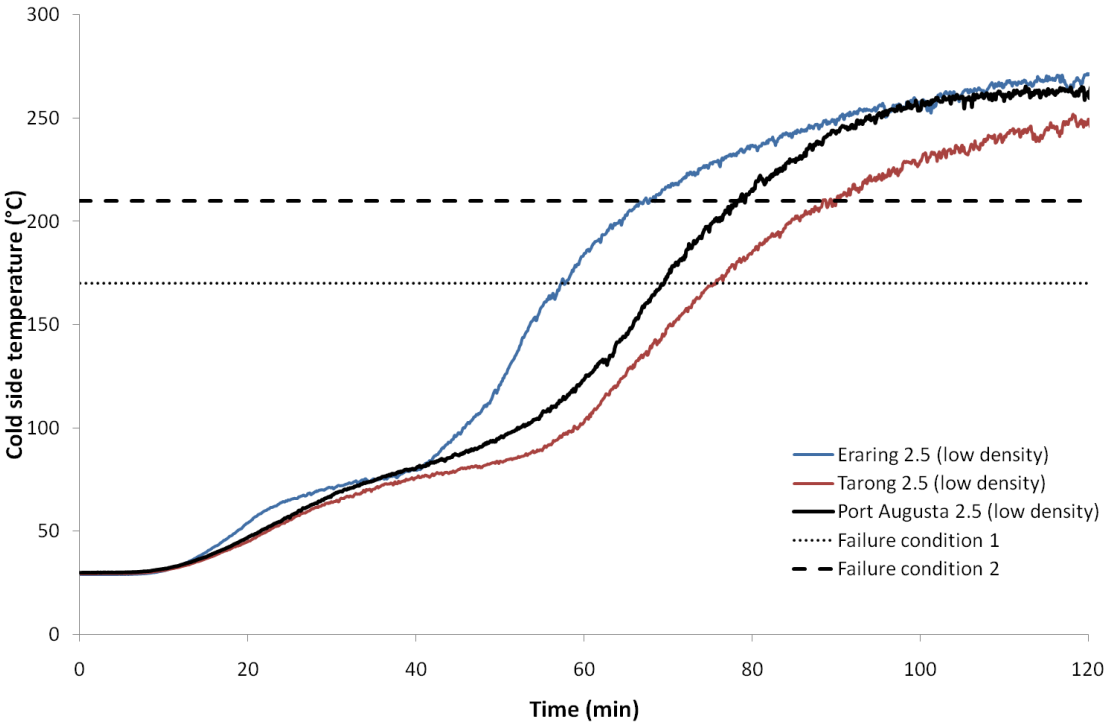

Figure 7-9 Evolution of the average cold side temperature of the three low density geopolymers during a 120 minute fire test.

Table 7.4 Times and temperatures at critical points during the fire testing of the solid and low density samples. Note: the ambient temperature in the furnace room where the fire testing was done was approximately 30 °C.

Sample	Time for T (average) > 170 °C (140 K above ambient) (min)	Time for T (any) > 210 °C (180 K above ambient) (min)	Temperature at 120 minutes (°C)
Eraring 2.5 (solid)	71.8	78.3	279
Tarong 2.5 (solid)	93.2	102.4	231
Port Augusta 2.5 (solid)	83.9	89.7	267
Eraring 2.5 (low density)	57.3	60.8	271
Tarong 2.5 (low density)	75.8	85.8	249
Port Augusta 2.5 (low density)	69.5	74.1	263

Samples were measured and weighed before and after the fire tests to assess their mass loss due to dehydration (Table 7.5). Samples were also ranked in terms of the extent of cracking as determined by a visual observation of the samples after testing. Further details on the cracking in the samples are presented in section 7.6. The time taken for the samples to exceed the failure conditions (Table 7.4) was found to be dependent on the amount of water in the structure, the density of the sample and the degree of cracking. The greatest influence was the water content in the samples, with samples that had a higher water content (equated to mass lost on firing) generally exhibiting longer fire ratings. Harmathy (1965) reported that if spalling does not occur, the presence of moisture is beneficial for the fire endurance of materials in a review of the effect of moisture on the fire endurance of building elements. No spalling was observed in the samples after the fire testing and as such the results in this study were in good agreement with Harmathy's observations.

Water content was not the only influence on the heating rate of the cold side during the fire test as the solid Port Augusta 2.5 sample with the greatest dehydration mass

loss did not have the longest fire rating. The solid Tarong sample had a longer fire rating than the Port Augusta sample due to its lower thermal conductivity and reduced amount of cracking during the test. Cracks allow the heat from the furnace to rapidly progress by convection along the gaps in the structure rather than conducting through the structure and as such greatly increase the heating rate of the cold side.

Table 7.5 Properties of the fire tested panels.

Sample	Density of test panel (g cm^{-3}) ± 0.09 g cm^{-3}	Mass loss during fire test (g) ± 0.01 g	Surface cracking ranking (1 best, 6 worse)
Eraring 2.5 (solid)	1.65	761.93	3
Tarong 2.5 (solid)	1.54	1038.24	4
Port Augusta 2.5 (solid)	1.85	1050.08	6
Eraring 2.5 (low density)	0.92	344.10	1
Tarong 2.5 (low density)	1.00	431.17	2
Port Augusta 2.5 (low density)	1.13	489.12	5

Figure 7-10 compares the fire test results for the solid and low density samples from each mix. It can be seen that the main reason why the low density samples exceed the failure temperature before the solid samples was due to the dehydration plateau being shorter. This was because the low density samples had significantly lower water content owing their lower mass of geopolymer. The other difference between the sample types was the rate of temperature increase towards the end of the test. The low density samples exhibited a low gradient of temperature increase after 100 minutes indicating that they were nearly at equilibrium and it is likely that if the test continued the cold side temperatures would not have increased significantly. The solid samples, however, all exhibited a moderate rate of temperature increase at the end of the test suggesting that they were not yet nearing an equilibrium condition. This was expected as the lower thermal conductivity of the low density geopolymers improved their ability to insulate the heat of the furnace during the test.

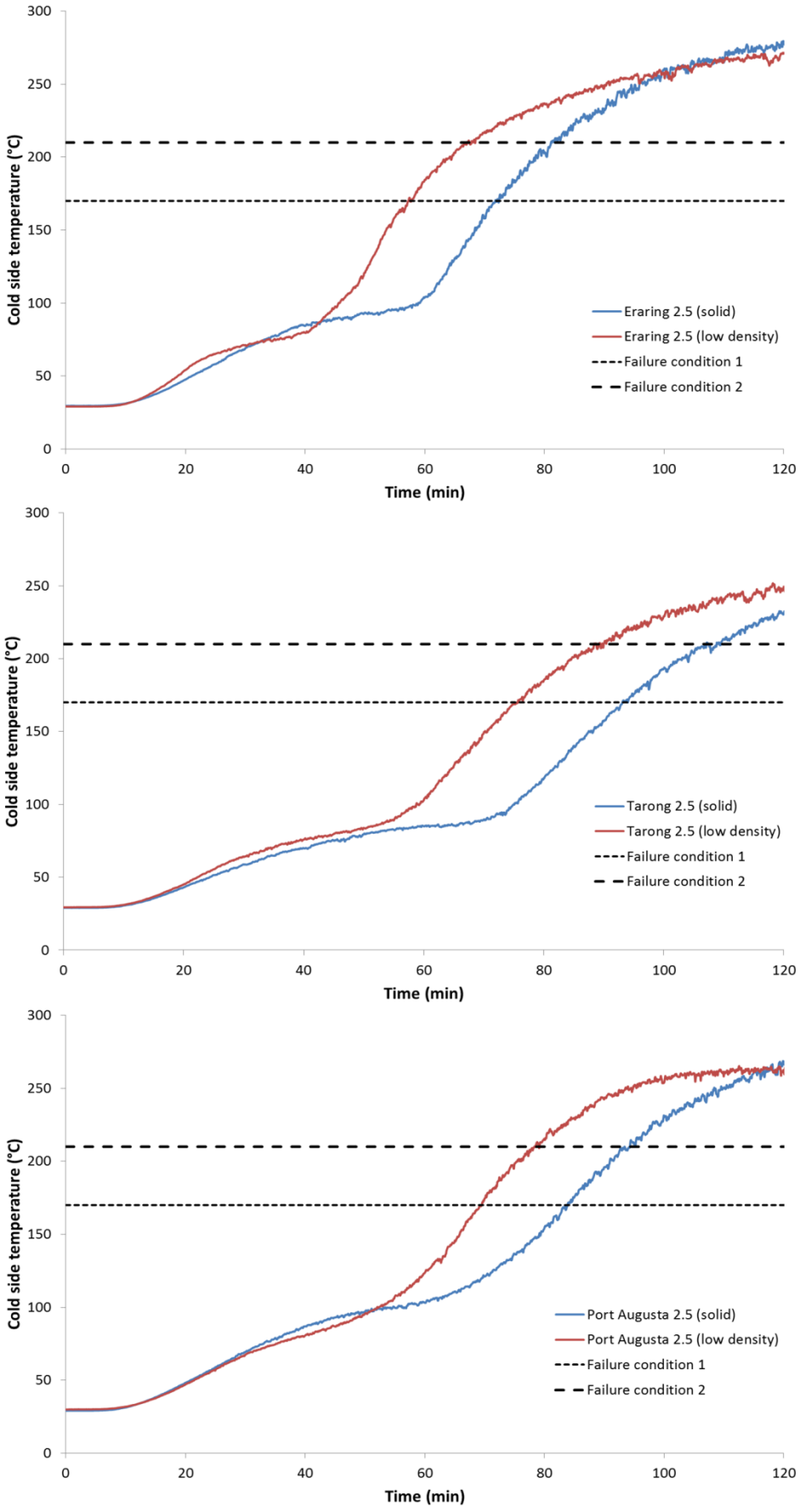

Figure 7-10 Comparison between the solid and low density samples from the Eraring 2.5 (top), Tarong 2.5 (middle) and Port Augusta 2.5 (bottom) geopolymers.

The fire rating for the samples in this study were at least 1 hour with the exception of the Eraring 2.5 sample, which had a fire rating of 57 minutes. The best performing sample was the solid Tarong 2.5 geopolymer which had a fire rating of 93 minutes. The solid geopolymers exhibited greater fire ratings than the low density geopolymers though it was found that the low density samples were better insulators after the samples had dehydrated.

Vilches et al. (2003) conducted small scale fire tests on fly ash based geopolymers and reported that a 33 mm thick geopolymer had a fire rating of just over 60 minutes. It should be noted that the authors of that study used a 180 K increase in cold side temperature as the failure time, whereas in this study a 140 K increase was used.

The fire ratings that were achieved in this study were shorter than common fire rating for fire resistant materials (often 2-4 hours) though they could be increased by simply increasing the thickness of the test panel. Increasing the water content of the mixes would also increase their fire ratings though this may also reduce their as-cured compressive strength and increase the degree of cracking during fire testing.

7.6 Structural Evolution of Geopolymers Exposed to a Simulated Fire

The structural integrity of a material exposed to a fire is important. Firing experiments in a furnace where the samples were heated uniformly at a constant and relatively slow rate showed that some of the geopolymer mixes exhibited strength increasing structural changes on heating. However, the samples that were fire tested were heated under much more severe conditions, namely a very high initial heat rate and heating on only part of one side of the sample. This induced much larger thermal gradients in the samples and hence the microstructure of the fire tested samples was different to the samples heated uniformly in a furnace.

7.6.1 Photographs of the Fire Test Samples

Figure 7-11 to Figure 7-13 show photographs of the hot and cold faces of the solid and low density samples after the 120 minute fire test. Figure 7-14 and Figure 7-15 contain cross-sectional images of the test panels after the fire tests. The hot side of the samples was subjected to a maximum temperature of 1049 °C, whereas the cold side was heated to between 230 and 280 °C.

One of the main concerns with binding materials exposed to a fire is spalling which is caused by the steam pressure build-up by the pore water (Shorter and Harmathy, 1961). The solid and low density samples in this study did not exhibit any spalling during or after the fire tests indicating that their microstructure had sufficient permeability to relieve pore pressure in order to prevent the dislodgement of material. It should be noted that the voids that can be seen on the surface of some of the samples in the following images, most particularly the low density samples, are pores that were present prior to testing and not caused by spalling.

Polypropylene fibres have been reported to reduce dehydration damage and in particular spalling of fire exposed materials as they melt at 160 °C and form dehydration pathways for escaping water, preventing pore pressure build-up (Nishida et al., 1995). Given that the solid samples did not spall upon fire exposure, the addition of fibres to the low density samples in this study was unlikely to have had a significant influence on the fire resistance of those samples.

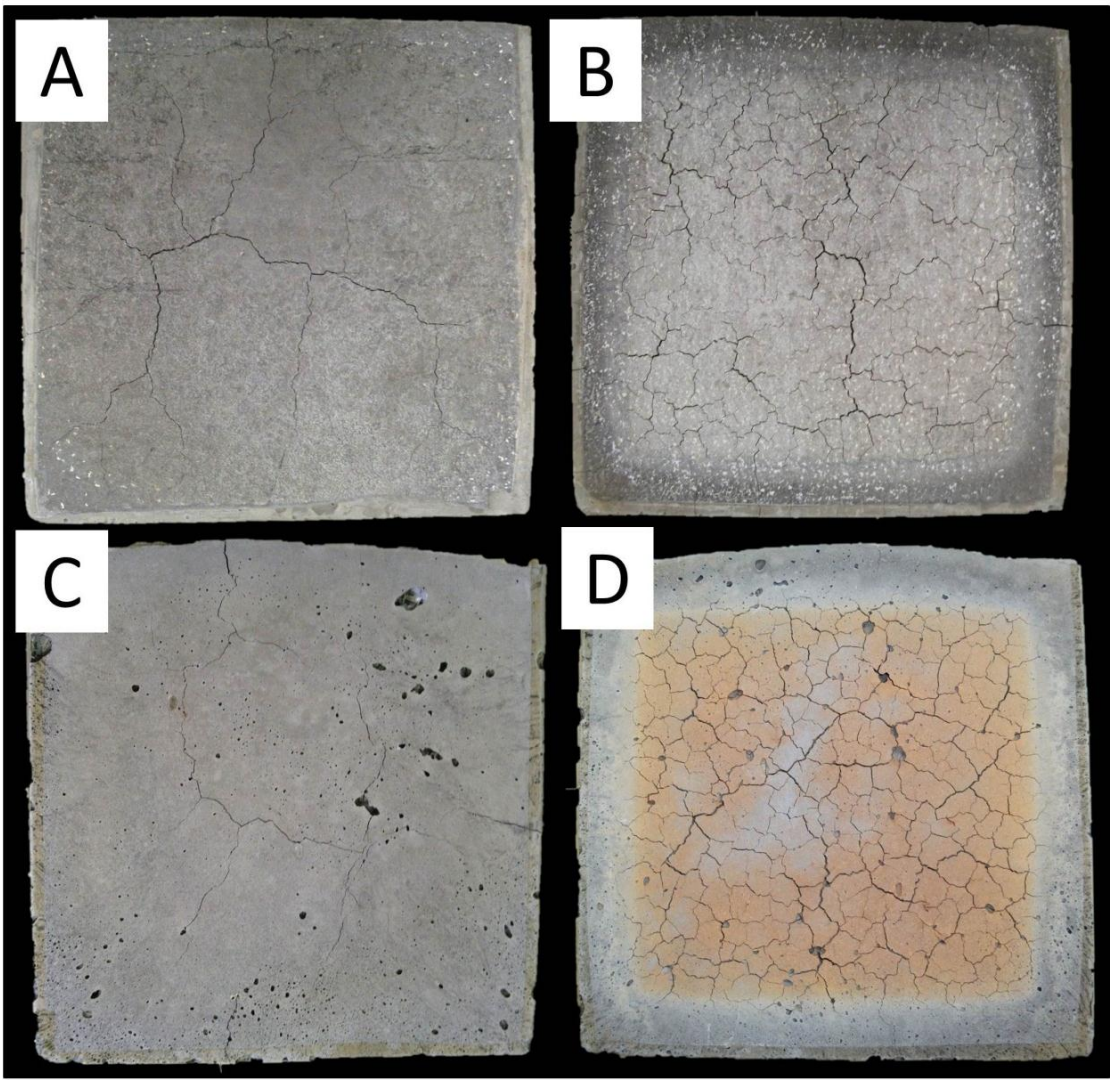

Figure 7-11 Images of the cold side and hot side surfaces of the Eraring 2.5 geopolymer panels after a 120 minute fire test. A: Solid – cold side. B: Solid – hot side. C: Low density - cold side. D: Low density - hot side.

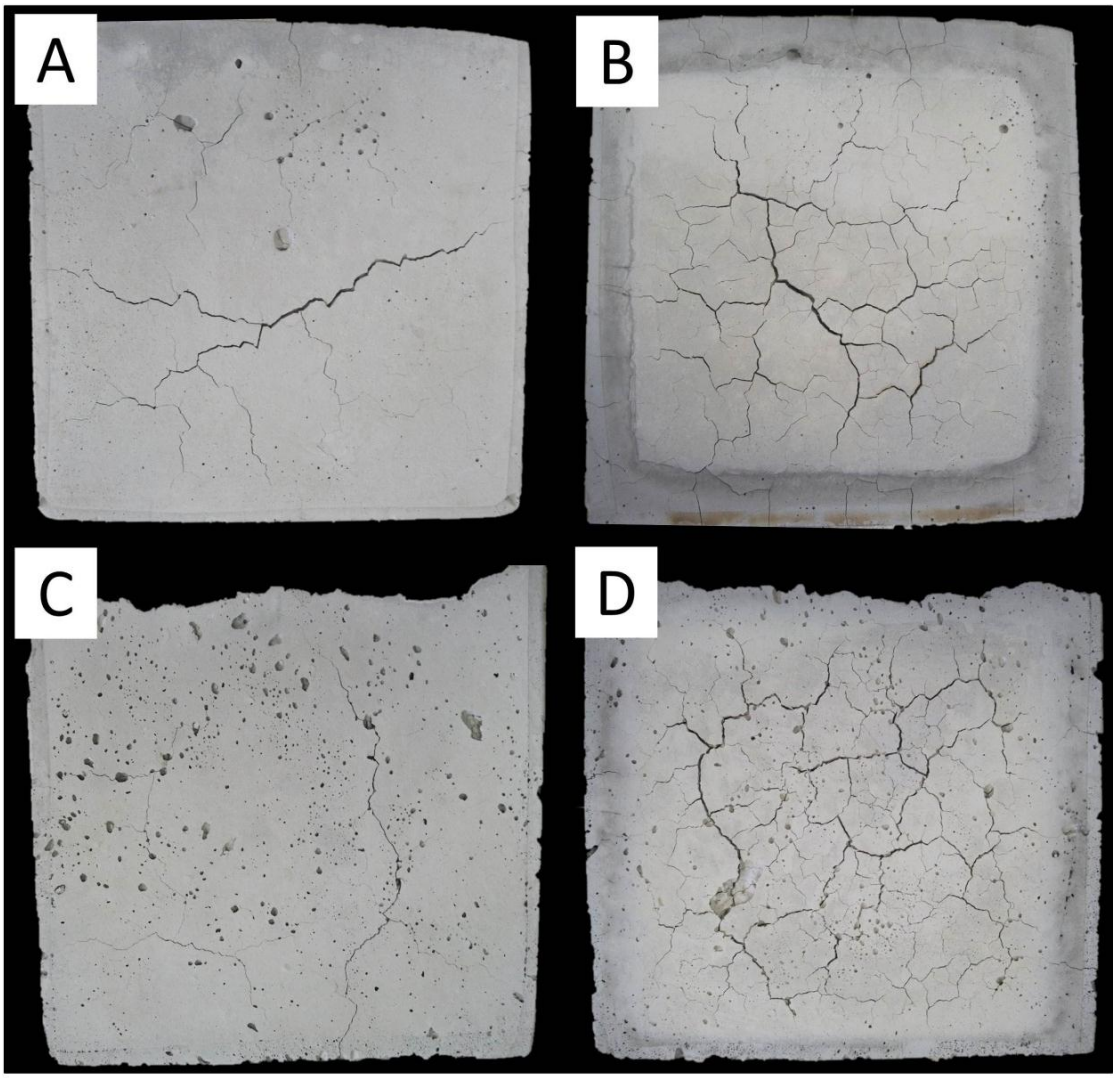

Figure 7-12 Images of the cold side and hot side surfaces of the Tarong 2.5 geopolymer panels after a 120 minute fire test. A: Solid – cold side. B: Solid – hot side. C: Low density - cold side. D: Low density - hot side.

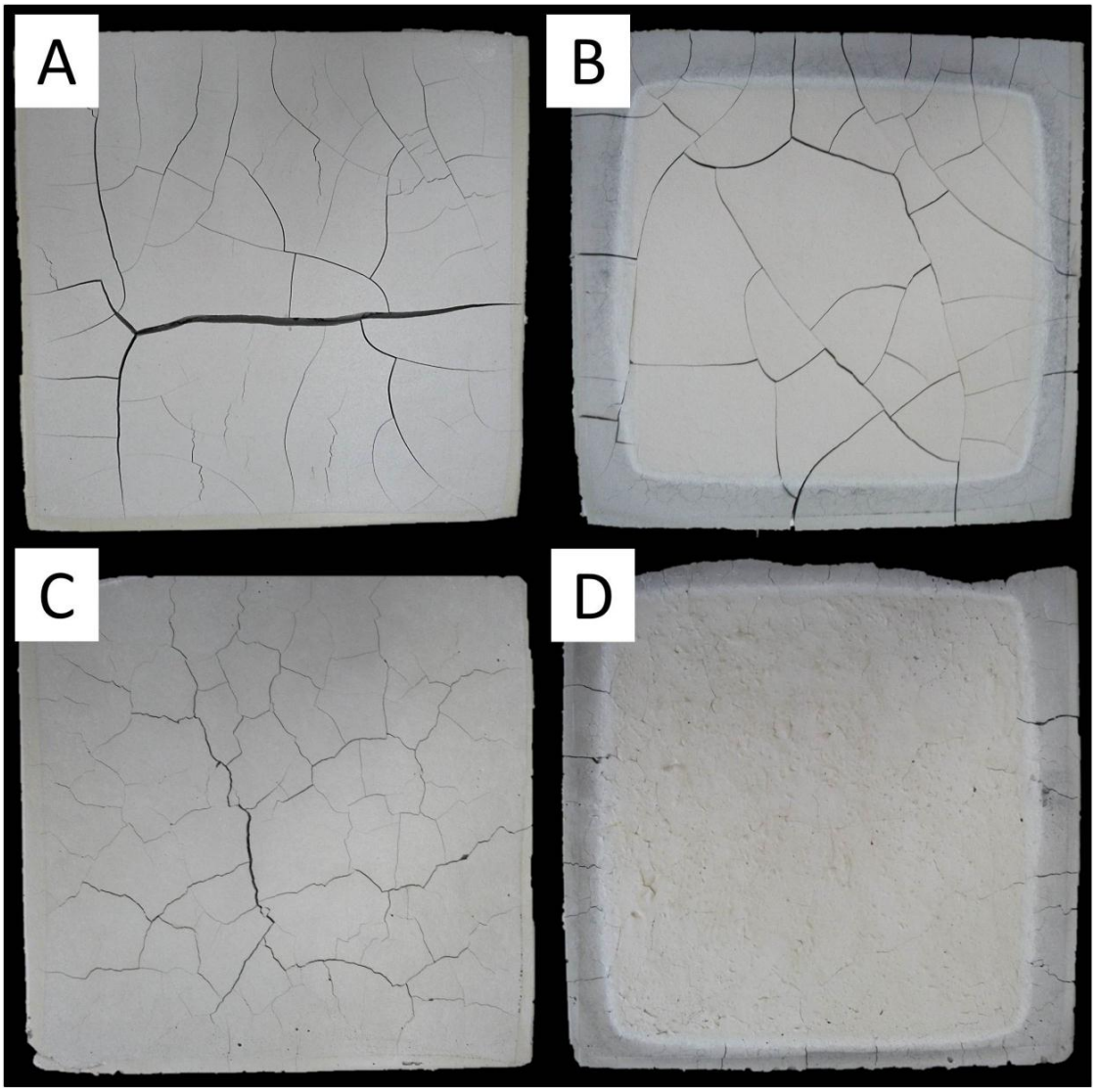

Figure 7-13 Images of the cold side and hot side surfaces of the Port Augusta 2.5 geopolymer panels after a 120 minute fire test. A: Solid – cold side. B: Solid – hot side. C: Low density - cold side. D: Low density - hot side.

All of the samples exhibited surface cracks to a varying degree. The cracks were not observed to form on the cold side of the samples until well after the initial dehydration period finished (approximately 60 minutes into the test) suggesting that the evaporation of water did not cause extensive damage. It is likely that the major cause of the cracking on the cold side of the samples was due differential shrinkage of the hot side to the cold side as the parts of the sample that were hot enough to sinter (between 600 °C to 900 °C, from Table 5.5) would have shrunk much more than the cooler regions, causing the cracking. This was supported by the fact that the largest cold side cracks generally occurred across the centre of the cold side where the tensile force created by the differential shrinkage would have been greatest.

The cracking on the hot side was found to be relatively shallow, and in some cases, there was evidence of crack healing. This is most noticeable in the low density Port Augusta 2.5 geopolymer which exhibited almost no surface cracks in the exposed region of the hot side (Figure 7-13D). Sintering is likely to induce crack healing and as such reduce the amount and extent of cracks.

From Table 5.5 in chapter 5 the sintering temperature or T_g for the three geopolymers was 761 °C, 778 °C and 591 °C for the Eraring 2.5, Tarong 2.5 and Port Augusta 2.5 geopolymers, respectively. The maximum temperature of the samples ranged from 1049 °C on the hot side to approximately 250 °C on the cold side (50 mm from the hot side). The depth of the sample that was exposed to temperatures sufficient to cause sintering was dependant on the thermal conductivity of the sample and also the T_g. Hence it can be inferred that the Port Augusta 2.5 sample, with a much lower T_g than the other samples, would be likely to have a larger portion of sample that sinters. The cross-sectional images in Figure 7-14 clearly show a smooth morphology for the first 25 mm of the solid Port Augusta 2.5 sample indicating that this region had sintered. Correspondingly, this sample also exhibited the largest cracks of all the samples tested. The demarcation between the sintered and un-sintered regions was much less evident in the other samples.

A lower degree of lateral cracking was observed in the cross sections of the low density samples (Figure 7-15) than the solid samples (Figure 7-14). It is believed that the cellular structure of the low density geopolymers was more resistant to the thermal stresses during the fire tests which made them more resistant to cracking.

Another feature that was observed in the cross-section of the fire tested samples was an iron oxidation layer, identified as the yellow to orange layer that was evident in the first 10 mm of all samples. This colour change was also evident in the samples uniformly heated to 1000 °C, though much more uniformly, and is due to the exposure and oxidation of previously encapsulated iron species as the covering aluminosilicates flow viscously at high temperatures (Rickard et al., 2010).

Figure 7-14 Cross-sections of the solid geopolymers after a 120 minute fire test. The fire exposed side of the sample is at the bottom of each of the cross sections. Top: Eraring 2.5, Middle: Tarong 2.5, Bottom: Port Augusta 2.5.

Figure 7-15 Cross-sections of the low density geopolymers after a 120 minute fire test. The fire exposed side of the sample is at the bottom of each of the cross sections. Top: Eraring 2.5, Middle: Tarong 2.5, Bottom: Port Augusta 2.5.

7.6.2 Microstructure of the Fire Test Samples

The microstructure of the fire tested geopolymers was analysed in a SEM. Fracture surfaces adjacent to the hot and cold sides of the samples were analysed as well as the faces of the samples.

Figure 7-16 through to Figure 7-21 contain a series of micrographs of the fire tested samples. The morphology of the fracture surfaces near the cold side of all of the samples was consistent with the morphology of the as-cured geopolymers as described in section 6.2.2 (solid samples) and section 7.3 (low density samples). The most obvious difference was the lack of fibres in the as-cured low density samples as they had been heated sufficiently high (>160 °C) to vaporise them out.

The bulk of the escaping water was observed to evaporate through the top (cold side) of the samples during the fire tests meaning that the structure in this region was forced to be a conduit for a significant amount of water to dehydrate through. The fact that the microstructure of the samples was unchanged after exposure to these conditions suggests that the geopolymers in this study were largely resistant to dehydration stress during fire exposure. This was further supported by observations during the fire tests where the macro cracks in the cold side of the samples did not develop until well after the dehydration period. However, it is not possible to eliminate the possibility that the macro cracks did indeed develop during the dehydration period but didn't manifest themselves visually until later in the test.

The cold faces of the samples also exhibited a microstructure consistent with an as-cured sample with the exception of the Port Augusta 2.5 sample. This sample had exhibited cracking on its cold surface, much more than what was observed in the fracture surface of the cold side. The high portion of geopolymer gel in this sample produced a much more homogenous surface with fewer voids than the other geopolymers. This surface structure is likely to be much less permeable than the other samples and may explain why this sample was more prone to dehydration cracking.

The hot side of the samples were heated to 1049 °C during the fire tests. The samples exhibited analogous microstructural changes to the samples that were gradually heated to 1000 °C (see section 6.2.2). The main difference was the consistency and extent of the microstructural changes, likely due to the much shorter exposure time to high temperatures.

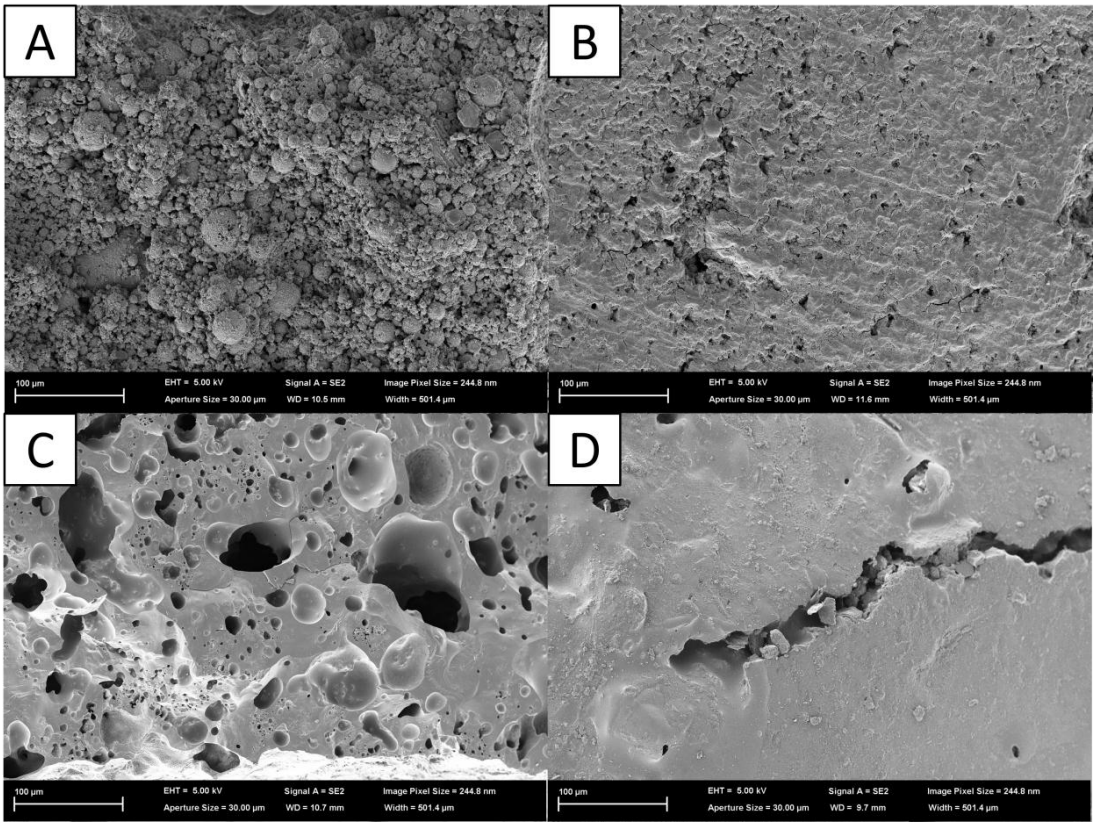

Figure 7-16 Micrographs of the Eraring 2.5 (solid) geopolymer after a 120 minute fire test. A: fracture surface immediately near the 'cold side'. B: cold side surface. C: fracture surface immediately near the 'hot side'. D: hot side surface.

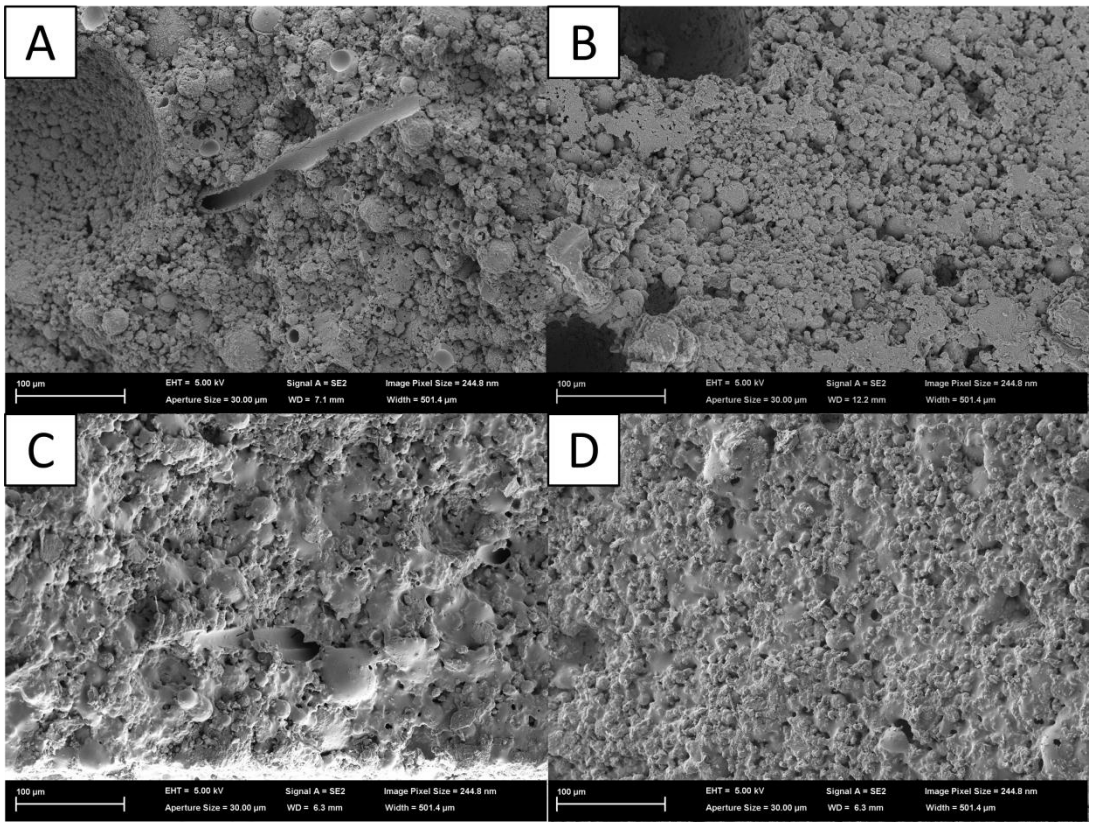

Figure 7-17 Micrographs of the Eraring 2.5 (low density) geopolymer after a 120 minute fire test. A: fracture surface immediately near the 'cold side'. B: cold side surface. C: fracture surface immediately near the 'hot side'. D: hot side surface.

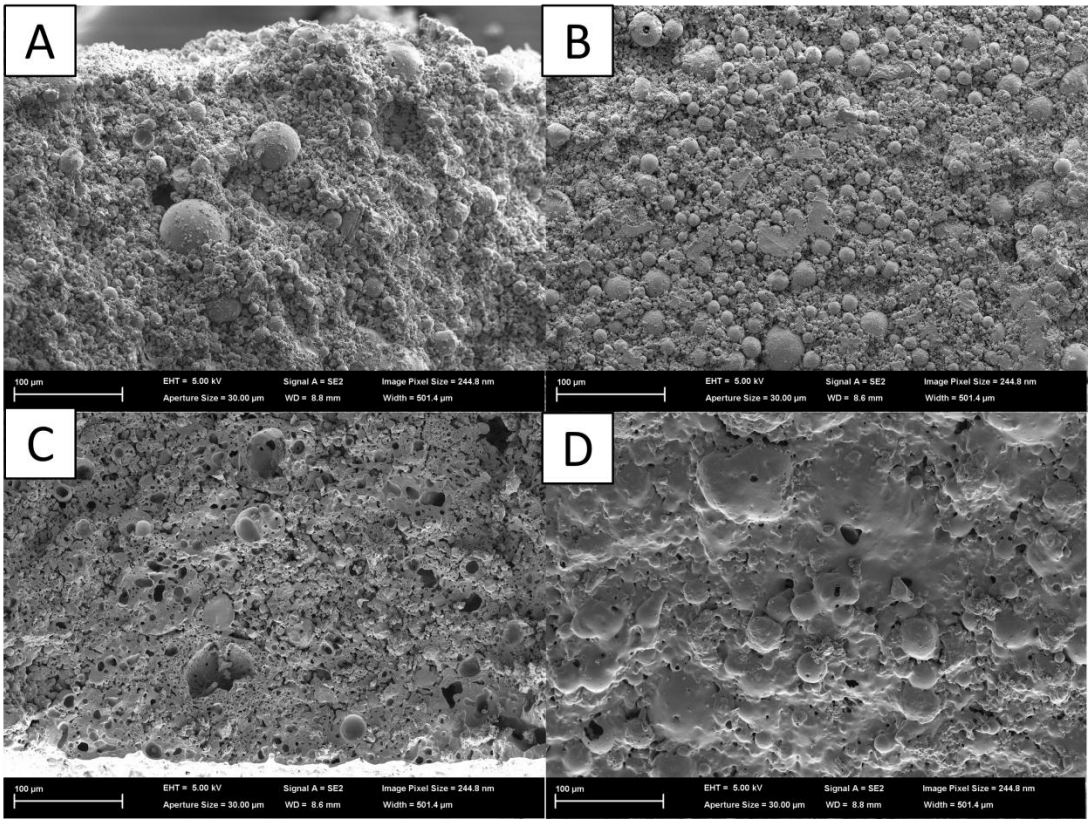

Figure 7-18 Micrographs of the Tarong 2.5 (solid) geopolymer after a 120 minute fire test. A: fracture surface immediately near the 'cold side'. B: cold side surface. C: fracture surface immediately near the 'hot side'. D: hot side surface.

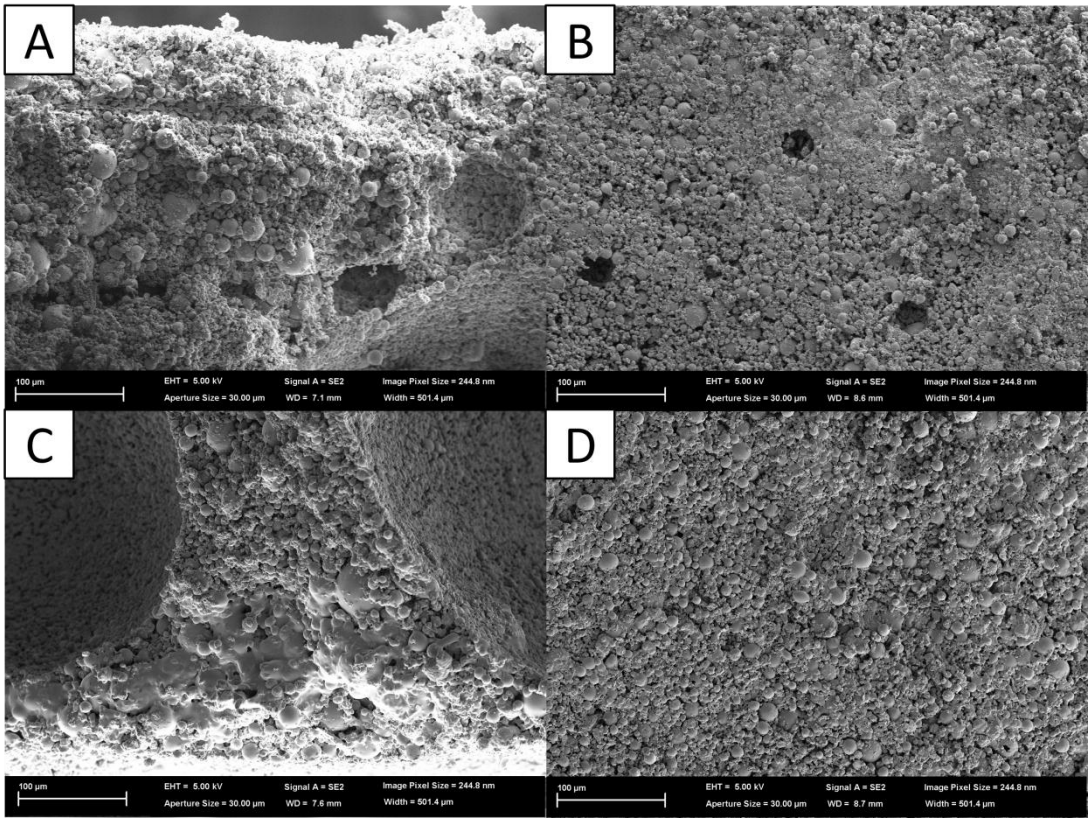

Figure 7-19 Micrographs of the Tarong 2.5 (low density) geopolymer after a 120 minute fire test. A: fracture immediately near the 'cold side'. B: cold side surface. C: fracture surface immediately near the 'hot side'. D: hot side surface.

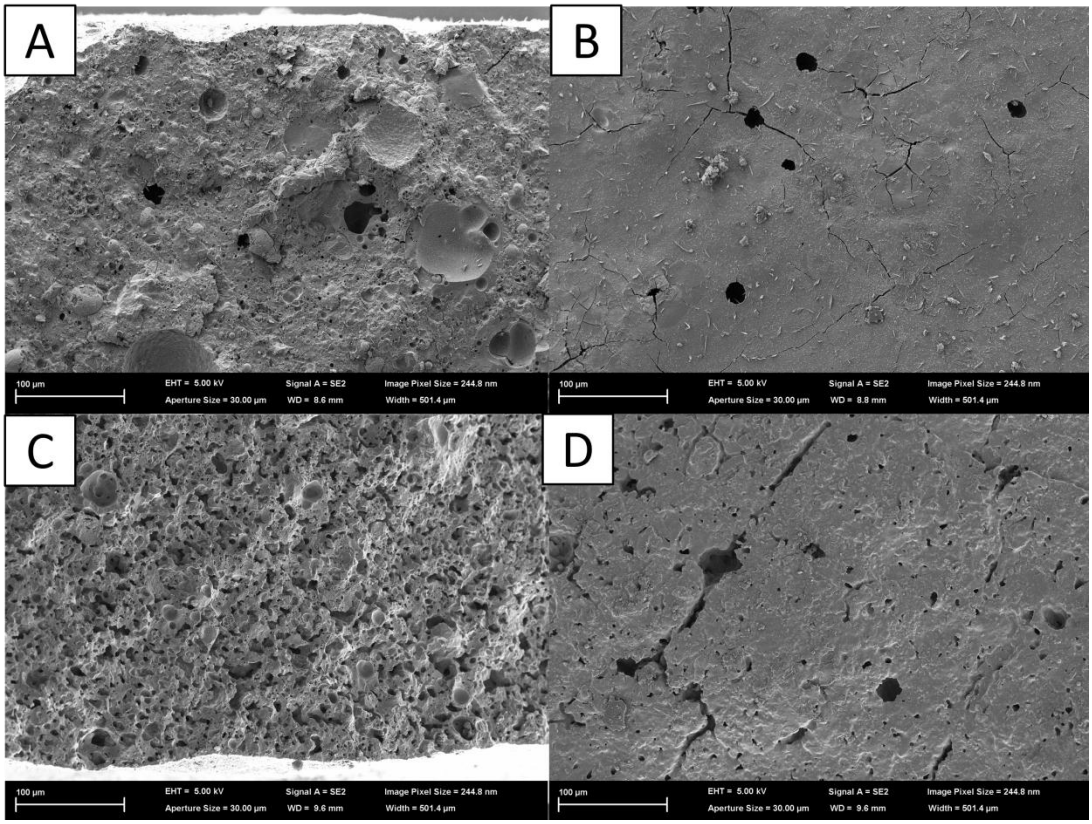

Figure 7-20 Micrographs of the Port Augusta 2.5 (solid) geopolymer after a 120 minute fire test. A: fracture surface immediately near the 'cold side'. B: cold side surface. C: fracture surface immediately near the 'hot side'. D: hot side surface.

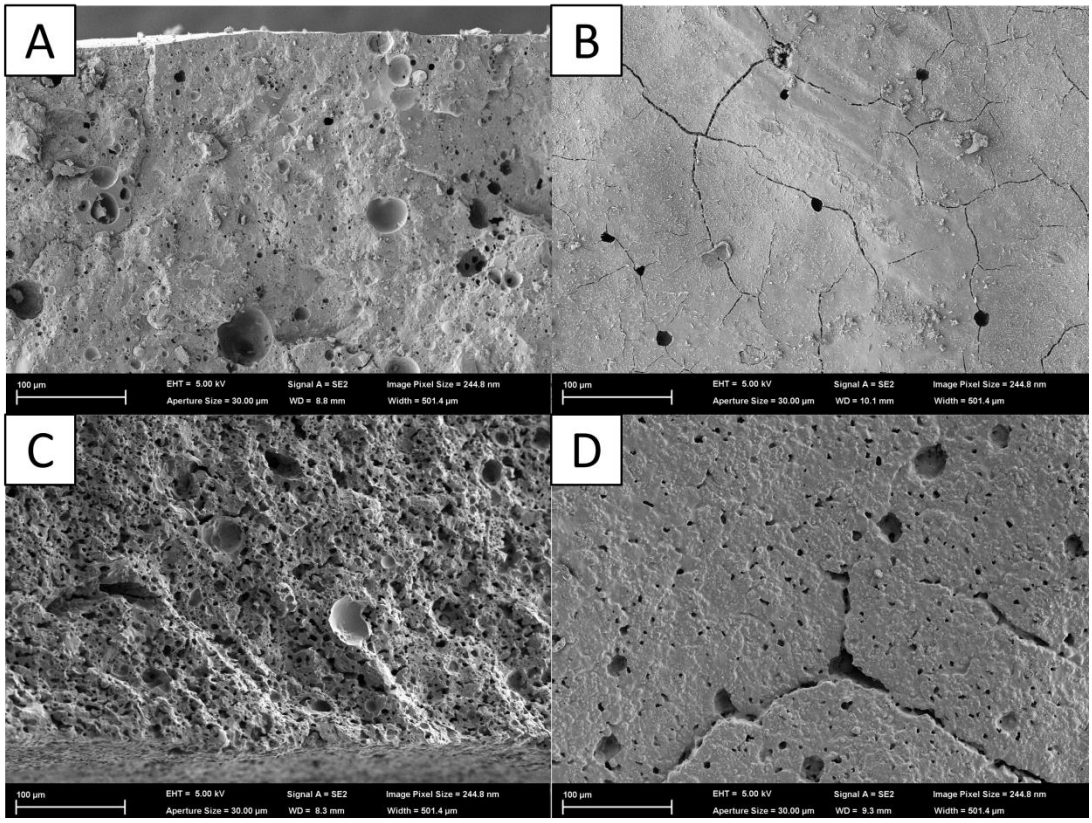

Figure 7-21 Micrographs of the Port Augusta 2.5 (low density) geopolymer after a 120 minute fire test. A: fracture surface near the 'cold side'. B: cold side surface. C: fracture surface perpendicular to the 'hot side'. D: hot side surface.

The hot faces of the Port Augusta 2.5 samples exhibited signs of crack healing (Figure 7-20 and Figure 7-21). This was caused by the extensive sintering in the Port Augusta 2.5 sample and is believed to be the reason why the optical images (Figure 7-13D) of the hot side of these samples showed less small cracks than the other samples.

The depth in the sample that exhibited extensive sintering-type microstructural changes varied between the samples. The boundary between the sintered and un-sintered region was not distinct and was more characteristic of a gradual reduction in the degree of sintering with distance from the hot face (as can be seen in Figure 7-22). The low density Tarong 2.5 sample was observed to have a very shallow depth of extensive sintering which can be seen in Figure 7-19, C.

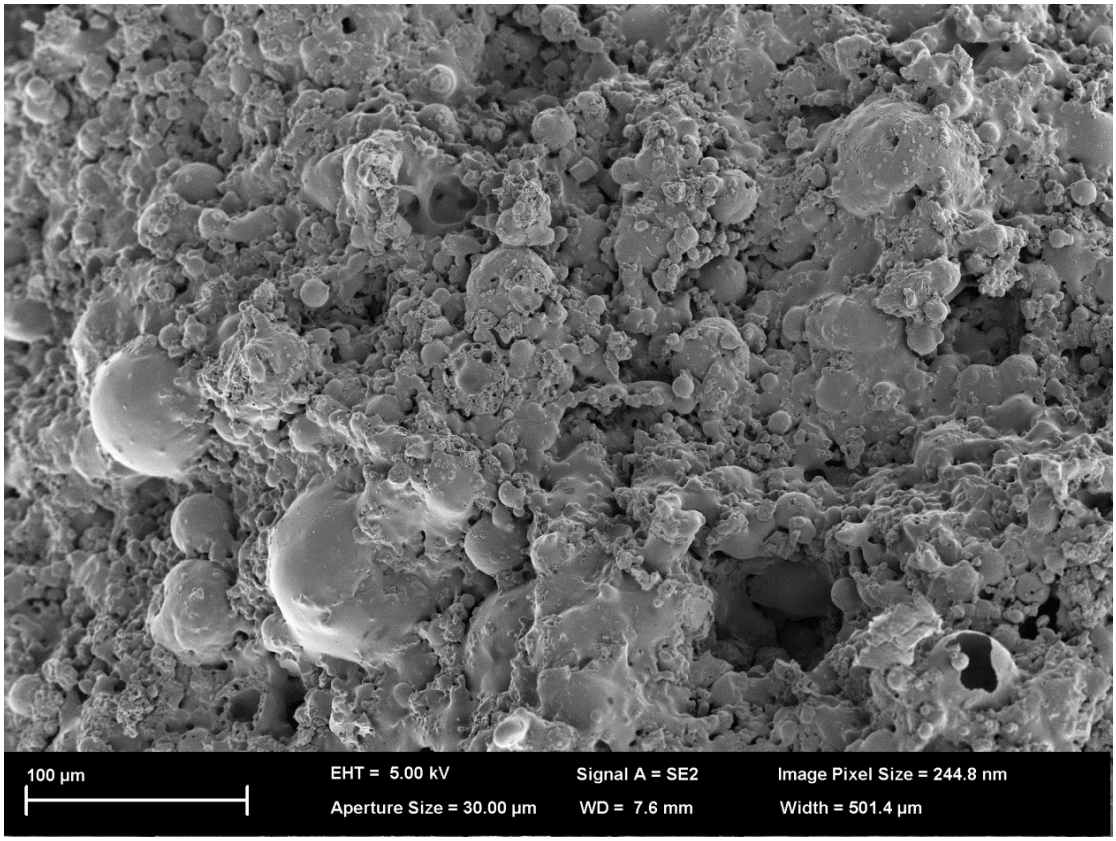

Figure 7-22 Micrograph from approximately 3 mm into the fracture surface of the hot side of the low density Tarong 2.5 geopolymer demonstrating a partially sintered sample morphology.

7.7 Phase Evolution of Geopolymers During Simulated Fire Exposure

An *in situ* high temperature XRD experiment was conducted at the Australian synchrotron. The experiment involved exposing geopolymer powders to a 120 minute heating regime as per the fire curve AS1530.4 / ISO 834 with the exception that the temperature was kept constant when the diffractions patterns were being collected (2 minute collection time). The heating conditions during the experiment closely reflected the conditions that would be experienced by the hot side of fire tested samples. More details of the experiment are available in chapter 3, section 3.7.2. Due to the limited beam time available, data was only able to be collected from the Eraring and Tarong 2.5 samples.

Figure 7-23 and Figure 7-24 show *ex situ* XRD patterns of the Eraring 2.5 and Tarong 2.5 geopolymers before and after the 120 minute simulated fire exposure as measured with synchrotron radiation. The wavelength for the experiment was 0.619 Å (20 keV) and as such the pattern was compressed over a smaller 2θ range than the laboratory patterns which were collected with an incident beam wavelength of 1.542 Å. The synchrotron diffraction patterns were found to contain platinum peaks from the sample holder and were also affected by peak shift, not just due to thermal expansion, but due to changes in sample displacement as the samples shrank on heating.

The fire exposed geopolymer powders exhibited the same phase composition before and after exposure as did the samples that were gradually heated (details of the phase composition of the gradually heated samples are in section 6.4). The only discernible difference was a smaller reduction in peak intensity in the quartz and mullite phases, most notably in the Tarong 2.5 geopolymer, when compared to the equivalent gradually heated sample. This is likely to be due to the fact that the dissolution of crystalline phases at elevated temperatures is not only temperature dependant but also time dependant (Ribeiro et al., 2005) and as such the fire tested samples that were exposed to high temperatures for a shorter time did not exhibit the same degree of quartz and mullite dissolution.

The following paragraphs summarise the changes in the diffraction patterns of the fire tested geopolymers;

Eraring 2.5 geopolymer - Decreased mullite and quartz peak intensity, maghemite-C destroyed, increased hematite peak intensity, zeolitic phases destroyed, nepheline and tridymite formed.

Tarong 2.5 geopolymer - Decreased mullite and quartz peak intensity (to a lesser extent than the Eraring 2.5 geopolymer), faujasite-Na and gibbsite destroyed, nepheline and tridymite formed.

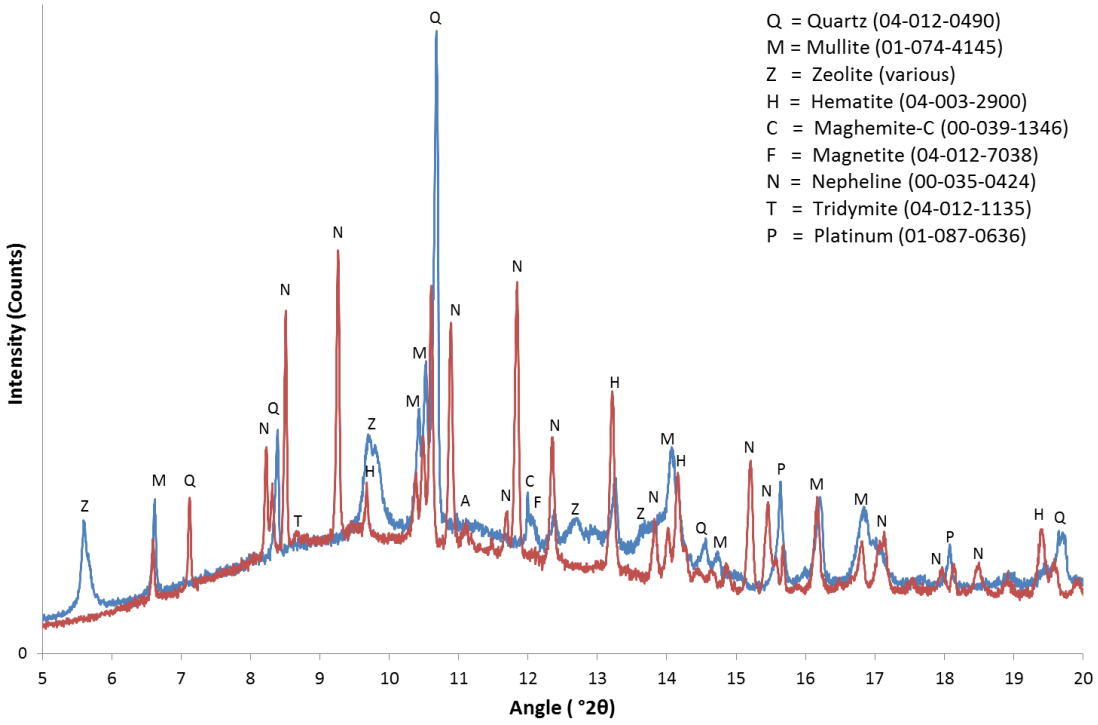

Figure 7-23 Ex-situ XRD patterns for the Eraring 2.5 geopolymer before and after exposure to a 120 minute simulated fire. Blue = as-cured, red = after fire testing.

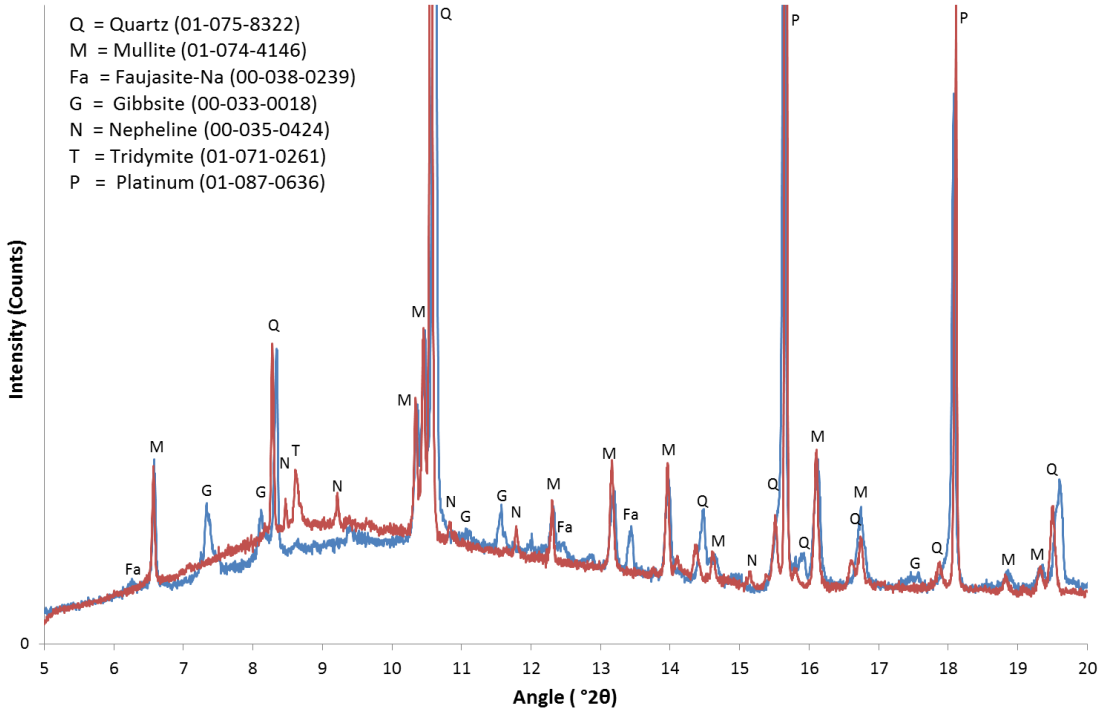

Figure 7-24 Ex-situ XRD patterns for the Tarong 2.5 geopolymer before and after exposure to a 120 minute simulated fire. Blue = as-cured, red = after fire testing.

The main benefit of the synchrotron experiment was that diffraction patterns were able to be collected during the elevated temperature exposure. *In situ* phase analysis was able to identify the temperature that phases formed or were destroyed as well as allowing transient phases to be identified. Figure 7-25 and Figure 7-26 contain 2D plots of the *in situ* diffraction patterns for the Eraring and Tarong 2.5 geopolymers as they were exposed to a 120 minute simulated fire.

By correlating the data set number with the heating regime, the time and temperature of the phase changes were able to be determined. Some of the phases changes were difficult to discern in the 2D plots so the precise point at which phase changes occurred was determined by analysing individual diffraction patterns. A summary of the temperature and times for the phase changes that were detected is presented below;

Eraring 2.5 geopolymer – Maghemite destroyed at 576 °C (5 minutes into the test), zeolitic phases destroyed at 902 °C (45 minutes into the test). Nepheline formed at 902 °C (45 minutes into the test), tridymite formed at 968 °C (71 minutes into the

test). The peaks of the iron oxide phase were also observed to sharpen with increasing temperature indicating an increase in the crystallographic order in those phases.

Tarong 2.5 geopolymer – Faujasite and gibbsite phases destroyed at 576 °C (5 minutes into the test). Nepheline formed between 842 and 885 °C (33 - 38 minutes into the test), tridymite formed at 945 °C (60 minutes into the test).

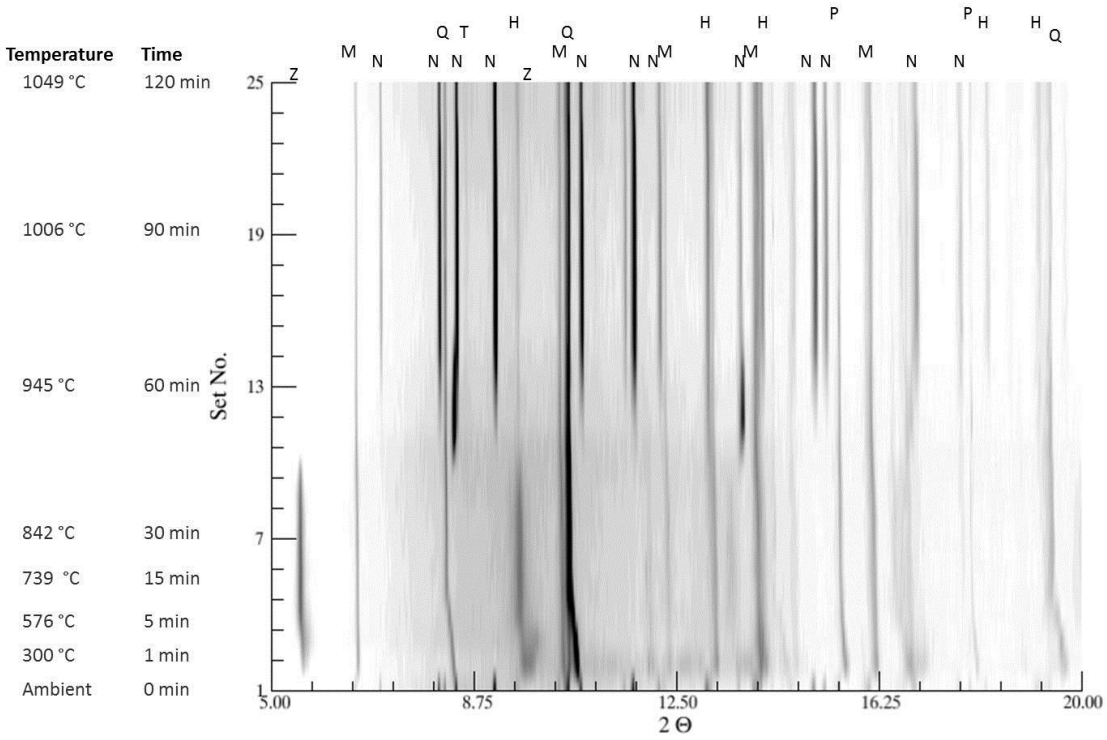

Figure 7-25 2D plot of the 25 XRD *in situ* patterns from the Eraring 2.5 geopolymer as it was exposed to a 120 minute simulated fire. P = Platinum (01-087-0636), H = Hematite (04-003-2900), Q = Quartz (04-012-0490), T = Tridymite (04-012-1135), M = Mullite (01-074-4145), N = Nepheline (00-035-0424), Z = Zeolite (various).

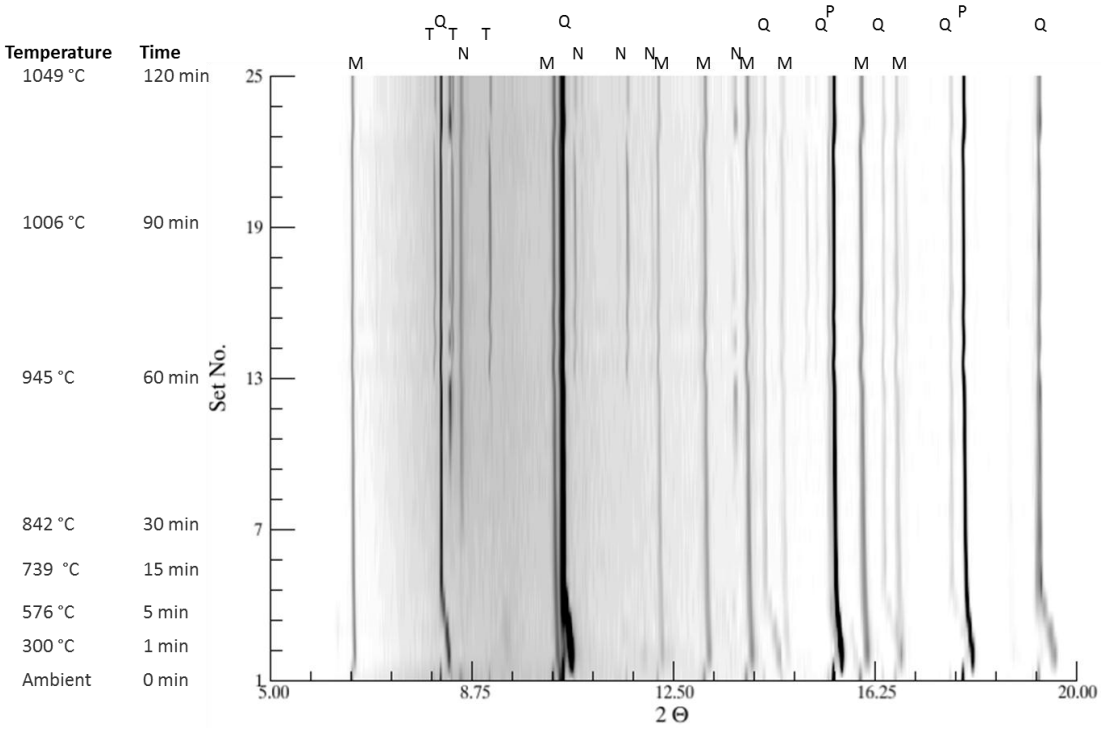

Figure 7-26 2D plot of the 25 XRD *in situ* patterns from the Tarong 2.5 geopolymer as it was exposed to a 120 minute simulated fire. P = Platinum (01-087-0636), Q = Quartz (01-075-8322), T = Tridymite (01-071-0261), N = Nepheline (00-035-0424), M = Mullite (01-074-4146). Note: Faujasite and gibbsite lines were not discernible in this plot.

The main phase transitions were found to occur above the sintering temperature of the two geopolymers (occurring at 761 °C and 778 °C for the Eraring and Tarong 2.5 geopolymers, respectively). However, the temperature of the phase transitions did closely correspond with the small high temperature expansion peaks determined by dilatometry to occur at 926 °C and 945 °C for the Eraring and Tarong 2.5 geopolymers, respectively. This indicates that crystallisation during high temperature exposure was a thermal expansion event in these samples.

The thermal expansion of the stable crystalline phases was also observable in the *in situ* XRD data. This was most noticeable in the diffraction peaks for the quartz phase which can be seen to move to a lower 2θ value in the first few patterns (data sets) on the 2D plots. A shift to a lower 2θ value is indicative of an expansion in the d-spacing of the crystallographic planes of the phase.

7.8 Conclusions

In this chapter the performance of three geopolymer mixes exposed to a simulated fire was assessed. Both solid and foamed samples were evaluated and compared.

The low density geopolymers were found to exhibit compressive strengths between 5 and 10 MPa at a density of approximately 0.9 g cm^{-3}. Upon firing (gradual heating to 1000 °C) the low density samples performed in an analogous fashion to their solid equivalents. The thermal conductivity of the low density geopolymers ranged between 0.25 and 0.39 W $m^{-1}K^{-1}$, or approximately half of the value of their solid equivalent. The microstructure of the low density geopolymers showed the concentration of the fibre reinforcement (0.25 wt.%) was too low to substantially influence the cured and post firing properties.

Fire testing showed that the geopolymers in this study achieved fire ratings of between 60 and 90 minutes for a sample thickness of 50 mm. The solid geopolymers exhibited better fire ratings than the low density geopolymers due to their higher water content. The geopolymer mixes ranked Tarong 2.5 > Port Augusta 2.5 > Eraring 2.5 in terms of their ability to insulate. No spalling was observed in the samples after fire testing though cracking to a varying degree was evident. The low density samples, particularly the Eraring and Tarong 2.5 samples, exhibited less cracking than the solid samples implying that the cellular structure was better at resisting thermally induced stresses during the fire testing. Microstructural analysis showed that the cold side of the geopolymers was not significantly damaged by dehydration and the hot side exhibited analogous changes to the samples that were gradually heated to 1000 °C.

Phase analysis of the Eraring and Tarong 2.5 geopolymers showed that the phase composition of the samples was largely independent of their thermal history as the fire exposed samples exhibited the analogous phase changes as the gradually heated samples.

Chapter 8
Conclusions

"Science, in the very act of solving problems, creates more of them"

Abraham Flexner

8.1 Conclusions

Research on fly ash based geopolymers is intrinsically challenging due to the complexity of the material. Fly ashes contain multiple crystalline and amorphous phases as well as volatile carbon. They also have enclosed pores and a variable particle size. Once synthesised into a geopolymer, the complexity of the system increases as the fly ash particles geopolymerise to a varying extent to form an amorphous binding phase, while the residual activating solution and partially activated aluminosilicates form other phases such as zeolites. The geopolymer phase also has its own porosity with many of the pores likely to contain water. Upon heating most of these phases change in some way and the post firing measurements are convoluted by the simultaneous contribution from each of the phases. Notwithstanding the inherent difficulties of studying this material, useful information was able to be obtained by careful analysis and detailed characterisation of the samples before and after thermal exposure.

Five fly ashes sourced from different Australian power stations were evaluated in this study. Quantitative phase analysis determined that only a portion of each of the fly ashes was available for geopolymerisation and that the reactive Si:Al ratio varied greatly between the fly ashes. Collie and Port Augusta fly ashes had relatively low amorphous Si:Al ratios (1.15 and 1.84, respectively) whereas the Eraring, Tarong and Bayswater fly ashes had high Si:Al ratios (4.98, 8.84 and 7.49, respectively). Other differences between the fly ashes that were identified as being significant were the concentration of iron oxides, the particle size distribution and the type of crystalline phases. A thorough understanding of the morphology of the fly ashes as well as the location of the various phases was also obtained by observing the interior structure of the fly ash particles by SEM.

Details, in particular the concentration and Si:Al ratio of the amorphous aluminosilicates from the characterisation of the fly ashes, were used to successfully synthesise geopolymers with moderate to high compressive strengths. Geopolymers from each fly ash were designed with Si:Al binder ratios of 2.0, 2.5 and 3.0. SEM and EDS analysis of the samples indicated that there was incomplete dissolution and

incorporation of the aluminosilicates from the fly ashes and activating solution which resulted in the geopolymers failing to achieve the targeted compositional ratio.

The geopolymers were assessed for their thermal performance after exposure (firing) to 1000 °C in a furnace. Mechanical testing of the samples before and after firing produced post firing strengths from less than 1 MPa to greater than 130 MPa. The most important fly ash characteristic was found to be the reactive Si:Al ratio in the glass. Fly ashes with a high reactive Si:Al ratio (≥5) produced geopolymers with moderate as-cured compressive strengths but exhibited excellent dimensional stability during heating and greater compressive strengths after heating. Fly ashes with a low reactive Si:Al ratio (<2) produced geopolymers with high as-cured compressive strengths but exhibited poor dimensional stability during heating and greatly reduced compressive strengths after heating. Iron concentration in the fly ashes was also found to influence the thermal performance of the geopolymers but only when it was present at relatively high concentrations (greater than 10 wt.%).

Detailed microstructural analysis of the geopolymers before and after firing indicated that the samples, regardless of the fly ash they were synthesised from, exhibited strength improving structural changes after firing. Inter-particle bonding was significantly improved after firing due to sintering and viscous flow of aluminosilicates at high temperatures. There were also less unreacted fly ash particles in the fired samples as they were found to have melted into the geopolymer phase. However, longer length scale structural changes, such as cracking, caused strength losses in low reactive Si:Al fly ash geopolymers after firing.

Phase analysis of the geopolymers by XRD indicated that the geopolymers contained an amorphous phase as well as the crystalline phases that were initially present in the fly ash precursor. Some of the samples, in particular the low strength samples (eg. the Bayswater geopolymers) contained poorly ordered zeolitic phases. After firing, the geopolymers remained largely amorphous though there were changes observed in the other phases. The hydrated zeolitic phases were destroyed and feldspars, most notably nepheline, were found to form.

Geopolymers from three of the fly ashes were assessed for their performance upon exposure to a simulated fire. Solid and low density ($\rho \approx 0.9$ g cm^{-3}, $k \approx 0.3$ W $m^{-1}K^{-1}$) variants of the mixes were used for fire testing. Fire ratings of between 60 and 90 minutes for a sample thickness of 50 mm were achieved. The solid geopolymers exhibited better fire ratings than the low density geopolymers due to their higher water content (as they contained more of the hydrated geopolymer phase). Microstructural analysis of the fire tested samples indicated that the geopolymers were not significantly damaged by dehydration and the fire exposed side exhibited analogous changes to the samples that were gradually heated to 1000 °C.

A model for the microstructural changes in fly ash geopolymers exposed to elevated temperatures was proposed based on the analysis of the samples in this study. This model can be used to predict changes in morphology of fly ash geopolymers upon firing which may aid in the design of future products from this material.

8.2 Summary and Outlook

Fly ash geopolymers can be synthesised from fly ashes with a wide range of Si:Al ratios to exhibit moderate to high as-cured compressive strengths. Cellular structured variants can also be easily produced with the addition of a small concentration of aluminium. Exposure to temperatures up to 1000 °C can result in fly ash geopolymers exhibiting impressive strength increases of up to 5 fold. They are also resistant to spalling when exposed to a simulated fire and are capable of insulating the extreme conditions for well over an hour.

The objective of this research was to characterise the thermal performance of a range of geopolymers synthesised from five different fly ash sources in order to assess their potential for utilisation in high temperature applications. This objective was met with the results in this thesis demonstrating that fly ash geopolymers indeed have great potential for use in high temperature applications, provided they are synthesised from a source material with suitable physical and compositional characteristics.

In a political climate where governments around the world are taxing CO_2 emissions and promoting sustainable and environmentally friendly materials, geopolymers are emerging as an important material of the future. A binding material that can be produced from an industrial waste product to exhibit satisfactory as-cured mechanical properties that actually improve when exposed to high temperatures is likely to be very attractive to commercial entities.

Fly ashes with characteristics outlined in this thesis to produce thermally resistant geopolymers may not always be locally available, however, beneficiation of previously unsuitable fly ashes is likely to enable a wider range of sources to be utilised.

Given the potential environmental and performance benefits over existing materials, it is likely that with continued development fly ash geopolymers will be produced commercially and used in various high temperature and fire resistant applications.

8.3 Recommendations for Future Work

There is an extensive scope for future work on the thermal properties of fly ash geopolymers. The promise of the material is likely to motivate scientists, engineers and commercial entities to continue its development. The analysis in this thesis was extensive though it was far from exhaustive as there is a lot more research that can be conducted on the topic. The following recommendations are suggested for future research endeavours:

- Assessment of the thermal performance of a more extensive range of fly ashes to improve the understanding of the influence of source characteristics. Class C fly ashes and blended fly ash mixtures could also be considered.
- Detailed investigation into the influence of a wider range of activating solutions would enable optimisation of the geopolymer microstructure for maximum fire resistance.
- A study on a wider range of Si:Al ratios would give further insight as to the role of the chemical composition of the geopolymer gel has on the thermal performance.
- *In situ* analysis of the physical properties and microstructure of fly ash geopolymers as they are heated would provide a better understanding of the temperature at which various structural changes occur.
- A detailed study on the role of pores in fly ash based geopolymers is required. Permeability is also an important characteristic to analyse.
- This study included a small study on low density geopolymers. Further research on samples with variable densities and fibre contents would give greater insight into the practical applications for this type of geopolymer.
- Commercialisation would not be possible without research into the cost of production and environmental benefits when producing this material with comparisons to existing products.

References

References

ALEKSANDROV, Y. A., TSYGANOVA, E. I. & PISAREV, A. L. 2003. Reaction of Aluminum with Dilute Aqueous NaOH Solutions. *Russian Journal of General Chemistry*, 73**,** 689-694.

ALY, Z., VANCE, E. R., PERERA, D. S., HANNA, J. V., GRIFFITH, C. S., DAVIS, J. & DURCE, D. 2008. Aqueous leachability of metakaolin-based geopolymers with molar ratios of Si/Al = 1.5-4. *Journal of Nuclear Materials*, 378**,** 172-179.

ANDINI, S., CIOFFI, R., COLANGELO, F., GRIECO, T., MONTAGNARO, F. & SANTORO, L. 2008. Coal fly ash as raw material for the manufacture of geopolymer-based products. *Waste Management*, 28**,** 416-423.

AS 1530.4 2005. Methods for fire tests on building materials, components and structures - Fire-resistance test of elements of construction. *Australian Standard*.

AS 3582.1 1991. Supplementary cementitious materials for use with portland cement – Part 1 Fly ash. *Australian Standard*.

AS/NZS 4859.1 2002. Materials for the thermal insulation of buildings - General criteria and technical provisions.

ASKELAND, D. R., FULAY, P. P. & WRIGHT, W. J. 2010. *The Science and Engineering of Materials: 6th Edition*, Stamford, USA, Global Engineering.

ASTM C39 2005. Standard Test Method for Compressive Strength of Cylindrical Concrete Specimens.

ASTM C177 2010. Standard Test Method for Steady-State Heat Flux Measurements and Thermal Transmission Properties by Means of the Guarded-Hot-Plate Apparatus.

ASTM C618-08A 2008. Standard Specification for Coal Fly Ash and Raw or Calcined Natural Pozzolan for Use in Concrete.

ASTM D5334-08 2008. Standard Test Method for Determination of Thermal Conductivity of Soil and Soft Rock by Thermal Needle Probe Procedure.

ASTM E119 2011. Standard Test Methods for Fire Tests of Building Construction and Materials. *American Standard Test Method*.

ASTM E831 2006. Standard test method for linear thermal expansion of solid materials by thermo mechanical analysis.

BAKHAREV, T. 2005. Resistance of geopolymer materials to acid attack. *Cement and Concrete Research*, 35**,** 658-670.

BAKHAREV, T. 2006. Thermal behaviour of geopolymers prepared using class F fly ash and elevated temperature curing. *Cement and Concrete Research,* 36**,** 1134-1147.

BAO, Y., GRUTZECK, M. W. & JANTZEN, C. M. 2005. Preparation and Properties of Hydroceramic Waste Forms Made with Simulated Hanford Low-Activity Waste. *Journal of the American Ceramic Society,* 88**,** 3287-3302.

BARBOSA, V. F. & MACKENZIE, K. J. 2003a. Thermal behaviour of inorganic geopolymers and composites derived from sodium polysialate *Materials Research Bulletin,* 38**,** 319-331.

BARBOSA, V. F. & MACKENZIE, K. J. 2003b. Synthesis and thermal behaviour of potassium silate geopolymers. *Materials Letters,* 57**,** 1477-1482.

BAZANT, Z. P. & KAPLAN, M. F. 1996. *Concrete at High Temperatures,* Essex, Longman Group Limited.

BELL, J., GORDON, M. & KRIVEN, W. 2008a. Use of Geopolymeric Cements as a Refractory Adhesive for Metal and Ceramic Joins. *Advances in Ceramic Coatings and Ceramic-Metal Systems: Ceramic Engineering and Science Proceedings.* John Wiley & Sons, Inc.

BELL, J. L., DRIEMEYER, P. E. & KRIVEN, W. M. 2009. Formation of Ceramics from Metakaolin-Based Geopolymers: Part I—Cs-Based Geopolymer. *Journal of the American Ceramic Society,* 92**,** 1-8.

BELL, J. L., SARIN, P., PROVIS, J. L., HAGGERTY, R. P., DRIEMEYER, P. E., CHUPAS, P. J., VAN DEVENTER, J. S. J. & KRIVEN, W. M. 2008b. Atomic structure of a cesium aluminosilicate geopolymer: A pair distribution function study. *Chemistry of Materials,* 20**,** 4768-4776.

BERRY, E. E. & MALHOTRA, V. M. 1980. Fly Ash for Use in Concrete - A Critical Review. *Journal of American Concrete Institute,* 77**,** 59-73.

BIGNOZZI, M. C., BARBIERI, L. & LANCELLOTTI, I. 2010. New Geopolymers Based on Electric Arc Furnace Slag. *Advances in Science and Technology,* 69**,** 117-122.

BLACKFORD, M. G., HANNA, J. V., PIKE, K. J., VANCE, E. R. & PERERA, D. S. 2007. Transmission Electron Microscopy and Nuclear Magnetic Resonance Studies of Geopolymers for Radioactive Waste Immobilization. *Journal of the American Ceramic Society,* 90**,** 1193-1199.

BODEN, T. A. G., MARLAND, A. J. & ANDRES, R. J. 2010. Global, Regional, and National Fossil-Fuel CO2 Emissions. *Carbon Dioxide Information Analysis Center. Oak Ridge National Laboratory, U.S. Department of Energy,* Available at: http://cdiac.ornl.gov/trends/emis/overview_2006.html.

BOURBIGOT, S. & DUQUESNE, S. 2007. Fire retardant polymers: recent developments and opportunities. *Journal of Materials Chemistry,* 17**,** 2283-2300.

BOUZOUBAÂ, N., ZHANG, M. H., MALHOTRA, V. M. & GOLDEN, D. M. 1999. Blended fly ash cements - A review. *ACI Materials Journal* 96**,** 641-650.

BREW, D. & MACKENZIE, K. 2007. Geopolymer synthesis using silica fume and sodium aluminate. *Journal of Materials Science,* 42**,** 3990-3993.

CHALLA, G. 1993. *Polymer chemistry: An introduction,* New York, Ellis Horwood

CHAN, Y. N., PENG, G. F. & ANSON, M. 1999. Residual strength and pore structure of high-strength concrete and normal strength concrete after exposure to high temperatures. *Cement and concrete composites,* 21**,** 23-27.

CHEN-TAN, N. W. 2010. *Geopolymer from a Western Australian Fly Ash.* PhD Thesis, Curtin University of Technology.

CHEN-TAN, N. W., VAN RIESSEN, A., CHI, V. L. Y. & SOUTHAM, D. C. 2009. Determining the Reactivity of a Fly Ash for Production of Geopolymer. *Journal of American Ceramic Society* 92**,** 881-887.

CHENG, T. W. & CHIU, J. P. 2003. Fire-resistant geopolymer produced by granulated blast furnace slag. *Minerals Engineering,* 16**,** 205-210.

CORNELL, R. M. & SCHWERTMANN, U. 1996. *The Iron Oxides: Structure, Properties, Reactions, Occurrence and Uses,* Weinheim, VCH.

CRUZ, C. R. & GILLEN, M. 1980. Thermal Expansion of Portland Cement Paste, Mortar and Concrete at High Temperatures. *Fire and Materials,* 4**,** 66-70.

DAVIDOVITS, J. 1984. *X-Ray Analysis and X-Ray Diffraction of Casing Stones from the Pyramids of Egypt, and the Limestone of the Associated Quarries.* Barry University, USA.

DAVIDOVITS, J. 1987. Properties of geopolymer cements. *Concrete International,* 9**,** 23-35.

DAVIDOVITS, J. 1991. Geopolymers: Inorganic Polymeric New Materials. *Journal of Thermal Analysis,* 37**,** 1633-1656.

DAVIDOVITS, J. 1994a. Global warming impact on the cement and aggregates industries. *World Resource Review,* 6**,** 263-278.

DAVIDOVITS, J. 1994b. High-Alkali Cements for 21st Century Concretes. Concrete Technology, Past, Present and Future. *V. Mohan Malhotra Symposium.*

DAVIDOVITS, J. 2000. *The dependence of geopolymers on Si:Al* [Online]. Available: www.geopolymer.org [Accessed 21/05/2010].

DAVIDOVITS, J. 2002. *30 years of success and failures in Geopolymer applications. Market trends and potential breakthroughs,* Saint Quentin, Geopolymer Institute.

DEER, W. A., HOWIE, R. A. & ZUSSMAN, J. 1996. *An Introduction to The Rock Forming Minerals. 2nd Edition,* Essex, England.

DEMIBORGA, R. 2003. Thermo-mechanical properties of sand and high volume mineral admixtures. *Energy and Buildings,* 35**,** 435-439.

DINNEBIER, R. E. & BILLINGE, S. J. L. (eds.) 2008. *Powder Diffraction - Theory and Practice* Cambribge: The Royal Society of Chemistry.

DOMBROWSKI, K., BUCHWALD, A. & WEIL, M. 2007. The influence of calcium content on the structure and thermal performance of fly ash based geopolymers. *Journal of Materials Science,* 42**,** 3033-3043.

DUXSON, P., FERNÁNDEZ-JIMÉNEZ, A., PROVIS, J., LUKEY, G., PALOMO, A. & VAN DEVENTER, J. 2007a. Geopolymer technology: the current state of the art. *Journal of Materials Science,* 42**,** 2917-2933.

DUXSON, P., LUKEY, G. C. & VAN DEVENTER, J. S. J. 2006a. Thermal Conductivity of Metakaolin Geopolymers Used as a First Approximation for Determining Gel Interconnectivity. *Materials and Interfaces,* 45**,** 7781-7788.

DUXSON, P., LUKEY, G. C. & VAN DEVENTER, J. S. J. 2006b. Thermal evolution of metakaolin geopolymers: Part 1 – Physical evolution. *Journal of Non-Crystalline Solids,* 352**,** 2186-2200.

DUXSON, P., LUKEY, G. C. & VAN DEVENTER, J. S. J. 2007b. Physical evolution of Na-geopolymer derived from metakaolin up to 1000 °C. *Journal of Materials Science,* 42**,** 3044-3054.

DUXSON, P., LUKEY, G. C. & VAN DEVENTER, J. S. J. 2007c. The thermal evolution of metakaolin geopolymers: Part 2 – Phase stability and structural development. *Journal of Non-Crystalline Solids,* 353**,** 2186-2200.

DUXSON, P., PROVIS, J. L., LUKEY, G. C., MALLICOAT, S. W., KRIVEN, W. M. & VAN DEVENTER, J. S. J. 2005. Understanding the relationship between geopolymer composition, microstructure and mechanical properties. *Colloids and Surfaces A: Physicochemical and Engineering Aspects,* 269**,** 47-58.

EN 1991-1-2 2008. Actions on structures – Part 1-2 : General actions – Actions on structures exposed to fire. *European Standard*.

EN 1992-1-2 2004. Eurocode 2: Design of concrete structures – Part 1-2: General rules – Structural fire design. *European Standard*.

FERET, R. 1939. Slags for the manufacture of cement. *Rev Mater Constr Trav*.

FERNANDEZ-JIMENEZ, A., PALOMO, A. & CRIADO, M. 2005. Microstructure development of alkali-activated fly ash cement: a descriptive model. *Cement and Concrete Research,* 35**,** 1204-1209.

FERNÁNDEZ-JIMÉNEZ, A., PALOMO, A., SOBRADOS, I. & SANZ, J. 2006. The role played by the reactive alumina content in the alkaline activation of fly ashes. *Microporous and Mesoporous Materials,* 91**,** 111-119.

FLETCHER, R. A., MACKENZIE, K. J. D., NICHOLSON, C. L. & SHIMADA, S. 2005. The composition range of aluminosilicate geopolymers. *Journal of the European Ceramic Society,* 25**,** 1471-1477.

FLY ASH AUSTRALIA. 2011. *Fine Grade Products - Fly ash technical data* [Online]. Available: http://www.flyashaustralia.com.au/Products.aspx?pgid=11&sec=1 [Accessed 31/08/2011].

GEOPOLYMER INSTITUTE. 2008. *Geopolymer composite material for structural or protective applications, temperature range 300°C to 1000°C.* [Online]. Available: http://www.geopolymer.org/applications/fire-proof-heat-resistant-composites [Accessed 3/8/2008].

GEOPOLYMER INSTITUTE. 2011. *Category Applications: List of selected technical applications* [Online]. Available: http://www.geopolymer.org/category/applications [Accessed 15/8/2011 2011].

GIANCASPRO, J., BALAGURU, P. N. & LYON, R. E. 2006. Use of Inorganic Polymer to Improve the Fire Response of Balsa Sandwich Structures. *Journal of Materials in Civil Engineering,* 18**,** 390-397.

GLATZMAIER, G. C. & RAMIREZ, F. W. 1988. Use of volume averaging for the modeling of thermal properties of porous materials. *Chemical Engineering Science,* 43**,** 3157-3169.

GLUKHOVSKY, V. D. 1959. *Soil Silicates,* Kiev, Ukraine, Gosstroyizdat.

GOMES, S. & FRANÇOIS, M. 2000. Characterization of mullite in silicoaluminous fly ash by XRD, TEM, and 29Si MAS NMR. *Cement and Concrete Research,* 30**,** 175-181.

GOODWIN, R. W. 1993. *Combustion Ash/Residue Management: An Engineering Perspective.*, Noyes Publications.

GORDON, M., BELL, J. & KRIVEN, W. M. 2005. Comparison of Naturally and Synthetically Derived, Potassium Based Geopolymers. *Ceramic Transactions,* 165**,** 95-106.

GOURLEY, J. T. & JOHNSON 2005. Development in geopolymer precast concrete. *In:* DAVIDOVITS, J. (ed.) *Geopolymer green chemistry and sustainable development solutions: Proceedings of the world congress geopolymer 2005.* Saint Quentin: Geopolymer Institute.

GOURLEY, T. 2005. Geopolymer Cement From Regional Waste Streams. *Geopolymer World Conference 2005.* Perth.

HAHN, T. A. 1970. Thermal Expansion of Copper from 20 to 800 K—Standard Reference Material 736 *Journal of Applied Physics,* 41**,** 5096-5101.

HAMMELL, J. A., BALAGURU, P. N. & LYON, R. E. 2000. Strength retention of fire resistant aluminosilicate-carbon composites under wet-dry conditions. *Composites Part B: Engineering,* 31**,** 107-111.

HARDJITO, D. & RANGAN, B. V. 2005. Development and properties of low-calcium fly ash based geopolymer concrete. Research Report. Perth, Australia: Faculty of Engineering, Curtin University of Technology.

HARMATHY, T. Z. 1965. Effect of moisture on the fire endurance of building elements. *ASTM Special Technical Publication,* 385**,** 74-95.

HAVERKAMP, R. G. & WALLWORK, K. S. 2009. X-ray pair distribution function analysis of nanostructured materials using a Mythen detector. *Journal of Synchrotron Radiation,* 16**,** 849-856.

HE, P., JIA, D., LIN, T., WANG, M. & ZHOU, Y. 2010. Effects of high-temperature heat treatment on the mechanical properties of unidirectional carbon fiber reinforced geopolymer composites. *Ceramics International,* 36**,** 1447-1453.

HEIKEN, G. 1972. Morphology and Petrography of Volcanic Ashes. *Geological Society of America Bulletin,* 83**,** 1961-1988.

HELMUTH, R. A. 1987. *Fly ash in cement and concrete,* Portland Cement Association Skokie Illinois.

HEMMINGS, R. T. & BERRY, E. E. 1987. On the Glass in Coal Fly Ashes: Recent Advances. *Fly Ash and Coal Conversion By-Products: Characterization, Utilization, and Disposal V: Symposium***,** 3-38.

HERTZ, K. D. 2005. Concrete strength for fire safety design. *Magazine of concrete research,* 57**,** 445-453.

INSTITUTION OF ENGINEERS 1989. Fire engineering for building structures and safety. Working party on fire engineering, the National Committee on Structural Engineering, Institution of Engineers.

ISO 834 1999. Fire resistance tests - Elements of building construction - Part 1: General requirements.

JAMIESON, E. J., VAN RIESSEN, A., KEALLEY, C. & HART, R. D. 2012. Development of Bayer Geopolymer Paste and use Concrete. *9th International Alumina Quality Workshop.* Perth.

JIMENEZ, M., DUQUESNE, S. & BOURBIGOT, S. 2006. Characterization of the performance of an intumescent fire protective coating. *Surface and Coatings Technology,* 201**,** 979-987.

KIRSHNER, A. V. & HARMUTH, H. 2004. Investigation of geopolymer binders with respect to their application for building materials. *Ceramics Silikaty,* 48**,** 117-120.

KITTEL, C. 2005. *Introduction to Solid State Physics*, John Wiley & Sons.

KOMNITSAS, K. A. 2011. Potential of geopolymer technology towards green buildings and sustainable cities. *Procedia Engineering,* 21**,** 1023-1032.

KONG, D., SANJAYAN, J. & SAGOE-CRENTSIL, K. 2007. Comparative performance of geopolymers made with metakaolin and fly ash after exposure to elevated temperatures. *Cement and Concrete Research,* 37**,** 1583-1589.

KONG, D., SANJAYAN, J. & SAGOE-CRENTSIL, K. 2008. Factors affecting the performance of metakaolin geopolymers exposed to elevated temperatures. *Journal of Materials Science,* 43**,** 824-831.

KONG, D., SANJAYAN, J. G. & SAGOE-CRENTSIL, K. 2005. The behaviour of Geopolymer Paste and Concrete at Elevated Temperatures. *Proceeding of the International Conference on Pozzolan, Concrete and Geoplymer.* Khon Kaen.

KONG, D. L. Y. & SANJAYAN, J. G. 2008. Damage behaviour of geopolymer composites exposed to elevated temperatures. *Cement and concrete composites* 30**,** 986-991.

KOVALCHUK, G., FERNÁNDEZ-JIMÉNEZ, A. & PALOMO, A. 2007. Alkali-activated fly ash: Effect of thermal curing conditions on mechanical and microstructural development - Part II. *Fuel,* 86**,** 315-322.

KOVALCHUK, G. & KRIVENKO, P. V. 2009. Producing fire- and heat-resistant geopolymers. *In:* PROVIS, J. L. & VAN DEVENTER, J. S. J. (eds.) *Geopolymers: Structures, Processing, Properties and Industrial Applications.* Cambridge, UK: Woodhead.

KRIVEN, W. M. 2007. From Geopolymers to Ceramics. *Proceedings of International Conference, Materials and Austceram. Sydney, Australia*.

KRIVEN, W. M., BELL, J. L. & GORDON, M. 2003. Microstructure and Microchemistry of Fully-Reacted Geopolymers and Geopolymer Matrix Composites. *Ceramic Transactions,* 153**,** 227-250.

KRIVENKO, P. 1994. Alkali cements. *First international conference of alkaline cements and concretes.* Kiev, Ukraine.

KRIVENKO, P. & KOVALCHUK, G. 2007. Directed synthesis of alkaline aluminosilicate minerals in a geocement matrix. *Journal of Materials Science,* 42**,** 2944-2952.

KUTCHKO, B. G. & KIM, A. G. 2006. Fly ash characterization by SEM-EDS. *Fuel,* 85**,** 2537-2544.

LEE, S. H., SAKAI, E., DAIMON, M. & BANG, W. K. 1999. Characterization of fly ash directly collected from electrostatic precipitator. *Cement and Concrete Research,* 29**,** 1791-1797.

LI, M., QIAN, C. & SUN, W. 2004. Mechanical properties of high-strength concrete after fire. *Cement and Concrete Research,* 34**,** 1001-1005.

LIEFKE, E. 1999. Industrial applications of foamed inorganic polymers. *Geopolymere '99.* Saint-Quintine, France.

LIN, T. S., JIA, D. C., HE, P. G. & WANG, M. R. 2009. Thermo-mechanical and microstructural characterization of geopolymers with α–Al_2O_3 particle filler. *International Journal of Thermophysics,* 30**,** 1568-1577.

LLOYD, R. R., PROVIS, J. L., SMEATON, K. J. & VAN DEVENTER, J. S. J. 2009. Spatial distribution of pores in fly ash-based inorganic polymer gels visualised by Wood's metal intrusion. *Microporous and Mesoporous Materials,* 126**,** 32-39.

LYON, R. E., BALAGURU, P. N., FODEN, A., SORATHIA, U., DAVIDOVITS, J. & DAVIDOVICS, M. 1997. Fire-resistant aluminosilicate composites. *Fire and Materials,* 21**,** 67-73.

MAITLAND, C. F., BUCKLEY, C. E., O'CONNOR, B. H., BUTLER, P. D. & HART, R. D. 2011. Characterization of the pore structure of metakaolin-derived geopolymers by neutron scattering and electron microscopy. *Journal of Applied Crystallography,* 44**,** 697-707.

MAJKO, R. 2004. *The Fly Ash Resource Center* [Online]. Available: http://www.geocities.com/CapeCanaveral/Launchpad/2095/flyash.html [Accessed 03/07/2008].

MALHOTRA, V. M. & MEHTA, P. K. 1996. *Pozzolanic and Cementitious Materials*, Gordon and Breach Publishers.

MALHOTRA, V. M. & MEHTA, P. K. 2002. *High-Performance High-Volume Fly Ash Concrete: Materials, Mixture Proportioning, Properties, Construction Practice and Case Histories*, Gordon and Breach Publishers.

MALLICOAT, S., SARIN, P. & KRIVEN, W. M. 2008. Novel, Alkali-Bonded, Ceramic Filtration Membranes. *Developments in Advanced Ceramics and Composites: Ceramic Engineering and Science Proceedings.* John Wiley & Sons, Inc.

MANZ, O. E. 1999. Coal fly ash: a retrospective and future look. *Fuel,* 78**,** 133-136.

MATSUNAGA, T., KIM, J. K., HARDCASTLE, S. & ROHATGI, P. K. 2002. Crystallinity and selected properties of fly ash particles. *Materials Science and Engineering A,* 325**,** 333-343.

MCLELLAN, B. C., WILLIAMS, R. P., LAY, J., VAN RIESSEN, A. & CORDER, G. D. 2011. Costs and carbon emissions for geopolymer pastes in comparison to ordinary portland cement. *Journal of Cleaner Production,* 19**,** 1080-1090.

MENDES, A., SANJAYAN, J. G. & COLLINS, F. 2008. Phase transformations and mechanical strength of OPC/slag pastes submitted to high temperatures. *Materials and structures* 42**,** 345-350.

MENDES, A., SANJAYAN, J. G. & COLLINS, F. 2009. Long-term progressive deterioration following fire exposure of OPC versus slag blended cement pastes. *Materials and structures,* 42**,** 95-101.

NAVE, R. 2005. *Thermal expansion* [Online]. Hyperphysics, Georgie State University. Available: http://hyperphysics.phy-astr.gsu.edu/hbase/thermo/thexp.html [Accessed 14/04/2008].

NEVILLE, A. M. 2000. *Properties of Concrete,* Harlow.

NISHIDA, A., YAMAZAKI, N. & INOUE, H. 1995. Study on the properties of high strength concrete with short polypropylene fibre for spalling resistance. *Shimizu Technical Research Bulletin,* 14**,** 1-6.

NORTON, G. A., MARKUSZEWSKL, R. & SHANKS, H. R. 1986. Morphological and chemical characterization of iron-rich fly ash fractions. *Environmental Science & Technology,* 20**,** 409-413.

NT FIRE 046 1993. Atrium Roof Construction: Fire Resistance. *Nordtest Method*.

O'CONNOR, S. & MACKENZIE, K. 2010. Synthesis, characterisation and thermal behaviour of lithium aluminosilicate inorganic polymers. *Journal of Materials Science,* 45**,** 3707-3713.

PACHECO-TORGAL, F., CASTRO-GOMES, J. & JALALI, S. 2008. Alkali-activated binders: A review: Part 1. Historical background, terminology, reaction mechanisms and hydration products. *Construction and Building Materials,* 22**,** 1305-1314.

PALOMO, A., GRUTZECK, M. W. & BLANCO, M. T. 1999. Alkali-activated fly ashes. A cement for the future. *Cement and Concrete Research,* 29**,** 1323-1329.

PAN, Z. & SANJAYAN, J. G. 2010. Stress-strain behaviour and abrupt loss of stiffness of geopolymer at elevated temperatures. *Cement and Concrete Composites,* 32**,** 657-664.

PAN, Z. & SANJAYAN, J. G. 2011. Factors influencing softening temperature and hot-strength of geopolymers. *Cement and concrete composites,* 34**,** 261-264.

PERERA, S. & TRAUTMAN, R. L. 2006. Geopolymer with the Potential use as Refractory Castables. *AZojomo,* 2**,** 1-5.

PROVIS, J. 2012. *RILEM Technical Committee on Alkali Activated Materials (TC 224-AAM).*

PROVIS, J. L., YONG, C. Z., DUXSON, P. & VAN DEVENTER, J. S. J. 2009. Correlating mechanical and thermal properties of sodium silicate-fly ash geopolymers. *Colloids and Surfaces A - Physicochemical and Engineering Aspects,* 336**,** 57-63.

PRUD'HOMME, E., MICHAUD, P., JOUSSEIN, E., PEYRATOUT, C., SMITH, A., ARRII-CLACENS, S., CLACENS, J. M. & ROSSIGNOL, S. 2010. Silica fume as porogent agent in geo-materials at low temperature. *Journal of the European Ceramic Society,* 30**,** 1641-1648.

PRUD'HOMME, E., MICHAUD, P., JOUSSEIN, E., PEYRATOUT, C., SMITH, A. & ROSSIGNOL, S. 2009. Consolidated Geo-Materials from Sand or Industrial Waste. *Mechanical Properties and Performance of Engineering Ceramics and Composites IV.* John Wiley & Sons, Inc.

PURDON, A. O. 1940. The action of alkalis on blast furnace slag. *Journal of the Society of Chemical Industry,* 59**,** 191-202.

RAHIER, H., DENAYER, J. F. & VAN MELE, B. 2003. Low-temperature synthesized aluminosilicate glasses - Part IV Modulated DSC study on the effect of particle size of metakaolinite on the production of inorganic polymer glasses. *Journal of Materials Science,* 38**,** 3131-3136.

RAHIER, H., SIMONS, W., VAN MELE, B. & BIESEMANS, M. 1997. Low-temperature synthesized aluminosilicate glasses. Part III Influence of the composition of the silicate solution on production, structure and properties. *Journal of Materials Science,* 32**,** 2237-2247.

RAHIER, H., WASTIELS, J., BIESEMANS, M., WILLEM, R., VAN ASSCHE, G. & VAN MELE, B. 2007. Reaction mechanism, kinetics and high temperature transformations of geopolymers. *Journal of Materials Science,* 42**,** 2982-2996.

RANGAN, B. V. 2007. *Low-Calcium Fly Ash-Based Geopolymer Concrete,* New York, CRC Press.

REIMER, L. 1998. *Scanning Electron Microscopy - Physics of Image Formation and Microanalysis,* Heidelburg, Germany, Springer - Verlag.

RIBEIRO, M., TULYAGAVOV, D., FERREIRA, J. & LABRINCHA, J. 2005. High temperature mullite dissolution in ceramic bodies derived from Al-rich sludge. *Journal of the European Ceramic Society,* 25**,** 703-710.

RICKARD. 2007. *Thermal properties of Geopolymers.* Bsc Physics (Honours) Honours Thesis, Curtin University of Technology.

RICKARD, W. D. A., VAN RIESSEN, A. & WALLS, P. 2010. Thermal character of geopolymers synthesized from Class F fly ash containing high concentrations of iron and α-quartz. *International Journal of Applied Ceramic Technology,* 7**,** 81-88.

RICKARD, W. D. A., WILLIAMS, R., TEMUUJIN, J. & VAN RIESSEN, A. 2011. Assessing the suitability of three Australian fly ashes as an aluminosilicate source for geopolymers in high temperature applications. *Materials Science and Engineering: A,* 528**,** 3390-3397.

RIETVELD, H. M. 1969. A profile refinement method for nuclear and magnetic structures. *Journal of Applied Crystallography* 65-71.

ROWLES, M. & O'CONNOR, B. 2003. Chemical optimisation of the compressive strength of aluminosilicate geopolymers synthesised by sodium silicate activation of metakaolinite. *Journal of Materials Chemistry,* 13**,** 1161.

SABIR, B. B., WILD, S. & BAI, J. 2001. Metakaolin and calcined clays as pozzolans for concrete: a review. *Cement and concrete composites,* 23**,** 441-454.

SANJAYAN, G. & STOCKS, L. J. 1993. Spalling of High-Strength Silica Fume Concrete in Fire. *ACI Materials Journal, American Concrete Institute,* 90**,** 170-173.

SCHAIRER, J. & BOWEN, N. 1956. The system Na2O-Al2O3-SiO2. *American Journal of Science,* 254**,** 129-195.

SCHMITT, B., BRÖNNIMANN, C., EIKENBERRY, E. F., GOZZO, F., HÖRMANN, C., HORISBERGER, R. & PATTERSON, B. 2003. Mythen detector system. *Nuclear Instruments and Methods in Physics Research Section A: Accelerators, Spectrometers, Detectors and Associated Equipment,* 501**,** 267-272.

SCHNEIDER, H., SCHREUER, J. & HILDMANN, B. 2008. Structure and properties of mullite - A review. *Journal of the European Ceramic Society,* 28**,** 329-344.

SCRIVENER, K. L., CABIRON, J. & LETOURNEUX, R. 1999. High-performance concretes from calcium aluminate cements *Cement and Concrete Research,* 29**,** 1215-1223.

SHORTER, G. W. & HARMATHY, T. Z. 1961. Discussion of the fire resistance of prestressed concrete beams. *Proceedings of the Institution of Civil Engineers,* 20**,** 313-315.

SIDDIQUE, R., KHAN, M. I. & IQBAL KHAN, M. 2011. Rice Husk Ash. *Supplementary Cementing Materials.* Springer Berlin Heidelberg.

SIDHU, P. S. 1988. Transformation of trace element-substituted maghemite to hematite. *Clays and Clay Minerals,* 36**,** 31-38.

ŠKVÁRA, F., JILEK, T. & KOPECKY, L. 2005. Geopolymer materials based on fly ash. *Ceramics Silikaty,* 49**,** 195-204.

SOFI, M., VAN DEVENTER, J., MENDIS, P. & LUKEY, G. 2007. Bond performance of reinforcing bars in inorganic polymer concrete (IPC). *Journal of Materials Science,* 42**,** 3107-3116.

STREET-DIRECTORY.COM.AU. 2011. *Australia Map Guide* [Online]. Available: http://www.street-directory.com.au/sd_new/home.cgi [Accessed 12/09/2011].

SUBAER. 2005. *Influence of aggregate on the microstructure of geopolymer*. PhD thesis, Curtin University of Technology.

SUBAER & VAN RIESSEN, A. 2006. Thermo-mechanical and microstructural characterisation of sodium-poly(silate-siloxo) (Na-PSS) geopolymers. *Journal of Materials Science,* 42**,** 3117-3123.

SUH, I.-K., OHTA, H. & WASEDA, Y. 1988. High-temperature thermal expansion of six metallic elements measured by dilatation method and X-ray diffraction. *Journal of Materials Science,* 23**,** 757-760.

SVINGALA, F. & VARELA, B. 2009. Alkali Activated Aerogels. *Mechanical Properties and Performance of Engineering Ceramics and Composites IV*. John Wiley & Sons, Inc.

TEMUUJIN, J., MINJIGMAA, A., LEE, M., CHEN-TAN, N. & VAN RIESSEN, A. 2011. Characterisation of class F fly ash geopolymer pastes immersed in acid and alkaline solutions. *Cement and concrete composites,* 33**,** 1086-1091.

TEMUUJIN, J., MINJIGMAA, A., RICKARD, W., LEE, M., WILLIAMS, I. & VAN RIESSEN, A. 2009a. Preparation of metakaolin based geopolymer coatings on metal substrates as thermal barriers. *Applied Clay Science,* 46**,** 265-270.

TEMUUJIN, J., MINJIGMAA, A., RICKARD, W. & VAN RIESSEN, A. 2012. Thermal properties of spray-coated geopolymer-type compositions. *Journal of Thermal Analysis and Calorimetry,* 107**,** 287-292.

TEMUUJIN, J., RICKARD, W., LEE, M. & VAN RIESSEN, A. 2010. Preparation and thermal properties of fire resistant metakaolin-based geopolymer-type coatings. *Journal of Non-Crystalline Solids,* 357**,** 1399-1404.

TEMUUJIN, J., WILLIAMS, R. P. & VAN RIESSEN, A. 2009b. Effect of mechanical activation of fly ash on the properties of geopolymer cured at ambient temperature. *Journal of Materials Processing Technology,* 209**,** 5276-5280.

VAN DEVENTER, J. S. J., PROVIS, J. L., DUXSON, P. & LUKEY, G. C. 2006. Reaction mechanisms in the geopolymeric conversion of inorganic waste to useful products. *Journal of Hazardous Materials,* 139**,** 506-513.

VAN JAARSVELD, J. G. S., VAN DEVENTER, J. S. J. & LORENZEN, L. 1997. The potential use of geopolymeric materials to immobilise toxic metals: Part I. Theory and applications. *Minerals Engineering,* 10**,** 659-669.

VAN JAARSVELD, J. G. S., VAN DEVENTER, J. S. J. & LUKEY, G. C. 2002. The effect of composition and temperature on the properties of fly ash and kaolinite based geopolymers *Chemical Engineering Journal,* 89**,** 63-73.

VAN JAARSVELD, J. G. S., VAN DEVENTER, J. S. J. & LUKEY, G. C. 2003. The characterisation of source materials in fly ash-based geopolymers *Materials Letters,* 57**,** 1272-1280.

VAN RIESSEN, A., RICKARD, W. & SANJAYAN, J. 2009. Thermal properties of geopolymers. *In:* PROVIS, J. L. & VAN DEVENTER, J. S. J. (eds.) *Geopolymers: Structures, Processing, Properties and Industrial Applications.* Cambridge, UK: Woodhead.

VAOU, V. & PANIAS, D. 2010. Thermal insulating foamy geopolymers from perlite. *Minerals Engineering,* 23**,** 1146-1151.

VILCHES, L. F., FERNÁNDEZ-PEREIRA, C., VALLE, J. 1. O. D. & VALE, J. 2003. Recycling potential of coal fly ash and titanium waste as new fireproof products. *Chemical Engineering Journal,* 95**,** 155-161.

WAGNERS. 2011. *Wagners Earth Friendly Concrete gets 'green' light from Toowoomba Regional Council* [Online]. Available: http://www.wagner.com.au/tabid/74/newsid479/418/Wagners-Earth-Friendly-Concrete-gets-green-light-from-Toowoomba-Regional-Council/language/en-US/Default.aspx [Accessed 19/09/2011].

WALLS, P. A. 2006. Optimising the Porcessing of Geopolymer Cements. *26th Conference on cement and concrete science.* Sheffield University, UK.

WALLWORK, K. S., KENNEDY, B. J. & WANG, D. 2007. The High Resolution Powder Diffraction Beamline for the Australian Synchrotron. *AIP Conference Proceedings,* 879**,** 879-882.

WANG, H., LI, H. & YAN, F. 2005. Synthesis and mechanical properties of metakaolinite-based geopolymer. *Colloids and Surfaces A: Physicochemical and Engineering Aspects,* 268**,** 1-6.

WEAST, R. C. 1986. *CRC Handbook of Chemistry and Physics,* Boca Raton, Florida, CRC Press Inc.

WEIL, E. D. 2011. Fire-Protective and Flame-Retardant Coatings - A State-of-the-Art Review. *Journal of Fire Sciences,* 29**,** 259-296.

WHITE, C. E., PROVIS, J. L., PROFFEN, T. & VAN DEVENTER, J. S. J. 2010. The effects of temperature on the local structure of metakaolion-based geopolymer binder: A neutron pair distribution function investigation. *J. Am Ceram. Soc. ,* 93**,** 3486-3492.

WILLIAMS, R. 2006. *Characterisation of Fly Ash for production of Geopolymer.* Honours Dissertation, Curtin University of Technology.

WILLIAMS, R. P., HART, R. D. & VAN RIESSEN, A. 2011. Quantification of the Extent of Reaction of Metakaolin-Based Geopolymers Using X-Ray Diffraction, Scanning Electron Microscopy, and Energy-Dispersive Spectroscopy. *Journal of the American Ceramic Society,* 94**,** 2663-2670.

WILLIAMS, R. P. & VAN RIESSEN, A. 2010. Determination of the reactive component of fly ashes for geopolymer production using XRF and XRD. *Fuel,* 89**,** 3683-3692.

WORRELL, E., PRICE, L., MARTIN, N., HENDRIKS, C. & MEIDA, L. O. 2001. CARBON DIOXIDE EMISSIONS FROM THE GLOBAL CEMENT INDUSTRY. *Annual Review of Energy and the Environment,* 26**,** 303-329.

ZAENI, A., BANDYOPADHYAY, S., YU, A., RIDER, J., SORRELL, C. S., DAIN, S., BLACKBURN, D. & WHITE, C. 2010. Colour control in fly ash as a combined function of particle size and chemical composition. *Fuel,* 89**,** 399-404.

ZEIML, M., LEITHNER, D., LACKNER, R. & MANG, H. A. 2006. How do polypropylene fibers improve the spalling behavior of in-situ concrete? *Cement and Concrete Research,* 36**,** 929-942.

ZEOBOND. 2011. *The Zeobond group: E-crete and GreenStar* [Online]. Available: http://www.zeobond.com/e-crete-greenstar.html [Accessed 07/09/2011].

ZHANG, S. & HORROCKS, A. R. 2003. A review of flame retardant polypropylene fibres. *Progress in Polymer Science,* 28**,** 1517-1538.

ZHAO, R. & SANJAYAN, J. G. 2011. Geopolymer and portland cement concretes in simulated fire. *Magazine of concrete research,* 63**,** 163-173.

ZUDA, L. & ČERNÝ, R. 2009. Measurement of linear thermal expansion coefficient of alkali-activated aluminosilicate composites up to 1000°C. *Cement and Concrete Composites,* 31**,** 263-267.

ZUDA, L., DRCHALOVÁ, J., ROVNANÍK, P., BAYER, P., KERŠNER, Z. & ČERNÝ, R. 2010. Alkali-activated aluminosilicate composite with heat-resistant lightweight aggregates exposed to high temperatures: Mechanical and water transport properties. *Cement and Concrete Composites,* 32**,** 157-163.

ZUDA, L., PAVLıK, Z., ROVNANıKOVA, P., BAYER, P. & CERNY, R. 2006. Properties of Alkali Activated Aluminosilicate Materials after Thermal Load. *International Journal of Thermophysics,* 27**,** 1250-1263.

Appendices

Appendix A

The refinement strategy and full details of the QXRD analysis from each of the fly ashes are listed in this appendix.

Refinement strategy

The Rietveld refinement strategy as used for the QXRD of the fly ashes was as follows;

- Load appropriate scan file
- Load emission profile 'CuKα5'
- Set background polynomial order to 5, set to refine
- Check 1/X Bkg box, set to refine
- Load instrument settings file 'Curtin LynxEye jan 09'
- Set LP factor to 0
- Select a split psuedo-Voigt peak at peak of amorphous hump, fix LOR left and LOR right to 0.5)
- Load the CIF's as identified by search / match. Correct for special positions
- Load 'Fluorite Topas.str' structure file
- Define the exact mass concentration of fluorite
- Run the refinement
- Load a secondary quartz phase
- Rename the original Quartz phase and set crystallite size to 200 nm
- Refine the lattice parameters and scale factor of both quartz phases
- Fix both quartz lattice parameters
- Refine the specimen displacement
- Refine individually each phase's lattice parameters, scale factors and crystallite size
- Refine all previously refined parameters until convergence
- Check final refinement in terms of the Rietveld weighted profile (Rwp), goodness of fit (GOF), density of calculated phases and R-Bragg values for each phase

Topas outputs

Collie Fly Ash;

File : "..\Collie_WRbatch+std low fluorescence run.raw"

R-Values

Rexp : 5.14	Rwp : 6.84	Rp : 5.16	GOF : 1.33
Rexp` : 18.00	Rwp` : 23.98	Rp` : 27.97	DW : 1.17

Quantitative Analysis, Wt%

		Rietveld	Spiked	Original
	Amorphous content	0	48.61(40)	54.00(45)
1	"Hematite ICSD 88417"	2.63(11)	1.349(57)	1.499(64)
2	"Magnetite ICSD 43001"	4.40(15)	2.259(75)	2.509(83)
3	"Mullite ICSD 66452"	27.68(31)	14.22(16)	15.80(18)
4	"Quartz low (P)ICSD 83849"	26.36(32)	13.55(17)	15.05(18)
5	"Quartz low ICSD 83849 "	19.51(36)	10.03(19)	11.14(21)
6	*"Fluorite ICSD 60559"	19.43(15)	9.984	0.000

Background

Chebychev polynomial, Coefficient	0	371.0(18)
	1	-328.6(28)
	2	170.8(11)
	3	-62.8(12)
	4	27.0(21)
	5	-3.8(20)
	6	0.3(12)

Instrument

Primary radius (mm)	250
Secondary radius (mm)	250
Linear PSD 2Th angular range (°)	3
FDS angle (°)	0.3
Full Axial Convolution	
Filament length (mm)	12
Sample length (mm)	25
Receiving Slit length (mm)	17
Primary Sollers (°)	2.5
Secondary Sollers (°)	2.5

Corrections

Specimen displacement	-0.01466(43)
LP Factor	0

Structure 1

Phase name	Hematite ICSD 88417
R-Bragg	1.877
Spacegroup	R-3cH
Scale	0.00001247(54)
Cell Mass	958.149
Cell Volume (Å^3)	301.37(10)
Wt% - Rietveld	2.63(11)
Wt% in Spiked sample	1.349(57)
Wt% in Original sample	1.499(64)
Crystallite Size	
Cry size Lorentzian (nm)	69.3(61)

Crystal Linear Absorption Coeff. (1/cm)	1134.78(39)
Crystal Density (g/cm^3)	5.2794(18)
Lattice parameters	
a (Å)	5.03283(68)
c (Å)	13.7385(30)

Site	Np	x	y	z	Atom	Occ	Beq
Fe1	12	0.00000	0.00000	0.35529	Fe+3	1	0.6
O1	18	0.69530	0.00000	0.25000	O-2	1	0.6

Structure 2

Phase name	Magnetite ICSD 43001
R-Bragg	1.668
Spacegroup	Fd-3mZ
Scale	0.00000555(19)
Cell Mass	1852.301
Cell Volume (Å^3)	586.61(25)
Wt% - Rietveld	4.40(15)
Wt% in Spiked sample	2.259(75)
Wt% in Original sample	2.509(83)
Crystallite Size	
Cry size Lorentzian (nm)	21.2(11)
Crystal Linear Absorption Coeff. (1/cm)	1163.89(49)
Crystal Density (g/cm^3)	5.2434(22)
Lattice parameters	
a (Å)	8.3711(12)

Site	Np	x	y	z	Atom	Occ	Beq
Fe1	8	0.12500	0.12500	0.12500	Fe+2	1	0.6
Fe2	16	0.50000	0.50000	0.50000	Fe+3	1	0.6
O1	32	0.25600	0.25600	0.25600	O-2	1	0.6

Structure 3

Phase name	Mullite ICSD 66452
R-Bragg	2.605
Spacegroup	Pbam
Scale	0.0007074(91)
Cell Mass	318.993
Cell Volume (Å^3)	168.298(20)
Wt% - Rietveld	27.68(31)
Wt% in Spiked sample	14.22(16)
Wt% in Original sample	15.80(18)
Crystallite Size	
Cry size Lorentzian (nm)	81.4(23)
Crystal Linear Absorption Coeff. (1/cm)	103.552(12)
Crystal Density (g/cm^3)	3.14739(37)
Lattice parameters	
a (Å)	7.56890(53)
b (Å)	7.69573(56)
c (Å)	2.88933(17)

Site	Np	x	y	z	Atom	Occ	Beq
Al1	2	0.00000	0.00000	0.00000	Al+3	1	1.23
Al2	4	0.14880	0.34090	0.50000	Al+3	0.5	1.23
Si2	4	0.14880	0.34090	0.50000	Si+4	0.36	1.23
Al3	4	0.26260	0.20680	0.50000	Al+3	0.14	1.23
O1	4	0.35770	0.42240	0.50000	O-2	1	1.23
O2	4	0.12690	0.22030	0.00000	O-2	1	1.23
O3	2	0.50000	0.00000	0.50000	O-2	0.58	1.23
O4	4	0.44280	0.05570	0.50000	O-2	0.14	1.23

Structure 4

Phase name	Quartz low P ICSD 83849
R-Bragg	4.832
Spacegroup	P3221
Scale	0.001775(26)
Cell Mass	180.252
Cell Volume (Å^3)	113.0484(45)
Wt% - Rietveld	26.36(32)
Wt% in Spiked sample	13.55(17)
Wt% in Original sample	15.05(18)
Crystallite Size	
Cry size Lorentzian (nm)	241.1(67)
Crystal Linear Absorption Coeff. (1/cm)	95.3458(38)
Crystal Density (g/cm^3)	2.64768(11)
Lattice parameters	
a (Å)	4.913940(75)
c (Å)	5.40598(14)

Site	Np	x	y	z	Atom	Occ	Beq
Si1	3	0.46980	0.00000	0.16667	Si+4	1	2.1
O1	6	0.41380	0.26510	0.28710	O-2	1	2.46

Structure 5

Phase name	Quartz low ICSD 83849
R-Bragg	2.711
Spacegroup	P3221
Scale	0.001303(29)
Cell Mass	180.252
Cell Volume (Å^3)	113.970(16)
Wt% - Rietveld	19.51(36)
Wt% in Spiked sample	10.03(19)
Wt% in Original sample	11.14(21)
Crystallite Size	
Cry size Lorentzian (nm)	94.4(25)
Crystal Linear Absorption Coeff. (1/cm)	94.575(13)
Crystal Density (g/cm^3)	2.62627(36)
Lattice parameters	
a (Å)	4.93117(26)
c (Å)	5.41201(46)

Site	Np	x	y	z	Atom	Occ	Beq
Si1	3	0.46980	0.00000	0.16667	Si+4	1	2.1
O1	6	0.41380	0.26510	0.28710	O-2	1	2.46

Structure 6

Phase name	Fluorite ICSD 60559
R-Bragg	2.307
Spacegroup	Fm-3m
Scale	0.0005230(22)
Cell Mass	312.300
Cell Volume (Å^3)	163.20154
Wt% - Rietveld	19.43(15)
Wt% in Spiked sample	9.984
Wt% in Original sample	0.000
Crystallite Size	
Cry size Lorentzian (nm)	279.7(39)
Crystal Linear Absorption Coeff. (1/cm)	302.930
Crystal Density (g/cm^3)	3.178
Lattice parameters	
a (Å)	5.4648061

Site	Np	x	y	z	Atom	Occ	Beq
Ca1	4	0.00000	0.00000	0.00000	Ca+2	1	0.578
F1	8	0.25000	0.25000	0.25000	F-1	1	0.7821

Peaks Phase 1

Phase name Peaks Phase:0

Type	Position	I		
FP	22.999(98)	16.7(44)	Cry size Lor(nm)	1.62(25)

Eraring Fly Ash;

File : "..\EraringFA + 10% CaF.raw"

R-Values

Rexp : 4.27 Rwp : 4.73 Rp : 3.69 GOF : 1.11
Rexp`: 18.78 Rwp`: 20.83 Rp` : 23.21 DW : 1.63

Quantitative Analysis, Wt%

		Rietveld	Spiked	Original
	Amorphous content	0	56.40(28)	62.74(31)
1	"Mullite ICSD 66449"	43.04(28)	18.77(12)	20.88(14)
2	"Magnetite ICSD 43001"	3.07(11)	1.340(47)	1.491(52)
3	"Quartz low ICSD 83849"	16.66(33)	7.27(14)	8.08(16)
4	"Quartz low Primary ICSD 83849"	14.04(29)	6.12(13)	6.81(14)
5	*"Fluorite ICSD 60559"	23.18(15)	10.105	0.000

Background

Chebychev polynomial, Coefficient	0	520.4(42)
	1	-300.7(63)
	2	157.6(25)
	3	-63.9(14)
	4	35.9(34)
	5	-9.2(35)
	6	2.0(21)

Instrument

Primary radius (mm)	250
Secondary radius (mm)	250
Linear PSD 2Th angular range (°)	3
FDS angle (°)	0.3
Full Axial Convolution	
Filament length (mm)	12
Sample length (mm)	25
Receiving Slit length (mm)	17
Primary Sollers (°)	2.5
Secondary Sollers (°)	2.5

Corrections

Specimen displacement	0.03373(33)
LP Factor	0

Structure 1

Phase name	Mullite ICSD 66449
R-Bragg	1.030
Spacegroup	Pbam

Scale	0.0008555(58)
Cell Mass	318.701
Cell Volume (Å^3)	167.8955(90)
Wt% - Rietveld	43.04(28)
Wt% in Spiked sample	18.77(12)
Wt% in Original sample	20.88(14)
Crystallite Size	
Cry size Lorentzian (nm)	101.4(15)
Crystal Linear Absorption Coeff. (1/cm)	103.6275(55)
Crystal Density (g/cm^3)	3.15206(17)
Lattice parameters	
a (Å)	7.56073(24)
b (Å)	7.69103(25)
c (Å)	2.887293(77)

Site	Np	x	y	z	Atom	Occ	Beq
Al1	2	0.00000	0.00000	0.00000	Al+3	1	1.14
Al2	4	0.14920	0.34080	0.50000	Al+3	0.5	1.14
Si2	4	0.14920	0.34080	0.50000	Si+4	0.352	1.14
Al3	4	0.26260	0.20650	0.50000	Al+3	0.148	1.14
O1	4	0.35700	0.42290	0.50000	O-2	1	1.14
O2	4	0.12730	0.21990	0.00000	O-2	1	1.14
O3	2	0.50000	0.00000	0.50000	O-2	0.556	1.14
O4	4	0.44210	0.05340	0.50000	O-2	0.148	1.14

Structure 2

Phase name	Magnetite ICSD 43001
R-Bragg	0.366
Spacegroup	Fd-3mZ
Scale	0.00000300(11)
Cell Mass	1852.301
Cell Volume (Å^3)	587.35(22)
Wt% - Rietveld	3.07(11)
Wt% in Spiked sample	1.340(47)
Wt% in Original sample	1.491(52)
Crystallite Size	
Cry size Lorentzian (nm)	27.8(15)
Crystal Linear Absorption Coeff. (1/cm)	1162.42(43)
Crystal Density (g/cm^3)	5.2368(19)
Lattice parameters	
a (Å)	8.3746(10)

Site	Np	x	y	z	Atom	Occ	Beq
Fe1	8	0.12500	0.12500	0.12500	Fe+2	1	0.6
Fe2	16	0.50000	0.50000	0.50000	Fe+3	1	0.6
O1	32	0.25600	0.25600	0.25600	O-2	1	0.6

Structure 3

Phase name	Quartz low ICSD 83849
R-Bragg	0.802
Spacegroup	P3221
Scale	0.000858(20)
Cell Mass	180.252
Cell Volume (Å^3)	114.594(20)
Wt% - Rietveld	16.66(33)
Wt% in Spiked sample	7.27(14)
Wt% in Original sample	8.08(16)
Crystallite Size	
Cry size Lorentzian (nm)	77.5(20)
Crystal Linear Absorption Coeff. (1/cm)	94.060(17)
Crystal Density (g/cm^3)	2.61197(46)

Lattice parameters	
a (Å)	4.93864(34)
c (Å)	5.42521(59)

Site	Np	x	y	z	Atom	Occ	Beq
Si1	3	0.46980	0.00000	0.16667	Si+4	1	2.1
O1	6	0.41380	0.26510	0.28710	O-2	1	2.46

Structure 4

Phase name	Quartz low P ICSD 83849
R-Bragg	0.884
Spacegroup	P3221
Scale	0.000731(17)
Cell Mass	180.252
Cell Volume (Å^3)	113.315(13)
Wt% - Rietveld	14.04(29)
Wt% in Spiked sample	6.12(13)
Wt% in Original sample	6.81(14)
Crystallite Size	
Cry size Lorentzian (nm)	127.2(38)
Crystal Linear Absorption Coeff. (1/cm)	95.122(11)
Crystal Density (g/cm^3)	2.64145(30)
Lattice parameters	
a (Å)	4.91846(21)
c (Å)	5.40878(39)

Site	Np	x	y	z	Atom	Occ	Beq
Si1	3	0.46980	0.00000	0.16667	Si+4	1	2.1
O1	6	0.41380	0.26510	0.28710	O-2	1	2.46

Structure 5

Phase name	Fluorite ICSD 60559
R-Bragg	3.087
Spacegroup	Fm-3m
Scale	0.0004836(14)
Cell Mass	312.300
Cell Volume (Å^3)	163.20154
Wt% - Rietveld	23.18(15)
Wt% in Spiked sample	10.105
Wt% in Original sample	0.000
Crystallite Size	
Cry size Lorentzian (nm)	220.8(18)
Crystal Linear Absorption Coeff. (1/cm)	302.930
Crystal Density (g/cm^3)	3.178
Lattice parameters	
a (Å)	5.4648061

Site	Np	x	y	z	Atom	Occ	Beq
Ca1	4	0.00000	0.00000	0.00000	Ca+2	1	0.578
F1	8	0.25000	0.25000	0.25000	F-1	1	0.7821

Peaks Phase 1

Type	Position	I		
FP	22.000(33)	94.7(92)	Cry size Lor(nm)	1.061(45)

Tarong Fly Ash;

File : "..\TarongFA + 10% CaF.raw"

R-Values

Rexp : 4.82	Rwp : 5.79	Rp : 4.40	GOF : 1.20
Rexp`: 13.16	Rwp`: 15.83	Rp` : 15.54	DW : 1.38

Quantitative Analysis, Wt%

		Rietveld	Spiked	Original
	Amorphous content	0	45.74(25)	50.82(28)
1	"Mullite ICSD 66452"	41.63(19)	22.59(10)	25.10(11)
2	"Quartz low Primary ICSD 83849"	22.84(21)	12.39(11)	13.77(13)
3	"Quartz low ICSD 83849"	17.10(23)	9.28(13)	10.31(14)
4	*"Fluorite ICSD 60559"	18.438(85)	10.005	0.000

Background

Chebychev polynomial, Coefficient	0	369.0(35)
	1	-300.4(53)
	2	165.3(22)
	3	-76.8(11)
	4	50.4(27)
	5	-19.0(29)
	6	5.6(19)

Instrument

Primary radius (mm)	250
Secondary radius (mm)	250
Linear PSD 2Th angular range (°)	3
FDS angle (°)	0.3
Full Axial Convolution	
Filament length (mm)	12
Sample length (mm)	25
Receiving Slit length (mm)	17
Primary Sollers (°)	2.5
Secondary Sollers (°)	2.5

Corrections

Specimen displacement	0.03326(26)
LP Factor	0

Structure 1

Phase name	Mullite ICSD 66452
R-Bragg	1.541
Spacegroup	Pbam
Scale	0.0013831(62)
Cell Mass	318.993
Cell Volume (Å^3)	167.9964(63)
Wt% - Rietveld	41.63(19)
Wt% in Spiked sample	22.59(10)
Wt% in Original sample	25.10(11)
Crystallite Size	
Cry size Lorentzian (nm)	91.67(90)
Crystal Linear Absorption Coeff. (1/cm)	103.7377(39)
Crystal Density (g/cm^3)	3.15305(12)
Lattice parameters	
a (Å)	7.55934(18)

b (Å)	7.69378(18)
c (Å)	2.888527(55)

Site	Np	x	y	z	Atom	Occ	Beq
Al1	2	0.00000	0.00000	0.00000	Al+3	1	1.23
Al2	4	0.14880	0.34090	0.50000	Al+3	0.5	1.23
Si2	4	0.14880	0.34090	0.50000	Si+4	0.36	1.23
Al3	4	0.26260	0.20680	0.50000	Al+3	0.14	1.23
O1	4	0.35770	0.42240	0.50000	O-2	1	1.23
O2	4	0.12690	0.22030	0.00000	O-2	1	1.23
O3	2	0.50000	0.00000	0.50000	O-2	0.58	1.23
O4	4	0.44280	0.05570	0.50000	O-2	0.14	1.23

Structure 2

Phase name	Quartz low P ICSD 83849
R-Bragg	1.566
Spacegroup	P3221
Scale	0.001990(22)
Cell Mass	180.252
Cell Volume (Å^3)	113.3836(53)
Wt% - Rietveld	22.84(21)
Wt% in Spiked sample	12.39(11)
Wt% in Original sample	13.77(13)
Crystallite Size	
Cry size Lorentzian (nm)	123.3(17)
Crystal Linear Absorption Coeff. (1/cm)	95.0639(45)
Crystal Density (g/cm^3)	2.63985(12)
Lattice parameters	
a (Å)	4.920389(88)
c (Å)	5.40780(16)

Site	Np	x	y	z	Atom	Occ	Beq
Si1	3	0.46980	0.00000	0.16667	Si+4	1	2.259(69)
O1	6	0.41380	0.26510	0.28710	O-2	1	2.90(18)

Structure 3

Phase name	Quartz low ICSD 83849
R-Bragg	1.122
Spacegroup	P3221
Scale	0.001473(23)
Cell Mass	180.252
Cell Volume (Å^3)	114.6457(94)
Wt% - Rietveld	17.10(23)
Wt% in Spiked sample	9.28(13)
Wt% in Original sample	10.31(14)
Crystallite Size	
Cry size Lorentzian (nm)	77.6(12)
Crystal Linear Absorption Coeff. (1/cm)	94.0174(77)
Crystal Density (g/cm^3)	2.61079(21)
Lattice parameters	
a (Å)	4.93952(16)
c (Å)	5.42573(28)

Site	Np	x	y	z	Atom	Occ	Beq
Si1	3	0.46980	0.00000	0.16667	Si+4	1	1.095(78)
O1	6	0.41380	0.26510	0.28710	O-2	1	0.91(18)

Structure 4

Phase name	Fluorite ICSD 60559
R-Bragg	0.776
Spacegroup	Fm-3m
Scale	0.0006442(16)
Cell Mass	312.300
Cell Volume (Å^3)	163.20154
Wt% - Rietveld	18.438(85)
Wt% in Spiked sample	10.005
Wt% in Original sample	0.000
Crystallite Size	
Cry size Lorentzian (nm)	242.5(17)
Crystal Linear Absorption Coeff. (1/cm)	302.930
Crystal Density (g/cm^3)	3.178
Lattice parameters	
a (Å)	5.4648061

Site	Np	x	y	z	Atom	Occ	Beq
Ca1	4	0.00000	0.00000	0.00000	Ca+2	1	0.578
F1	8	0.25000	0.25000	0.25000	F-1	1	0.7821

Peaks Phase 1

Phase name Peaks Phase:0

Type	Position	I		
FP	21.605(24)	114.0(73)	Cry size Lor(nm)	1.112(32)

Port Augusta Fly Ash;

File : "..\Pt Aug FA + 10%CaF rietveld.raw"

R-Values

Rexp : 3.43 Rwp : 5.25 Rp : 4.03 GOF : 1.53
Rexp` : 6.41 Rwp` : 9.81 Rp` : 7.96 DW : 0.85

Quantitative Analysis, Wt%

		Rietveld	Spiked	Original
	Amorphous content	0	45.22(66)	50.24(73)
1	"Quartz low (p) 83849"	19.29(58)	10.57(32)	11.74(36)
2	"Corundum 51687"	1.41(20)	0.77(11)	0.86(12)
3	"Hematite 81248"	1.42(15)	0.776(81)	0.862(38)
4	*"Fluorite 60559"	18.26(22)	10.003	0.000
5	"Mullite 99328"	43.72(53)	23.95(29)	26.62(33)
6	"Maghemite C 87119"	1.39(15)	0.760(80)	0.844(27)
7	"Rutile 82081"	1.205(82)	0.660(45)	0.734(50)
8	"Quartz low 83849"	13.31(63)	7.29(35)	8.10(39)

Background

One on X		13260(110)
Chebychev polynomial, Coefficient	0	432.8(35)
	1	-97.7(35)
	2	42.9(17)

Instrument

Primary radius (mm)	250
Secondary radius (mm)	250

Linear PSD 2Th angular range (°)	3
FDS angle (°)	0.3
Full Axial Convolution	
Filament length (mm)	12
Sample length (mm)	25
Receiving Slit length (mm)	17
Primary Sollers (°)	2.5
Secondary Sollers (°)	2.5

Corrections

Specimen displacement	0.03739(91)
LP Factor	0

Structure 1

Phase name	Quartz low (p) 83849
R-Bragg	2.203
Spacegroup	P3221
Scale	0.002515(90)
Cell Mass	180.252
Cell Volume (Å^3)	113.0545(64)
Wt% - Rietveld	19.29(58)
Wt% in Spiked sample	10.57(32)
Wt% in Original sample	11.74(36)
Crystallite Size	
Cry size Lorentzian (nm)	233(10)
Crystal Linear Absorption Coeff. (1/cm)	95.3407(54)
Crystal Density (g/cm^3)	2.64754(15)
Lattice parameters	
a (Å)	4.91421(11)
c (Å)	5.40568(18)

Site	Np	x	y	z	Atom	Occ	Beq
Si1	3	0.46980	0.00000	0.16667	Si+4	1	2.1
O1	6	0.41380	0.26510	0.28710	O-2	1	2.46

Structure 2

Phase name	Corundum 51687
R-Bragg	3.358
Spacegroup	R-3cH
Scale	0.0000239(34)
Cell Mass	611.768
Cell Volume (Å^3)	256.07(30)
Wt% - Rietveld	1.41(20)
Wt% in Spiked sample	0.77(11)
Wt% in Original sample	0.86(12)
Crystallite Size	
Cry size Lorentzian (nm)	64(19)
Crystal Linear Absorption Coeff. (1/cm)	125.93(15)
Crystal Density (g/cm^3)	3.9671(47)
Lattice parameters	
a (Å)	4.7796(21)
c (Å)	12.943(10)

Site	Np	x	y	z	Atom	Occ	Beq
Al1	12	0.00000	0.00000	0.35230	Al+3	1	0.21
O1	18	0.30650	0.00000	0.25000	O-2	1	0.29

Structure 3

Phase name	Hematite 81248
R-Bragg	1.995
Spacegroup	R-3cH

Scale	0.0000130(14)
Cell Mass	958.149
Cell Volume (Å^3)	301.17(39)
Wt% - Rietveld	1.42(15)
Wt% in Spiked sample	0.776(81)
Wt% in Original sample	0.862(90)
Crystallite Size	
Cry size Lorentzian (nm)	35.9(61)
Crystal Linear Absorption Coeff. (1/cm)	1135.5(15)
Crystal Density (g/cm^3)	5.2828(68)
Lattice parameters	
a (Å)	5.0317(25)
c (Å)	13.736(11)

Site	Np	x	y	z	Atom	Occ	Beq
Fe1	12	0.00000	0.00000	0.35528	Fe+3	1	1
O1	18	0.69389	0.00000	0.25000	O-2	1	1

Structure 4

Phase name	Fluorite 60559
R-Bragg	1.058
Spacegroup	Fm-3m
Scale	0.0009516(38)
Cell Mass	312.300
Cell Volume (Å^3)	163.2692(37)
Wt% - Rietveld	18.26(22)
Wt% in Spiked sample	10.003
Wt% in Original sample	0.000
Crystallite Size	
Cry size Lorentzian (nm)	211.4(25)
Crystal Linear Absorption Coeff. (1/cm)	302.8048(69)
Crystal Density (g/cm^3)	3.176262(72)
Lattice parameters	
a (Å)	5.465561(42)

Site	Np	x	y	z	Atom	Occ	Beq
Ca1	4	0.00000	0.00000	0.00000	Ca+2	1	0.578
F1	8	0.25000	0.25000	0.25000	F-1	1	0.7821

Structure 5

Phase name	Mullite 99328
R-Bragg	3.622
Spacegroup	Pbam
Scale	0.002160(25)
Cell Mass	319.357
Cell Volume (Å^3)	168.418(30)
Wt% - Rietveld	43.72(53)
Wt% in Spiked sample	23.95(29)
Wt% in Original sample	26.62(33)
Crystallite Size	
Cry size Lorentzian (nm)	47.3(10)
Crystal Linear Absorption Coeff. (1/cm)	103.693(18)
Crystal Density (g/cm^3)	3.14874(55)
Lattice parameters	
a (Å)	7.57065(82)
b (Å)	7.70610(80)
c (Å)	2.88682(26)

Site	Np	x	y	z	Atom	Occ	Beq
Al1	2	0.00000	0.00000	0.00000	Al+3	1	3.96
Al2	4	0.15360	0.34170	0.50000	Al+3	0.5	4.44

Si1	4	0.15360	0.34170	0.50000	Si+4	0.37	4.44
Al3	4	0.27900	0.22000	0.50000	Al+3	0.13	1
O1	4	0.35630	0.42180	0.50000	O-2	1	4
O2	4	0.13000	0.22330	0.00000	O-2	1	4.9
O3	2	0.50000	0.00000	0.50000	O-2	0.61	4.5
O4	4	0.42300	0.12000	0.50000	O-2	0.13	4

Structure 6

Phase name	Maghemite C 87119
R-Bragg	2.177
Spacegroup	P4332
Scale	0.00000373(40)
Cell Mass	1692.416
Cell Volume (Å^3)	583.16(68)
Wt% - Rietveld	1.39(15)
Wt% in Spiked sample	0.760(80)
Wt% in Original sample	0.844(89)
Crystallite Size	
Cry size Lorentzian (nm)	25.0(40)
Crystal Linear Absorption Coeff. (1/cm)	1034.2(12)
Crystal Density (g/cm^3)	4.8191(56)
Lattice parameters	
a (Å)	8.3547(32)

Site	Np	x	y	z	Atom	Occ	Beq
Fe1	4	0.62500	0.62500	0.62500	Fe+3	0.35	0.5
Fe2	8	-0.00440	-0.00440	-0.00440	Fe+3	1	0.71
Fe3	12	0.12500	0.36690	0.88310	Fe+3	0.98	0.71
O1	8	0.38170	0.38170	0.38170	O-2	0.99	0.7
O2	24	0.38170	0.87360	0.88190	O-2	1	0.8

Structure 7

Phase name	Rutile 82081
R-Bragg	2.969
Spacegroup	P42/mnm
Scale	0.000335(23)
Cell Mass	152.863
Cell Volume (Å^3)	62.532(19)
Wt% - Rietveld	1.205(82)
Wt% in Spiked sample	0.660(45)
Wt% in Original sample	0.734(50)
Crystallite Size	
Cry size Lorentzian (nm)	171(30)
Crystal Linear Absorption Coeff. (1/cm)	491.76(15)
Crystal Density (g/cm^3)	4.0593(13)
Lattice parameters	
a (Å)	4.59555(51)
c (Å)	2.96090(64)

Site	Np	x	y	z	Atom	Occ	Beq
Ti1	2	0.00000	0.00000	0.00000	Ti+4	0.928	1
O1	4	0.30290	0.30290	0.00000	O-2	1	1

Structure 8

Phase name	Quartz low (s) 83849
R-Bragg	2.093
Spacegroup	P3221
Scale	0.001729(93)
Cell Mass	180.252
Cell Volume (Å^3)	113.484(16)
Wt% - Rietveld	13.31(63)

Wt% in Spiked sample	7.29(35)
Wt% in Original sample	8.10(39)
Crystallite Size	
Cry size Lorentzian (nm)	134.2(51)
Crystal Linear Absorption Coeff. (1/cm)	94.980(13)
Crystal Density (g/cm^3)	2.63751(36)
Lattice parameters	
a (Å)	4.92064(27)
c (Å)	5.41205(45)

Site	Np	x	y	z	Atom	Occ	Beq
Si1	3	0.46980	0.00000	0.16667	Si+4	1	2.1
O1	6	0.41380	0.26510	0.28710	O-2	1	2.46

Peaks Phase 1

Phase name — Peaks Phase:0

Type	Position	I		
SPV	25.03(11)	108.9(18)	h1	4.41(13)
			h2	5.35(14)
			Lorentzian mix 1	0.5
			Lorentzian mix 2	0.5

Bayswater Fly Ash;

File : "..\Bays FA + 10%CaF rietveld.raw"

R-Values

Rexp : 3.34	Rwp : 5.02	Rp : 3.88	GOF : 1.51
Rexp`: 5.28	Rwp`: 7.94	Rp` : 6.40	DW : 0.89

Quantitative Analysis, Wt%

		Rietveld	Spiked	Original
	Amorphous content	0	61.38(36)	68.21(39)
1	"Quartz low 849"	28.41(42)	10.97(16)	12.19(18)
2	Corundum	0.67(17)	0.257(64)	0.286(71)
3	"Maghemite C ICSD#87119"	2.45(16)	0.944(62)	1.049(69)
4	*"Fluorite ICSD 60559"	25.91(24)	10.008	0.000
5	"Mullite ICSD#66449"	17.17(34)	6.63(13)	7.37(15)
6	"Quartz low"	25.40(45)	9.81(17)	10.90(19)

Background

One on X		16760(110)
Chebychev polynomial, Coefficient	0	359.4(30)
	1	-43.3(30)
	2	20.9(15)

Instrument

Primary radius (mm)	250
Secondary radius (mm)	250
Linear PSD 2Th angular range (°)	3
FDS angle (°)	0.3
Full Axial Convolution	
Filament length (mm)	12
Sample length (mm)	25
Receiving Slit length (mm)	17

Primary Sollers (°)	2.5
Secondary Sollers (°)	2.5

Corrections

Specimen displacement	0.02380(98)
LP Factor	0

Structure 1

Phase name	Quartz low 849
R-Bragg	2.235
Spacegroup	P3221
Scale	0.002814(51)
Cell Mass	180.252
Cell Volume (Å^3)	113.581(11)
Wt% - Rietveld	28.41(42)
Wt% in Spiked sample	10.97(16)
Wt% in Original sample	12.19(18)
Crystallite Size	
Cry size Lorentzian (nm)	112.1(26)
Crystal Linear Absorption Coeff. (1/cm)	94.8986(88)
Crystal Density (g/cm^3)	2.63526(25)
Lattice parameters	
a (Å)	4.92314(18)
c (Å)	5.41117(32)

Site	Np	x	y	z	Atom	Occ	Beq
Si1	3	0.46980	0.00000	0.16667	Si+4	1	2.1
O1	6	0.41380	0.26510	0.28710	O-2	1	2.46

Structure 2

Phase name	Corundum
R-Bragg	3.322
Spacegroup	R-3cH
Scale	0.0000087(22)
Cell Mass	611.768
Cell Volume (Å^3)	254.06(29)
Wt% - Rietveld	0.67(17)
Wt% in Spiked sample	0.257(64)
Wt% in Original sample	0.286(71)
Crystallite Size	
Cry size Lorentzian (nm)	150(93)
Crystal Linear Absorption Coeff. (1/cm)	126.92(15)
Crystal Density (g/cm^3)	3.9985(46)
Lattice parameters	
a (Å)	4.7541(21)
c (Å)	12.9801(96)

Site	Np	x	y	z	Atom	Occ	Beq
Al1	12	0.00000	0.00000	0.35230	Al+3	1	0.21
O1	18	0.30650	0.00000	0.25000	O-2	1	0.29

Structure 3

Phase name	Maghemite C ICSD#87119
R-Bragg	2.097
Spacegroup	P4332
Scale	0.00000500(33)
Cell Mass	1692.416
Cell Volume (Å^3)	586.45(45)
Wt% - Rietveld	2.45(16)
Wt% in Spiked sample	0.944(62)
Wt% in Original sample	1.049(69)

Crystallite Size	
Cry size Lorentzian (nm)	25.0(26)
Crystal Linear Absorption Coeff. (1/cm)	1028.38(79)
Crystal Density (g/cm^3)	4.7921(37)
Lattice parameters	
a (Å)	8.3703(22)

Site	Np	x	y	z	Atom	Occ	Beq
Fe1	4	0.62500	0.62500	0.62500	Fe+3	0.35	0.5
Fe2	8	-0.00440	-0.00440	-0.00440	Fe+3	1	0.71
Fe3	12	0.12500	0.36690	0.88310	Fe+3	0.98	0.71
O1	8	0.38170	0.38170	0.38170	O-2	0.99	0.7
O2	24	0.38170	0.87360	0.88190	O-2	1	0.8

Structure 4

Phase name	Fluorite ICSD 60559
R-Bragg	1.363
Spacegroup	Fm-3m
Scale	0.0010304(39)
Cell Mass	312.300
Cell Volume (Å^3)	163.2727(39)
Wt% - Rietveld	25.91(24)
Wt% in Spiked sample	10.008
Wt% in Original sample	0.000
Crystallite Size	
Cry size Lorentzian (nm)	195.8(21)
Crystal Linear Absorption Coeff. (1/cm)	302.7983(73)
Crystal Density (g/cm^3)	3.176194(76)
Lattice parameters	
a (Å)	5.465601(44)

Site	Np	x	y	z	Atom	Occ	Beq
Ca1	4	0.00000	0.00000	0.00000	Ca+2	1	0.578
F1	8	0.25000	0.25000	0.25000	F-1	1	0.7821

Structure 5

Phase name	Mullite ICSD#66449
R-Bragg	2.853
Spacegroup	Pbam
Scale	0.000650(14)
Cell Mass	318.701
Cell Volume (Å^3)	168.045(33)
Wt% - Rietveld	17.17(34)
Wt% in Spiked sample	6.63(13)
Wt% in Original sample	7.37(15)
Crystallite Size	
Cry size Lorentzian (nm)	87.1(42)
Crystal Linear Absorption Coeff. (1/cm)	103.535(20)
Crystal Density (g/cm^3)	3.14925(62)
Lattice parameters	
a (Å)	7.55783(91)
b (Å)	7.69687(94)
c (Å)	2.88878(28)

Site	Np	x	y	z	Atom	Occ	Beq
Al1	2	0.00000	0.00000	0.00000	Al+3	1	1.14
Al2	4	0.14920	0.34080	0.50000	Al+3	0.5	1.14
Si2	4	0.14920	0.34080	0.50000	Si+4	0.352	1.14
Al3	4	0.26260	0.20650	0.50000	Al+3	0.148	1.14
O1	4	0.35700	0.42290	0.50000	O-2	1	1.14
O2	4	0.12730	0.21990	0.00000	O-2	1	1.14

O3	2	0.50000	0.00000	0.50000	O-2	0.556	1.14
O4	4	0.44210	0.05340	0.50000	O-2	0.148	1.14

Structure 6

Phase name	Quartz low
R-Bragg	2.373
Spacegroup	P3221
Scale	0.002487(54)
Cell Mass	180.252
Cell Volume (Å^3)	114.871(17)
Wt% - Rietveld	25.40(45)
Wt% in Spiked sample	9.81(17)
Wt% in Original sample	10.90(19)
Crystallite Size	
Cry size Lorentzian (nm)	80.1(20)
Crystal Linear Absorption Coeff. (1/cm)	93.833(14)
Crystal Density (g/cm^3)	2.60568(39)
Lattice parameters	
a (Å)	4.94362(29)
c (Å)	5.42737(51)

Site	Np	x	y	z	Atom	Occ	Beq
Si1	3	0.46980	0.00000	0.16667	Si+4	1	2.1
O1	6	0.41380	0.26510	0.28710	O-2	1	2.46

Peaks Phase 1

Phase name — Peaks Phase:0

Type	Position	I		
SPV	21.528(41)	164.7(11)	h1	3.181(47)
			h2	4.908(48)
			Lorentzian mix 1	0.5
			Lorentzian mix 2	0.5
SPV	89.77168	48.3	h1	0.05
			h2	0.05
			Lorentzian mix 1	0.5
			Lorentzian mix 2	0.5

Appendix B

This appendix contains additional images and graphs not listed in the main part of the thesis.

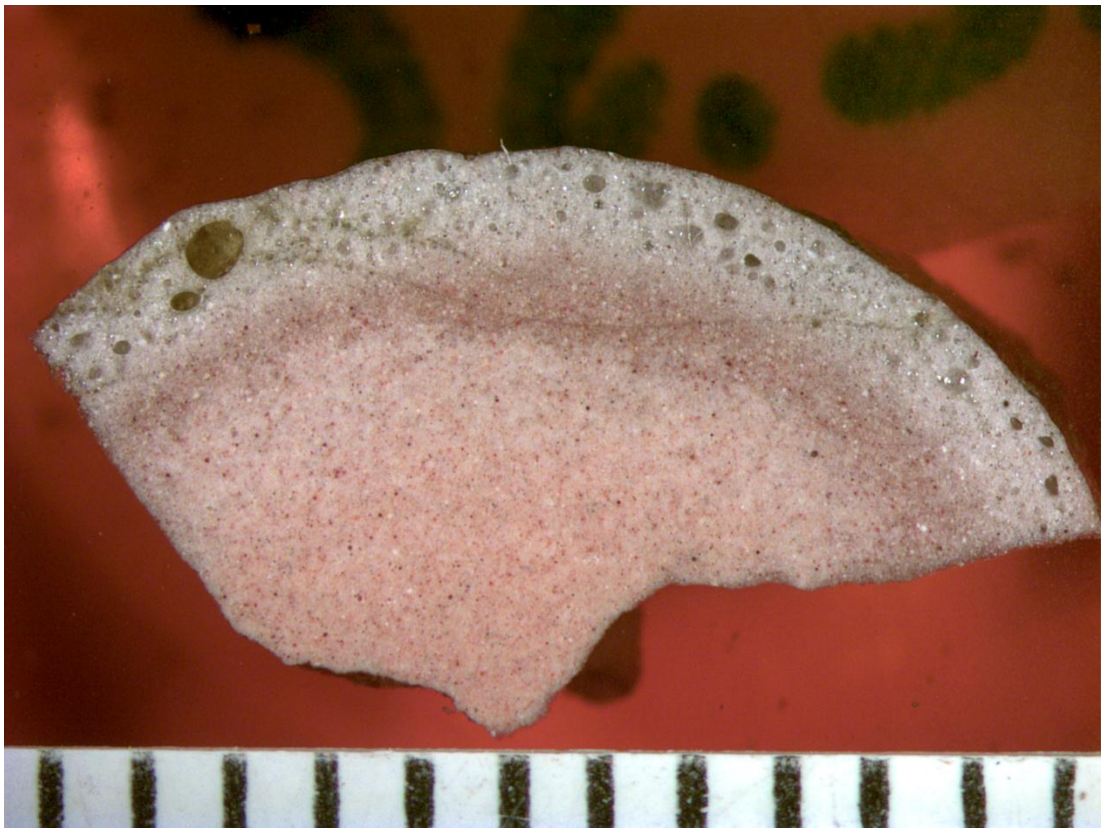

Figure A-1 Optical microscope image of a Bayswater 2.5 geopolymer after firing (embedded in epoxy resin) showing an increase in porosity around the edge of the sample. Scale bar divisions are 1 mm.

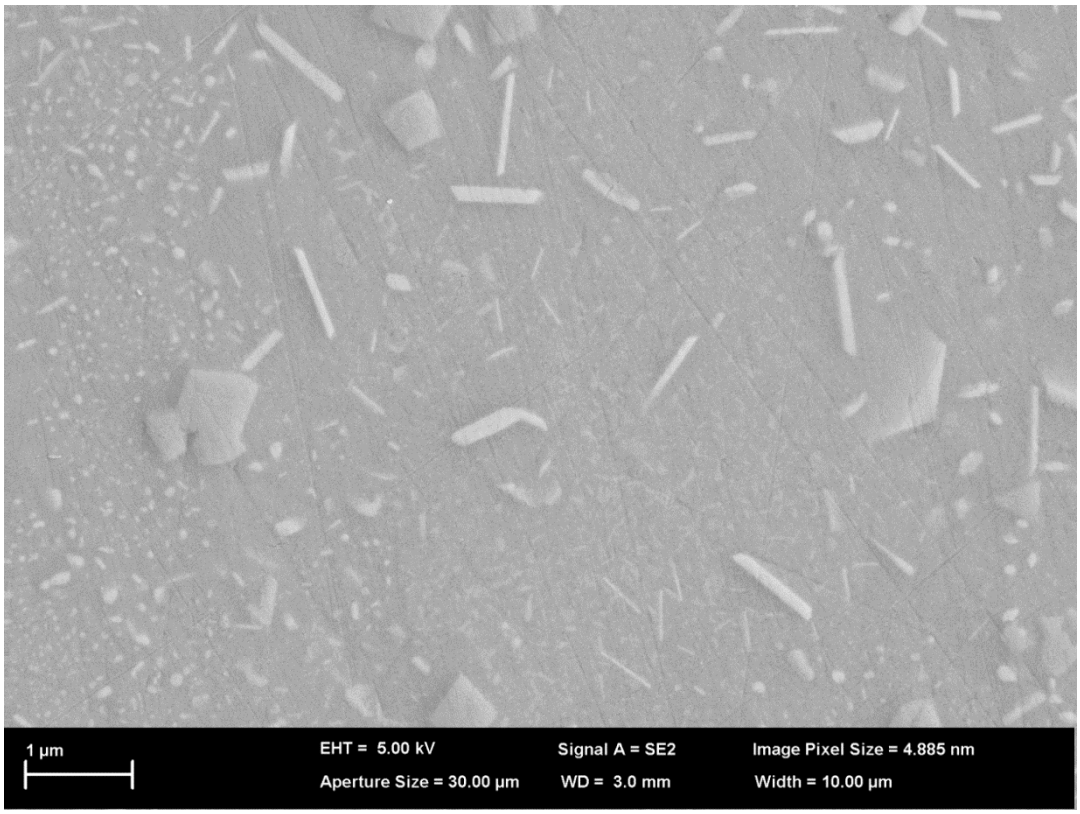

Figure A-2 High magnification SEM micrograph from the Port Augusta 2.5 geopolymer (polished) after firing indicating the presence of small crystallites in the geopolymer gel.

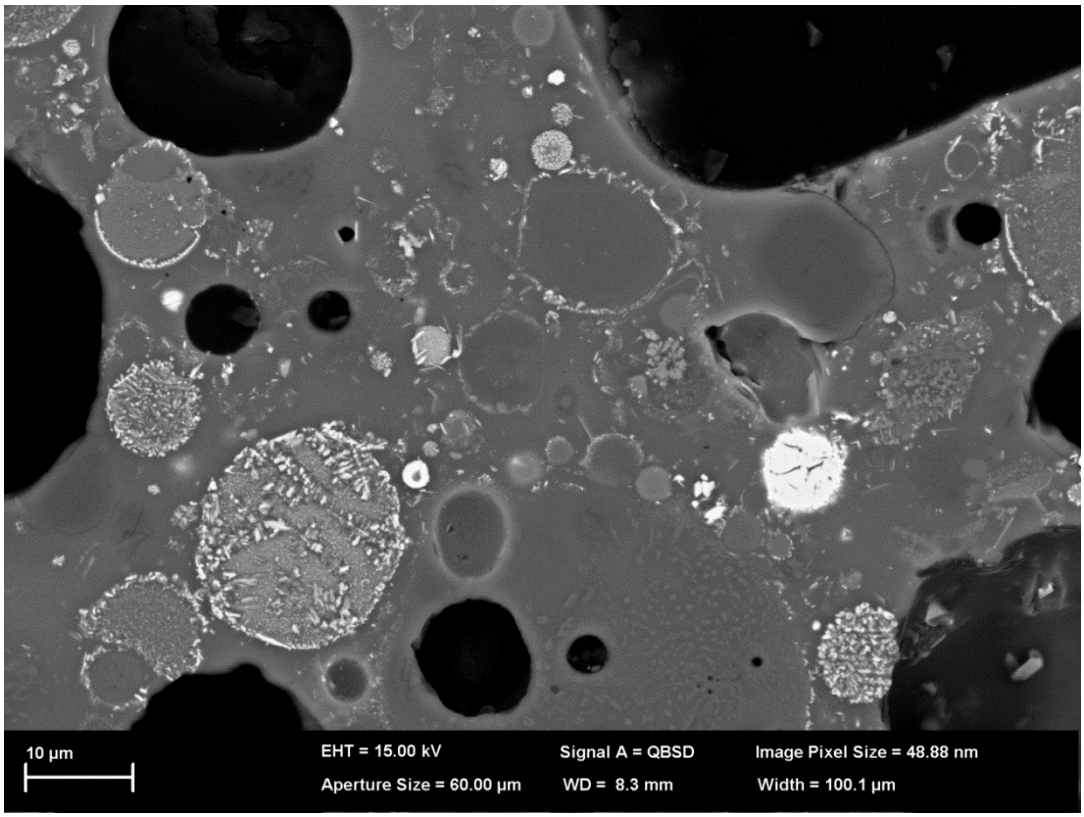

Figure A-3 SEM micrograph from the Collie 2.5 geopolymer (polished) showing that most of the discrete fly ash particles after firing contained high atomic number material (bright regions in the BSE image).

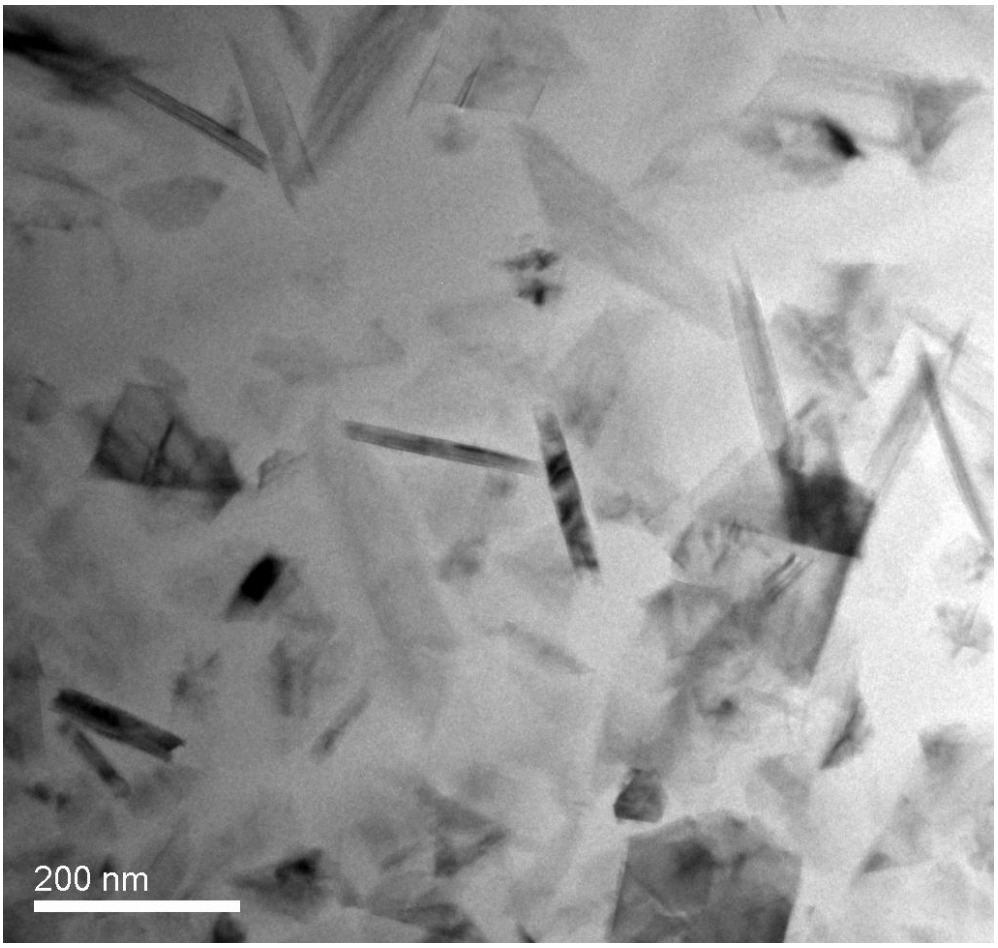

Figure A-4 TEM micrograph of a 100 nm thick lamella that was cut out of a Collie fly ash particle using a focussed ion beam. EDS confirmed the needle shaped particles were mullite.

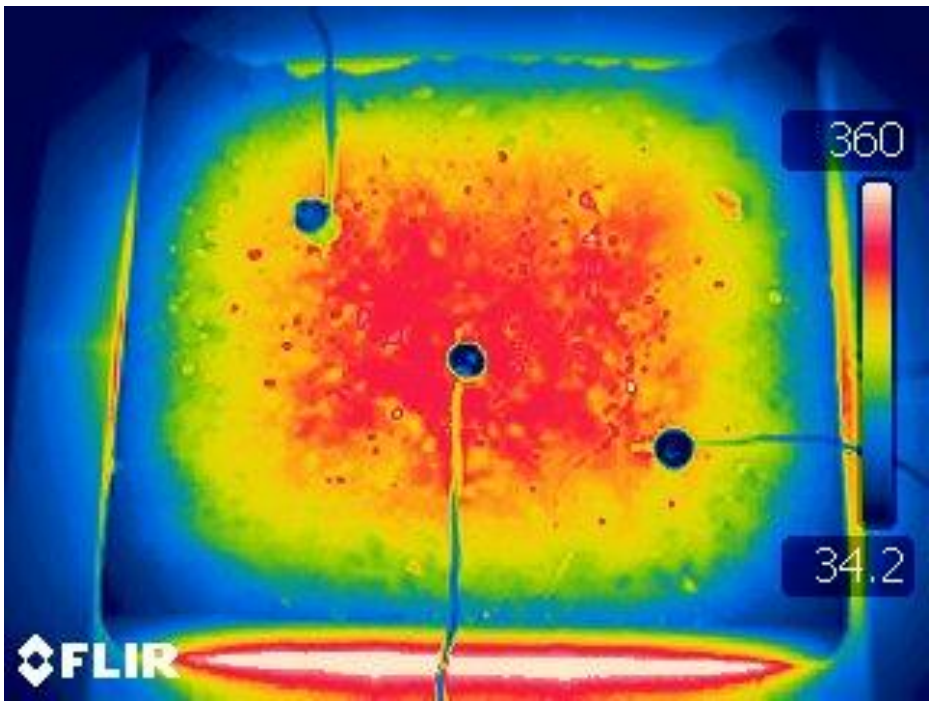

Figure A-5 Thermal image of the cold side of the low density Tarong 2.5 geopolymer 120 minutes into a fire test. Thermal images indicated that the hottest part of the fire tested samples was near the centre.

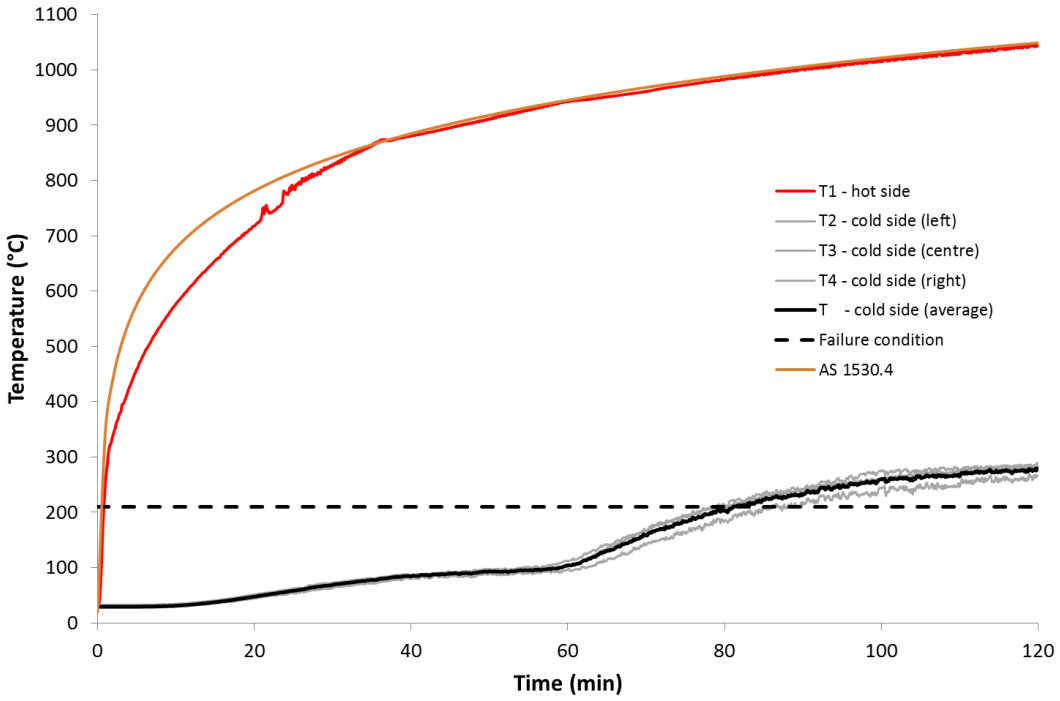

Figure A-6 Graph showing details of the Eraring 2.5 geopolymer fire test.

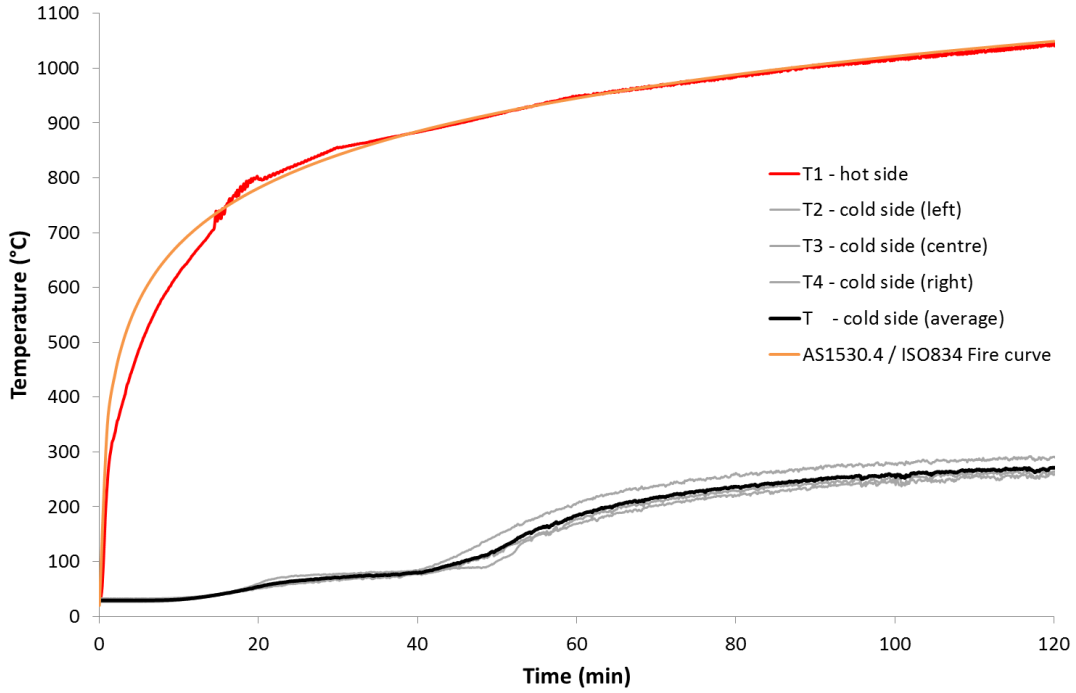

Figure A-7 Graph showing details of the Eraring 2.5 low density geopolymer fire test.

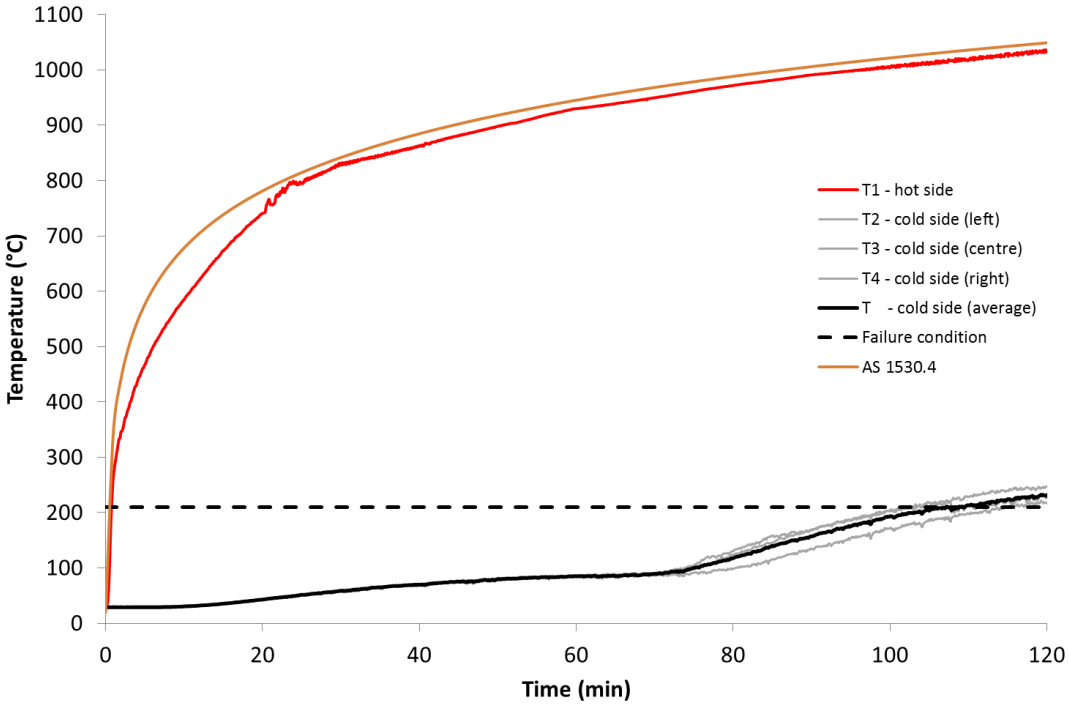

Figure A-8 Graph showing details of the Tarong 2.5 geopolymer fire test.

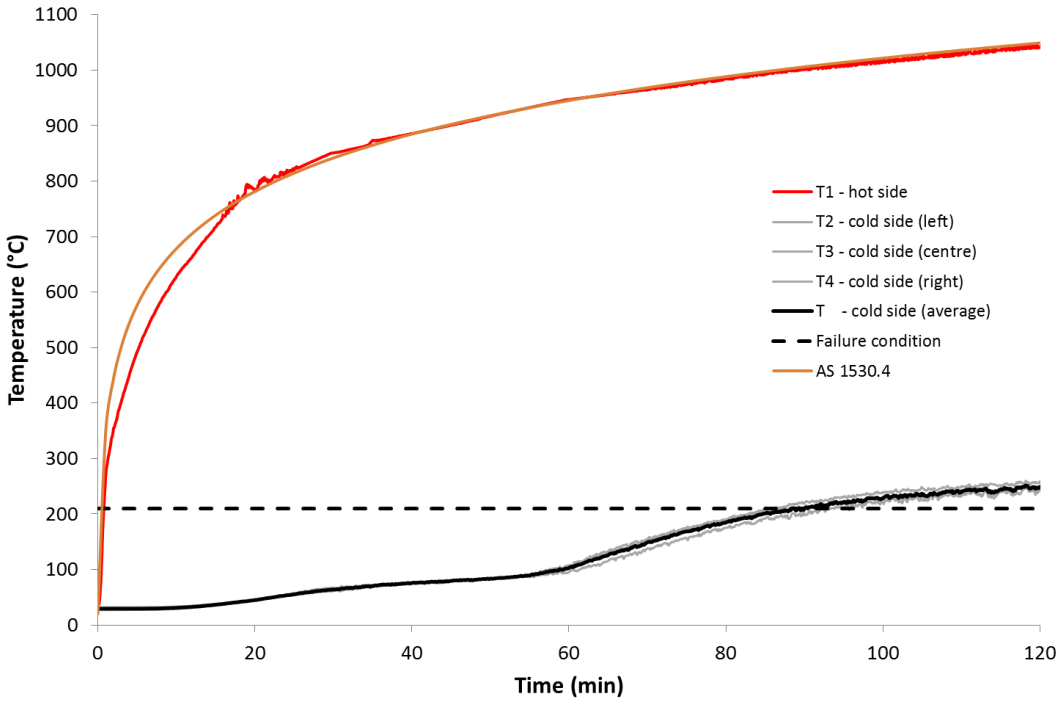

Figure A-9 Graph showing details of the Tarong 2.5 low density geopolymer fire test.

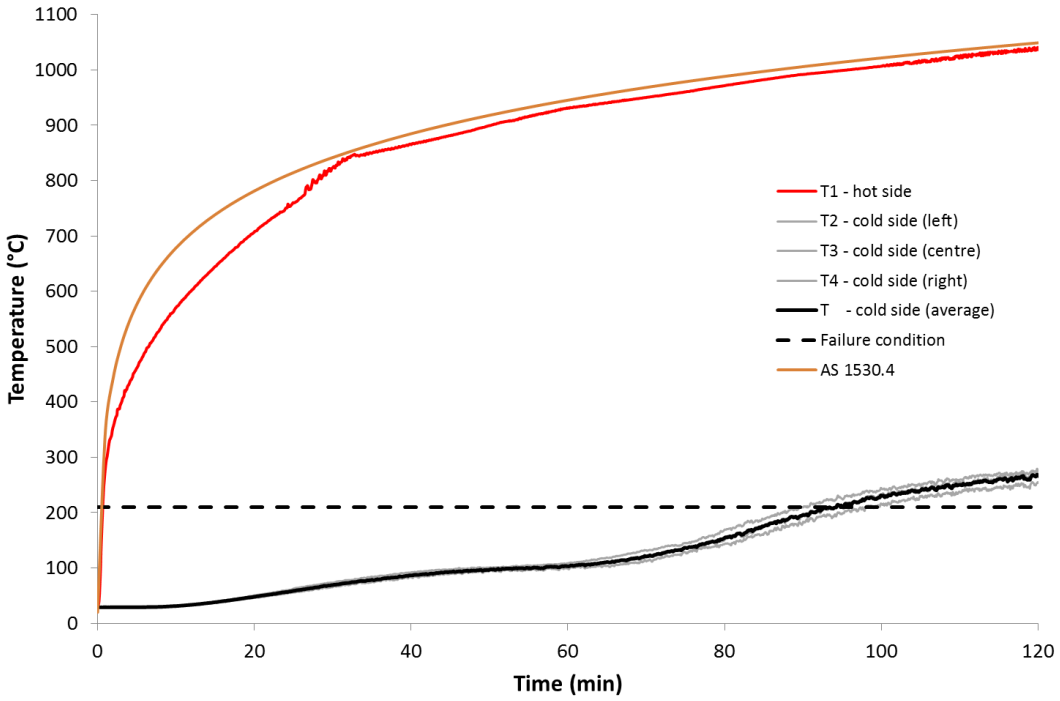

Figure A-10 Graph showing details of the Port Augusta 2.5 geopolymer fire test.

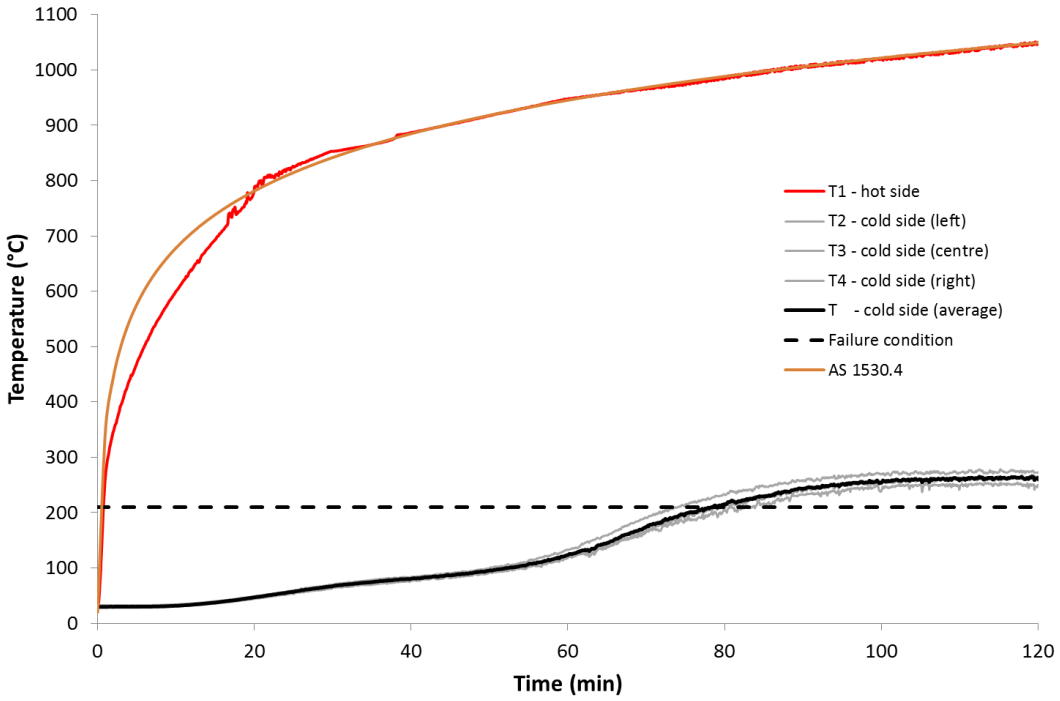

Figure A-11 Graph showing details of the Port Augusta 2.5 low density geopolymer fire test.

Appendix C

Publications resulting from this research at the time of printing;

RICKARD, W. & VAN RIESSEN, A. 2008a. Thermal Character of Geopolymers Synthesised from Class F Fly Ash Containing High Concentrations of Iron and α-Quartz. *Centre for Sustainable Resource Processing (CSRP) conference.* Brisbane, Australia.

RICKARD, W. & VAN RIESSEN, A. 2008b. Thermal Character of Geopolymers Synthesised from Class F Fly Ash Containing High Concentrations of Iron and α-Quartz. *The 2nd International Congress on Ceramics. Conference poster.* Verona, Italy.

RICKARD, W. & VAN RIESSEN, A. 2008c. Thermal Properties of fly ash geopolymers. *Centre for Sustainable Resource Processing (CSRP) geopolymer conference.* Perth, Australia.

RICKARD, W. 2009a. Assessing the Suitability of Geopolymeric Materials for High Temperature Industrial Applications. *Centre for Sustainable Resource Processing (CSRP) student symposium.* Pinjarra, Australia.

RICKARD, W. 2009b. From waste to paste: Fireproof concrete that has risen from the ashes. *Cooperative Research Centres Association (CRCA) conference.* Canberra, Australia.

RICKARD, W. & VAN RIESSEN, A. 2009a. Assessing the Suitability of Geopolymeric Materials for High Temperature Industrial Applications. *Centre for Sustainable Resource Processing (CSRP) annual geopolymer conference.* Perth, Australia.

RICKARD, W. & VAN RIESSEN, A. 2009b. Assessing the Suitability of Geopolymeric Materials for High Temperature Industrial Applications. *Departmental Seminar. Department of Imaging and Applied Physics, Curtin University of Technology.* Perth, Australia.

VAN RIESSEN, A., RICKARD, W. D. A. & SANJAYAN, J. 2009. Thermal Properties of Geopolymers. *In:* PROVIS, J. L. & VAN DEVENTER, J. S. J. (eds.) *Geopolymers: Structure, processing, properties and industrial applications.* Woodhead Publishing Ltd.

RICKARD, W. & VAN RIESSEN, A. 2010. Phase and Strength Evolution of Fly Ash Geopolymers Exposed to Standard Fire Conditions. *12th International Ceramics conference (CIMTEC).* Montecatini Terme, Italy.

RICKARD, W. D. A., VAN RIESSEN, A. & WALLS, P. 2010. Thermal Character of Geopolymers Synthesized from Class F Fly Ash Containing High Concentrations of Iron and α-Quartz. *International Journal of Applied Ceramic Technology,* 7**,** 81-88.

RICKARD, W., NATALI, A., BIGNOZZI, M. C. & VAN RIESSEN, A. 2011a. The Fire Resistant Properties of Geopolymers Synthesised from a Range of Aluminosilicate Sources. *PacRim 9. The 9th International Meeting of Pacific Rim Ceramic Societies.* Cairns, Australia.

RICKARD, W., WILLIAMS, R. P., TEMUUJIN, J. & VAN RIESSEN, A. 2011b. In situ characterisation of fly ash geopolymers exposed to an Australian standard fire curve using synchrotron and laboratory XRD techniques. *Australian X-ray Analytical Association conference.* Sydney, Australia.

RICKARD, W. D. A., WILLIAMS, R., TEMUUJIN, J. & VAN RIESSEN, A. 2011c. Assessing the suitability of three Australian fly ashes as an aluminosilicate source for geopolymers in high temperature applications. *Materials Science and Engineering: A,* 528**,** 3390-3397.

RICKARD, W., TEMUUJIN, J. & VAN RIESSEN, A. 2012. Thermal analysis of geopolymer pastes synthesised from five fly ashes of variable composition. *Journal of Non-Crystalline Solids,* 358, 1830-1839.

VAN RIESSEN, A. & RICKARD, W. In press 2012. Thermal Properties of Geopolymers. *In:* PROVIS, J. L. (ed.) *RILEM Technical Committee on Alkali Activated Materials (TC 224-AAM).*

RICKARD, W. & VAN RIESSEN, A. Submitted 2012. Performance of solid and cellular structured fly ash geopolymers exposed to a simulated fire. *Cement and Concrete Composites.*

Appendix D

The following information contains details of the licence agreements / clearances that were granted in order to use the copyrighted images in this thesis.

Elsevier Journals

ELSEVIER LICENSE TERMS AND CONDITIONS

Nov 03, 2011

This is a License Agreement between William D Rickard ("You") and Elsevier ("Elsevier") provided by Copyright Clearance Center ("CCC"). The license consists of your order details, the terms and conditions provided by Elsevier, and the payment terms and conditions.

Figure 2-6;

Supplier	Elsevier Limited The Boulevard,Langford Lane Kidlington,Oxford,OX5 1GB,UK
Registered Company Number	1982084
Customer name	William D Rickard
Customer address	Kent st Bentley, Western Australia 6147
License number	2781170952526
License date	Nov 03, 2011
Licensed content publisher	Elsevier
Licensed content publication	Fuel
Licensed content title	Fly ash characterization by SEM–EDS
Licensed content author	Barbara G. Kutchko,Ann G. Kim
Licensed content date	December 2006
Licensed content volume number	85
Licensed content issue number	17-18
Number of pages	8
Start Page	2537
End Page	2544
Type of Use	reuse in a thesis/dissertation
Intended publisher of new work	other
Portion	figures/tables/illustrations
Number of figures/tables/illustrations	1
Format	both print and electronic
Are you the author of this Elsevier article?	No

Figure 2-7;

Supplier	Elsevier Limited The Boulevard,Langford Lane Kidlington,Oxford,OX5 1GB,UK
Registered Company Number	1982084
Customer name	William D Rickard
Customer address	Kent st
Bentley, Western Australia 6147	
License number	2781170516638
License date	Nov 03, 2011
Licensed content publisher	Elsevier
Licensed content publication	Cement and Concrete Research
Licensed content title	Microstructure development of alkali-activated fly ash cement: a descriptive model
Licensed content author	A. Fernández-Jiménez,A. Palomo,M. Criado
Licensed content date	June 2005
Licensed content volume number	35
Licensed content issue number	6
Number of pages	6
Start Page	1204
End Page	1209
Type of Use	reuse in a thesis/dissertation
Portion	figures/tables/illustrations
Number of figures/tables/illustrations	1
Format	both print and electronic
Are you the author of this Elsevier article?	Yes
Will you be translating?	No

Figure 2-12;

Supplier	Elsevier Limited The Boulevard,Langford Lane Kidlington,Oxford,OX5 1GB,UK
Registered Company Number	1982084
Customer name	William D Rickard
Customer address	Kent st
Bentley, Western Australia 6147	
License number	2781171368445
License date	Nov 03, 2011
Licensed content publisher	Elsevier
Licensed content publication	Journal of Non-Crystalline Solids
Licensed content title	Thermal evolution of metakaolin geopolymers: Part 1 – Physical evolution
Licensed content author	Peter Duxson,Grant C. Lukey,Jannie S.J. van Deventer
Licensed content date	15 December 2006
Licensed content volume number	352
Licensed content issue number	52-54
Number of pages	15
Start Page	5541
End Page	5555
Type of Use	reuse in a thesis/dissertation
Intended publisher of new work	other
Portion	figures/tables/illustrations
Number of figures/tables/illustrations	1
Format	both print and electronic
Are you the author of this	No

Figure 2-17 and 2-20;

Supplier	Elsevier Limited The Boulevard,Langford Lane Kidlington,Oxford,OX5 1GB,UK
Registered Company Number	1982084
Customer name	William D Rickard
Customer address	Kent st
Bentley, Western Australia 6147	
License number	2781170795761
License date	Nov 03, 2011
Licensed content publisher	Elsevier
Licensed content publication	Cement and Concrete Research
Licensed content title	Thermal behaviour of geopolymers prepared using class F fly ash and elevated temperature curing
Licensed content author	T. Bakharev
Licensed content date	June 2006
Licensed content volume number	36
Licensed content issue number	6
Number of pages	14
Start Page	1134
End Page	1147
Type of Use	reuse in a thesis/dissertation
Intended publisher of new work	other
Portion	figures/tables/illustrations
Number of figures/tables/illustrations	2
Format	both print and electronic
Are you the author of this	No

Figure 2-26;

Supplier	Elsevier Limited The Boulevard,Langford Lane Kidlington,Oxford,OX5 1GB,UK
Registered Company Number	1982084
Customer name	William D Rickard
Customer address	Kent st
Bentley, Western Australia 6147	
License number	2781180661940
License date	Nov 03, 2011
Licensed content publisher	Elsevier
Licensed content publication	Chemical Engineering Journal
Licensed content title	Recycling potential of coal fly ash and titanium waste as new fireproof products
Licensed content author	Luis F - Valle,José Vale
Licensed content date	15 September 2003
Licensed content volume number	95
Licensed content issue number	1-3
Number of pages	7
Start Page	155
End Page	161
Type of Use	reuse in a thesis/dissertation
Intended publisher of new work	other
Portion	figures/tables/illustrations
Number of figures/tables/illustrations	1
Format	both print and electronic
Are you the author of this	No

Figure 2-21;

License Number	2781180086038
License date	Nov 03, 2011
Licensed content publisher	Springer
Licensed content publication	Journal of Materials Science (full set)
Licensed content title	Physical evolution of Na-geopolymer derived from metakaolin up to 1000 °C
Licensed content author	Peter Duxson
Licensed content date	May 1, 2007
Volume number	42
Issue number	9
Type of Use	Thesis/Dissertation
Portion	Figures
Author of this Springer article	Yes and you are the sole author of the new work
Order reference number	
Title of your thesis / dissertation	Assessing the suitability of geopolymers for high temperature industrial applications
Expected completion date	Jul 2012
Estimated size(pages)	250
Total	0.00 USD

Other Publishers

Figure 2-4;

PERMISSION TO USE COPYRIGHT MATERIAL AS SPECIFIED BELOW:

Figure 4 from the following article;
ROWLES, M. & O'CONNOR, B. 2003. Chemical optimisation of the compressive strength of aluminosilicate geopolymers synthesised by sodium silicate activation of metakaolinite. ***Journal of Materials Chemistry, vol 13, issue 5, pages 1161-1165.***

I hereby give permission for **William Rickard** to include the abovementioned material in his higher degree thesis for the Curtin University of Technology, and to communicate this material via the Australasian Digital Thesis Program. This permission is granted on a non-exclusive basis and for an indefinite period.

~~I confirm that I am the copyright owner of the specified material.~~ see below

Permission to use this material is subject to the following conditions: [Delete if not applicable]

Signed: Gill Cockhead

Name: Gill Cockhead

Position: Publishing Contracts + Copyright Executive

Date: 8/10/11

The Royal Society of Chemistry (RSC) has a licence from the copyright owner which entitles the RSC to grant this permission. As far as the RSC is aware, the material does not infringe upon the copyright or other rights of anyone.

The RSC recommends the following style for acknowledgements:

[original citation] – Reproduced by permission of the Royal Society of Chemistry

Please return signed form to;

William Rickard
Department of Imaging and Applied Physics
GPO Box U1987 Perth
Western Australia 6845

Or email completed copy to;
w.rickard@curtin.edu.au

PERMISSION GRANTED

The Royal Society of Chemistry is a Signatory to the S.T.M. Guidelines on Permissions

Figure 2-19;

PERMISSION TO USE COPYRIGHT MATERIAL AS SPECIFIED BELOW:

Figure 15.12 from the following book chapter;
van Riessen, A., Rickard, W., & Sanjayan, J. (2009). Thermal properties of geopolymers. In J. L. Provis & J. S. J. van Deventer (Eds.), *Geopolymers: Structures, Processing, Properties and Industrial Applications* (pp. 317-344). Cambridge, UK: Woodhead.

I hereby give permission for **William Rickard** to include the abovementioned material in his higher degree thesis for the Curtin University of Technology, and to communicate this material via the Australasian Digital Thesis Program. This permission is granted on a non-exclusive basis and for an indefinite period.

I confirm that I am the copyright owner of the specified material.

Permission to use this material is subject to the following conditions: [Delete if not applicable]

Signed:

Name: JULIE PLEASANCE

Position: RIGHTS MANAGER

Date: 7/11/11

PLEASE GIVE FULL ACKNOWLEDGEMENT TO THE TITLE, ISBN, AUTHOR AND PUBLISHER.

Please return signed form to;

William Rickard
Department of Imaging and Applied Physics
GPO Box U1987 Perth
Western Australia 6845

Or email completed copy to;
w.rickard@curtin.edu.au

Figure 2-8;

-----Original Message-----
From: PermissionsUS@wiley.com on www.wiley.com [mailto:webmaster@wiley.com]
Sent: Tuesday, November 01, 2011 10:26 AM
To: Permissions - US
Subject: Republication/Electronic Request Form

A01_First_Name: William
A02_Last_Name: Rickard
A03_Company_Name: Curtin University
A04_Address: Kent street
A05_City: Bentley
A06_State: Western Australia
A07_Zip: 6102
A08_Country: Australia
A09_Contact_Phone_Number: +61 428269455
A10_Fax: +61 8 92662377
A11_Emails: w.rickard@curtin.edu.au
A12_Reference:
A13_Book_Title: Ceramic Transactions Vol 153
A40_Book_or_Journal: Journal
A14_Book_Author:
A15_Book_ISBN:
A16_Journal_Month:
A17_Journal_Year: 2003
A18_Journal_Volume: 153
A19_Journal_Issue_Number: 153
A20_Copy_Pages: Figure 5
A21_Maximum_Copies: 3
A22_Your_Publisher: Curtin University
A23_Your_Title: Assessing the suitability of geopolymers for high temperature industrial applications
A24_Publication_Date: July 2012
A25_Format: print
A41_Ebook_Reader_Type:
A26_If_WWW_URL:
A27_If_WWW_From_Adopted_Book:
A28_If_WWW_Password_Access:
A45_WWW_Users:
A29_If_WWW_Material_Posted_From:
A30_If_WWW_Material_Posted_To:
A42_If_Intranet_URL:
A32_If_Intranet_From_Adopted_Book:
A33_If_Intranet_Password_Access:
A48_Intranet_Users:
A34_If_Intranet_Material_Posted_From:
A35_If_Intranet_Material_Posted_To:
A50_If_Software_Print_Type:
A60_If_Other_Type:
A37_Comments_For_Request: I would like to reproduce an extract of this work in the literature review section of a doctoral thesis which I am currently undertaking at Curtin University of Technology in Perth, Western Australia. The subject of my research is fire resistant geopolymeric materials. I am carrying out this research in my own right and have no association with any commercial organisation or sponsor.

I would like to use figure 5 from the following article;
KRIVEN, W. M., BELL, J. L. & GORDON, M. 2003. Microstructure and Microchemistry of Fully-Reacted Geopolymers and Geopolymer Matrix Composites. Ceramic Transactions, 153, 227-250.

PERMISSION GRANTED
BY: _____
Global Rights Dept., John Wiley & Sons, Inc.

NOTE: No rights are granted to use content that appears in the work with credit to another source

Figure 2-10;

-----Original Message-----
From: PermissionsUS@wiley.com on www.wiley.com [mailto:webmaster@wiley.com]
Sent: Tuesday, November 01, 2011 10:32 AM
To: Permissions - US
Subject: Republication/Electronic Request Form

A01_First_Name: William
A02_Last_Name: Rickard
A03_Company_Name: Curtin University
A04_Address: Kent st
A05_City: Bentley
A06_State: Western Australia
A07_Zip: 6102
A08_Country: Australia
A09_Contact_Phone_Number: +61 428269455
A10_Fax: +61 8 92662377
A11_Emails: w.rickard@curtin.edu.au
A12_Reference:
A13_Book_Title: Ceramic Transactions Vol 165 Fig 14
A40_Book_or_Journal: Journal
A14_Book_Author:
A15_Book_ISBN:
A16_Journal_Month:
A17_Journal_Year: 2005
A18_Journal_Volume: 165
A19_Journal_Issue_Number: 165
A20_Copy_Pages: Figure 14, Gordon arcticle
A21_Maximum_Copies: 3
A22_Your_Publisher: Curtin University
A23_Your_Title: Assessing the suitability of geopolymers for high temperature industrial applications
A24_Publication_Date: July 2012
A25_Format: print
A41_Ebook_Reader_Type:
A26_If_WWW_URL:
A27_If_WWW_From_Adopted_Book:
A28_If_WWW_Password_Access:
A45_WWW_Users:
A29_If_WWW_Material_Posted_From:
A30_If_WWW_Material_Posted_To:
A42_If_Intranet_URL:
A32_If_Intranet_From_Adopted_Book:
A33_If_Intranet_Password_Access:
A48_Intranet_Users:
A34_If_Intranet_Material_Posted_From:
A35_If_Intranet_Material_Posted_To:
A50_If_Software_Print_Type:
A60_If_Other_Type:
A37_Comments_For_Request: I would like to reproduce an extract of this work in the literature review section of a doctoral thesis which I am currently undertaking at Curtin University of Technology in Perth, Western Australia. The subject of my research is fire resistant geopolymeric materials. I am carrying out this research in my own right and have no association with any commercial organisation or sponsor. The specific material that I would like to use for the purposes of the thesis is;

Figure 14 from the following article;
GORDON, M., BELL, J. & KRIVEN, W. M. 2005. Comparison of Naturally and Synthetically Derived, Potassium Based Geopolymers. Ceramic Transactions, 165, 95-106.

PERMISSION GRANTED
BY: _____
Global Rights Dept., John Wiley & Sons, Inc.

NOTE: No rights are granted to use content that appears in the work with credit to another source